Flame-synthesized ceria- and titania-supported Co and Ni catalysts for CO2 hydrogenation

Citation for published version (APA):
Evtushkova, A. (in press). *Flame-synthesized ceria- and titania-supported Co and Ni catalysts for CO2 hydrogenation*. [Phd Thesis 1 (Research TU/e / Graduation TU/e), Chemical Engineering and Chemistry]. Eindhoven University of Technology.

Document status and date:
Accepted/In press: 13/05/2025

Document Version:
Publisher’s PDF, also known as Version of Record (includes final page, issue and volume numbers)

Please check the document version of this publication:

• A submitted manuscript is the version of the article upon submission and before peer-review. There can be important differences between the submitted version and the official published version of record. People interested in the research are advised to contact the author for the final version of the publication, or visit the DOI to the publisher's website.
• The final author version and the galley proof are versions of the publication after peer review.
• The final published version features the final layout of the paper including the volume, issue and page numbers.

Link to publication

General rights
Copyright and moral rights for the publications made accessible in the public portal are retained by the authors and/or other copyright owners and it is a condition of accessing publications that users recognise and abide by the legal requirements associated with these rights.

- Users may download and print one copy of any publication from the public portal for the purpose of private study or research.
- You may not further distribute the material or use it for any profit-making activity or commercial gain
- You may freely distribute the URL identifying the publication in the public portal.

If the publication is distributed under the terms of Article 25fa of the Dutch Copyright Act, indicated by the “Taverne” license above, please follow below link for the End User Agreement:

www.tue.nl/taverne

Take down policy
If you believe that this document breaches copyright please contact us at:

openaccess@tue.nl

providing details and we will investigate your claim.

Download date: 06. May. 2025

Flame-synthesized ceria- and titania-supported Co and Ni catalysts for CO_2 hydrogenation

PROEFSCHRIFT

ter verkrijging van de graad van doctor aan de Technische Universiteit Eindhoven, op gezag van de rector magnificus prof.dr. S.K. Lenaerts, voor een commissie aangewezen door het College voor Promoties, in het openbaar te verdedigen op dinsdag 13 mei 2025 om 13:30 uur

door

Angelina Evtushkova

geboren te Toguchin, Rusland

Dit proefschrift is goedgekeurd door de promotoren en de samenstelling van de promotiecommissie is als volgt:

voorzitter:	prof.dr.ir. A.R.A. Palmans
1e promotor:	prof.dr.ir. E.J.M. Hensen
2e promotor:	dr. N. Kosinov
leden:	Prof.Dr. J.-D. Grunwaldt (Karlsruher Institut für Technologie)
	prof.dr. A. Urakawa (TU Delft)
	prof.dr.eng. F. Gallucci
adviseur	dr.ir. I.A.W. Filot

Het onderzoek of ontwerp dat in dit proefschrift wordt beschreven is uitgevoerd in overeenstemming met de TU/e Gedragscode Wetenschapsbeoefening.

To my parents
To Ruud

Angelina Evtushkova

Flame-synthesized ceria- and titania-supported Co and Ni catalysts for CO_2 hydrogenation

A catalogue record is available from the Eindhoven University of Technology Library

ISBN: 978-90-386-6367-8

The work described in this thesis has been carried out at the Laboratory of Inorganic materials and Catalysis, Eindhoven University of Technology, The Netherlands. This work was financially supported by the Dutch Research Council (NWO) through Vici grant and the Netherlands Center for Multiscale Catalytic Energy Conversion (MCEC), an NWO Gravitation programme funded by the Ministry of Education, Culture and Science of the government of the Netherlands.

Cover design: Angelina Evtushkova

Printed by: Gildeprint - Enschede, The Netherlands

Contents

Chapter 1

Introduction and scope

Heterogeneous catalysts

Heterogeneous catalysts play a pivotal role in modern chemical processes, offering numerous advantages over other catalytic technologies, such as ease of separation, reusability, and enhanced stability.[1] Since the development of the Haber-Bosch process for ammonia synthesis, [2] heterogeneous catalysts became an essential component in various industrial applications, including petrochemical refining, environmental protection, and the synthesis of fine chemicals.[3]

The development of heterogeneous catalysts continues, with ongoing research focused on the dynamic nature of catalytic surfaces and understanding the mechanisms of reactions at the molecular level. This knowledge is essential for designing next-generation catalysts to meet the demands of the future circular chemical industry and ensure sustainable development.

CO/CO_2 utilization concepts

The rising levels of CO_2 in the atmosphere are a significant cause of global climate change, highlighting the need for effective strategies to reduce emissions and find ways to recycle CO_2.[4–6] CO_2 hydrogenation is a promising approach to storing renewable energy (H_2) while mitigating CO_2 emissions and producing valuable chemicals.[7–9] In particular, the catalytic CO_2 hydrogenation to CH_4 (synthetic natural gas, SNG) has gained significant attention from both academia and industry researchers because SNG can be easily transported with the existing infrastructure to various available markets.[10,11]

The catalytic conversion of CO_2 into alcohols, such as methanol and ethanol, holds significant potential for transforming CO_2 into valuable chemical building blocks.[12–14] Specifically, methanol is one of the top five chemicals produced globally each year, serving as a primary raw material for the chemical industry. It is widely used in methanol-to-olefins (MTO) and methanol-to-hydrocarbons (MTH) processes. Additionally, methanol can be utilized directly in fuel cells and has proven to be an excellent fuel blend for internal combustion engines. Cu–ZnO–based catalysts remain the key industrial methanol synthesis catalysts from syngas.[15,16] While structure-activity relationships have been established for these catalysts, the structure of active sites and the exact mechanism remain a topic of heated discussions and research. In contrast, the design of the catalyst structure has shifted towards the synthesis of specific interfaces, which have been shown to enhance methanol production from CO_2.[17,18] Implementation of reducible oxides such as In_2O_3, CeO_2, Ga_2O_3 offers alternatives to conventional Cu–ZnO–based catalysts with enhanced activity and methanol selectivity due to the unique structure of active sites, metal-support interactions, and oxygen vacancy formation.[19–21]

Another alternative approach is the Fischer-Tropsch (FT) process, where CO_2 is converted into valuable hydrocarbons, such as synthetic fuels and chemicals.[22,23] The conventional FT process involves the catalytic conversion of syngas, a mixture of carbon monoxide (CO) and hydrogen (H_2), into long-chain hydrocarbons. Two promising strategies for the direct synthesis of C_{2+} hydrocarbons and fuels from CO_2 include the combination of the reverse water-gas shift (RWGS; converting CO_2 to CO) with FT synthesis and the pairing of high-temperature methanol synthesis with MTH over bifunctional or multifunctional catalysts.[24]

Another emerging pathway of CO_2 utilization is fixing CO_2 as valuable solid carbon products, such as carbon nanofibers or nanotubes (CNFs or CNTs), to achieve net-negative CO_2 emissions.[25] The molten salt method uses external voltage, high temperature, and the exothermic reaction of alkali metal oxides with CO_2, which ensures high ion conductivity for the electrochemical reduction of carbonates to solid carbon. The direct conversion of CO_2 to solid carbon over Ga-In liquid metal (LM) alloy has produced 319 $\mu mol \cdot h^{-1}$ of carbon at 200 °C, enabling CO_2 utilization without H_2. [26] The electrochemical-thermochemical (EC-TC) tandem approach combines two strategies within one process: electro-reduction of CO_2 to CO and CO carbonization in the TC step.[27] All three methods for converting CO_2 to solid carbon involve using catalysts to activate and transform CO_2. The development and design of new-generation catalysts for CO_2 to solid carbon transformation require further optimization to enhance their activity and stability.

Overall, for CO_2 valorization to become a widely applied technology, further development of active catalysts and efficient processes is crucial for sustainable transition and remains one of the main focuses in both academia and industry.

Supported catalysts for CO_x hydrogenation

Supported catalysts for CO_2 hydrogenation can be classified based on the nature of the support material and the active phase. Common supports include amorphous and crystalline inorganic oxides and carbon materials, while active phases often consist of transition metals, metal oxides, or metal sulfides. The choice of support and active phase significantly influences the catalyst's performance.

Irreducible oxide supports, such as SiO_2 and Al_2O_3, are commonly used in the synthesis of supported catalysts due to their thermal stability, low cost and high surface area.[28–31] Recently reducible oxides (CeO_2, In_2O_3, and TiO_2) have attracted particular interest due to their unique redox properties, ability to form oxygen vacancies, prominent metal-support interaction (MSI), and enhanced dispersion of active metal particles.[32–39]

As for the active phase, noble metals (Ru, Rh, and Pd) have been extensively investigated as active metals for CO/CO_2 hydrogenation, with excellent catalytic performance reported for Ru-based catalysts.[35,40,41] However, the high loading of noble metals and their high price makes it challenging for practical applications. Transition base metals (mainly Ni, Co, and Fe) have acquired considerable attention for their potential in CO/CO_2 methanation due to decent activity and lower price.[7,35,39,42–53]

The catalytic performance of supported metal catalysts in CO/CO_2 hydrogenation usually depends on active metal dispersion, the structure of active sites, the morphology of active sites, metal–support interactions (MSI), etc.[54–58] However, challenges such as catalyst deactivation, sintering, and active metal encapsulation into support's growing overlayer remain critical issues that must be addressed to improve catalyst efficiency and stability. The future of supported heterogeneous catalysis likely lies in developing more sustainable and efficient catalysts. This includes exploring new materials, enhancing catalyst stability, and improving the understanding of catalytic mechanisms at the atomic level.

Nanosized catalysts: New trend in heterogeneous catalysts?

Nanosized catalysts (particles ranging from 1 to 100 nm) have attracted extensive attention in academia and industry. The unique properties of nanocatalysts, including a high fraction of surface atoms, size-dependent electronic characteristics, and increased surface reactivity, result in significant improvement of the catalytic performance in comparison with conventional catalysts.[59–62] By controlling the size, shape, and composition of nanocatalysts, their optimization for specific processes can be achieved, leading to improved selectivity for desired products. Furthermore, analyzing the structure-activity relationship of nanocatalysts using advanced in-situ and operando spectroscopy can enable the design of catalysts with optimal performance.

Extremely small cluster catalysts, consisting of few metal atoms or even single atoms, showed distinctly different catalytic properties than corresponding metal nanoparticle catalysts. In the case of the CO_2 hydrogenation reaction, it is suggested that CH_4 can only be formed on metal nanoparticles, while single-atom or small-cluster catalysts produce mainly CO.[29,63–66] This is because single-site or small cluster catalysts do not provide sufficiently large ensembles of surface atoms for low-barrier C-O dissociation.

A limited number of recent studies have addressed tailoring the catalytic selectivity of supported metal catalysts by tuning the chemical state of the active metal via metal-support interaction or stabilization of isolated metal sites via special synthesis methods.[17,31,34,67,68] It was suggested the chemical/ionic nature of the smaller particle has a significant impact on catalytic selectivity rather than the size of the very small metal nanoparticles/cluster.

Although significant research has been conducted on the structure-activity relationships in CO/CO_2 hydrogenation over heterogeneous catalysts, our understanding of these catalysts at sub-nano scales remains limited. One of the main challenges is synthesizing comparable catalysts with varying chemical compositions and particle sizes.

Recent research has focused on developing novel synthesis methods to create catalysts with tailored properties. Conventional catalyst synthesis involves impregnation or coprecipitation methods to load active metal on a support. However, the synthesis of well-defined catalysts using classical methods is complex due to the poor control over the particle and the phase formation during the process.[69] Moreover, these methods are limited by the relatively low active metal loading that can be achieved.

Spray pyrolysis (SP) is a versatile process to synthesize powder particles and thin films with various structures (**Figure 1.1**). It enables the production of nanomaterials that are difficult to create using other methods, as the morphology of these materials is controlled by forming metastable phases rather than dominating thermodynamic factors. Consequently, SP is particularly effective for producing mixed metal oxides, metal powders, composite particles, and semiconductor thin films.[70]

Flame-spray pyrolysis (FSP) has emerged as a versatile and scalable technique for the synthesis of nanomaterials.[71,72] This method leverages high-temperature combustion processes to produce a wide range of metal and metal oxide nanoparticles with tailored properties. The significance of FSP lies in its ability to generate high-purity, uniform nanoparticles rapidly and efficiently, making it a useful method in the field of nanotechnology. Additionally, FSP offers flexibility in terms of precursor selection, enabling the synthesis of a diverse array of materials.

For example, Dreyer et al. have investigated the influence of support of one-step FSP-synthesized 5 wt.%Ru-based catalysts for CO_2 methanation.[73] Among four catalysts Ru/CeO_2, Ru/MnO_x, Ru/Al_2O_3, and Ru/ZnO, the Ru/CeO_2 catalyst demonstrated the highest catalytic performance, attributed to optimal CO adsorption, achieving high CO coverage, but still maintaining a sufficient amount of active sites for H_2 dissociation. In contrast, Ru/Al_2O_3 catalysts exhibited the highest CO coverage and a lower amount of accessible sites for H_2 dissociation, resulting in lower activity in CO_2 hydrogenation. NiO and CeO_2 supports were prepared by FSP and further impregnated with Ce- and Ni-containing precursors, respectively, to achieve catalysts with high Ni content (80 wt.%). Impregnation of Ce onto FSP-derived NiO hinders the sintering of Ni during reductive pretreatment, ensuring the formation of small Ni nanoparticles and superior activity in CO_2 methanation. The impregnation of Ni onto FSP CeO_2 resulted in an inhomogeneous distribution of Ni and the formation of large Ni nanoparticles during reductive pretreatment, and therefore lower activity in CO_2 methanation.[74] Using a two-nozzle spray pyrolysis approach, Gäßler and co-workers recently prepared a series of Co/TiO_2, Co/SiO_2, and Co/Ti-SiO_2 catalysts with identical Co particle size.[75] They found that the Co/TiO_2 catalysts had a higher CO_2 activity and CH_4 selectivity than FSP-derived Co-SiO_2.

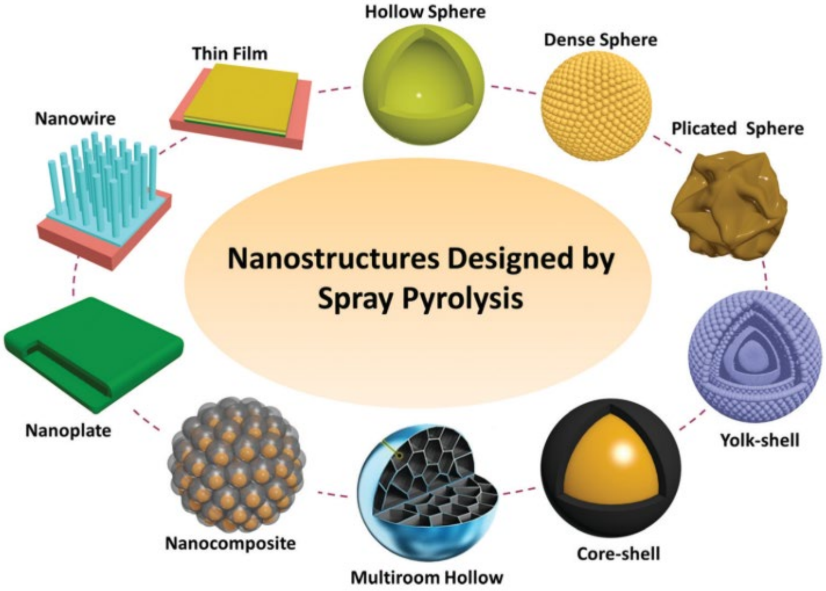

Figure 1.1. Different nanostructures designed by spray pyrolysis. Reprinted with permission from J. S. Cho et al. Nano Energy, 2016, 26, 466–478. Copyright © 2016, Elsevier

Furthermore, Schubert et al. demonstrated that efficient Co-Al_2O_3 catalysts with very low Pt promoter (0.03 wt.% Pt) can be prepared by double flame spray pyrolysis to convert CO_2 into CH_4 due to enhanced reducibility of Co by Pt addition.[76] The series of 20 wt.%Co-Al_2O_3 with Pt, ZrO_x, SmO_x promoters were synthesized using the double FSP with identical structure and morphology (the same size distribution and Co dispersion) to define the influence of promoters in CO_x hydrogenation.[77] ZrO_2- and Pt-containing catalysts outperformed SmO_x-Co-Al_2O_3 in CO_2 hydrogenation. Enhanced CH_4 selectivity over Pt-Co-Al_2O_3 was attributed to the facilitated H_2 absorption and dissociation, while for ZrO_2-Co-Al_2O_3 – with enhanced CO_2 adsorption capacity due to oxide sites of zirconia with medium basicity. A set of 1 wt.% Rh/Al_2O_3 catalysts, prepared by using two-nozzle FSP with K and Ba promoters, was tested in CO_2 hydrogenation.[78] Ba-doped catalysts demonstrated a highly selective conversion of CO_2 to CH_4 at temperatures below 500 °C, with the maximum yield around 400 °C. In contrast, K-doped catalysts did not produce any CH_4; instead, all CO_2 was converted directly to CO from 300 °C to 800 °C.

Besides CO_2 methanation, FSP-derived catalysts have attracted interest for CO_2 hydrogenation to methanol. FSP provides broad possibilities for versatile catalyst synthesis for methanol production, enabling precise control over the particle formation and metal-support interfaces. Jensen et al. demonstrated that flame-made $Cu/ZnO/Al_2O_3$ catalysts with a relatively high specific surface area (>100 m^2/g_{cat}) and various compositions may be obtained, indicating versatility and broad spectra for the FSP application in catalyst synthesis.[79] Copéret and co-workers have prepared a series of Cu/ZrO_2 catalysts with only the varied Cu particle size by using a two-nozzle spray pyrolysis approach.[80] A smaller Cu particle size catalyst possesses a higher CH_3OH activity and selectivity. The efficient Cu/ZrO_2 catalysts with high Cu loadings (up to 80 wt.%) can be prepared by flame spray pyrolysis to convert CO_2 into methanol.[81] Zhu et al. showed that FSP-made Cu/ZnO–CeO_2 catalysts with high Cu loading (~40 wt.%) displayed a substantially higher CH_3OH selectivity than binary FSP-derived Cu/CeO_2 and Cu/ZnO, and commercially available Cu–ZnO catalysts due to synergistic Cu–CeO_2 and Cu–ZnO interactions.[82] FSP-derived Cu-SiO_2 demonstrated a methanol selectivity of 79% at a CO_2 of 5.2%.[83] A slightly distorted Cu–O–Si structure in the FSP-prepared catalyst was considered to enrich the Cu^+ species, which could stabilize and facilitate the hydrogenation of the *CO intermediate to methanol via an RWGS + CO hydrogenation pathway.

Along with Cu-based catalysts for methanol synthesis, In_2O_3 is considered a promising catalyst for CO_2 hydrogenation to methanol because it can be used in a broader temperature range than conventional Cu-Zn catalysts. Various promoters (suck as Al, Cr; Ni, ZrO_2) in combination with In_2O_3 were systematically investigated in CO_2-to-methanol through FSP synthesis.[84–86] In situ IR spectroscopy suggested that adsorbed $CO_2^* \rightarrow HCOO^* \rightarrow CH_3O^* \rightarrow$ methanol mechanism is dominant for all In_2O_3 -based catalysts independent on the promoter. The synergy between Co, Ni, Cu, Pd and In_2O_3 was probed by using a one-step FSP synthesis in a CO_2-to-methanol reaction.[20] The highest CH_3OH rate (~0.25 g_{MeOH}/ (g_{cat} ·h), 250 °C, and 30 bar) is obtained for a 6 wt.% NiO-In_2O_3 catalyst and was assigned to facilitate hydrogenation of adsorbed CO_2 on oxygen vacancy of In_2O_3 and formation of Ni single atoms and clusters. Flame-synthesized Pd-In_2O_3-ZrO_2 catalysts demonstrated remarkable methanol production due to improved metal utilization, unique catalyst architecture, and enhanced oxygen vacancy formation.[87] Scott et al. have investigated a series of impregnated Ni/SiO_2 catalysts on FSP-derived SiO_2 in CO_2 reforming of CH_4 ($CH_4 + CO_2 \rightarrow 2H_2 + 2CO$). [88] The silica properties were altered by varying injection rates during FSP synthesis, resulting in different particle sizes of the support. As the surface area of silica increased, the dispersion of nickel improved, leading to enhanced catalyst performance.

FSP and double FSP enable the control and separation of the particle formation process of different catalyst components. They can be used to evaluate the effects of active metals, support materials, dopants, promoters, particle size distribution, and porosity. The development of efficient catalysts requires not only well-established synthesis methods but also a detailed understanding of structure-activity relationships. Recent advances in spectroscopy and electronic structure calculations have provided tools for studying catalytic materials at the molecular level.

Recent advances in CO_x hydrogenation

Catalyst characterization employed on as-prepared catalysts and their evolution under pretreatment and reaction conditions is critical to establishing structure-activity relationships. Conventional ex-situ techniques typically focus on analyzing the state of the catalyst pre- and post-reduction, and post-reaction, rather than studying its state during the ongoing catalytic reaction.[89] However, catalyst exposure during chamber-to-chamber transfer may change (re-oxidize) the active metals and even introduce undesirable impurities, which interfere with detecting potential active sites. However, the ex-situ characterizations provide extensive information about the structure of the catalysts, the study of dynamic changes in the catalyst's structure under actual reduction/reaction conditions is necessary to identify the actual active sites and establish the reaction mechanism. By employing various in-situ characterization techniques (**Figure 1.2**), we can gain valuable insights into catalyst evolution and reaction intermediates associated with active sites.[90,91] Combining knowledge about active site structure and reaction mechanism with kinetics analysis enables the design of new catalysts and the optimization of existing ones to meet industrial challenges.

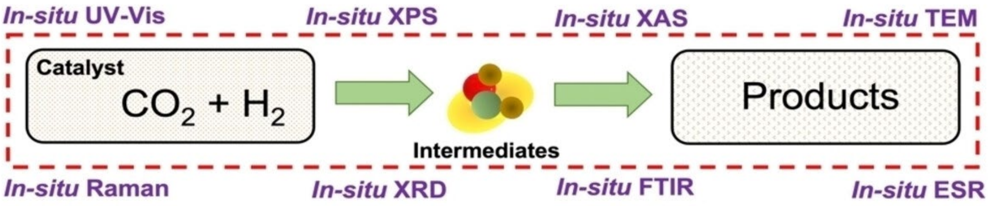

Figure 1.2. Various *in-situ* techniques and their design components to study the catalyst evolution and reaction progress during CO_2 hydrogenation. Reprinted with permission from R. Singh, L. Wang, and J. Huang, *Chempluschem*, 2024, vol. 89, no. 9. Copyright © 2016, Elsevier

X-ray diffraction (XRD) is commonly used to identify the crystal phases of catalysts and their changes during pretreatment and/or reduction related to long-range periodicity in material. Utilizing XRD enables the estimation of volume-average particle size, unit cell parameters, and the phases of components under reaction conditions. However, the XRD technique is limited to analyzing only crystalline samples and nanoparticles above 2 nm. In turn, the pair distribution function (PDF) analysis uses the whole measured spectrum, containing Bragg and diffuse components, to extract the total scattering structure function.[92] The information derived from total scattering gives us a probability of finding two atoms at a given separation distance. Refinement of PDF data allows us to find information about local structure, including bond length, geometry, unit cell, disorder in the material, coordination number.[93,94] The synchrotron-based element-specific X-ray absorption spectroscopy (XAS), which includes the X-ray absorption near-edge structure (XANES) spectrum and the extended X-ray absorption fine structure (EXAFS) spectrum, enables the analysis of oxidation states and local structure of the selected element under pretreatment/reaction conditions. Quasi-in situ X-ray photoelectron spectroscopy (XPS) and near ambient pressure XPS (NAP-XPS) are powerful tools for the exploration of the interaction of the catalytic surface with gases during pretreatment and the ongoing reaction while also monitoring their chemical composition and oxidation states.[95,96] Infrared spectroscopy (IR) studies enable the identification of surface species, whether those are reaction intermediates or spectator species.[97,98] However, the analysis of surface species can be challenging due to the gas-phase rotovibrational spectrum of CO and/or the overlap of IR bands of spectator and reaction intermediate species.[99–103] Despite the challenges, IR spectroscopy remains a powerful tool for the investigation of active site structure and reaction mechanisms.[98]

Nuzzo et al demonstrated that XAS and XPS techniques should be employed for single-atom catalyst characterization.[104] Operando XRD and XAS spectroscopy in combination with operando IR coupled with (isotopic) transient experiments revealed the decreased methanation activity and the related higher CO selectivity on small nanoparticles was linked to lower availability of step edges that are active for CO dissociation.[29] In situ XRD and XPS studies in combination with PDF analysis and TEM study of samples revealed metal−support interaction and synergism of redox properties of the Ni and ceria-zirconia facilitate CO and CO_2 hydrogenation.[105] A combination of XRD, XAS, NAP-XPS, transmission electron microscopy (TEM), and IR provides insight into the active sites at the interface between cobalt and ceria-zirconia involved in CO_2 methanation.[106] By implementing in situ XRD with XAS, XPS, and IR spectroscopy, Rodriguez and co-authors showed that cobalt–ceria interface is less active in H_2 dissociation, resulting in a lower CO_2 hydrogenation.[107]

By combining in situ DRIFTS, in situ Raman, in situ XPS and in situ XAS spectroscopies with extensive ex situ characterization, Wang et al. showed that the cobalt species in Co–O–SiO_n provides a nearly optimum structure for hindering the side reactions and facilitating methanol formation from spectroscopically identified *CH_3O intermediates.[17]

By combining well-defined synthesis strategies (such as FSP) with advanced spectroscopy and electronic structure calculations, new generation catalysts or optimization of existing ones with desired properties can be developed.

Scope of thesis

This work aims to elucidate the structure-activity relationships of transition-metal-based catalysts for CO/CO_2 hydrogenation processes. The combination of relatively cheap and active transition metals with reducible oxide supports (such as CeO_2 and TiO_2) has gained particular interest in the last decades due to enhanced active metal dispersion and peculiar structural properties (such as metal-support interaction, stabilization of isolated active metal centers, etc.). As such, we aim to develop synthetic procedures that will allow us to derive structure-activity relations and probe support effects for Co/Ni-based methanation catalysts.

Conventional and advanced synthesis methods such as flame-spray pyrolysis (FSP) are employed to prepare CeO_2- and TiO_2-supported catalysts with Co or Ni as nanoparticles, clusters, and single atoms. By thoroughly investigating the structure of the catalysts and their evolution during catalyst activation, structure-activity relationships in CO_2 hydrogenation are established.

Chapter 2 explores how the Co content in one-step FSP-derived Co-CeO_2 catalysts influences catalytic performance in CO_2 hydrogenation. We have prepared a set of catalysts with a Co content varying from 1 mol.% to 30 mol.%. The combination of advanced spectroscopy with catalytic experiments revealed that Co nanoparticles are active in CH_4 formation, while Co-O-Ce interfaces/small clusters are apt to CO production.

This approach is broadened in **Chapter 3**, where the results of the previous chapter are compared to a conventionally prepared Co/CeO_2 by wet impregnation in which cobalt is impregnated on FSP-derived cerium dioxide. Using in situ spectroscopic techniques, the high activity of the reduced catalysts towards methane was linked to the formation of Co nanoparticles and oxygen vacancies formation caused by partial reduction of CeO_2. Additionally, the activity and stability of Co/CeO_2 catalysts were tested in CO/CO_2 hydrogenation.

Chapter 4 demonstrates that FSP-derived Ni-CeO_2 catalysts do require the formation of Ni nanoparticles to hydrogenate CO_2 to CH_4 efficiently, similar to one-step FSP-derived Co-CeO_2 catalysts. A reduced catalyst with 1 mol.% Ni prepared by one-step flame spray pyrolysis remains highly dispersed and displays higher activity in converting CO_2 to CO. FSP-derived Ni-CeO_2 catalysts display enhanced activity in CO_2 hydrogenation than Ni nanoparticles impregnated on a commercial CeO_2 support. The Ni nanoparticles formed during reduction are more stable than isolated Ni centers under reaction conditions in FSP-made catalysts. The higher stability of Ni nanoparticles in FSP-made catalysts can be linked to extensive H_2 dissociation and spillover in such materials.

Chapter 5 explores how the Co content and size of one-step flame-synthesized Co-TiO_2 catalysts influence catalytic performance in CO_2 hydrogenation. A set of catalysts with varying Co content was prepared from 2.5 mol.% to 40 mol.%. The Co content profoundly affects activity and product selectivity in CO_2 hydrogenation. One-step FSP-made Co-TiO_2 displays higher activity than Co impregnated on FSP-derived TiO_2, linked to a difference in TiO_2 morphology and its different metal-support interaction with cobalt.

The last chapter summarizes the key findings of this work and provides an outlook.

References

1. Nørskov, J. K. ., Studt, Felix., Abild-Pedersen, Frank. & Bligaard, Thomas. Fundamental concepts in heterogeneous catalysis. (2015).

2. Boreskov, G. K. Heterogeneous catalysis, Nova Science Publishers (2003).

3. Moulijn, J. A. & van Santen, R. A. History of Catalysis. Stud Surf Sci Catal 123, 3–28 (2017).

4. Solomon, S., Plattner, G. K., Knutti, R. & Friedlingstein, P. Irreversible climate change due to carbon dioxide emissions. Proc Natl Acad Sci U S A 106, 1704–1709 (2009).

5. Mulvaney, D. Energy and the Environment I: Fossil Fuels. Sustainable Energy Transitions 81–108 (2020)

6. Cox, P. M., Betts, R. A., Jones, C. D., Spall, S. A. & Totterdell, I. J. Acceleration of global warming due to carbon-cycle feedbacks in a coupled climate model. Nature 408, 184–187 (2000).

7. Guo, L., Guo, X., He, Y. & Tsubaki, N. CO_2 heterogeneous hydrogenation to carbon-based fuels: recent key developments and perspectives. J Mater Chem A Mater 11, 11637–11669 (2023).

8. Ashok, J. et al. A review of recent catalyst advances in CO_2 methanation processes. Catal Today 356, 471–489 (2020).

9. Kondratenko, E. V., Mul, G., Baltrusaitis, J., Larrazábal, G. O. & Pérez-Ramírez, J. Status and perspectives of CO_2 conversion into fuels and chemicals by catalytic, photocatalytic and electrocatalytic processes. Energy Environ Sci 6, 3112–3135 (2013).

10. Ren, J. et al. Methanation of CO/CO_2 for power to methane process: Fundamentals, status, and perspectives. Journal of Energy Chemistry 80, 182–206 (2023).

11. Rönsch, S. et al. Review on methanation – From fundamentals to current projects. Fuel 166, 276–296 (2016).

12. Álvarez, A. et al. Challenges in the Greener Production of Formates/Formic Acid, Methanol, and DME by Heterogeneously Catalyzed CO_2 Hydrogenation Processes. Chem Rev 117, 9804–9838 (2017).

13. Zhong, J. et al. State of the art and perspectives in heterogeneous catalysis of CO_2 hydrogenation to methanol. Chem Soc Rev 49, 1385–1413 (2020).

14. Jiang, X., Nie, X., Guo, X., Song, C. & Chen, J. G. Recent Advances in Carbon Dioxide Hydrogenation to Methanol via Heterogeneous Catalysis. Chem Rev 120, 7984–8034 (2020).

15. Kuld, S. et al. Quantifying the promotion of Cu catalysts by ZnO for methanol synthesis. Science (1979) 352, 969–974 (2016).

16. Bansode, A. & Urakawa, A. Towards full one-pass conversion of carbon dioxide to methanol and methanol-derived products. J Catal 309, 66–70 (2014).

17. Wang, L. et al. Silica accelerates the selective hydrogenation of CO_2 to methanol on cobalt catalysts. Nature Communications 2020 11:1 11, 1–9 (2020).

18. Liu, S. et al. Hetero-site cobalt catalysts for higher alcohols synthesis by CO_2 hydrogenation: A review. Journal of CO_2 Utilization 67, 102322 (2023).

19. Larmier, K. et al. CO_2-to-Methanol Hydrogenation on Zirconia-Supported Copper Nanoparticles: Reaction Intermediates and the Role of the Metal–Support Interface. Angewandte Chemie International Edition 56, 2318–2323 (2017).

20. Zhu, J. et al. Ni-In Synergy in CO_2 Hydrogenation to Methanol. ACS Catal 11, 11371–11384 (2021).

21. Zhu, J. et al. Mechanism and Nature of Active Sites for Methanol Synthesis from CO/CO_2 on Cu/CeO_2. ACS Catal 10, 11532–11544 (2020).

22. Suppiah, D. D., Daud, W. M. A. W. & Johan, M. R. Supported metal oxide catalysts for CO_2 Fischer−Tropsch conversion to liquid fuels - A review. Energy and Fuels 35, 17261–17278 (2021).

23. Ye, R.-P. et al. CO_2 hydrogenation to high-value products via heterogeneous catalysis. Nature Communications 2019 10:1 10, 1–15 (2019).

24. Gao, P., Zhang, L., Li, S., Zhou, Z. & Sun, Y. Novel heterogeneous catalysts for CO_2 hydrogenation to liquid fuels. ACS Cent Sci 6, 1657–1670 (2020).

25. Xie, Z. & Chen, J. G. Comparison of Approaches for CO_2 Sequestration as Solid Carbon Products. CCS Chemistry 1–11 (2024).

26. Zuraiqi, K. et al. Direct conversion of CO_2 to solid carbon by Ga-based liquid metals. Energy Environ Sci 15, 595–600 (2022).

27. Xie, Z. et al. CO_2 fixation into carbon nanofibres using electrochemical–thermochemical tandem catalysis. Nature Catalysis 2024 7:1 7, 98–109 (2024).

28. Lovell, E. C., Scott, J. & Amal, R. Ni-SiO_2 Catalysts for the Carbon Dioxide Reforming of Methane: Varying Support Properties by Flame Spray Pyrolysis. Molecules 2015, Vol. 20, Pages 4594-4609 20, 4594–4609 (2015).

29. Simons, J. F. M. et al. Structure Sensitivity of CO_2 Hydrogenation on Ni Revisited. J Am Chem Soc 145, 20289–20301 (2023).

30. Díez-Ramírez, J. et al. Effect of support nature on the cobalt-catalyzed CO_2 hydrogenation. Journal of CO_2 Utilization 21, 562–571 (2017).

31. Ilsemann, J. et al. Cobalt@Silica Core-Shell Catalysts for Hydrogenation of CO/CO_2 Mixtures to Methane. ChemCatChem 11, 4884–4893 (2019).

32. Kim, S. S., Lee, H. H. & Hong, S. C. The effect of the morphological characteristics of TiO_2 supports on the reverse water–gas shift reaction over Pt/TiO_2 catalysts. Appl Catal B 119–120, 100–108 (2012).

33. Xu, J. et al. Influence of pretreatment temperature on catalytic performance of rutile TiO_2-supported ruthenium catalyst in CO_2 methanation. J Catal 333, 227–237 (2016).

34. Have, I. C. ten et al. Uncovering the reaction mechanism behind CoO as active phase for CO_2 hydrogenation. Nature Communications 2022 13:1 13, 1–11 (2022).

35. Kattel, S. et al. CO_2 Hydrogenation over Oxide-Supported PtCo Catalysts: The Role of the Oxide Support in Determining the Product Selectivity. Angewandte Chemie

International Edition 55, 7968–7973 (2016).

36. Liu, J. et al. Enhanced low-temperature activity of CO_2 methanation over highly-dispersed Ni/TiO_2 catalyst. Catal Sci Technol 3, 2627–2633 (2013).

37. Lykaki, M., Papista, E., Kaklidis, N., Carabineiro, S. & Konsolakis, M. Ceria Nanoparticles' Morphological Effects on the N_2O Decomposition Performance of Co_3O_4/CeO_2 Mixed Oxides. Catalysts 9, 233 (2019).

38. Qiu, N., Zhang, J. & Wu, Z. Peculiar surface-interface properties of nanocrystalline ceria-cobalt oxides with enhanced oxygen storage capacity. Physical Chemistry Chemical Physics 16, 22659–22664 (2014).

39. Du, Y. et al. Deep Understanding into the Effect of Fe on CO_2 Methanation: A Support-Dependent Phenomenon. Ind Eng Chem Res (2021).

40. Guo, Y. et al. Low-Temperature CO_2 Methanation over CeO_2-Supported Ru Single Atoms, Nanoclusters, and Nanoparticles Competitively Tuned by Strong Metal−Support Interactions and H-Spillover Effect. (2018).

41. Kattel, S., Yan, B., Chen, J. G. & Liu, P. CO_2 hydrogenation on Pt, Pt/SiO_2 and Pt/TiO_2: Importance of synergy between Pt and oxide support. J Catal 343, 115–126 (2016).

42. Melaet, G. et al. Evidence of highly active cobalt oxide catalyst for the Fischer-Tropsch synthesis and CO_2 hydrogenation. J Am Chem Soc 136, 2260–2263 (2014).

43. Li, W. et al. CO_2 Hydrogenation on Unpromoted and M-Promoted Co/TiO_2 Catalysts (M = Zr, K, Cs): Effects of Crystal Phase of Supports and Metal-Support Interaction on Tuning Product Distribution. ACS Catal 9, 2739–2751 (2019).

44. Bertella, F., Concepción, P. & Martínez, A. TiO_2 polymorph dependent SMSI effect in Co-Ru/TiO_2 catalysts and its relevance to Fischer-Tropsch synthesis. Catal Today 289, 181–191 (2017).

45. Scarfiello, C. et al. Modified Co/TiO_2 catalysts for CO_2 hydrogenation to fuels. J Catal 428, 115202 (2023).

46. Toyao, T., Kayamori, S., Maeno, Z., Siddiki, S. M. A. H. & Shimizu, K. I. Heterogeneous Pt and MoOx Co-Loaded TiO_2 Catalysts for Low temperature CO_2 Hydrogenation to Form CH_3OH. ACS Catal 9, 8187–8196 (2019).

47. Frontera, P. et al. Catalytic activity of Ni-Co supported metals in carbon dioxides methanation. Canadian Journal of Chemical Engineering 98, 1924–1934 (2020).

48. Li, W. et al. A short review of recent advances in CO_2 hydrogenation to hydrocarbons over heterogeneous catalysts. RSC Adv 8, 7651–7669 (2018).

49. Zhang, Z. et al. Advances in studies of the structural effects of supported Ni catalysts for CO_2 hydrogenation: from nanoparticle to single atom catalyst. J Mater Chem A Mater 10, 5792–5812 (2022).

50. Scarfiello, C., Pham Minh, D., Soulantica, K. & Serp, P. Oxide Supported Cobalt Catalysts for CO_2 Hydrogenation to Hydrocarbons: Recent Progress. Adv Mater Interfaces 10, 2202516 (2023).

51. Gao, J. et al. Recent advances in methanation catalysts for the production of

synthetic natural gas. RSC Adv 5, 22759–22776 (2015).

52. Yao, B. et al. Transforming carbon dioxide into jet fuel using an organic combustion-synthesized Fe-Mn-K catalyst. Nat Commun 11, 1–12 (2020).

53. Xu, D. et al. Advances in Higher Alcohol Synthesis from CO_2 Hydrogenation. Chem (2020).

54. Vogt, C. & Weckhuysen, B. M. The concept of active site in heterogeneous catalysis. Nat Rev Chem 6, 89–111 (2022).

55. Che, M. & Bennett, C. O. The Influence of Particle Size on the Catalytic Properties of Supported Metals. Advances in Catalysis 36, 55–172 (1989).

56. Fischer, N., Van Steen, E. & Claeys, M. Structure sensitivity of the Fischer–Tropsch activity and selectivity on alumina supported cobalt catalysts. J Catal 299, 67–80 (2013).

57. Van Santen, R. A. Complementary structure sensitive and insensitive catalytic relationships. Acc Chem Res 42, 57–66 (2009).

58. Lin, Y., Zhu, Y., Pan, X. & Bao, X. Modulating the methanation activity of Ni by the crystal phase of TiO_2. Catal Sci Technol 7, 2813–2818 (2017).

59. Leybo, D. et al. Metal–support interactions in metal oxide-supported atomic, cluster, and nanoparticle catalysis. Chem Soc Rev 53, 10450–10490 (2024).

60. Khan, H., Kunchala, R. K. & Ganguli, A. K. Nanomaterials in catalysis: insights from electrocatalysis, photocatalysis and photoelectrocatalysis. Proceedings of the Indian National Science Academy 2024 1–25 (2024).

61. Lakhani, P., Bhanderi, D. & Modi, C. K. Nanocatalysis: recent progress, mechanistic insights, and diverse applications. Journal of Nanoparticle Research 2024 26:7 26, 1–20 (2024).

62. Klankermayer, J., Wesselbaum, S., Beydoun, K. & Leitner, W. Selective Catalytic Synthesis Using the Combination of Carbon Dioxide and Hydrogen: Catalytic Chess at the Interface of Energy and Chemistry. Angewandte Chemie International Edition 55, 7296–7343 (2016).

63. Zhou, X., Price, G. A., Sunley, G. J. & Copéret, C. Small Cobalt Nanoparticles Favor Reverse Water-Gas Shift Reaction Over Methanation Under CO_2 Hydrogenation Conditions. Angewandte Chemie - International Edition 62, (2023).

64. Bezemer, G. L. et al. Cobalt particle size effects in the Fischer-Tropsch reaction studied with carbon nanofiber supported catalysts. J Am Chem Soc 128, 3956–3964 (2006).

65. Zhou, G. et al. CO_2 hydrogenation to methane over mesoporous Co/SiO_2 catalysts: Effect of structure. Journal of CO_2 Utilization 26, 221–229 (2018).

66. Iablokov, V. et al. Size-controlled model Co nanoparticle catalysts for CO_2 hydrogenation: Synthesis, characterization, and catalytic reactions. Nano Lett 12, 3091–3096 (2012).

67. Matsubu, J. C., Yang, V. N. & Christopher, P. Isolated metal active site concentration and stability control catalytic CO_2 reduction selectivity. J Am Chem Soc 137,

3076–3084 (2015).

68. Li, S. et al. Tuning the Selectivity of Catalytic Carbon Dioxide Hydrogenation over Iridium/Cerium Oxide Catalysts with a Strong Metal–Support Interaction. Angewandte Chemie International Edition 56, 10761–10765 (2017).

69. Khodakov, A. Y., Chu, W. & Fongarland, P. Advances in the development of novel cobalt Fischer-Tropsch catalysts for synthesis of long-chain hydrocarbons and clean fuels. Chem Rev 107, 1692–1744 (2007).

70. Leng, J. et al. Advances in nanostructures fabricated via spray pyrolysis and their applications in energy storage and conversion. Chem Soc Rev 48, 3015–3072 (2019).

71. Wegner, K., Schimmoeller, B., Thiebaut, B., Fernandez, C. & Rao, T. N. Pilot Plants for Industrial Nanoparticle Production by Flame Spray Pyrolysis. KONA Powder and Particle Journal 29, 251–265 (2011).

72. Mueller, R., Mädler, L. & Pratsinis, S. E. Nanoparticle synthesis at high production rates by flame spray pyrolysis. Chem Eng Sci 58, 1969–1976 (2003).

73. Dreyer, J. A. H. et al. Influence of the oxide support reducibility on the CO_2 methanation over Ru-based catalysts. Appl Catal B 219, 715–726 (2017).

74. Fujiwara, K. et al. Porous NiO prepared by flame spray pyrolysis for 80 wt.% Ni-CeO_2 catalyst and its activity for CO_2 methanation. Journal of the Japan Petroleum Institute 64, 261–270 (2021).

75. Gäßler, M. et al. The Impact of Support Material of Cobalt-Based Catalysts Prepared by Double Flame Spray Pyrolysis on CO_2 Methanation Dynamics. ChemCatChem 14, e202200286 (2022).

76. Schubert, M. et al. Highly active Co–Al_2O_3 -based catalysts for CO_2 methanation with very low platinum promotion prepared by double flame spray pyrolysis. Catal Sci Technol 6, 7449–7460 (2016).

77. Stahl, J. et al. Comparing Co-catalytic Effects of ZrO_x, SmO_x, and Pt on CO_x Methanation over Co-based Catalysts Prepared by Double Flame Spray Pyrolysis. ChemCatChem 13, 2815–2831 (2021).

78. Büchel, R., Baiker, A. & Pratsinis, S. E. Effect of Ba and K addition and controlled spatial deposition of Rh in Rh/Al_2O_3 catalysts for CO_2 hydrogenation. Appl Catal A Gen 477, 93–101 (2014).

79. Jensen, J. R., Johannessen, T., Wedel, S. & Livbjerg, H. A study of Cu/ZnO/Al_2O_3 methanol catalysts prepared by flame combustion synthesis. J Catal 218, 67–77 (2003).

80. Tada, S., Larmier, K., Büchel, R. & Copéret, C. Methanol synthesis via CO_2 hydrogenation over CuO–ZrO_2 prepared by two-nozzle flame spray pyrolysis. Catal Sci Technol 8, 2056–2060 (2018).

81. Tada, S. et al. Flame spray pyrolysis makes highly loaded Cu nanoparticles on ZrO_2 for CO_2-to-methanol hydrogenation. Chemical Engineering Journal 381, 122750 (2020).

82. Zhu, J. et al. Flame Synthesis of Cu/ZnO-CeO_2 Catalysts: Synergistic Metal-

Support Interactions Promote CH_3OH Selectivity in CO_2 Hydrogenation. ACS Catal 11, 4880–4892 (2021).

83. Yu, J. et al. Stabilizing Cu^+ in Cu/SiO_2 catalysts with a shattuckite-like structure boosts CO_2 hydrogenation into methanol. ACS Catal 10, 14694–14706 (2020).

84. Liu, L., Gao, Y., Zhang, H., Kosinov, N. & Hensen, E. J. M. Ni and ZrO_2 promotion of In_2O_3 for CO_2 hydrogenation to methanol. Applied Catalysis B: Environment and Energy 356, 124210 (2024).

85. Liu, L., Mezari, B., Kosinov, N. & Hensen, E. J. M. Al Promotion of In_2O_3 for CO_2 Hydrogenation to Methanol. ACS Catal 13, 15730–15745 (2023).

86. Liu, L., Cannizzaro, F., Kaychouhi, A., Kosinov, N. & Hensen, E. J. M. Cr as a promoter for the In_2O_3-catalyzed hydrogenation of CO_2 to methanol. Chemical Engineering Journal 494, 153204 (2024).

87. Pinheiro Araújo, T. et al. Flame-made ternary Pd-In_2O_3-ZrO_2 catalyst with enhanced oxygen vacancy generation for CO_2 hydrogenation to methanol. Nature Communications 2022 13:1 13, 1–12 (2022).

88. Lovell, E. C., Scott, J. & Amal, R. Ni-SiO_2 Catalysts for the Carbon Dioxide Reforming of Methane: Varying Support Properties by Flame Spray Pyrolysis. Molecules 2015, Vol. 20, 4594–4609 (2015).

89. Li, Y. & Wu, Z. A review of in situ/operando studies of heterogeneous catalytic hydrogenation of CO_2 to methanol. Catal Today 420, 114029 (2023).

90. Saeidi, S. et al. Recent advances in CO_2 hydrogenation to value-added products — Current challenges and future directions. Prog Energy Combust Sci 85, 100905 (2021).

91. Singh, R., Wang, L. & Huang, J. In-Situ Characterization Techniques for Mechanism Studies of CO_2 Hydrogenation. Chempluschem 89, e202300511 (2024).

92. Takeshi Egami, Simon J.L.Billinge. Underneath the Bragg Peaks: Structural Analysis of Complex Materials, Pergamon Materials Series (2003).

93. Farrow, C. L. et al. PDFfit2 and PDFgui: computer programs for studying nanostructure in crystals. Journal of Physics: Condensed Matter 19, 335219 (2007).

94. Bordet, P. Local structure studies using the pair distribution function. EPJ Web Conf 104, 1003 (2015).

95. Zhong, L., Chen, D. & Zafeiratos, S. A mini review of in situ near-ambient pressure XPS studies on non-noble, late transition metal catalysts. Catal Sci Technol 9, 3851–3867 (2019).

96. Zafeiratos, S. et al. A comparative in situ XPS study of PtRuCo catalyst in methanol steam reforming and water gas shift reactions. Catal Today 157, 250–256 (2010).

97. Vogt, C., Monai, M., Kramer, G. J. & Weckhuysen, B. M. The renaissance of the Sabatier reaction and its applications on Earth and in space. Nature Catalysis 2019 2:3 2, 188–197 (2019).

98. Meunier, F. C. Hydrogenation of CO and CO_2: Contributions of IR operando studies. Catal Today 423, 113863 (2023).

99. Meunier, F. C. On the contamination with nickel and nickel tetracarbonyl during FT-IR investigation of catalysts under CO-containing gases. J Catal 372, 388 (2019).

100. Daly, H., Ni, J., Thompsett, D. & Meunier, F. C. On the usefulness of carbon isotopic exchange for the operando analysis of metal–carbonyl bands by IR over ceria-containing catalysts. J Catal 254, 238–243 (2008).

101. Paredes-Nunez, A., Jbir, I., Bianchi, D. & Meunier, F. C. Spectrum baseline artefacts and correction of gas-phase species signal during diffuse reflectance FT-IR analyses of catalysts at variable temperatures. Appl Catal A Gen 495, 17–22 (2015).

102. Lorito, D., Paredes-Nunez, A., Mirodatos, C., Schuurman, Y. & Meunier, F. C. Determination of formate decomposition rates and relation to product formation during CO hydrogenation over supported cobalt. Catal Today 259, 192–196 (2016).

103. Paredes-Nunez, A. et al. CO Hydrogenation on Cobalt-Based Catalysts: Tin Poisoning Unravels CO in Hollow Sites as a Main Surface Intermediate. Angewandte Chemie 130, 556–559 (2018).

104. Kottwitz, M., Li, Y., Wang, H., Frenkel, A. I. & Nuzzo, R. G. Single Atom Catalysts: A Review of Characterization Methods. Chemistry–Methods 1, 278–294 (2021).

105. Pakharukova, V. P. et al. Investigation of the Structure and Interface Features of Ni/$Ce_{1-x}Zr_xO_2$ Catalysts for CO and CO_2 Methanation. Journal of Physical Chemistry C 125, 20538–20550 (2021).

106. Parastaev, A. et al. Boosting CO_2 hydrogenation via size-dependent metal–support interactions in cobalt/ceria-based catalysts. Nat Catal 3, 526–533 (2020).

107. Deng, K. et al. Studies of CO_2 hydrogenation over cobalt/ceria catalysts with in situ characterization: the effect of cobalt loading and metal–support interactions on the catalytic activity. Catal Sci Technol 10, 6468–6482 (2020).

Chapter 2

Flame Synthesized Co–CeO_2 Catalysts for CO_2 methanation

Abstract

Flame synthesis (flame spray pyrolysis, FSP) was used to prepare a set of Co-CeO_2 catalysts with varying Co content to evaluate the impact of the location and structure of Co relative to nanosized CeO_2 particles on the CO_2 methanation activity. All FSP samples contain small CeO_2 nanoparticles of ~8 nm with a higher surface area than conventional CeO_2 with a nearly constant amount (3.8 mol.%) of Co^{2+} ions in strong interaction with CeO_2. These firmly bound Co ions cannot be reduced in H_2 at 500 °C. Catalysts containing 5 mol.% or more Co also contain segregated CoO and Co_3O_4 particles, which are partially reduced to metallic Co upon reduction at 300 °C for 4 h. The highest Co-weight-normalized activity at 200 °C was 3.9 ± 0.2 $mmol_{CO2}/mol_{Co}/s$ (CH_4 selectivity 85%) for reduced 10 mol.% Co-CeO_2, with a Co reduction degree of ~50% and ~4-5 nm Co metal nanoparticles. The sample with the lowest Co content of 2.5 mol.% had a Co reduction degree of 10%, the resulting very small Co clusters being primarily active in CO formation (CO selectivity 79%). The small amount of CH_3OH among the reaction products at low Co content was linked to CO_2 hydrogenation on oxygen vacancies assisted by H_2 dissociation on very small Co clusters. Catalysts containing more and larger Co nanoparticles mainly yield CH_4, small amounts of CO and no CH_3OH. The outstanding CO_2 methanation activity of FSP-prepared Co-CeO_2 catalysts is linked to the synergy between relatively small metallic Co nanoparticles and Co^{2+}-O-Ce sites, involving oxygen vacancies.

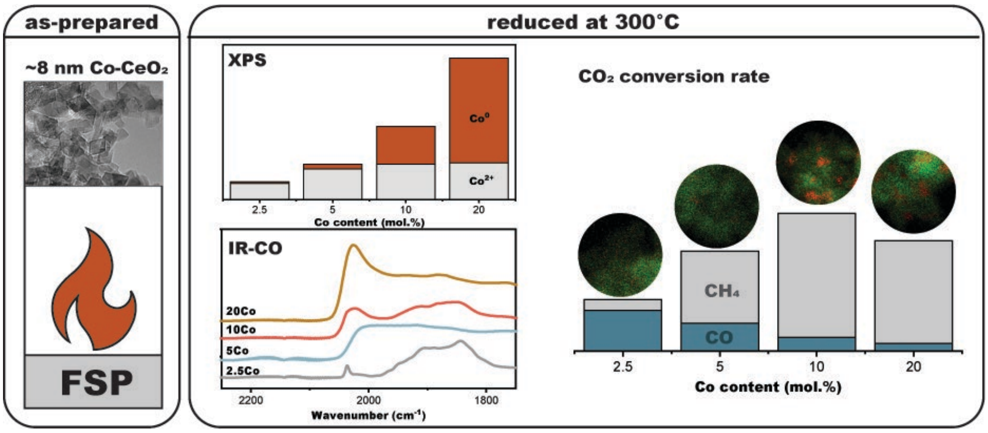

Introduction

Carbon dioxide (CO_2) is a greenhouse gas, anthropogenically released in the atmosphere, causing climate change and acidification of the oceans. Mitigation of the net flow of CO_2 into the atmosphere can be achieved by (i) reducing CO_2 emissions, (ii) CO_2 capture and storage, and (iii) utilization of (captured) CO_2.[1–3] CO_2 hydrogenation with H_2 obtained from renewable energy sources into fuels and chemicals is a promising approach to close carbon cycles. Converting CO_2 to methane (CH_4) is a viable technology for reusing CO_2 by temporarily storing hydrogen (H_2) in a widely used energy carrier.[4,5] CH_4 can be used directly in existing natural gas infrastructure in many countries.[6] The chemical transformation of CO_2 can be done via electrocatalytic[7], photocatalytic[8] and thermocatalytic reduction of CO_2.[9] The latter approach is the most developed for sustainable CH_4 production from CO_2 and renewable energy. Catalyst design approaches can help improve the performance of heterogeneous catalysts for hydrogenating CO_2 into CH_4.

Catalysts based on first-row transition metals have gained particular interest due to their abundance and lower cost than noble metals. Cu is the metal of choice in the heterogeneous hydrogenation of CO_2 to CH_3OH.[10,11] Nickel-based catalysts are most extensively considered as catalysts for CO_2 methanation.[12–14] Iron-based catalysts are promising for the direct Fischer-Tropsch synthesis from CO_2/H_2 mixtures.[15] Co can be used to hydrogenate CO_2 to hydrocarbons[16] or higher alcohols.[17] Given their high activity in Fischer-Tropsch synthesis from CO/H_2 mixtures,[18–21] indirect CO_2 utilization by the reverse water-gas shift (rWGS) reaction followed by FTS is the preferred way for CO_2-based FTS. Given its high activity towards C-O bond scission, it is worthwhile exploring using Co for CO_2 methanation. A recent review mentioned that Co-based catalysts perform better at lower reaction temperatures than Ni-based catalysts.[22]

The support plays a critical role in the formation of active sites in heterogeneous catalysts.[23] Interactions between Co and reducible oxide supports (e.g., CeO_2 and TiO_2) are particularly interesting. Fu et al. demonstrated that the combination of the CoO-CeO_2 and CoO-Co interfaces is very active in the water-gas shift (WGS) reaction.[24] Wang et al. showed that metallic Co nanoparticles are active in CO_2 hydrogenation to CO and CH_4. In contrast, Co-O-SiO_n structures close to metallic Co can catalyze CO_2 hydrogenation to CH_3OH in catalysts with strong Co-silica interactions.[25] Another study of CO_2 hydrogenation concluded that CoO on TiO_2 results in higher CO_2 conversion and C_{2+} selectivity caused by H-assisted CO_2 dissociation compared to conventional Co metal nanoparticles on TiO_2.[16] Parastaev et al. showed that small Co clusters dispersed on the surface of CoO nanoparticles, which are stabilized by a CeO_2-ZrO_2 support, are much more active in CO_2 methanation than metallic Co particles.[26] The use of reducible supports is a promising approach to promote CO_2 conversion by metal phases due to their unique redox properties and enhanced metal-support interactions.[27] However, the exact role of these metal-support interactions in these catalysts has not yet been entirely resolved.

This study deals with a series of Co–CeO_2 catalysts prepared by one-step flame spray pyrolysis (FSP) to study the impact of Co–CeO_2 structure on CO_2 methanation. The catalytic activity determined at 200 – 300 °C and atmospheric pressure showed that catalysts with a low Co content mainly produced CO at a low CO conversion, while samples with a high Co content presented CH_4 formation at much higher CO conversion. The as-prepared and reduced catalysts were extensively characterized by N_2 physisorption, transmission electron microscopy (TEM), X-ray diffraction (XRD), H_2-TPR, X-ray photoelectron spectroscopy (NAP-XPS), and X-ray absorption spectroscopy (XAS). Structural changes of the catalysts during reductive pretreatment were monitored by in situ synchrotron XRD in combination with PDF analysis. Partial reduction of the CeO_2 surface was observed for all Co-containing CeO_2 samples, indicating a higher abundance of surface oxygen vacancies than the FSP-prepared CeO_2 support. The high activity and CH_4 selectivity of catalysts with a Co content >5 mol.% is due to the formation of Co metal nanoparticles during reduction. On the other hand, samples with a lower Co content are hardly reduced, with only a very small amount of metallic Co in the form of clusters.

Experimental Section

Materials

Co (II) acetylacetonate (Co $(C_5H_7O_2)_3$, 97%, Sigma-Aldrich), glacial acetic acid (99% Sigma-Aldrich) and 2-ethylhexanoic acid (99% Fisher Scientific), cerium (III) acetate hydrate (Ce $(CH_3CO_2)_3\cdot 1H_2O$, 98%, TCI Europe NV) were used as received without further purification.

Catalyst Preparation

Flame Spray Pyrolysis

CeO_2 and Co-CeO_2 samples were prepared by flame spray pyrolysis (FSP) in a Tethis NPS10 apparatus. The Tethis NPS10 apparatus was placed in a standard chemical laboratory fume hood modified to comply with EN 14172, EN 1822, and ISO 45H standards (modifications realized by Interflow). The air inflow of the fume hood was kept at a minimum of 0.7 m/s using active control systems. The exhaust flow to the (external) ventilation was equipped with HEPA H14 and ULPA U17 filters. The experiments were conducted after assessing all safety aspects, including those related to working with nanomaterials, in a risk-inventory and evaluation (RI&E) procedure, as required by the Dutch labor law. Appropriate amounts of $Co(C_5H_7O_2)_3$ and $Ce(CH_3CO_2)_3\cdot H_2O$ were dissolved in an equivolumetric solvent mixture of acetic acid and 2-ethylhexanoic acid. The Co and Ce concentrations were 0.15 M. This solution was stirred at 80 °C for approximately 1 h until the metal precursors were completely dissolved. The precursor solution was fed using a syringe pump (injection rate of 5 mL/min) through a nozzle to obtain a fine spray in the center of the flame. The pressure drop at the capillary tip was kept at 2.5 bar by adjusting the orifice gap area at the nozzle. The flame was maintained by a feed of 1.5 L/min methane and 3.0 L/min oxygen. Solid samples were collected on a glass microfiber filter (Whatman) using a membrane vacuum pump. The as-prepared CeO_2 and Co–CeO_2 catalysts are denoted as CeFSP and xCoFSP, where x stands for the molar Co content (mol.%) with respect to the support (Co/(Co+Ce)).

Catalyst Characterization

Inductively Coupled Plasma Optical Emission Spectroscopy (ICP-OES)

The elemental composition (Co and Ce) of the as-prepared catalysts was determined by ICP-OES analysis (Spectro CIROS CCD Spectrometer). Prior to the analytical measurements, the catalysts were dissolved in 5 mL of concentrated sulfuric acid (H_2SO_4) at 200 °C under stirring for at least 30 min, followed by dilution in water.

N_2 Physisorption

The textural properties of the as-prepared catalysts were determined by N_2 physisorption at a temperature of −196 °C using a Micrometrics TriStar II 3020 instrument. Prior to the physisorption measurements, the samples were heated to 160 °C in a N_2 flow for 4 h. The specific surface area (SSA) was determined by the Brunauer – Emmett – Teller (BET) method.

X-ray diffraction (XRD)

X-ray powder diffraction patterns were collected at the ID31 beamline of the European Synchrotron Radiation Facility (ESRF, Grenoble, France). The measurements were performed with an incident X-ray energy of 68 keV using a 0.5 mm x 0.5 mm (H x V) X-ray beam in transmission mode using a DECTRIS Pilatus 3X CdTe 2M detector. These measurements were done at room temperature. The samples were sealed in Kapton tubes (Goodfellow, 3 mm o.d., 0.03 mm wall thickness). Beeswax (Alfa) was used to seal the two ends of the tube. Detector broadening was calibrated using a CeO_2 reference obtained from NIST. The diffraction patterns, specifically the presence of CeO_2 and Co_3O_4 phases, were analyzed by Rietveld refinement using the GSAS software.

In situ synchrotron X-ray diffraction patterns were collected at the ID15A beamline of the ESRF. The measurements were carried out in transmission mode using an incident X-ray energy of 100 keV. A Pilatus3X CdTe 2M detector was used to collect the scattered signal. About 20 mg of sieved catalyst (125-250 μm) was loaded into a quartz capillary (2 mm o.d. wall thickness 0.1 mm) and retained between two glass wool layers. The capillary was sealed with PTFE ferrules in a home-built Clausen-type flow cell. The sample was heated using a gas blower (Cyberstar). The temperature was measured by a thin (0.25 mm) K-type thermocouple placed inside the catalyst bed. Typically, the temperature was raised from 50 °C to 300 °C at a rate of 8.5 °C/min in a flow of 50 mL/min of a mixture of 20 vol.% H_2 in Ar, followed by an isothermal dwell of 0.5 h at 300 °C. Then, the system was cooled to 250 °C in the same mixture. After reaching this temperature, the reduction mixture was replaced by a reaction mixture of 5 vol.% CO_2 and 20 vol.% H_2 balanced by Ar fed at a 50 mL/min flow rate for 0.5 h. The detector distance, energy, and tilt were calibrated using a standard CeO_2 powder obtained from NIST. The CeO_2 phase in these XRD data was analyzed by Rietveld refinement using the GSAS software. PDF data up to q = 28 $Å^{-1}$ were reduced from the XRD data using the pdfgetX3.[28] Real-space refinements were carried out using the PDFgui software.[29] To this end, the PDF is described using the G(r) formalism, which reflects the probability of finding a pair of atoms separated by a distance r with an integrated intensity dependent on the pair multiplicity and the scattering factors of the elements involved. G(r) was experimentally determined by the Fourier transform of the total scattering function F(Q), corresponding to the coherent scattering coming from the sample (Bragg peaks and diffuse scattering) after normalization.

Ultraviolet-visible diffuse reflectance spectroscopy (UV-Vis DRS)

UV-Vis DRS spectra were collected at room temperature with a Shimadzu UV-2401PC spectrometer equipped with an integrating sphere coated with $BaSO_4$ reference. Samples were diluted with $BaSO_4$ (30 mg sample mixed with 120 mg $BaSO_4$).

Transmission Electron Microscopy (TEM)

The morphology and particle size distribution of as-prepared and reduced catalysts were investigated by TEM using an FEI Titan Cryo-TEM instrument operating at an acceleration voltage of 300 kV. An appropriate amount of finely ground material was ultrasonically dispersed in analytical-grade absolute ethanol before deposition on holey Cu TEM grids.

Scanning transmission electron microscopy combined with energy dispersive X-ray analysis (STEM-EDX) was performed to determine the nanoscale distribution of elements in the samples. These measurements were performed on a FEI-cubed Cs-corrected Titan instrument operating at an acceleration voltage of 300 kV. The Co-CeO_2 samples were reduced at 300 °C in a flow of 20 vol.% H_2 in He for 4 h, followed by passivation at room temperature in a flow of 2 vol.% O_2 in He for 1 h. The passivated samples were crushed and sonicated in analytical-grade absolute ethanol, before deposition on holey Cu TEM grids.

Temperature-Programmed Reduction (H_2-TPR)

The reducibility of the samples was evaluated by H_2-TPR with a Micromeritics AutoChem II instrument. Typically, ca. 100 mg sample was loaded into a quartz U-tube between two quartz wool layers. Before H_2-TPR, the sample was treated at 350 °C for 1 h in a 50 mL/min flow of 5 vol.% O_2 in He. TPR profiles were recorded while heating the sample from 40 to 700 °C at a rate of 10 °C/min in a 50 mL/min flow of 4 vol.% H_2 in He. The H_2 consumption was measured by a thermal conductivity detector (TCD), which was calibrated using a AgO reference.

CO and H_2 Chemisorption

CO and H_2 chemisorption measurements were performed with a Micromeritics ASAP2010C instrument. Typically, about 100 mg sample was loaded into a quartz U-tube between two quartz wool layers. Before chemisorption measurements, the catalyst was reduced in a H_2 flow at 300 °C by heating to this temperature at a rate of 10°C/min, followed by an isothermal dwell of 4 h. After evacuation at 320 °C for 1 h, CO and H_2 adsorption isotherms(double) were recorded at 35 °C and 150 °C, respectively.

IR Spectroscopy

IR spectra were recorded on a Bruker Vertex 70v FTIR spectrometer equipped with a DTGS detector. The experiments were performed in situ by using a home-built environmental transmission IR cell. Self-supporting pellets were made by pressing ~10 mg sample in a disc with a diameter of 13 mm. Each spectrum was collected by averaging 32 scans with a resolution of 2 cm^{-1} in the 4000 – 1000 cm^{-1} range.

For CO IR spectroscopy, the sample was first reduced in a flow of 20 vol.% H_2 in He at 300 °C (rate 10 °C/min) for 4 h. After outgassing at 300 °C in vacuum and cooling to 50 °C, IR spectra were recorded as a function of the CO partial pressure in the 0 – 10 mbar range. CO IR measurements were also carried out at liquid N_2 temperatures. For these measurements, the same reduction procedure was followed. After outgassing, the sample was cooled by liquid N_2. The sample temperature was approximately -168 °C. IR spectra were recorded as a function of CO partial pressure in the 0 – 10 mbar range. As-prepared samples were also investigated by CO IR spectroscopy at liquid N_2 temperature. For this purpose, the samples were evacuated at 50 °C for 1 h, before cooling to liquid N_2 temperature. CO_2 IR spectra were recorded at 50 °C after a similar pretreatment procedure as described for the CO IR spectroscopy measurement. The CO_2 IR spectra were obtained as a function of CO_2 partial pressure in the 0 – 10 mbar range. All spectra were background subtracted, and the intensity was normalized to the weight of the pellet.

X-ray Photoelectron Spectroscopy (XPS)

The surface chemical properties of the as-prepared catalysts were studied with a K-Alpha XPS instrument (Thermo Scientific) equipped with an aluminum anode (Al Kα = 1486.68 eV) monochromatized X-ray source. Finely ground samples were placed on double-sided carbon tape. All spectra were acquired using a flood gun to compensate for surface charging. A pass energy of 40 eV was used for region scans with a step size of 0.1 eV and a dwell time of 0.5 s. The spectra were analyzed using the CasaXPS software (version 3.2.23). Energy calibration was performed using the same procedure described in the NAP-XPS description.

Near-Ambient Pressure X-ray Photoelectron Spectroscopy (NAP-XPS)

XPS spectra were recorded in situ during the reduction of the as-prepared catalysts using a SPECS NAP-XPS system. Core-line spectra were acquired using monochromatized Al Kα radiation (1486.6 eV) generated by an Al anode (SPECS XR-50) operated at 50 W. The differential pumping system of the electron analyzer (SPECS Phoibos NAP-150) allows for normal emission XPS measurements in the presence of gases (up to ~20 mbar). The catalyst powder was pelletized into a disc of 12 mm, which was fixed onto a stainless-steel sample holder. Reduction was performed in a flow of 1 mL/min H_2 and 2 mL/min Ar. High-purity gases (99.999%) were used. The total pressure in the NAP reaction cell was kept at 3 mbar using an electronic back-pressure regulator. A typical experiment consisted of heating the sample in the reduction mixture to 550 °C while recording XPS spectra during isothermal dwells at 50 °C intervals. The total acquisition time of the XPS spectra, which included a survey scan and O 1s, C 1s, Ce 3d, and Co $2p_{3/2}$ spectra, was approximately 2-3 h. A pass energy of 40 eV was used with a dwell time of 0.5 s and a step size of 0.1 eV. The U"' (Ce^{4+}) component of the Ce 3d line with a characteristic position of 916.7 eV was used to correct the binding energies of the Co $2p_{3/2}$ and Ce 3d regions.[30,31] A standard procedure involving Shirley background subtraction and atomic sensitivity factors was applied for data processing. Spectral lines were fitted with the CasaXPS software (version 3.2.23) using a symmetric pseudo-Voigt function GL (30). The main metallic component of Co was fitted with the asymmetric LA (1.2,5,5) line shape. The Ce 3d line was fitted according to a model described in the literature.[32,33]

Quasi in situ X-ray Photoelectron Spectroscopy (XPS)

The surface chemical properties of the reduced and deactivated catalysts were studied using a Kratos AXIS Ultra 600 equipped with a monochromatic X-ray source (Al Kα = 1486.68 eV). Self-supporting pellets were made by pressing approximately 40 mg of a sample in a disk with a diameter of 13 mm. Pretreatment of catalysts was carried out in a high-temperature reaction cell (Kratos, WX-530), allowing vacuum sample transfer into the analysis chamber. The samples were reduced in 20 vol.%

H_2 in Ar at a flow rate of 50 mL/min at 300 °C for 4 h at 10 °C/min and ambient pressure. Then, the sample was cooled to 100 °C in the pretreatment mixture, and the reaction cell was evacuated to a pressure below 10^{-8} mbar. Then, the sample was transferred to the XPS analysis chamber. A pass energy of 40 eV was typically used for region scans with a step size of 0.1 eV and a dwell time of 0.5 s. Energy calibration and fitting of Ce 3d and Co2p were performed using the same procedure described in the XPS section.

X-ray Absorption Spectroscopy (XAS)

Extended X-ray absorption fine structure (EXAFS) measurements at the Co K-edge (7.7 keV) were carried out in fluorescence mode at the BL22 beamline of ALBA (Spain). The Co_3O_4 and CoO references were measured in transmission mode. Energy calibration was done with a Co foil (E_0 = 7.709 KeV). Energy selection was achieved with a Si (111) monochromator. The EXAFS data was background-subtracted and normalized. These operations and further EXAFS fitting analysis were carried out using the Demeter package (Athena/Artemis software).[34,35] Scattering paths were calculated using the FEFF6 code based on Co_3O_4, Co metal, and CeO_2 crystal structures. A Co-O-Ce single scattering path was modeled by substituting a Co atom with Ce in the Co_3O_4 structure. The energy shift (E_0), the distance change (ΔR), the coordination number (CN), and the Debye – Waller factor (σ^2) were fitted. The amplitude reduction factors (S_0^2) were determined from fitting of EXAFS data of the Co foil. The amplitude reduction factors were fixed during the fitting of other parameters. Fourier-transformed EXAFS is plotted as k^3-weighted data without phase correction.

Catalytic Activity Measurements

CO_2 hydrogenation

The catalytic performance of CeO_2 and Co-CeO_2 samples in CO_2 hydrogenation was carried out in a down-flow stainless-steel reactor with an internal diameter of 4 mm. The reaction pressure was atmospheric, and the temperature varied in the 200 – 300 °C range. The samples were pressed, crushed, and sieved to a fraction of 125 – 250 µm. Typically, the reactor was filled with 50 mg catalyst diluted with 200 mg of SiC of the same sieve fraction. Before the reaction, the catalyst was reduced in a flow of 100 mL/min of 20 vol.% H_2 in He whilst heating from room temperature to 300 °C at a rate of 10 °C/min, followed by an isothermal dwell for 4 h. The reduced catalyst was cooled to the initial reaction temperature of 200 °C in the same flow. The reaction was started by replacing the reduction gas mixture with a flow of 50 mL/min of 60 vol.% H_2, 15 vol.% CO_2, and 25 vol.% Ar (CO_2:H_2 ratio = 1:4). The temperature was increased in steps of 25 °C using a rate of 5 °C/min. At each isothermal dwell of 160 min, the effluent gas was sampled and analyzed by an online gas chromatograph (Shimadzu, GC-2014) equipped with RT-Q-Bond (FID) and Shincarbon ST 80/100

(TCD) analysis stions. CO_2 conversion, carbon product selectivity, and product formation rates were calculated as follows:

$$X(CO_2) = \frac{F(CO)_{out} + F(CH_4)_{out} + F(CH_3OH)_{out} + xF\left(C_xH_y\right)_{out}}{F(CO_2)_{out} + F(CO)_{out} + F(CH_4)_{out} + F(CH_3OH)_{out} + xF\left(C_xH_y\right)_{out}} \quad (1)$$

$$S(product) = \frac{F(product)_{out}}{F(CO)_{out} + F(CH_4)_{out} + F(CH_3OH)_{out} + xF\left(C_xH_y\right)_{out}} \quad (2)$$

where C_xH_y represents hydrocarbons with more than one carbon atom formed during the reaction. *F* stands for the volumetric flow rate determined from the concentration measured by gas chromatography. Ar was used as an internal standard. The FID and TCD response factors were determined using gas calibration mixtures.

The reaction rate (r_{CO2} in $mol_{CO2} \cdot mol_{Co}^{-1} \cdot s^{-1}$) was calculated and normalized to the Co content in the following manner:

$$r_{CO2} = \frac{X\,(CO_2) * F(CO_2)_{in}}{n_{Co} * V_m} \quad (3)$$

where $F\ (CO_2)_{in}$ is the known CO_2 volumetric flow rate at the reactor inlet and V_m is the molar volume of an ideal gas at standard temperature and pressure. The rates of CH_4 and CO were calculated similarly.

The influence of the H_2/CO_2 ratio on the CO_2 hydrogenation performance was evaluated for the 5CoFSP catalyst. For these activity measurements, 50 mg catalyst was mixed with 200 mg SiC of the same fraction. The same reaction setup as for the other CO_2 hydrogenation activity measurements was employed. The reaction was started by replacing the reducing gas mixture with a flow of 50 mL/min of 18.8 vol.% CO_2, 56.2 vol.% H_2, and 25 vol.% Ar for a H_2/CO_2 ratio of 3, while a flow of 50 mL/min of 25 vol.% CO_2, 50 vol.% H_2, and 25 vol.% Ar was used for a H_2/CO_2 ratio of 2. The influence of the total reaction pressure was evaluated for the 5CoFSP catalyst (50 mg of catalysts and 200 mg of SiC of the same sieve fraction) in the same reactor used for CO_2 hydrogenation at 1 bar. The reaction was started by replacing the reducing gas mixture with a flow of 50 mL/min (18.8 vol.% CO_2, 56.2 vol.% H_2, and 25 vol.% Ar for a H_2/CO_2 ratio of 3), followed by increasing the total pressure in the reactor to 10 bar using a back-pressure regulator.

Results

Catalyst Characterization

CoFSP and CeFSP samples were prepared by flame spray pyrolysis. The most important physicochemical properties of the CoFSP samples are listed in **Table 2.1**. The Co content of the samples determined by ICP-OES elemental analysis agrees reasonably with the targeted values. Synchrotron XRD patterns of the as-prepared

CoFSP samples are shown in **Figure 2.1a**. The dominant crystalline phase is fluorite CeO_2. At a Co content of 10 mol.% and higher, additional diffraction lines belong to Co_3O_4 (**Figure 2.1b**). The CeO_2 lattice parameter (a_{CeO2}) and CeO_2 particle size were estimated by Rietveld refinement (**Table 2.1**). The CeO_2 lattice parameter was smaller for the CoFSP samples containing less than 10 mol.% Co than for the CeO_2 reference sample prepared by flame spray pyrolysis. This can be attributed to the substitution of some Ce cations in the CeO_2 lattice with smaller Co cations.[36] The CeO_2 lattice parameter of the other samples containing more Co is similar to the one determined for CeFSP. The average CeO_2 particle size determined from the XRD data is around 9 nm. There is no clear correlation between the average CeO_2 particle size and the Co content. The specific surface areas, determined by N_2 physisorption vary in the 110-180 m^2/g range decrease with increasing Co content. For the samples containing Co_3O_4, the Rietveld refinement showed that the Co_3O_4 particle size increased from 3.9 nm for 10CoFSP, 5.5 nm for 20CoFSP to 6.6 nm for 30CoFSP.

UV-Vis spectra of CeFSP and as-prepared CoFSP catalysts (**Figure 2.1c**) are characterized by bands in the 260 – 280 nm range, which can be assigned to CeO_2.[37] The formation of Co doped in CeO_2 in samples containing less than 10 mol.% can be judged from the broad band in the 400 – 600 nm range (**Figure 2.1c**).[38] The samples containing 10 mol.% Co and more showed bands in 400 – 480 and 700 – 760 nm ranges characteristic of Co_3O_4. These bands represent ligand-to-metal O^{2-} - Co^{2+} and O^{2-}- Co^{3+} charge transfer, respectively.[39]

Table 2.1. Physicochemical properties of as-prepared CoFSP and CeFSP samples.

Catalyst	Co (mol.%)[a]	S_{BET} (m^2/g)[b]	d_{CeO2} (nm)[c]	d_{Co3O4} (nm)[c]	a_{CeO2} (Å)[c]	d_{CeO2} (nm)[d]	Co/Ce (at.%/at.%)[e]
CeFSP	0	181	9.5 ± 0.6	-	5.411	5.0 ± 2.0	-
1CoFSP	0.9	166	10.1 ± 0.8	-	5.410	4.6 ± 1.8	0.01
2.5CoFSP	2.3	166	8.3 ± 0.6	-	5.403	4.8 ± 1.9	0.04
5CoFSP	4.6	155	9.4 ± 0.6	-	5.404	4.2 ± 1.9	0.06
10CoFSP	9.5	118	9.9 ± 0.4	3.9 ± 0.4	5.410	5.0 ± 2.0	0.11
20CoFSP	18	151	10.0 ± 0.6	5.5 ± 0.4	5.411	6.0 ± 2.4	0.23
30CoFSP	27	97	8.7± 0.6	6.6 ± 0.4	5.411	5.9 ± 1.8	0.35

a – determined from ICP analysis, b -determined by N_2 physisorption on as-prepared samples, c – determined by Rietveld refinement of synchrotron XRD on as-prepared samples, d – determined by TEM for as-prepared samples, e – determined by XPS for as-prepared samples

Representative TEM images (**Figure A1**) show that the samples contain octahedrally shaped particles, irrespective of the Co content. The average particle size is in the 4 – 6 nm range without a noticeable trend with the Co content.[40] Due to the poor contrast, no clear Co-oxide particles could be distinguished. STEM-EDX maps of some of the as-prepared CoFSP samples in **Figure 2.2** reflect the nanoscale distribution of Co. At the lowest Co content (2.5CoFSP), the maps suggest a homogeneous distribution of Co in the CeO_2 particles. At higher Co content (5CoFSP), some Co-containing particles become visible. These particles are even more evident in the 10CoFSP sample with an average size of ~4 nm.

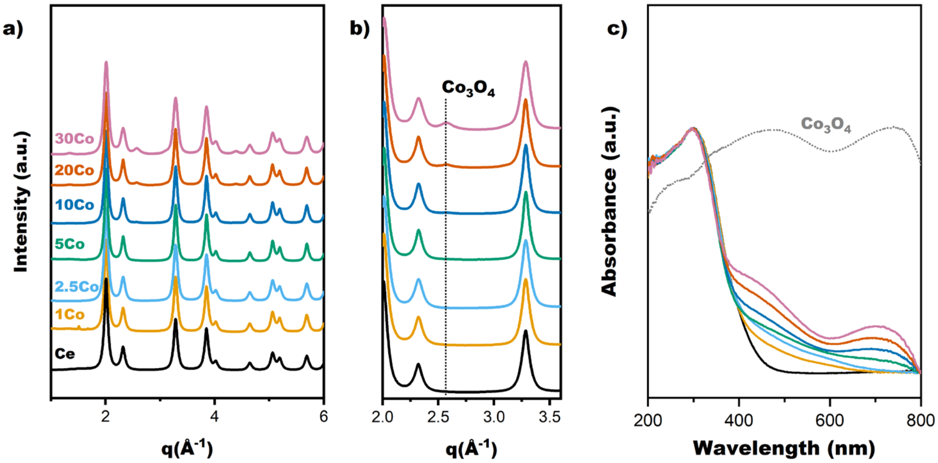

Figure 2.1. Synchrotron XRD patterns (λ = 0.182 Å) of (a) CoFSP and CeFSP with (b) a zoom in the q = 2.0 - 3.6 Å $^{-1}$ region, highlighting the Co_3O_4 (220) diffraction line (c) UV-Vis spectra of CeFSP, CoFSP, and the Co_3O_4 reference.

XPS and CO IR spectroscopy were used to probe the surface composition of the as-prepared samples. Deconvoluted XP spectra are shown in **Figure A2**. The XP spectra of 1CoFSP, 2.5CoFSP, and 5CoFSP catalysts can be fitted by a single Co^{2+} component, as reflected by the single Co $2p_{3/2}$ peak at a binding energy of 781.0 eV and the accompanying satellite at 786.5 eV. At Co contents above 5 mol.%, the spectra can be fit by a $2p_{3/2}$ contribution of Co^{3+} at 778.8 eV and two Co^{2+} contributions at 780.6 eV and 782.4 eV.[41] The Co^{3+} fraction for these samples is ~45%, which is lower than the expected Co^{3+} fraction in Co_3O_4. This means that these samples also contain Co^{2+} ions in the CeO_2 lattice (Co-CeO_2 solid solution) or CoO.[42] The surface Co/Ce ratios determined by XPS increase with the Co content and are slightly higher than the bulk values, suggesting that most Co is located in the surface region. The presence of Co^{2+} was also evident from the CO IR spectra recorded at liquid N_2 temperature (**Figure A3**). In addition to narrow bands at 2150 – 2155 cm^{-1} related to CO adsorption on Ce^{4+}, [43–45] the CO IR spectra of the CoFSP samples contain a sharp band at 2090 – 2100 cm^{-1} due to CO adsorption on Co^{2+}.[46,47] A band due to CO adsorption on Co^{3+}, which is expected at 2180 cm^{-1} [46], was not observed in these CO IR spectra.

STEM-EDX, XRD, XPS, and UV-Vis results indicate that all CoFSP catalysts contain highly dispersed Co^{2+} at the CeO_2 surface as CoO or doped into the CeO_2 surface.

At a Co content of 10 mol.% and above, Co-oxide particles are formed, which are most likely Co_3O_4. **Figure 2.3a** shows the amount of Co^{2+} and Co^{3+} as a function of the Co content. The amount of Co^{2+} does not vary substantially, increasing to ca. 4.6 mol.% for 5CoFSP and then plateauing at values ~3 mol.% for 10CoFSP, 20CoFSP, and 30CoFSP. Highly dispersed Co^{2+} ions in the CeO_2 surface likely represent this nearly constant amount of Co^{2+}. In contrast, the amount of Co^{3+} increases strongly with Co content, indicative of the agglomeration of Co at higher content as Co_3O_4.

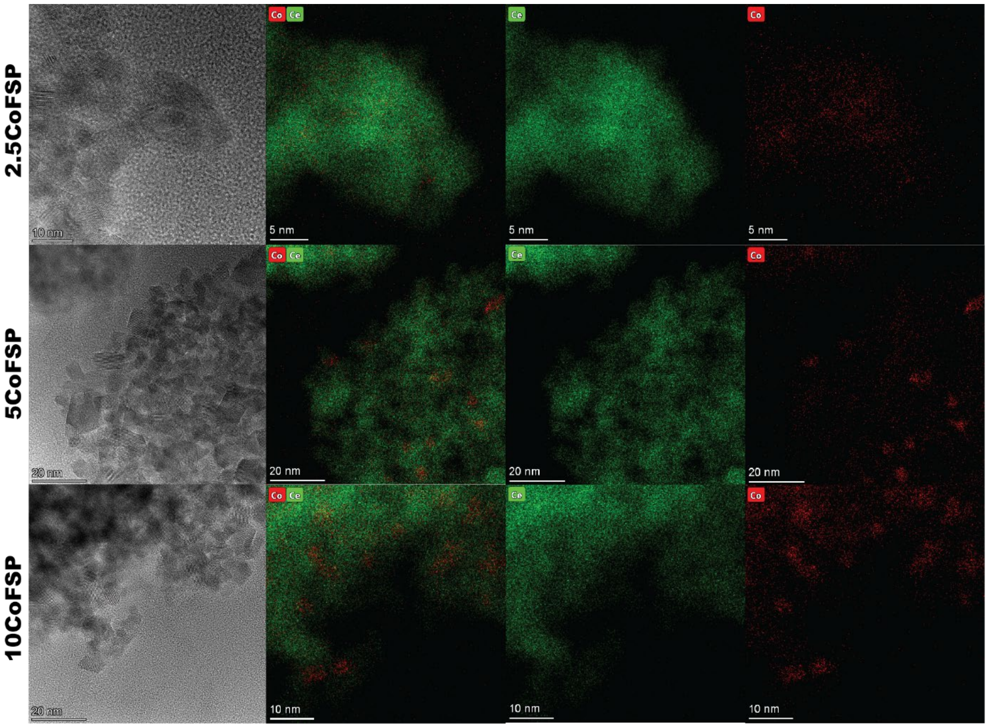

Figure 2.2. STEM-EDX images: (left) HAADF-STEM images and corresponding EDX elemental maps of mixed Co and Ce (in the middle), Ce (right), Co (right) for as-prepared CoFSP catalyst.

Normalized XANES spectra at the Co K-edge are presented in **Figure 2.3b**. The edge energy of the samples containing 10 mol.% and more Co is 7722.0 eV, similar to the edge energy of the Co_3O_4 reference. Thus, these samples contain a significant amount of Co_3O_4. The edge energy of the samples containing less Co is 7714.7 eV, significantly lower than that of CoO (7716.6 eV). We speculate that this is due to the different electronic states of Co^{2+} ions substituting for Ce^{4+} in CeO_2 and Co^{2+} in CoO. To determine the amount of Co in the lattice and in Co_3O_4, we employed linear combination fitting of the XANES spectra. For this purpose, we prepared a 1CoFSP sample with a Co content of 1 mol.% and used its XANES spectrum as the reference for isolated Co in CeO_2. The bulk Co_3O_4 powder was used as the reference for Co_3O_4. The results in **Figure 2.3c** show that the amount of Co_3O_4 is small in the samples with 5 mol.% or less Co and strongly increases for samples containing more Co. The amount of isolated Co^{2+} ions increases with Co content until a Co content of 5 mol.% and then levels off at slightly lower values, in good agreement with the XPS analysis.

We also analyzed Co K-edge EXAFS data to determine the local structure around the Co atoms. The real-space fits are provided in **Figure 2.3d**, while the fit parameters of the k^3-weighted EXAFS are listed in **Table S1**. The 1CoFSP, 2.5CoFSP and 5CoFSP samples contain Co – O (~1.95 Å) and Co – O – Ce (~3.21 Å) shells with coordination numbers (CNs) of 3.6 and 3.2 for 1CoFSP, 5.2 and 2.1 for 2.5CoFSP, 4.0 and 4.1 for 5CoFSP, respectively. These distances and coordination numbers are in reasonable agreement with the proposed structure of Co substituted for Ce^{4+} in CeO_2 [48]. It is also seen that an increase of the Co content from 2.5 mol.% to 30 mol.% results in a decrease of the CNs of the Co – O shell from 5.4 to 4.0 and the Co – O – Ce shell from 3.2 to 1.8, while the CN of the Co – O – Co shell(~2.67 Å) and Co – O – Co shell(~3.21 Å) increase from 0.45 to 2.7 and from 1.3 to 4.9, respectively. Trend-wise, these structural changes agree with the growing contribution of Co_3O_4, which contains Co in tetrahedral and distorted octahedral coordination, next to the presence of Co in the CeO_2 lattice.

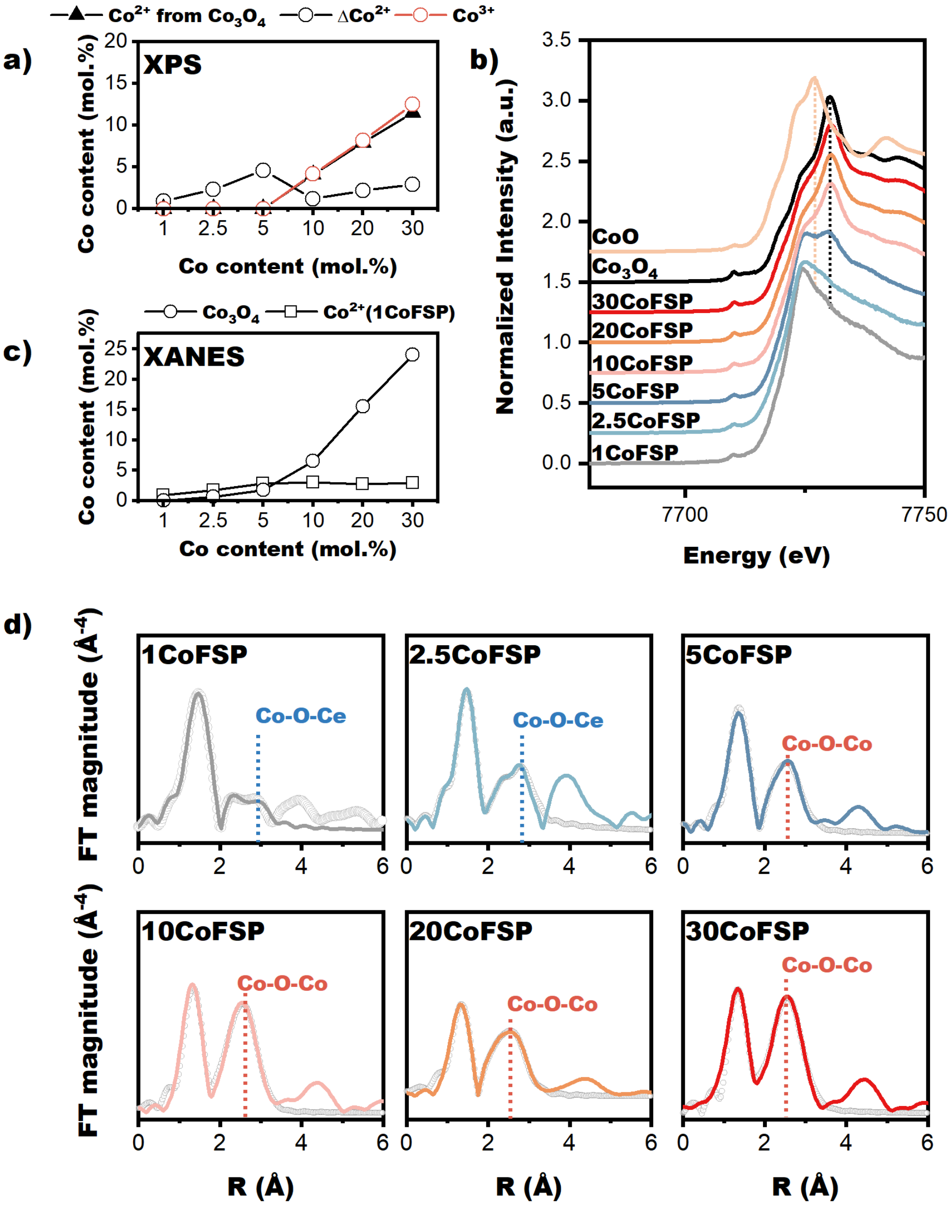

Figure 2.3. (a) Deconvolution results of Co $2p_{3/2}$ for as-prepared CoFSP catalysts (dark grey round– the difference between total Co^{2+} and Co^{2+}, arising from Co_3O_4; orange round – Co^{3+}; dark grey triangle – the estimated amount of Co^{2+} from Co_3O_4. (b) Normalized XANES spectra at the Co K-edge of the as-prepared CoFSP catalysts with a Co_3O_4 reference (black) and CoO (beige). (c) Amount of isolated Co^{2+} and Co_3O_4 as a function of the Co content, following from linear combination fitting of XANES spectra. (d) Co K-edge k^3-weighted R-space plots of the as-prepared CoFSP catalysts with the dashed lines indicating the uncorrected distances of the Co – O – Ce and Co – O – Co shells.

Reduction of CeFSP and CoFSP

Next, we studied the reduction behavior of these samples. Reducing Co ions strongly interacting with CeO_2 requires higher temperatures than Co in Co-oxides. The reduction of Co_3O_4 will also depend on other aspects, such as the Co-oxide dispersion and their interaction with the CeO_2 support.[49,50] **Figure 2.4a** shows the weight-normalized H_2-TPR profiles for the CoFSP and CeFSP samples. Typically, the reduction of Co_3O_4 proceeds in two steps: (i) the reduction of Co_3O_4 to CoO and (ii) the reduction of CoO to Co.[50–52] While the surface of CeO_2 can already be reduced at relatively low temperatures in the presence of metals that can activate H_2, bulk reduction of CeO_2 occurs at temperatures above 700 °C.[53,54] CeFSP exhibits a single reduction feature at 580 °C, attributed to the reduction of surface Ce^{4+} to Ce^{3+}.[55, 56–58] All CoFSP catalysts exhibit a low-temperature peak at 200 °C, which is due to the reduction of surface-adsorbed oxygen species.[59,60] The H_2-TPR profiles of 1CoFSP and 2.5CoFSP are characterized by a main reduction peak at 350 °C. The broad reduction peak at 350 °C can be assigned to the reduction of CoO in strong interaction with CeO_2 or Co in a Co-CeO_2 solid solution.[58] This interpretation is consistent with the XAS, XRD, and XPS findings, indicating the predominance of Co^{2+} species at low Co content. Increasing the Co content from 1 mol.% to 2.5 mol.% shifts the main reduction peak to lower temperatures. This suggests Co in 1CoFSP is more difficult to reduce and might be due to the reduction of Co in Co–O–Ce interface, typically observed at 400 – 600 °C.[58] At a Co content of 5 mol.% and above, the H_2-TPR profiles show two peaks at 300 °C and 425 °C, owing to the reduction Co_3O_4 to CoO and CoO to Co, respectively.[50–52] The corresponding H_2 consumption and estimated CeO_2 reduction degree are shown in **Table 2.2**. The excess of consumed H_2 is defined as the difference between the total H_2 consumed and H_2 required to reduce CoO/Co_3O_4 completely. This excess is substantial for all catalysts and varies slightly with the Co content (**Figure 2.4b**). Thus, the formation of metallic Co facilitates hydrogen spillover and partial reduction of the CeO_2 surface.

Table 2.2. Catalyst reducibility of CeFSP and CoFSP catalysts determined by H_2-TPR.

Catalyst	CeFSP	1Co FSP	2.5Co FSP	5Co FSP	10Co FSP	20Co FSP	30Co FSP
H_2 (mmol/g)[a]	0.59	0.78	0.66	1.12	1.45	2.11	2.89
Excess H_2 consumed (mmol/g)[b]	-	0.61	0.52	0.44	0.33	0.54	0.39

a – determined from H_2-TPR in 100 – 650 °C range, b - estimated from the difference between total H_2 consumption and H_2 required to fully reduce CoO/Co_3O_4 during H_2-TPR.

To facilitate the assignment of the reduction peaks in the H_2-TPR profiles, we investigated the reduction of the 5CoFSP and 20CoFSP samples by in situ NAP-XPS. The total pressure in these NAP-XPS measurements was 3 mbar, which is significantly lower than in the H_2-TPR measurements. **Figure 2.4c** shows the deconvoluted Co

$2p_{3/2}$ and Ce 3d spectra of 20CoFSP obtained during a H_2-TPR treatment in NAP-XPS. The corresponding results for 5CoFSP are shown in **Figure A4**. The most significant changes in the XP spectra occurred in the 200 – 400 °C range. **Figure 2.4d** plots the Co speciation (fractions of Co^{3+}, Co^{2+}, and Co^0) and the Ce^{3+} fraction as a function of the reduction temperature for both samples. The contribution of Ce^{3+} increased gradually to ~30% between 200 and 400 °C, already before the observation of Co^0. The Co^0 fraction increased to ~19% (representing an amount of ~1 mol.% Co) for 5CoFSP and 80% (representing ~14 mol.% Co) for 20CoFSP, confirming the substantial difference in Co reduction degree. The 20CoFSP sample showed the conventional reduction behavior where Co_3O_4 first transformed to CoO in the 200 – 250 °C range, followed by Co^0 formation at higher temperatures.

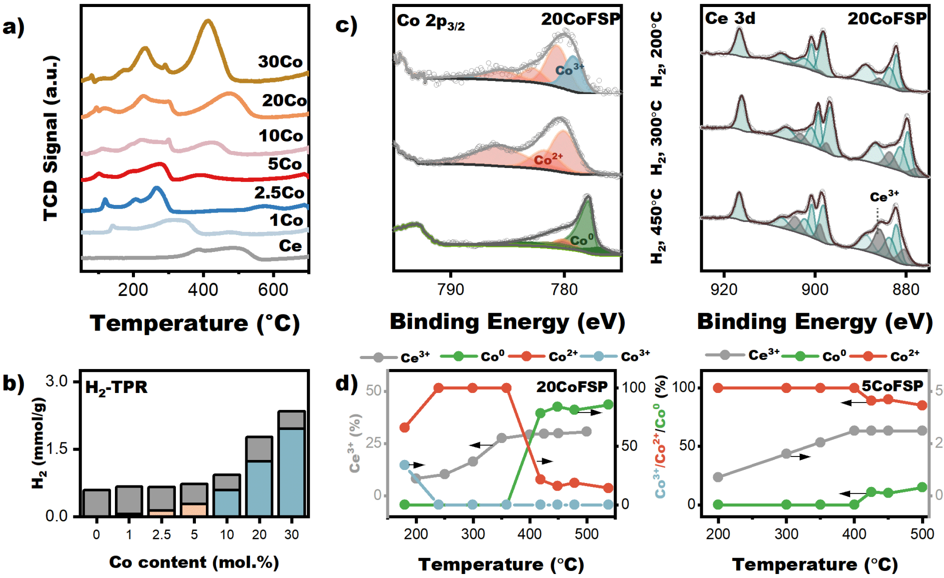

Figure 2.4. (a) Weight-normalized TPR profiles of CeFSP support and CoFSP catalysts (conditions: 4 vol.% H_2, 50 mL/min). (b) Amount of H_2 consumed during TPR experiments (grey – excess H_2; light orange – H_2 required for complete CoO reduction; light blue – H_2 required for complete Co_3O_4 reduction. (c) Deconvoluted Co $2p_{3/2}$ (left) and Ce 3d (right) spectra obtained during H_2-TPR of 20CoFSP followed by NAP-XPS (conditions: 33.3 vol.% H_2 in Ar, 3 mbar, 200 – 500 °C). (d) Co^{3+} (light blue), Co^{2+} (orange), Co^0 (green) and Ce^{3+} (grey) contributions for 20CoFSP and 5CoFSP (conditions: 33.3 vol.% H_2 in Ar, 3 mbar, 200 – 500 °C; spectra in **Figure 2.4c** and **A4**).

Based on the XPS analysis after reduction at 500 °C, we determined that the reduced samples contain almost the same amount of Co^{2+}, i.e., 3.7 mol.% for 5CoFSP and 3.8 mol.% for 20CoFSP. Likely, these species are highly dispersed Co^{2+} ions in strong interaction with the CeO_2 support, which cannot be reduced at 500 °C. The high reduction degree of the CeO_2 surface observed when the samples are reduced above 400 °C, aligning with the formation of Co^0, supports the notion of H spillover from metallic Co to CeO_2, which implies the formation of oxygen vacancies.[61] Based on this data, we can attribute the broad feature above 300 °C in the TPR profile of 5CoFSP and 20CoFSP to the reduction of Co^{2+} to metallic Co and partial reduction of CeO_2.

Overall, the H_2-TPR and NAP-XPS results showed a similar reduction degree of CeO_2, independent of the Co content of the CoFSP samples. Significant reduction of the CeO_2 surface goes together with the formation of metallic Co at temperatures in the 350 – 400 °C range. H_2 dissociation is easier on the samples containing more than 5 mol.% Co. Samples with a low Co content contain a relatively large fraction of Co^{2+} ions in strong interaction with CeO_2, which cannot be reduced at 500 °C. The amount of such stable Co^{2+} species is nearly the same in all samples, ca. 3.8 mol.%.

Catalytic Activity Measurements

As mentioned above, the catalytic performance of the reduced CeFSP and CoFSP samples in CO_2 hydrogenation was evaluated after reduction at 300 °C. The CO_2 hydrogenation reaction was carried out at atmospheric pressure and in the 200 – 300 °C temperature range **(Figure A5.1)**. The catalytic results will be discussed first, followed by a detailed study of the catalyst surface structures obtained after reduction at 300 °C. While CeFSP and 1CoFSP were not active in CO_2 hydrogenation, the reduced CoFSP catalysts containing more Co hydrogenated CO_2 to CO and CH_4 (**Figure 2.5**). Small amounts of CH_3OH, C_2H_6, and C_3H_8 were also observed at low reaction temperatures. The 2.5CoFSP catalyst shows a high selectivity towards CO (~79%) and the highest CH_3OH selectivity of ~4% at 200 °C at a low CO_2 conversion of 0.2%. The CO_2 conversion rate and the CH_4 selectivity increase with the Co content. The 5CoFSP sample also produced a small amount of CH_3OH, while only CO and CH_4 were observed for the other samples with a higher Co content. The 30CoFSP sample achieved a CH_4 selectivity of 92% at a CO_2 conversion of 4.8% at 200 °C. Increasing the reaction temperature also led to a higher CO conversion rate and CH_4 selectivity (**Figure A5.1**), in line with suggestions that CO_2 methanation follows the $CO_2 \rightarrow CO \rightarrow CH_4$ pathway.[62,63]

The influence of the H_2/CO_2 ratio on the catalytic performance was evaluated for the 5CoFSP catalyst reduced at 300 °C and atmospheric pressure (**Figure A5.2**). The CO_2 conversion and CH_4 selectivity increase with increasing H_2/CO_2 ratio. The highest CH_3OH selectivity of ~2% at 200 °C (CO_2 conversion 0.7%) was found for a H_2/CO_2 ratio of 4. **Figure A5.3** reports the impact of the reaction pressure on the catalytic performance of 5CoFSP at a H_2/CO_2 ratio of 3. The CO_2 conversion and CH_4 selectivity decrease from 2.9% to 1.2% and 58% to 10%, respectively, when the pressure is increased from 1 to 10 bar. At higher pressure, the CO selectivity was much higher at 85%. accompanied by an increase in the CH_3OH selectivity from 0.8% at 1 bar to 2% at 10 bar.

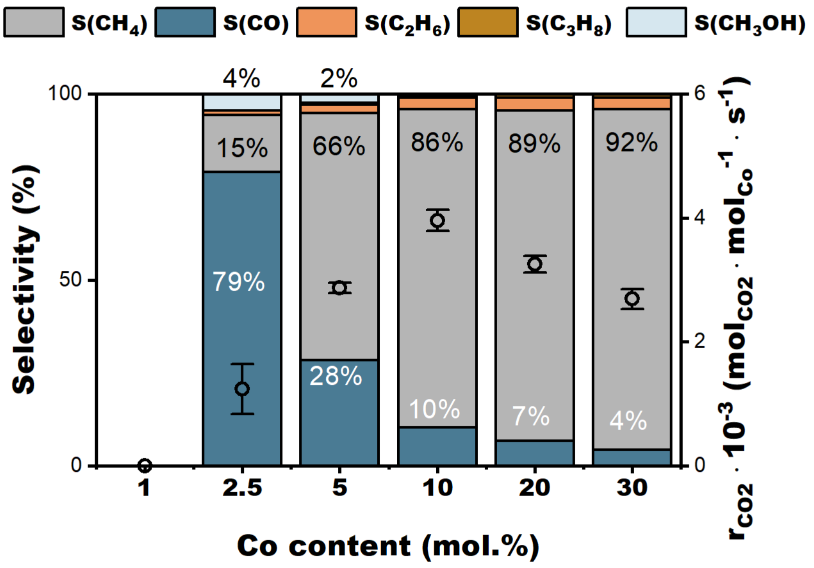

Figure 2.5. Catalytic activity and product distribution of the CoFSP catalysts reduced at 300 °C in CO_2 hydrogenation at 200 °C. The reaction rate was normalized to the total Co content (conditions: 200 °C, 1 bar, 50 mg of sample, 15 vol.% CO_2, 60 vol.% H_2, 25 vol.% Ar, 50 mL/min, 1 bar).

Figure 2.5 shows Co-normalized reaction rates obtained at 200 °C and differential conditions (CO_2 conversion below 10%) as a function of the Co content. The highest reaction rate of $3.9 \pm 0.2 \times 10^{-3}$ $mol_{CO2} \cdot mol_{Co}^{-1} \cdot s^{-1}$ was obtained with the 10CoFSP catalyst. Normalizing the reaction rates to the number of metallic Co sites is challenging due to hydrogen spillover to the CeO_2 support. Several mechanistic studies emphasized that CO_2 hydrogenation to CH_4 requires sufficiently large metallic nanoparticles exposing step-edge sites for C-O bond dissociation in the CO intermediate [26,64]. As small metallic Co clusters lack such sites, a high selectivity to CO has been reported for catalysts with very high Co dispersion.[42,65,66] For Co-CeO_2 catalysts, Co–O–Ce interfaces are also considered to be selective for the rWGS reaction.[42,65,66] On the other hand, the work of Parastaev showed that very small Co clusters stabilized on CoO can catalyze CO_2 methanation with high reaction rates.[26] The catalysts under study here contain (i) isolated Co^{2+} in the CeO_2 surface, which cannot be reduced at 300 °C and likely catalyze the conversion of CO_2 to CO and (ii) Co metal nanoparticles, whose amount and size increase with Co content, resulting in an increasing CO_2 methanation activity. The 2.5CoFSP sample with the lowest Co content shows the highest CO formation rate and the lowest CH_4 formation rate, which is due to the predominance of Co^{2+} in this sample. We speculate that such highly dispersed Co – O – Ce species catalyze CO formation, while a very small amount of metallic Co is responsible for CH_4 formation. CH_4 formation may occur on very small Co clusters in close contact with Co^{2+} sites in a configuration resembling that of Co-CoO interfaces suggested by Parastaev et al. [26] or on a small number of larger Co particles. The former Co^0-Co^{2+}-O-Ce sites might also play a role in the hydrogenation of CO_2 to CH_3OH. With increasing Co content, the reduced catalysts contain an increasing amount of metallic Co nanoparticles at a nearly constant amount of Co^{2+}. While it is likely that the rate of CO formation on the latter sites does not very much with the Co content, CO will be further converted to CH_4 on the metallic Co nanoparticles. The metallic Co nanoparticles provide sites for the conventional hydrogenation of CO_2 to CH_4 via CO intermediate. Moreover, CH_3OH will likely be decomposed on metallic Co, which provides a reasonable explanation for the absence of CH_3OH among the reaction products for the other catalysts. While the CO formation rate decreases with an increasing amount of metallic Co, the CH_4 formation rate goes through a maximum for the 10CoFSP sample. We speculate that this is due to the increasing size of Co nanoparticles, although we cannot exclude a role of the interface between Co nanoparticles and CeO_2 in CO_2 methanation. This interface of Co nanoparticles with the support will decrease with increasing Co nanoparticle size. To understand the structure sensitivity of this set of catalysts, we investigated their structure after reduction at 300 °C.

Structure characterization reduced catalysts

The Co particle size in the reduced and passivated CoFSP catalysts was estimated from HAADF-STEM-EDX maps (**Figure 2.6**). At low Co content (2.5CoFSP), Co remains highly dispersed on CeO_2, similar to the EDX maps of the as-prepared 2.5CoFSP (**Figure 2.2**). Increasing the Co content to 5 mol.% led to some Co clusters with a size of ~1.5 nm. The average Co particle sizes were ~4.5 nm and ~6.5 nm for reduced 10CoFSP and 20CoFSP, respectively. The EDX maps indicate that all the catalysts also contained highly dispersed Co.

We employed quasi-in situ XPS to study the surface composition and reduction degree of the reduced CoFSP samples. The samples were reduced in the reactor chamber of a Kratos XPS system. The reduction was carried out at 300 °C for 4 h at atmospheric pressure in a flow of 20 vol.% H_2 in He. The resulting Co $2p_{3/2}$ and Ce 3d XP spectra and their fits are shown in **Figure 2.7a**, and the fit results are given in **Table 2.3**. The fraction of metallic Co in the reduced samples was 9% for 2.5CoFSP, 14% for 5CoFSP, 52% for 10CoFSP, and 74% for 20CoFSP. The amount of highly dispersed Co^{2+} in the reduced samples was nearly constant, i.e., ~4 mol.%, (**Figure 2.7b**). The contribution of metallic Co increased with Co content, indicating that segregated CoO and Co_3O_4 particles in the as-prepared samples are easier to reduce than Co incorporated into CeO_2. If we assume that XPS can probe all Co, the amount of reduced Co atoms increased from 0.2 mol.% for 2.5CoFSP to 13.5 mol.% for 20CoFSP. Deconvolution of the Ce 3d XP spectra shows that reduction led to an increase of the Ce^{3+} fraction from ~8% in the as-prepared samples to ~33% in the reduced catalysts. The XPS Co/Ce surface ratios in the reduced CoFSP catalysts were lower compared to the corresponding ratios in the as-prepared catalysts (**Table 2.1 and Table 2.3**). This points to sintering of Co species during the reduction step, considering that the encapsulation of Co by CeO_2 is not likely to occur at the low reduction temperature used.

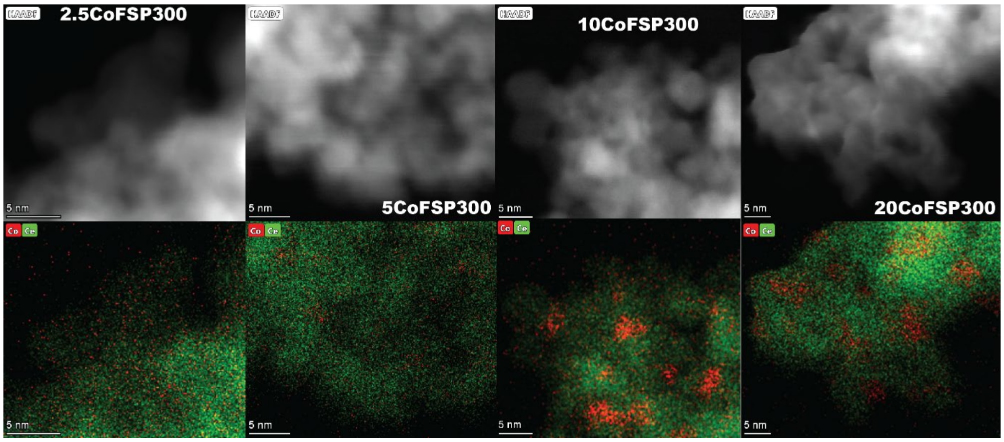

Figure 2.6. STEM-EDX images: (top) HAADF-STEM images and corresponding EDX elemental maps of Co and Ce and (bottom) Co for reduced and passivated CoFSP catalyst.

H_2 chemisorption measurements show that the reduced catalysts with a Co content 5 mol.% and above chemisorb H_2 irreversibly (**Table 2.3, Figure 2.7c, Figure A6**). The 1CoFSP and 2.5CoFSP catalysts do not chemisorb H_2 at 150 °C, which is likely due to the very small amount of metallic Co. The amount of chemisorbed H_2 increased with the Co content, reaching the highest value for 10CoFSP. The theoretical amount of chemisorbed H_2 was estimated based on the Co particle sizes estimated from STEM-EDX maps and assuming a spherical particle shape, a H/Co adsorption stoichiometry of unity, and the Co reduction degrees determined by quasi-in situ XPS. The dispersion of a small amount of Co particles in 2.5CoFSP was assumed to be 100%. The resulting theoretical estimates of 0.013 mmol/g for 5CoFSP, 0.033 mmol/g for 10CoFSP, and 0.065 mmol/g 20CoFSP are substantially lower than the experimental H_2 chemisorption values of 0.36 mmol/g for 5CoFSP, 0.38 mmol/g for 10CoFSP and 0.35 mmol/g for 20CoFSP. The difference is caused by hydrogen spillover to CeO_2 in supported metal nanoparticle catalysts.[67,68]

CO chemisorption revealed strong CO chemisorption on the reduced CoFSP catalysts and CeFSP (**Table 2.3, Figure 2.7c, Figure A7**). The amount of irreversibly chemisorbed CO on CeFSP indicates the presence of oxygen vacancies upon reduction.[69,70] As the H_2 chemisorption data show that more oxygen vacancies are formed in the presence of Co, a significant fraction of CO chemisorbed on the reduced Co-containing catalysts is likely due to oxygen vacancies. At a Co content of 2.5 mol.% and higher, the amount of chemisorbed CO increases strongly. Although part of the chemisorbed CO is on metallic Co [71–73], it is clear that CO chemisorption data cannot be used to determine the number of metallic Co sites.

Table 2.3. Physicochemical properties of reduced at 300 °C CoFSP and CeFSP samples.

Catalyst	Ce FSP	1Co FSP	2.5Co FSP	5Co FSP	10Co FSP	20Co FSP	30Co FSP
d_{Co} (nm)[a]		n.a.	n.a.	1.5	4.5	6.5	n.a.
H_2 (mmol/g)[b]	0.00	0.00	0.00	0.36	0.38	0.35	0.35
Theoretical H_2 (mmol/g)[c]	-	-	0.007	0.013	0.033	0.065	-
CO (mmol/g)[d]	0.06	0.02	0.16	0.23	0.21	0.24	0.28
Co reduction degree[e]	-	-	0.09	0.14	0.52	0.74	-
Ce^{3+} (%)[e]	-	-	35	32	33	32	-
Co/Ce (at.%/at.%)[e]	-	-	0.01	0.02	0.03	0.07	-

a – Co particle size determined by STEM-EDX on reduced at 300 °C and passivated CoFSP catalysts; b – determined by H_2 chemisorption at 150 °C on pre-reduced samples at 300 °C; c - estimated assuming a spherical shape of the Co particles and a H/Co adsorption stoichiometry of 1, the Co reduction degree, derived from XPS of reduced CoFSP catalysts, and STEM-EDX-derived Co particle sizes; d – determined by CO chemisorption at 35 °C on pre-reduced samples at 300 °C; e – Co reduction degree $Co^0/(Co^0+Co^{2+})$ and Ce^{3+} fraction determined by quasi-in situ XPS on samples reduced at 300 °C.

The Co speciation in the reduced catalysts was also investigated by CO IR spectroscopy at 50 °C and liquid N_2 temperature (**Figure 2.8 and A8-10**). The assignment of the IR bands is shown in **Table A2**. The spectra recorded at 50 °C are characterized by linear and bridged carbonyl bands in the 2060 – 2000 cm^{-1} and 1970 – 1840 cm^{-1} ranges, respectively.[74] The narrow carbonyl band in the 2020 – 2040 cm^{-1} range for 2.5CoFSP points to CO adsorption on very small Co clusters.[26,74,75] It is unlikely that atomically reduced Co is stable on CeO_2. In line with this, the spectra of 2.5CoFSP also contain a band due to bridged carbonyls. With increasing Co content, the position of the linear carbonyl band shifts to lower wavenumbers (2000 cm^{-1}. This carbonyl band is already significantly broader at low CO coverage compared to the carbonyl band in 2.5CoFSP. This can be explained by CO adsorption on larger metallic Co particles in reduced 5CoFSP, 10CoFSP and 20CoFSP. With increasing CO partial pressure, the carbonyl band shifts to 2040 cm^{-1} due to lateral interactions between adsorbed CO molecules, which is typical for metallic Co nanoparticles.[76,77] The IR spectra of the CoFSP samples also contain indications of various formate species (formate-I at 2838, 1584, and 1565 cm^{-1}; formate-II at 2838, 1565, and 1359 cm^{-1}; formate-III at 1550, 1371 cm^{-1}) with a minor contribution of carbonate species (**Figure A8**).[78]

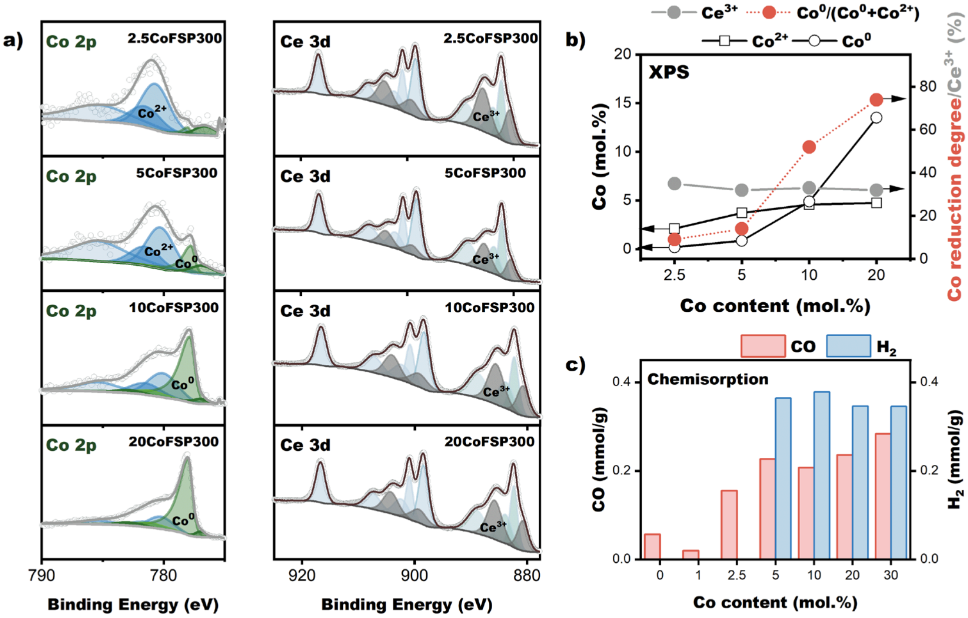

Figure 2.7. (a) Deconvolution of Co $2p_{3/2}$ and Ce 3d XP spectra of 2.5CoFSP, 5CoFSP, 10CoFSP and 20CoFSP after reduction at 300 °C (conditions: 20 vol.%H_2 in Ar, 50 mL/min, 10 °C/min, 4 h). (b) Co reduction degree ($Co^0/(Co^0+Co^{2+})$) and Ce^{3+} fraction derived from XP spectra in panel (a). (c) Amount of H_2 and CO chemisorbed during chemisorption measurements on CeFSP and CoFSP samples reduced at 300 °C.

The corresponding IR spectra recorded at liquid N_2 temperature are shown in **Figure A9-10**. The carbonyl band for 2.5CoFSP is narrower than the carbonyl bands for the other samples, further supporting the conclusion that this sample contains small Co clusters. The relatively narrow band at ~1933 cm^{-1}, due to bridged carbonyls on Co clusters, was only observed for the reduced 2.5CoFSP. Moreover, the carbonyl bands on the small Co clusters in 2.5CoFSP are much broader in the IR spectra recorded at liquid N_2 temperature than those recorded at 50 °C. This is likely due to lateral interactions of these carbonyls with CO adsorbed on proximate Co^{2+} sites and other sites. While the reduced 2.5CoFSP sample likely contains very small metallic Co clusters, the reduced 5CoFSP, 10CoFSP, and 20CoFSP contain metallic Co nanoparticles, as evident from the IR spectra. With increasing Co content, the band at ~2030 cm^{-1} broadens and shifts to ~2055 cm^{-1}.

CO_2 activation was studied by CO_2 IR spectroscopy at 50 °C (**Figure 2.9 and A11**). All IR spectra contain a strong band due to the asymmetric stretching vibration of gaseous CO_2 at ~2346 cm^{-1}.[76] The presence of significant carbonyl bands in the 2025 – 2084 cm^{-1} range implies that CO_2 dissociation occurs already at 50 °C. Notably, the carbonyl bands for 2.5CoFSP are narrower and sharper than those for the other samples, which is in line with the CO IR spectra presented above. At a Co content of 5 mol.% and above, the spectra contain a strong carbonyl feature at 2000 cm^{-1} due to CO adsorbed on Co nanoparticles. In line with the CO IR spectra above, this carbonyl band blue-shifted with increasing CO_2 partial pressure, pointing to lateral interaction between CO molecules on metallic Co particles. Compared to 2.5CoFSP, the IR spectra of 2.5CoFSP, the 5CoFSP, 10CoFSP, and 20CoFSP catalysts contained much stronger carbonyl bands. Notably, the (bi)carbonate/formate bands are stronger than the carbonyl bands for all CoFSP catalysts. Such formate and carbonate species might also be involved in CO_2 dissociation. The 2.5CoFSP sample contains much more formate species than 5CoFSP, 10CoFSP and 20CoFSP, which can probably be linked to the presence of Co small clusters with a high perimeter surface with the support in the former sample. The higher intensity of the formate bands for 2.5CoFSP together with the lower intensity of Co carbonyls may indicate that the rWGS reaction on 2.5CoFSP involves highly dispersed Co^{2+} species, whereas Co nanoparticles convert CO_2 to CO and CH_4 via conventional metal-catalyzed reactions.

The negative band at 2090 cm^{-1} in the CO_2 IR spectra indicates that CeO_2 was partially reoxidized by CO_2 in the reduced CoFSP catalysts. Moreover, a broad band was observed in the 2110 – 2135 cm^{-1} range for the reduced CeO_2-based catalysts, which is due to the $^2F5/2 \rightarrow {}^2F7/2$ electronic transition of Ce^{3+}.[43] The appearance of this band upon reduction evidences the partial reduction of CeO_2 in the CeFSP and CoFSP catalysts.[61] Various formate (formate-I at 2838, 1584, and 1565 cm^{-1}; formate-II at 2838, 1565 and 1359 cm^{-1}; formate-III at 1550, 1371 cm^{-1}) and carbonate and bicarbonate (1635, 1425, 1222 cm^{-1}) species are also observed for all CoFSP catalysts (**Figure A11**), which implies the high surface reactivity towards CO_2. Earlier, Parastaev et al. concluded that CO_2 activation in partially reduced Co/CeO_2-ZrO_2 catalysts takes place at sites at the interface between metallic Co and reducible components in the catalysts, namely CoO and CeO_2.[26]

The structural changes of the CoFSP catalysts and the bare CeFSP support during reduction and subsequent CO_2 hydrogenation were also investigated by in situ synchrotron XRD. The XRD patterns of all CoFSP catalysts can be described well by CeO_2 (**Figure A12**). No reflections related to Co-containing phases were observed on 2.5CoFSP and 5CoFSP, suggesting that the reduced Co particles were very small, which is in line with the STEM-EDX maps. The 10CoFSP and 20CoFSP show a stepwise reduction of Co_3O_4 to Co metal following the sequence $Co_3O_4 \rightarrow CoO \rightarrow Co$ at temperatures around 175 °C and 225 °C, respectively (**Figure A12**). The ΔXRD shows that, with increasing Co content, the contribution at $q = 2.96$ $Å^{-1}$ due to metallic Co becomes stronger (**Figure 2.10a**). The negative features at $q = 2.58$ and 4.36 $Å^{-1}$ in the subtracted XRD patterns (ΔXRD) of the 10CoFSP and 20CoFSP catalysts are due to the reduction of Co_3O_4.

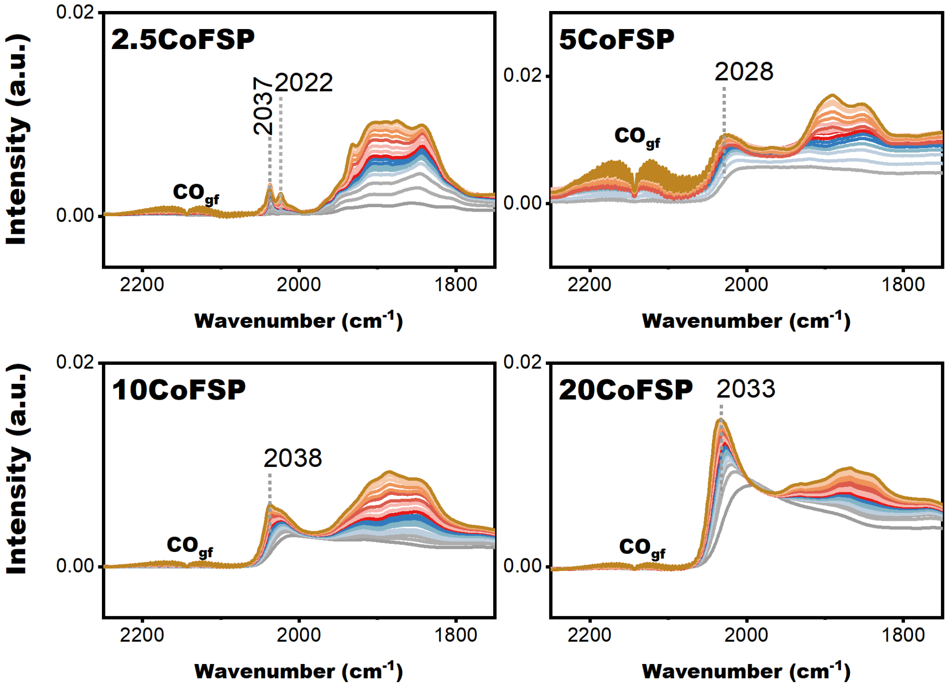

Figure 2.8. IR spectra of the CoFSP samples reduced at 300 °C after CO adsorption at 50 °C (conditions: 1 – 10 mbar CO).

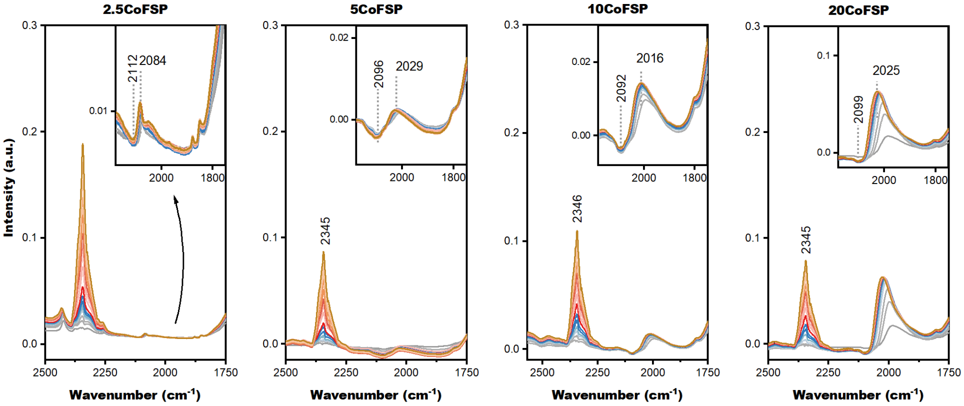

Figure 2.9. IR spectra of the CoFSP reduced at 300 °C after CO_2 adsorption at 50 °C (conditions: 1 – 10 mbar CO_2).

Rietveld refinement of the XRD patterns revealed an increase in the CeO_2 unit cell parameter during reduction for all catalysts and the CeFSP sample (**Figure 2.10b**), along with a minor increase of the CeO_2 crystallite size from 8 nm to 12 nm (**Figure 2.10c**). In addition to gradual thermal expansion, a more abrupt expansion of the CeO_2 unit cell parameter from 5.405 to 5.444 Å was observed in the 100 – 250 °C temperature range for all CoFSP catalysts and the CeFSP support (**Figure 2.10b**). Nevertheless, the expansion of the CeFSP unit cell is more gradual, and the change in the unit cell parameter is less pronounced than that of the CoFSP catalysts (**Figure 2.10b**). The reduction of Ce^{4+} to the larger Ce^{3+} ion and the electrostatic repulsion between oxygen vacancies and the surrounding cations cause this abrupt increase of the unit cell parameter.[79]

The G(r) derived from the PDF of CoFSP and CeFSP before and after reduction are shown in **Figure A13**. The observed peaks at distances r = 3.8, 4.5, 5.4, 5.9, and 6.6 Å are characteristic of the CeO_2 structure. The refined lattice parameters of as-prepared CeFSP, 2.5CoFSP, 5CoFSP, and 10CoFSP catalysts are 5.408 Å, 5.398 Å, 5.399 Å, and 5.400 Å, respectively (**Table A3**). The decrease in the unit cell parameter for CoFSP samples can be explained by shortening of the average distance between Ce-Ce atom pairs due to Co insertion in the CeO_2 lattice, which is in good agreement with the other characterization results.[80] The change in the unit cell parameter is less pronounced for the catalysts containing more Co. The experimental PDF curves were also fitted by a Gaussian to the expected peak at a Ce-Ce distance of ~3.8 Å in the CeO_2 fluorite structure. The resulting CeO_2 peaks of as-prepared CoFSP catalysts exhibit shorter interatomic distances than the CeFSP peaks, which supports the insertion of Co in the CeO_2 structure (**Table A4**). To identify small changes due to Co, ΔG(r) was determined by subtracting G(r) of CeFSP from the G(r) of the CoFSP catalysts (**Figure A14**). Following an example in literature for Ni-ZrO_2-CeO_2 [81], the PDFs of Co_3O_4, CoO, Co, and Co doped in CeO_2 were modeled. Comparison of the experimental PDF to these models shows that the ΔG(r) of the as-prepared 10CoFSP catalyst contains features of Co_3O_4 and Co doped in the CeO_2 lattice (r = 3.8 and 4.5 Å) (**Figure A14**), while the ΔG(r) of the 2.5CoFSP and 5CoFSP shows mostly peaks matching those of Co doped in the CeO_2 lattice (r = 3.8 and 4.5 Å).

The direct G(r) analysis and Rietveld refinement of the PDF data of the reduced catalysts show an increase in the interatomic distances, implying an expansion of the CeO_2 lattice. This can be attributed to thermal expansion and the formation of Ce^{3+} ions. The likely random distribution of Ce^{3+} in the reduced catalysts and the increased thermal motion at higher temperatures can explain the broader peaks in the PDF (**Figure A13**). The ΔG(r) of the reduced CoFSP catalysts shows features of metallic Co (r = 2.5; 4.3 and 5.6 Å) and Co doped into the CeO_2 lattice (r = 3.8 and 4.5 Å) (**Figure A14**). The latter implies that not all Co^{2+} ions were reduced under these conditions, which is consistent with the quasi-in situ XPS and STEM-EDX results of the reduced catalysts.

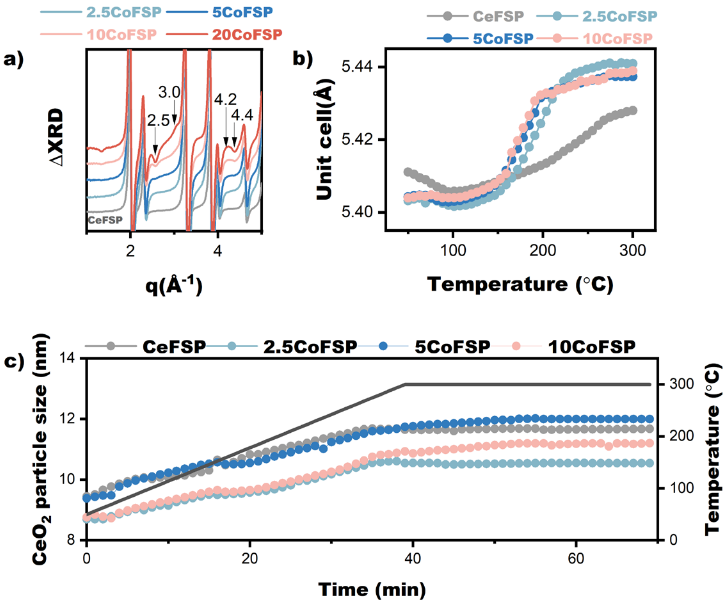

Figure 2.10. (a) Synchrotron ΔXRD (λ = 0.124 Å) of CeFSP and CoFSP before and after reductive pretreatment. ΔXRD difference is obtained by subtraction of the diffractogram of as-prepared sample from reduced diffractogram of the same sample. (b) Refined unit cell parameter of CeO_2 for CeFSP and CoFSP during reductive pretreatment. (c) Refined CeO_2 particle size of CeFSP and CoFSP during pretreatment (conditions: 20 vol.% H_2 in Ar, 50 mL/min, 50 – 300 °C, 1 bar).

Discussion

Combined XRD, XAS, and STEM-EDX data demonstrate that the introduction of Co into CeO_2 first leads to the formation of highly dispersed Co^{2+}, most likely dispersed in the surface of CeO_2 as a solid solution (1CoFSP and 2.5CoFSP). The substitution of Ce with Co is evident from the unit cell contraction probed by XRD. A higher Co content led to Co-oxide particles in addition to a nearly constant amount of highly dispersed Co^{2+}. The presence of Co species differing in their interaction with CeO_2 led to different reduction behavior as followed from H_2-TPR and NAP-XPS measurements. Reduction at 500 °C led to a small amount of Co^0 with most (~80%) of Co remaining as highly dispersed Co^{2+}. On the other hand, the same reduction treatment led to the reduction of nearly 80% of Co in 20CoFSP, resulting in the predominance of Co metal nanoparticles. The amount of highly dispersed Co^{2+} was found to be nearly constant in all samples, suggesting that these species are too strongly bound to CeO_2 to be reduced under the given conditions. The presence of such uniformly distributed Co species was confirmed by STEM-EDX maps in the as-prepared and reduced samples. Thus, while highly dispersed Co – O – Ce species are not reduced, the CoO and Co_3O_4 particles in the as-prepared CoFSP precursor result in nanometer-sized Co particles upon reduction. Irrespective of the Co content, the surface of CeO_2 was found to become partially reduced, indicating the formation of oxygen vacancies for all CoFSP catalysts during reduction. Oxygen vacancies in CeO_2 are thought to be involved in CO_2 hydrogenation, for example, by enhancing CO_2 adsorption.[82,83] The 2.5CoFSP sample with the lowest Co content exhibited the highest CO formation rate and the lowest CH_4 formation rate, which is likely due to the small amount of metallic Co in the form of very small clusters. We cannot exclude that the highly dispersed Co – O – Ce species also contribute to CO formation.[65,84,85] Active sites at the interface between small Co^0 clusters and Co^{2+}-O-Ce moieties might play a role in the hydrogenation of CO_2 to CH_3OH [17], which was observed for 2.5CoFSP and 5CoFSP. With increasing Co content, the reduced catalysts contain more metallic Co nanoparticles at a nearly constant amount of Co^{2+}. The metallic Co nanoparticles provide sites for H_2 dissociation and conventional hydrogenation of CO_2 to CH_4 via CO intermediate.[62,86,87] These samples showed very little or no CH_3OH formation, likely because CH_3OH is decomposed on metallic Co. Comparison of the Co-weight normalized activity with literature data (**Figure A15 and Table A5**) shows that the 10CoFSP catalyst is more active in CO_2 methanation than the most active Co/CeO_2 and Co/TiO_2 catalysts reported before. It is speculated that the combination of small Co nanoparticles with oxygen vacancies in the CeO_2 surface contributes to the high activity in CO_2 methanation.

Conclusions

In this work, a set of Co-CeO_2 samples with varying Co content (1 – 30 mol.%) prepared by FSP was evaluated for their catalytic performance in CO_2 methanation. FSP preparation of Co-CeO_2 resulted in small CeO_2 nanoparticles of ~8 nm with a higher surface area than conventional CeO_2. Catalysts with low Co content contain a relatively large fraction of Co^{2+} ions in strong interaction with CeO_2, which cannot be reduced at 500 °C. The amount of such stable Co^{2+} species is nearly the same in all samples containing 5 mol.% Co or more, i.e., ~3.8 mol.%. Catalysts containing 5 mol.% Co or more also contain segregated Co-oxide particles as CoO and Co_3O_4. These particles can be partially reduced to metallic Co nanoparticles upon reduction at 300 °C. The highest Co-weight-normalized activity of 3.9 ± 0.2 $mmol_{CO2}/mol_{Co}/s$ at a temperature of 200 °C was found for the 10CoFSP sample. The Co reduction degree of this sample is ~50%, represented by on average 4.5 nm Co nanoparticles, with the other half of Co present as highly dispersed Co^{2+} in strong interaction with the CeO_2 support. This sample exhibited a CH_4 selectivity of 85% at 200 °C. A very low Co reduction degree of ca. 10% in 2.5CoFSP with only very small Co clusters as metallic phase led to the predominant formation of CO (79%) and less CH_4 (17%). A small amount of CH_3OH among the reaction products is associated with the hydrogenation of CO_2 on oxygen vacancies assisted by H_2 dissociation on very small Co clusters. Catalysts containing more and larger Co nanoparticles mainly yield CH_4, small amounts of CO and no CH_3OH. The outstanding CO_2 methanation activity of FSP-prepared Co-CeO_2 catalysts is linked to the synergy between relatively small metallic Co nanoparticles and Co^{2+}-O-Ce sites, involving oxygen vacancies.

References

1. Stavitski, E. et al. Complexity behind CO_2 capture on NH_2-MIL-53(Al). Langmuir 27, 3970–3976 (2011).

2. Ronda-Lloret, M., Rothenberg, G. & Shiju, N. R. A Critical Look at Direct Catalytic Hydrogenation of Carbon Dioxide to Olefins. ChemSusChem 12, 3896–3914 (2019).

3. Aziz, M. A. A., Jalil, A. A., Triwahyono, S. & Ahmad, A. CO_2 methanation over heterogeneous catalysts: recent progress and future prospects. Green Chemistry 17, 2647–2663 (2015).

4. Ren, J. et al. Methanation of CO/CO_2 for power to methane process: Fundamentals, status, and perspectives. Journal of Energy Chemistry 80, 182–206 (2023).

5. Ashok, J. et al. A review of recent catalyst advances in CO_2 methanation processes. Catal Today 356, 471–489 (2020).

6. Rönsch, S. et al. Review on methanation – From fundamentals to current projects. Fuel 166, 276–296 (2016).

7. Kondratenko, E. V., Mul, G., Baltrusaitis, J., Larrazábal, G. O. & Pérez-Ramírez, J. Status and perspectives of CO_2 conversion into fuels and chemicals by catalytic, photocatalytic and electrocatalytic processes. Energy Environ Sci 6, 3112–3135 (2013).

8. Shinde, G. Y., Mote, A. S. & Gawande, M. B. Recent Advances of Photocatalytic Hydrogenation of CO_2 to Methanol. Catalysts 2022, Vol. 12, Page 94 12, 94 (2022).

9. Centi, G., Quadrelli, E. A. & Perathoner, S. Catalysis for CO_2 conversion: a key technology for rapid introduction of renewable energy in the value chain of chemical industries. Energy Environ Sci 6, 1711–1731 (2013).

10. Kuld, S. et al. Quantifying the promotion of Cu catalysts by ZnO for methanol synthesis. Science (1979) 352, 969–974 (2016).

11. Graciani, J. et al. Highly active copper-ceria and copper-ceria-titania catalysts for methanol synthesis from CO_2. Science (1979) 345, 546–550 (2014).

12. Jalama, K. Carbon dioxide hydrogenation over nickel-, ruthenium-, and copper-based catalysts: Review of kinetics and mechanism. Catalysis Reviews 59, 95–164 (2017).

13. Li, X. et al. Strong Metal-Support Interactions of Ni-CeO_2 Effectively Improve the Performance of a Molten Hydroxide Direct Carbon Fuel Cell. ACS Omega 7, 24646–24655 (2022).

14. Zhang, Z. et al. Advances in studies of the structural effects of supported Ni catalysts for CO_2 hydrogenation: from nanoparticle to single atom catalyst. J Mater Chem A Mater 10, 5792–5812 (2022).

15. Suppiah, D. D., Daud, W. M. A. W. & Johan, M. R. Supported metal oxide catalysts for CO_2 Fischer−Tropsch conversion to liquid fuels - A review. Energy and Fuels 35, 17261–17278 (2021).

16. Have, I. C. ten et al. Uncovering the reaction mechanism behind CoO as active phase for CO_2 hydrogenation. Nature Communications 2022 13:1 13, 1–11 (2022).

17. Liu, S. et al. Hetero-site cobalt catalysts for higher alcohols synthesis by CO_2 hydrogenation: A review. Journal of CO_2 Utilization 67, 102322 (2023).

18. Diehl, F. & Khodakov, A. Y. Promotion of Cobalt Fischer-Tropsch catalysts with noble metals: A review. Oil and Gas Science and Technology 64, 11–24 (2009).

19. Tauster, S. J., Fung, S. C., Baker, R. T. K. & Horsley, J. A. Strong interactions in supported-metal catalysts. Science (1979) 211, 1121–1125 (1981).

20. Eschemann, T. O. & De Jong, K. P. Deactivation behavior of Co/TiO_2 catalysts during fischer-tropsch synthesis. ACS Catal 5, 3181–3188 (2015).

21. Zhang, Q., Kang, J. & Wang, Y. Development of Novel Catalysts for Fischer-Tropsch Synthesis: Tuning the Product Selectivity. ChemCatChem 2, 1030–1058 (2010).

22. He, X., Wang, X. & Xu, H. Advancements in Cobalt-Based Catalysts for Enhanced CO_2 Hydrogenation: Mechanisms, Applications, and Future Directions: A Short Review. Catalysts 2024, Vol. 14, Page 560 14, 560 (2024).

23. van Deelen, T. W., Hernández Mejía, C. & de Jong, K. P. Control of metal-support interactions in heterogeneous catalysts to enhance activity and selectivity. Nature Catalysis vol. 2 955–970 (2019).

24. Fu, X. P. et al. Boosting reactivity of water-gas shift reaction by synergistic function over CeO_{2-x}/CoO_{1-x}/Co dual interfacial structures. Nature Communications 2023 14:1 14, 1–11 (2023).

25. Wang, L. et al. Silica accelerates the selective hydrogenation of CO_2 to methanol on cobalt catalysts. Nature Communications 2020 11:1 11, 1–9 (2020).

26. Parastaev, A. et al. Breaking structure sensitivity in CO_2 hydrogenation by tuning metal–oxide interfaces in supported cobalt nanoparticles. Nat Catal 5, 1051–1060 (2022).

27. Boaro, M., Colussi, S. & Trovarelli, A. Ceria-based materials in hydrogenation and reforming reactions for CO_2 valorization. Front Chem 7, 426236 (2019).

28. Juhás, P., Davis, T., Farrow, C. L. & Billinge, S. J. L. PDFgetX3: a rapid and highly automatable program for processing powder diffraction data into total scattering pair distribution functions. urn:issn:0021-8898 46, 560–566 (2013).

29. Farrow, C. L. et al. PDFfit2 and PDFgui: computer programs for studying nanostructure in crystals. Journal of Physics: Condensed Matter 19, 335219 (2007).

30. Stadnichenko, A. I. et al. Study of active surface centers of Pt/CeO_2 catalysts prepared using radio-frequency plasma sputtering technique. Surf Sci 679, 273–283 (2019).

31. Larachi, F., Pierre, J., Adnot, A. & Bernis, A. Ce 3d XPS study of composite $CexMn_{1-x}O_{2-y}$ wet oxidation catalysts. Appl Surf Sci 195, 236–250 (2002).

32. Kato, S. et al. Quantitative depth profiling of Ce^{3+} in Pt/CeO_2 by in situ high-energy XPS in a hydrogen atmosphere. Physical Chemistry Chemical Physics 17,

5078–5083 (2015).

33. Skála, T., Šutara, F., Prince, K. C. & Matolín, V. Cerium oxide stoichiometry alteration via Sn deposition: Influence of temperature. J Electron Spectros Relat Phenomena 169, 20–25 (2009).

34. Newville, M. IFEFFIT: Interactive XAFS analysis and FEFF fitting. J Synchrotron Radiat 8, 322–324 (2001).

35. Ravel, B. & Newville, M. ATHENA, ARTEMIS, HEPHAESTUS: data analysis for X-ray absorption spectroscopy using IFEFFIT. urn:issn:0909-0495 12, 537–541 (2005).

36. Abbas, F. et al. Differential cytotoxicity of ferromagnetic Co doped CeO_2 nanoparticles against human neuroblastoma cancer cells. J Alloys Compd 648, 1060–1066 (2015).

37. Hagfeldt, A. & Grätzel, M. Light-Induced Redox Reactions in Nanocrystalline Systems. Chem Rev 95, 49–68 (1995).

38. Wu, T. S. et al. Dramatic band gap reduction incurred by dopant coordination rearrangement in Co-doped nanocrystals of CeO_2. Scientific Reports 2017 7:1 7, 1–7 (2017).

39. Khodakov, A. Y., Chu, W. & Fongarland, P. Advances in the development of novel cobalt Fischer-Tropsch catalysts for synthesis of long-chain hydrocarbons and clean fuels. Chem Rev 107, 1692–1744 (2007).

40. Muravev, V. et al. Size of cerium dioxide support nanocrystals dictates reactivity of highly dispersed palladium catalysts. Science (1979) 380, 1174–1178 (2023).

41. Lykhach, Y. et al. Quantitative Analysis of the Oxidation State of Cobalt Oxides by Resonant Photoemission Spectroscopy. Journal of Physical Chemistry Letters 10, 6129–6136 (2019).

42. Deng, K. et al. Studies of CO_2 hydrogenation over cobalt/ceria catalysts with in situ characterization: the effect of cobalt loading and metal–support interactions on the catalytic activity. Catal Sci Technol 10, 6468–6482 (2020).

43. Binet, C., Badri, A., Boutonnet-Kizling, M. & Lavalley, J. C. FTIR study of carbon monoxide adsorption on ceria: CO_2 carbonite dianion adsorbed species. Journal of the Chemical Society, Faraday Transactions 90, 1023–1028 (1994).

44. Wu, W., Savereide, L. M., Notestein, J. & Weitz, E. In-situ IR spectroscopy as a probe of oxidation/reduction of Ce in nanostructured CeO_2. Appl Surf Sci 445, 548–554 (2018).

45. Binet, C., Daturi, M. & Lavalley, J. C. IR study of polycrystalline ceria properties in oxidised and reduced states. Catal Today 50, 207–225 (1999).

46. Busca, G., Guidetti, R. & Lorenzelli, V. Fourier-transform Infrared Study of the Surface Properties of Cobalt Oxides. 86, 989–994 (1990).

47. Ferstl, P. et al. Adsorption and Activation of CO on Co_3O_4(111) Thin Films. Journal of Physical Chemistry C 119, 16688–16699 (2015).

48. Kottwitz, M., Li, Y., Wang, H., Frenkel, A. I. & Nuzzo, R. G. Single Atom

Catalysts: A Review of Characterization Methods. Chemistry–Methods 1, 278–294 (2021).

49. Das, T. K. et al. Fischer-tropsch synthesis: Kinetics and effect of water for a Co/SiO_2 catalyst. Energy and Fuels 19, 1430–1439 (2005).

50. Khodakov, A. Y., Griboval-Constant, A., Bechara, R. & Villain, F. Pore-size control of cobalt dispersion and reducibility in mesoporous silicas. Journal of Physical Chemistry B 105, 9805–9811 (2001).

51. Karaca, H. et al. In situ XRD investigation of the evolution of alumina -supported cobalt catalysts under realistic conditions of Fischer-Tropsch synthesis. Chemical Communications 46, 788–790 (2010).

52. Castner, D. G., Watson, P. R. & Chan, I. Y. X-ray Absorption Spectroscopy, X-ray Photoelectron Spectroscopy, and Analytical Electron Microscopy Studies of Cobalt Catalysts. 2. Hydrogen Reduction Properties. J. Phys. Chem 94, 819–828 (1990).

53. Perrichon, V. et al. Reduction of cerias with different textures by hydrogen and their reoxidation by oxygen. Journal of the Chemical Society, Faraday Transactions 90, 773–781 (1994).

54. Yao, H. C. & Yao, Y. F. Y. Ceria in automotive exhaust catalysts: I. Oxygen storage. J Catal 86, 254–265 (1984).

55. Ocampo, F., Louis, B. & Roger, A. C. Methanation of carbon dioxide over nickel-based $Ce_{0.72}Zr_{0.28}O_2$ mixed oxide catalysts prepared by sol–gel method. Appl Catal A Gen 369, 90–96 (2009).

56. Fornasiero, P. et al. Rh-Loaded CeO_2-ZrO_2 Solid-Solutions as Highly Efficient Oxygen Exchangers: Dependence of the Reduction Behavior and the Oxygen Storage Capacity on the Structural-Properties. J Catal 151, 168–177 (1995).

57. Wang, H., Ye, J. L., Liu, Y., Li, Y. D. & Qin, Y. N. Steam reforming of ethanol over Co_3O_4/CeO_2 catalysts prepared by different methods. Catal Today 129, 305–312 (2007).

58. Carvalho, F. L. S., Asencios, Y. J. O., Bellido, J. D. A. & Assaf, E. M. Bio-ethanol steam reforming for hydrogen production over Co_3O_4/CeO_2 catalysts synthesized by one-step polymerization method. Fuel Processing Technology 142, 182–191 (2016).

59. Zhang, F. et al. In Situ Elucidation of the Active State of Co-CeO_x Catalysts in the Dry Reforming of Methane: The Important Role of the Reducible Oxide Support and Interactions with Cobalt. ACS Catal 8, 3550–3560 (2018).

60. Luo, J. Y. et al. Mesoporous Co_3O_4–CeO_2 and Pd/Co_3O_4–CeO_2 catalysts: Synthesis, characterization and mechanistic study of their catalytic properties for low-temperature CO oxidation. J Catal 254, 310–324 (2008).

61. Parastaev, A. et al. Boosting CO_2 hydrogenation via size-dependent metal–support interactions in cobalt/ceria-based catalysts. Nat Catal 3, 526–533 (2020).

62. Kattel, S., Liu, P. & Chen, J. G. Tuning Selectivity of CO_2 Hydrogenation Reactions at the Metal/Oxide Interface. Journal of the American Chemical Society vol. 139

9739–9754 (2017).

63. Simons, J. F. M. et al. Structure Sensitivity of CO_2 Hydrogenation on Ni Revisited. J Am Chem Soc 145, 20289–20301 (2023).

64. Bezemer, G. L. et al. Cobalt particle size effects in the Fischer-Tropsch reaction studied with carbon nanofiber supported catalysts. J Am Chem Soc 128, 3956–3964 (2006).

65. Dostagir, N. H. M. et al. Co Single Atoms in ZrO_2 with Inherent Oxygen Vacancies for Selective Hydrogenation of CO_2 to CO. ACS Catal 11, 9450–9461 (2021).

66. Matsubu, J. C., Yang, V. N. & Christopher, P. Isolated metal active site concentration and stability control catalytic CO_2 reduction selectivity. J Am Chem Soc 137, 3076–3084 (2015).

67. Chen, S. et al. Probing surface structures of CeO_2, TiO_2, and Cu_2O nanocrystals with CO and CO_2 chemisorption. Journal of Physical Chemistry C 120, 21472–21485 (2016).

68. Yang, Z., He, B., Lu, Z. & Hermansson, K. Physisorbed, chemisorbed, and oxidized CO on highly active Cu-CeO_2(111). Journal of Physical Chemistry C 114, 4486–4494 (2010).

69. Bridge, M. E., Comrie, C. M. & Lambert, R. M. Hydrogen chemisorption and the carbon monoxide-hydrogen interaction on cobalt (0001). J Catal 58, 28–33 (1979).

70. Weststrate, C. J., van de Loosdrecht, J. & Niemantsverdriet, J. W. Spectroscopic insights into cobalt-catalyzed Fischer-Tropsch synthesis: A review of the carbon monoxide interaction with single crystalline surfaces of cobalt. J Catal 342, 1–16 (2016).

71. Yang, J., Frøseth, V., Chen, D. & Holmen, A. Particle size effect for cobalt Fischer–Tropsch catalysts based on in situ CO chemisorption. Surf Sci 648, 67–73 (2016).

72. Weststrate, C. J., van de Loosdrecht, J. & Niemantsverdriet, J. W. Spectroscopic insights into cobalt-catalyzed Fischer-Tropsch synthesis: A review of the carbon monoxide interaction with single crystalline surfaces of cobalt. J Catal 342, 1–16 (2016).

73. Matsubu, J. C., Yang, V. N. & Christopher, P. Isolated metal active site concentration and stability control catalytic CO_2 reduction selectivity. J Am Chem Soc 137, 3076–3084 (2015).

74. Chen, W., Zijlstra, B., Filot, I. A. W., Pestman, R. & Hensen, E. J. M. Mechanism of Carbon Monoxide Dissociation on a Cobalt Fischer–Tropsch Catalyst. ChemCatChem 10, 136–140 (2018).

75. Zijlstra, B. et al. Coverage Effects in CO Dissociation on Metallic Cobalt Nanoparticles. ACS Catal 9, 7365–7372 (2019).

76. Struijs, J. J. C., Muravev, V., Verheijen, M. A., Hensen, E. J. M. & Kosinov, N. Ceria-Supported Cobalt Catalyst for Low-Temperature Methanation at Low Partial Pressures of CO_2. Angewandte Chemie 135, e202214864 (2023).

77. Marrocchelli, D., Bishop, S. R., Tuller, H. L. & Yildiz, B. Understanding

Chemical Expansion in Non-Stoichiometric Oxides: Ceria and Zirconia Case Studies. Adv Funct Mater 22, 1958–1965 (2012).

78. Coduri, M., Scavini, M., Allieta, M., Brunelli, M. & Ferrero, C. Defect structure of Y-doped ceria on different length scales. Chemistry of Materials 25, 4278–4289 (2013).

79. Pakharukova, V. P. et al. Investigation of the Structure and Interface Features of Ni/$Ce_{1-x}Zr_xO_2$Catalysts for CO and CO_2 Methanation. Journal of Physical Chemistry C 125, 20538–20550 (2021).

80. Hussain, I. et al. A review of the indispensable role of oxygen vacancies for enhanced CO_2 methanation activity over CeO2-based catalysts: Uncovering, influencing, and tuning strategies. Int J Hydrogen Energy 48, 24663–24696 (2023).

81. Xu, S., Xie, F., Xie, H., Zhou, G. & Liu, X. Effect of structure and composition on the CO_2 hydrogenation properties over bimodal mesoporous CeCo composite catalyst. Chemical Engineering Journal 375, 122023 (2019).

82. Oh, R. et al. Insights into CeO_2 Particle Size Dependent Selectivity Control for CO_2 Hydrogenation Using Co/CeO_2 Catalysts. ACS Catal 897–906 (2024).

83. Qiu, N., Zhang, J. & Wu, Z. Peculiar surface-interface properties of nanocrystalline ceria-cobalt oxides with enhanced oxygen storage capacity. Physical Chemistry Chemical Physics 16, 22659–22664 (2014).

84. Pan, C. J. et al. Tuning/exploiting Strong Metal-Support Interaction (SMSI) in Heterogeneous Catalysis. J Taiwan Inst Chem Eng 74, 154–186 (2017).

85. Wang, L. X., Wang, L. & Xiao, F. S. Tuning product selectivity in CO_2 hydrogenation over metal-based catalysts. Chem Sci 12, 14660–14673 (2021).

Appendix A

Figures.

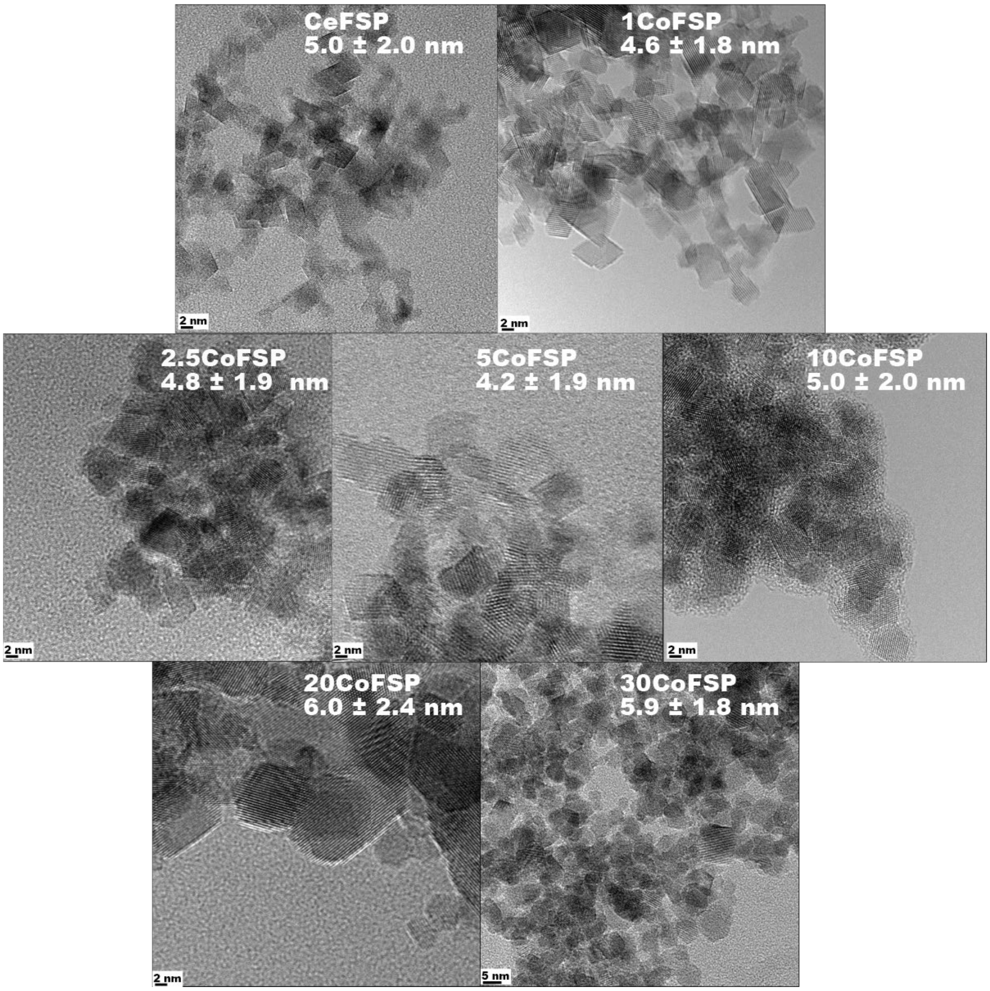

Figure A1. TEM images of as-prepared CeFSP and CoFSP catalyst with corresponding particle size estimations (scale = 2nm).

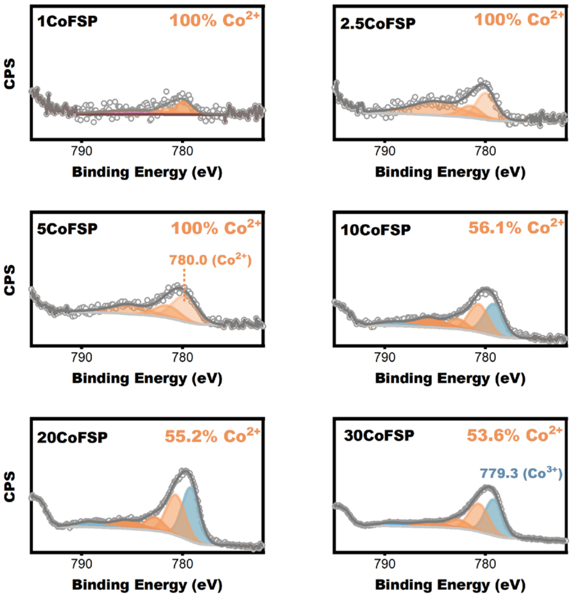

Figure A2. Deconvolution of Co $2p_{3/2}$ XP spectra of as-prepared CoFSP catalysts.

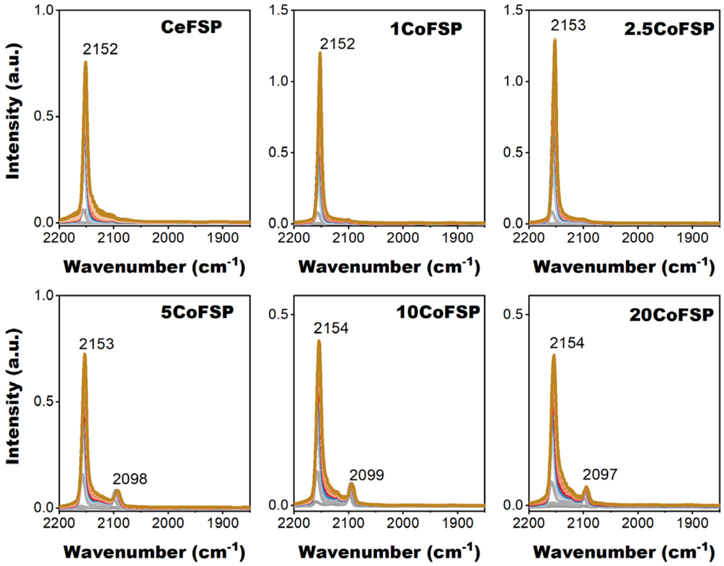

Figure A3. IR spectra of the as-prepared CeFSP and CoFSP after CO adsorption at liquid N_2 temperature (conditions: 1 – 10 mbar CO).

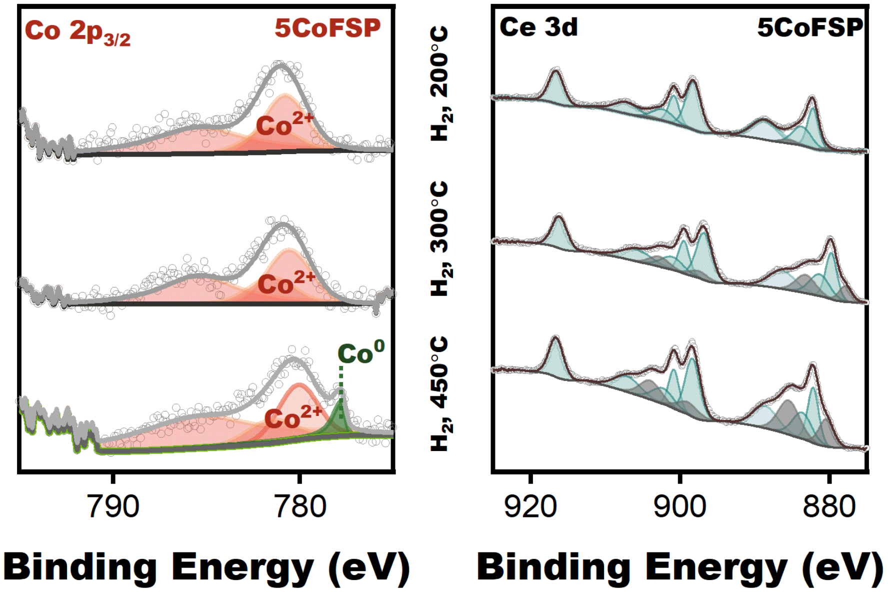

Figure A4. Deconvoluted Co 2p3/2 (left) and Ce 3d (right) spectra obtained during H_2-TPR of 5CoFSP followed by NAP-XPS (conditions: 33.3 vol.% H_2 in Ar, 3 mbar, 200 – 500 °C).

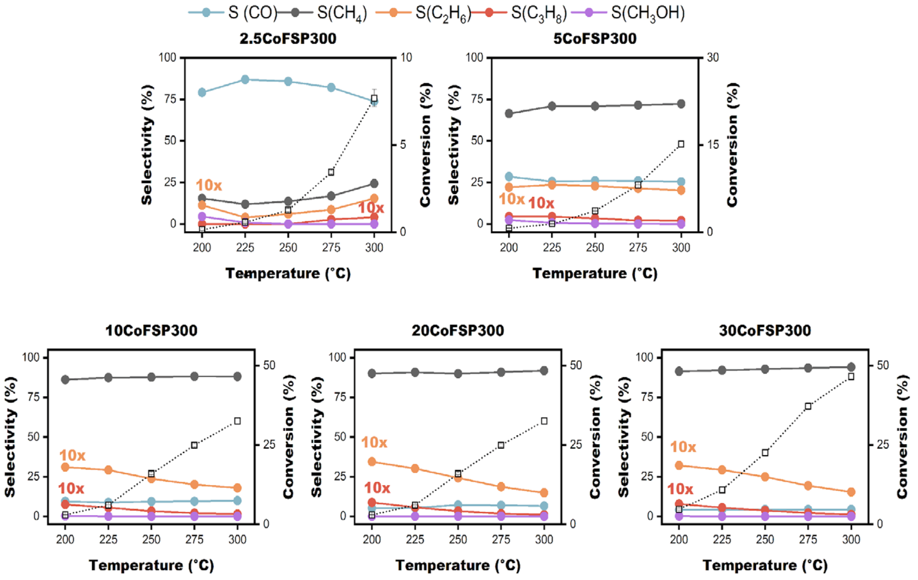

Figure A5.1 Catalytic performance of CoFSP catalysts reduced at 300 °C in CO_2 hydrogenation as a function of temperature (conditions: 200 – 300 °C, 1 bar, 50 mg of sample, 15 vol.% CO_2, 60 vol.% H_2, 25 vol.% Ar, 50 mL/min, 1 bar).

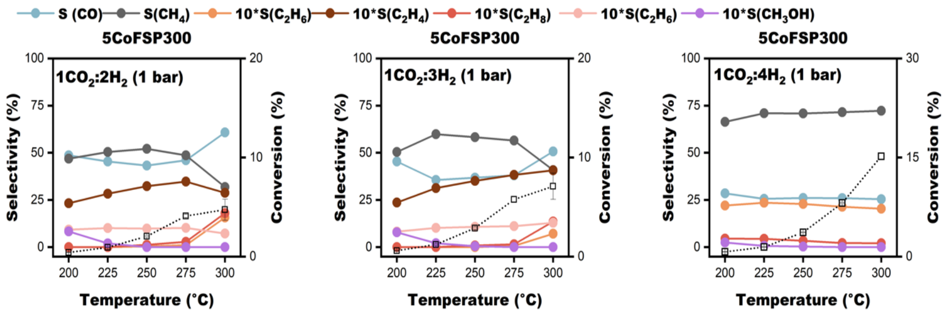

Figure A5.2 Catalytic performance of 5CoFSP catalysts reduced at 300 °C in CO_2 hydrogenation as a function of temperature and CO_2/H_2 ratios (conditions: 200 – 300 °C, 1 bar, 50 mg of sample, 15 vol.% CO_2, 60 vol.% H_2, 25 vol.% Ar, 50 mL/min (1:4); 18.8 vol.% CO_2, 56.2 vol.% H_2, 25 vol.% Ar, 50 mL/min (1:3); 25 vol.% CO_2, 50 vol.% H_2, 25 vol.% Ar, 50 mL/min (1:2)).

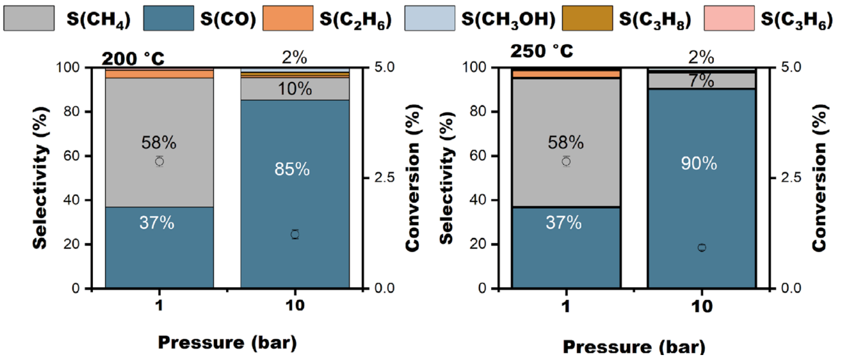

Figure A5.3 Catalytic performance of 5CoFSP catalysts reduced at 300 °C in CO_2 hydrogenation as a function of pressure (conditions: 200 and 250 °C, 1 or 10 bar, 50 mg of sample, 18.8 vol.% CO_2, 56.2 vol.% H_2, 25 vol.% Ar, 50 mL/min (1:3)).

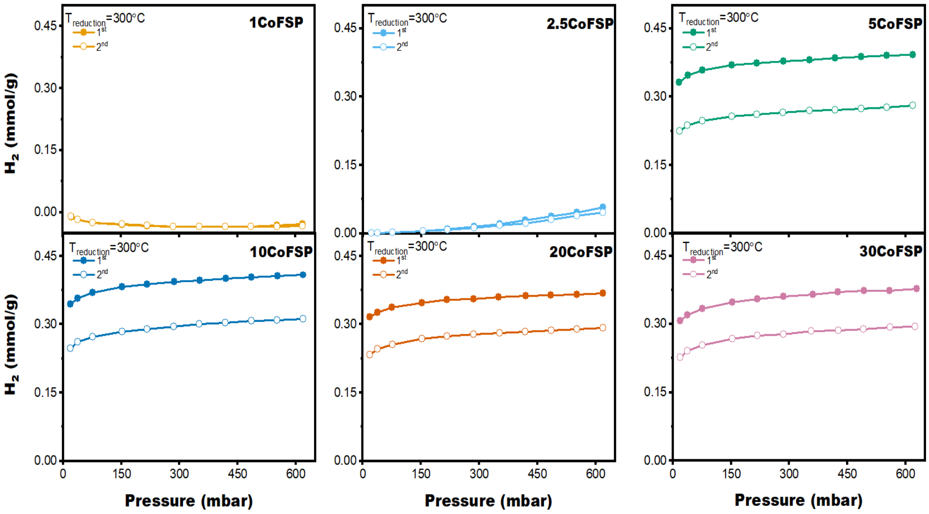

Figure A6. H_2 chemisorption at 150 °C of CoFSP reduced at 300 °C for 4 h.

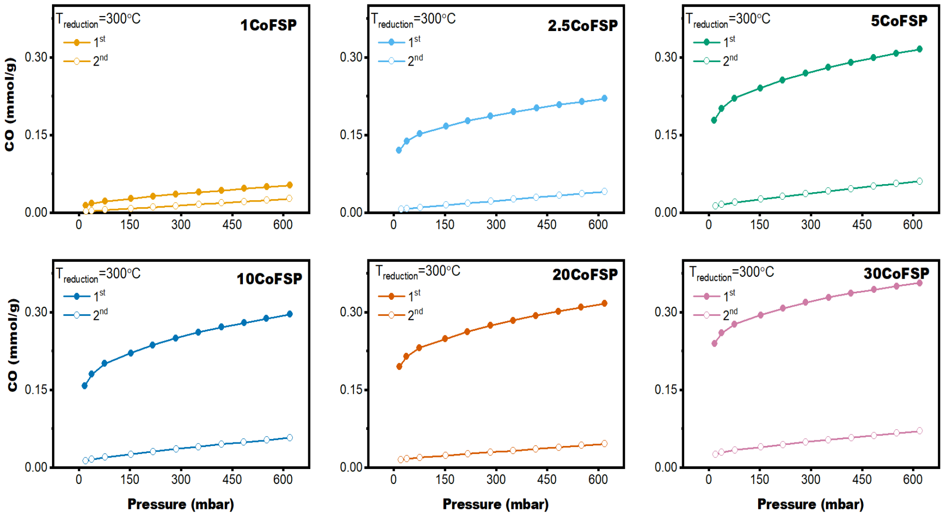

Figure A7. CO chemisorption at 35 °C results of CoFSP reduced at 300 °C for 4 h.

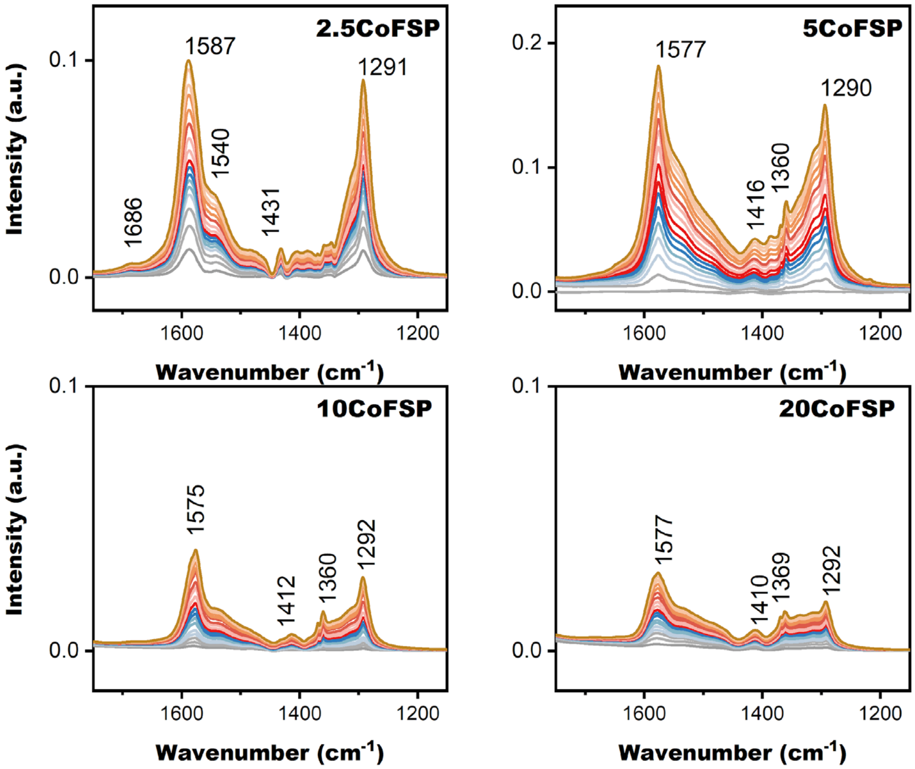

Figure A8. Carbonate region of the IR spectra of CoFSP catalysts reduced at 300 °C after CO adsorption at 50 °C (conditions: 0 – 10 mbar CO).

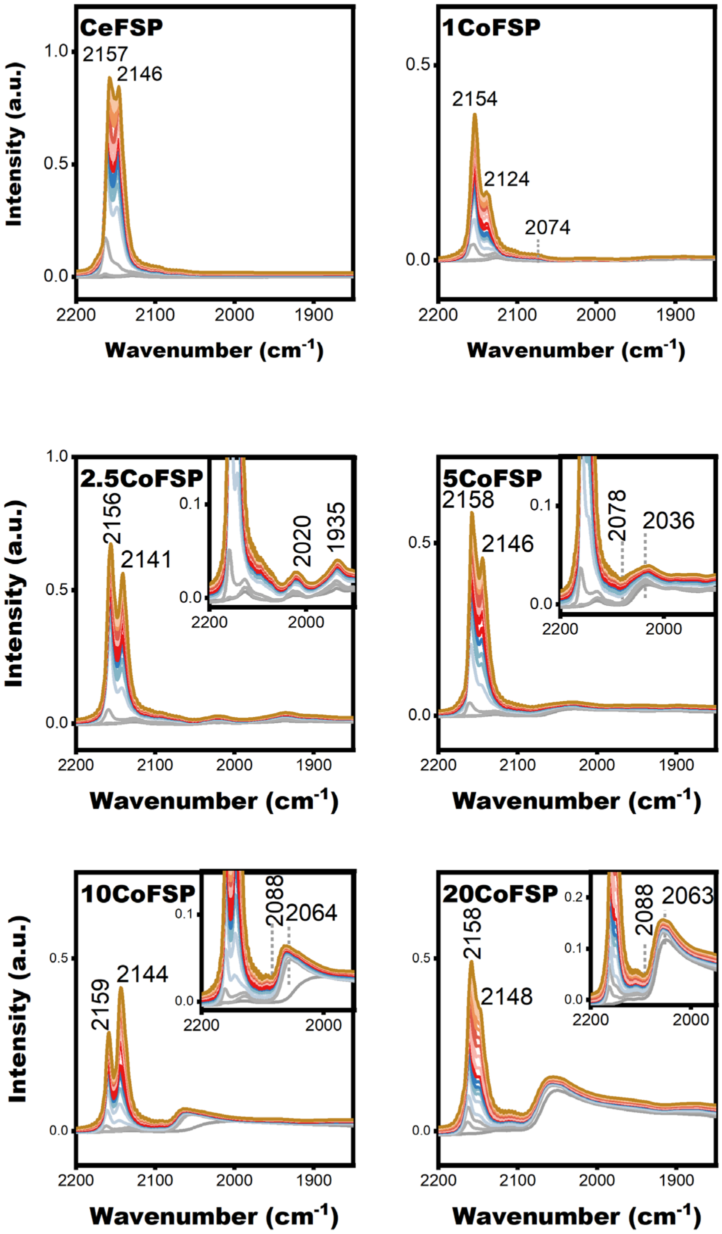

Figure A9. IR spectra of the CeFSP and CoFSP reduced at 300 °C after CO adsorption at liquid N_2 temperature (conditions: 0 – 10 mbar CO).

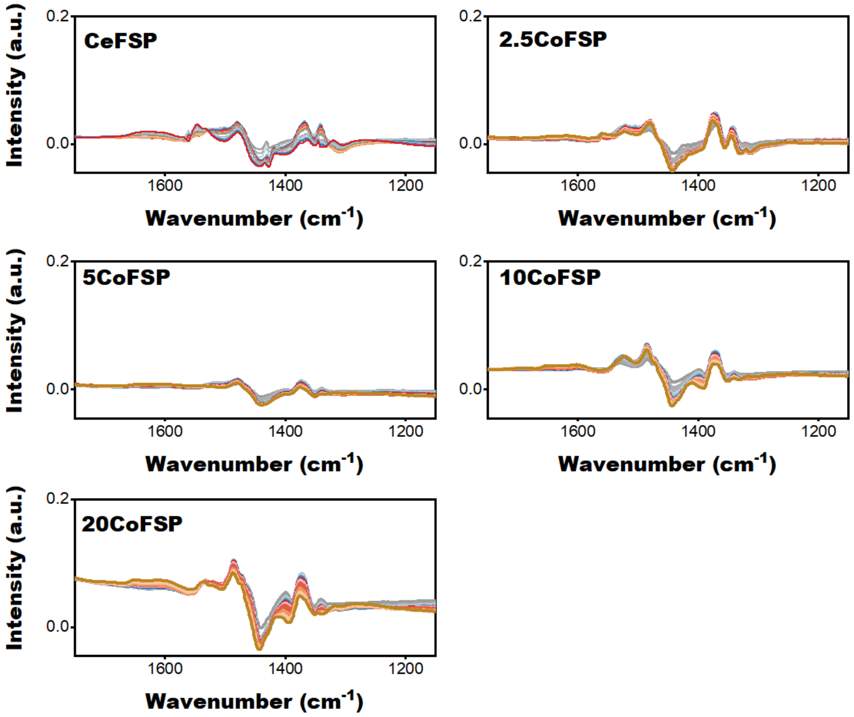

Figure A10. Carbonate regions of IR spectra of the CeFSP and CoFSP reduced at 300 °C after CO adsorption at liquid N_2 temperature (conditions: 0 – 10 mbar CO).

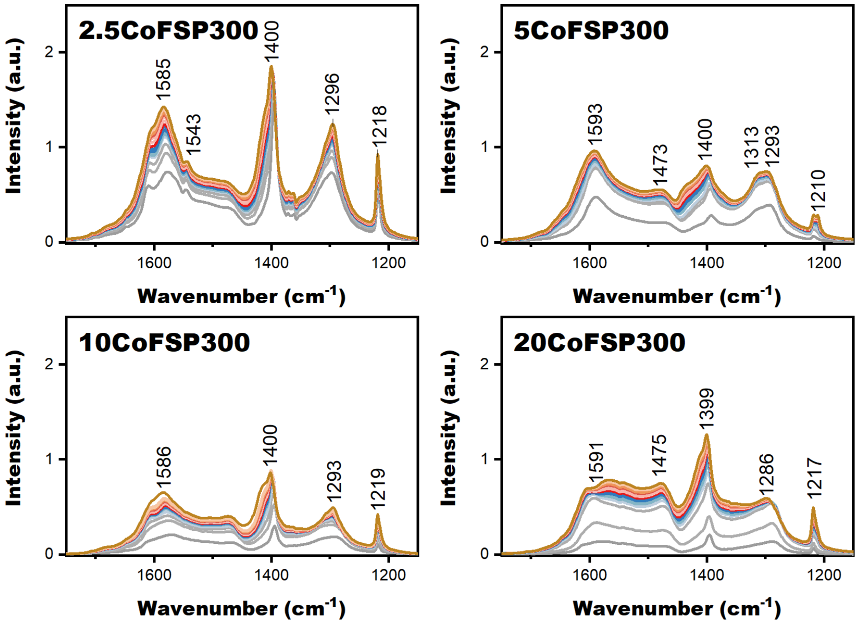

Figure A11. Carbonate region of IR spectra of CoFSP reduced at 300 °C after CO_2 adsorption at 50 °C (conditions: 0 – 10 mbar CO_2).

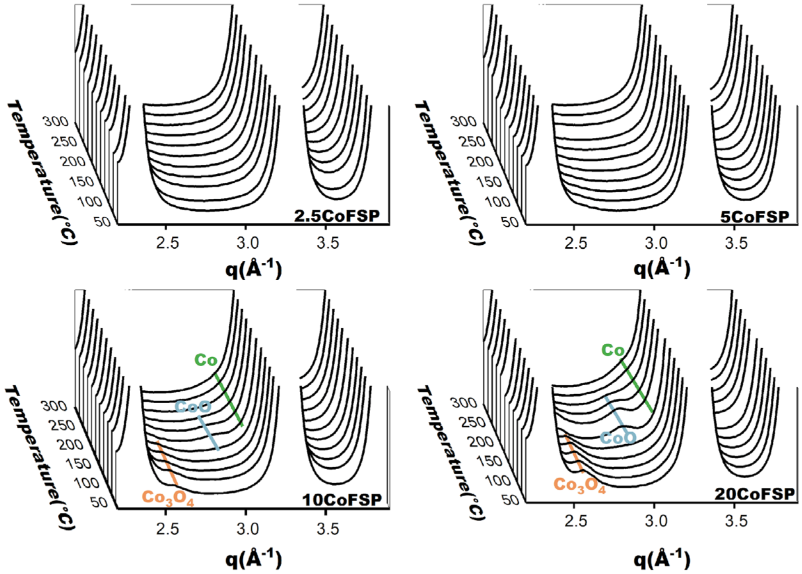

Figure A12. Synchrotron XRD diffractograms of CoFSP during reduction (conditions: 20 vol.% H_2 in Ar, 50 mL/min, 1 bar, 50 – 300 °C, 8.5 °C/min).

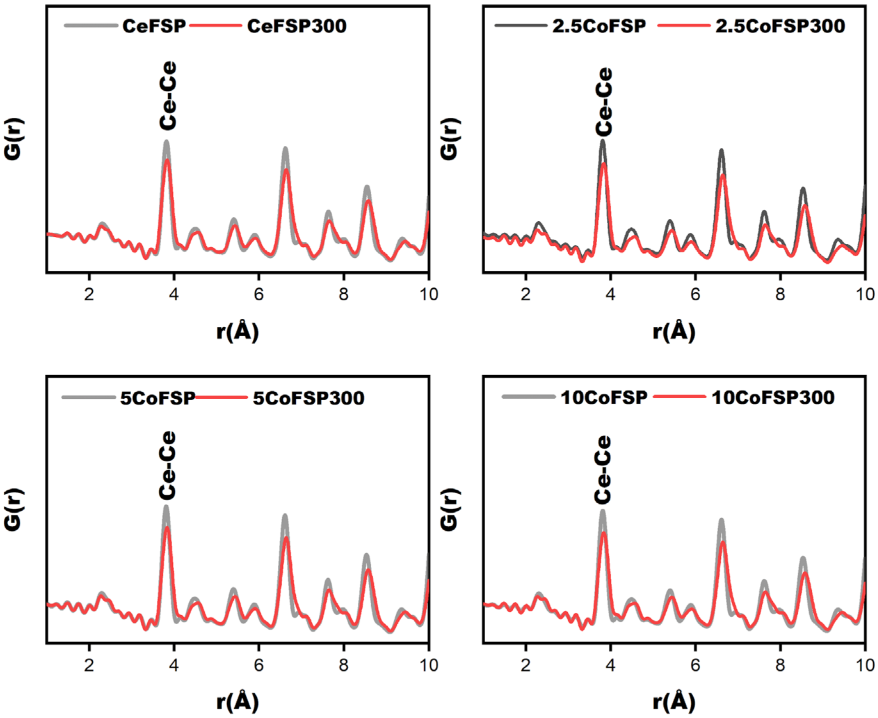

Figure A13. G(r) of CeFSP and CoFSP before and after reduction (conditions: 20 vol.% H_2 in Ar, 50 mL/min, 1 bar, 50 – 300 °C, 8.5 °C/min).

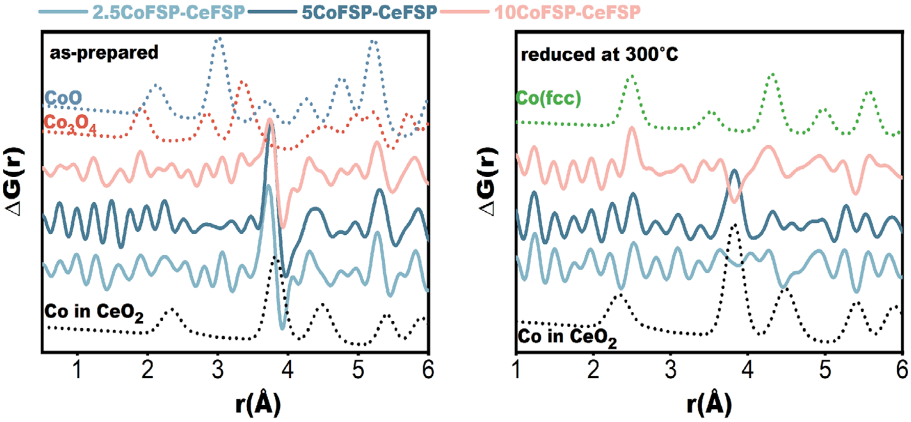

Figure A14. ΔG(r) of CoFSP and modeled G(r) of Co_3O_4, CoO, Co metal, and Co incorporated into CeO_2. ΔG(r) is obtained by subtraction of G(r) of CeFSP from G(r) of CoFSP recorded under the same conditions (pretreatment conditions: 20 vol.% H_2 in Ar, 50 mL/min, 1 bar, 50 – 300 °C, 8.5 °C/min).

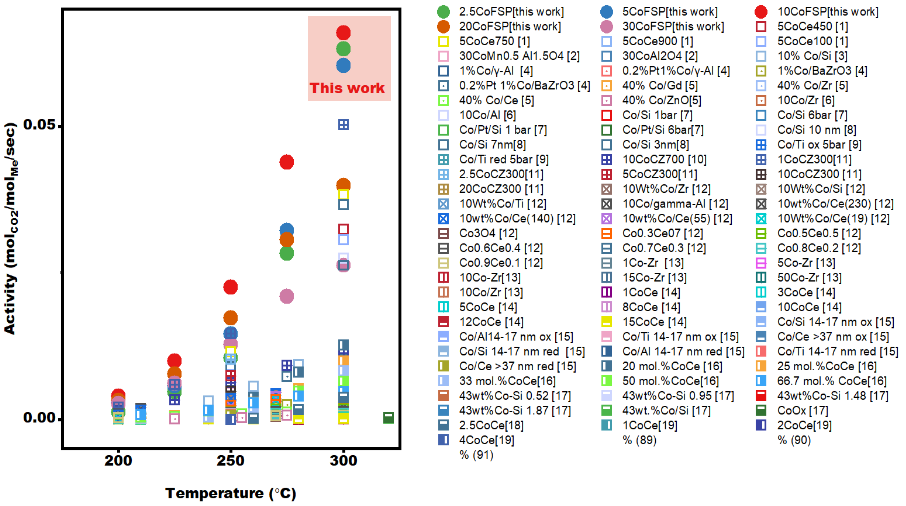

Figure A15. Catalytic activity of CoFSP in comparison to literature.

Tables.

Table A1. Co K-edge EXAFS fit results of CoFSP samples (error margins reported in brackets).

Catalyst	Path	CN [±]	R (A) [±]	E0 (eV)	δ2 (A2)	R-factor
1CoFSP	Co-O	3.6[0.4]	1.950[0.007]	-3.36	0.004	0.014
	Co-O-Ce	3.2[1.6]	3.214[0.022]		0.001	
	Co-Co [1]	0.45[0.4]	2.676[0.060]		0.003	
	Co-Co [2]	1.3[0.6]	3.214[0.030]		0.004	
2.5CoFSP	Co-Co [2]	5.2[0.3]	1.952[0.005]	-4.28	0.010	0.013
	Co-O-Ce	2.1[1.4]	2.982[0.028]		0.004	
	Co-Co [1]	0.9[0.3]	2.872[0.027]		0.004	
	Co-Co [2]	1.0[0.3]	3.211[0.026]		0.009	
5CoFSP	Co-O	4.0[0.3]	1.893[0.007]	-7.47	0.004	0.010
	Co-O-Ce	4.1[1.8]	3.014[0.017]		0.002	
	Co-Co [1]	1.8[0.5]	2.706[0.021]		0.002	
	Co-Co [2]	1.9[0.5]	3.355[0.017]		0.004	
10CoFSP	Co-O	5.2[0.3]	1.844[0.004]	-8.27	0.003	0.002
	Co-Co [1]	2.4[0.2]	2.726[0.007]		0.002	
	Co-Co [2]	4.7[0.5]	3.204[0.007]		0.004	
20CoFSP	Co-O	4.2[0.2]	1.848[0.008]	-5.94[1.1]	0.001	0.005
	Co-Co [1]	2.8[0.2]	2.740[0.010]		0.001	
	Co-Co [2]	4.0[0.4	3.232[0.011]		0.002	
30CoFSP	Co-O	4.2[0.3]	1.832[0.007]	-7.91	0.001	0.011
	Co-Co [1]	2.7[0.4]	2.724[0.009]		0.001	
	Co-Co [2]	4.9[0.6]	3.212[0.008]		0.002	

Table A2. Assignment of IR bands.

Wavenumber (cm^{-1})	Assignment		Ref.
2172; 2117		rotovibrational spectrum of gas-phase CO	[1], [2]
2358		CO_2 gas-phase	[3]
Ce			
2140-2125	Ce^{3+}	CO ads	[4], [5]
2157	Ce^{4+}	CO ads	
1580 v (CO), 1335 v (CO), ~1370 δ (OCH)	Formate I (on Ce^{3+})		[6], [7], [8]
1561 v (CO), 1356 v (CO), ~1370 δ (OCH)	Formate II (on Ce^{3+})		
1550 v (CO), 1371 v (CO), ~1370 δ (OCH)	Formate III (on Ce^{4+})		
1400-1440; 1580-1585		Monodentate carbonate (CO_3)	[9], [10]
1560-1567, 1289-1300, 1014 – 1030;		Bidentate carbonate (CO_3)	[4], [8], [11]
1490, 1380, 1085	Ce^{3+}	Tridentate carbonate (CO_3)	[7]
1451-1500; 1342-1380; 1038-1065	Ce^{4+}	Tridentate carbonate (CO_3)	
1465-1460; 1359-1460; 1080		Polydentate/ monodentate carbonates (CO_3)	[4], [5], [9], [11]
1220-1225; 1420-1425; 1635-1640		Bicarbonates (HCO_3)	[10]
Co			
2136	Co_3O_4		[12]
2125	CoO		
2120	Co2+	CO adsorption	[13]
2070	Co2+	CO adsorption	
2143-2180	Co3+	CO adsorption	
2015	Co	a-top CO	[14], [15]
2000-2057	Co	a-top CO on Co nanoparticles	
2030-2040	Co	a-top CO on Co clusters	
1850-1862	Co	hollow CO	[16], [17]
1930-1970	Co	bridge CO	

Table A3. Results of Rietveld refinement of PDF of CeFSP and CoFSP using CeO_2 fluorite model (error margins are reported in brackets).

Sample	a (A) (error)	dCeO2 (A)	Rw
CeFSP	5.40807 (0.00058)	59.9 (2.7)	0.13811
CeFSP300	5.42949 (0.00082)	67.6 (4.4)	0.147708
2.5CoFSP	5.39847 (0.00064)	52.4 (2.0)	0.147665
2.5CoFSP300	5.43021 (0.00093)	57.7 (3.1)	0.150841
5CoFSP	5.39869 (0.00056)	58.5 (2.4)	0.146947
5CoFSP300	5.42758 (0.0008)	67.1 (4.1)	0.142615
10CoFSP	5.40019 (0.00061)	55.1 (2.2)	0.145461
10CoFSP300	5.43095 (0.0009)	62.5 (3.8)	0.147448

Table A4. Results of direct PDF analysis of CeFSP and CoFSP.

Sample	FWHM (A) Gauss function	Position	Area (a.u.)
CeFSP	0.113	3.821	2.62665
CeFSP300	0.145	3.838	2.73816
2.5CoFSP	0.113	3.813	2.65109
2.5CoFSP300	0.145	3.838	2.79109
5CoFSP	0.110	3.814	2.71007
5CoFSP300	0.145	3.837	2.83795
10CoFSP	0.111	3.815	2.60705
10CoFSP300	0.149	3.837	2.72874

Table A5. Catalytic performance in CO_2 hydrogenation.

Catalyst	H_2: CO_2	P (bar)	CO_2 initial (%)	Treact (°C)	Activity*10-3 (molCO_2/molMe/s)	Ref. Fig. A15	Ref.
2.5Co FSP	4	1	15	200	1.23	This work	This work
				225	4.72		
				250	10.43		
				275	28.30		
				300	63.22		
5Co FSP				200	3.04		
				225	6.23		
				250	18.97		
				275	34.90		
				300	52.53		
10Co FSP				200	3.92		
				225	9.89		
				250	22.37		
				275	43.49		
				300	65.38		
20Co FSP				200	4.52		
				225	10.75		
				250	24.08		
				275	42.59		
				300	55.52		
30Co FSP				200	4.35		
				225	9.90		
				250	20.59		
				275	33.97		
				300	42.53		

Table A5. Catalytic performance in CO_2 hydrogenation (continuation).

Catalyst	H_2: CO_2	P (bar)	CO_2 initial (%)	T_{react} (°C)	Activity*10^{-3} (molCO_2/molMe/s)	Ref. Fig. A15	Ref.
5Co/Ce450	1	1	45	250	10.31	[1]	[18]
				300	32.49		
5Co/Ce750				250	11.50		
				300	38.36		
5Co/Ce900				250	9.21		
				300	30.68		
5Co/Ce1000				250	7.66		
				300	30.68		
30Co $Mn_{0.5}Al_{1.5}O_4$	4	1		200	0.74	[2]	[19]
				250	4.56		
				300	9.73		
				350	10.50		
				400	10.70		
				450	10.60		
				500	10.30		
30CoAl				300	0.25		
				350	1.78		
				400	6.22		
				450	8.28		
				500	8.51		
10% Co/Si	4	1	10	240	3.11	[3]	[20]
				260	5.60		
				280	9.35		
				300	12.70		
				320	15.70		
				340	17.80		
				360	19.40		
				380	21.10		
				400	22.10		
1%Co/γ-Al	4	1	3	300	0.91	[4]	[21]
				325	2.40		
				350	4.05		
0.2%Pt1%Co/γ-Al				300	2.02		
				325	4.97		
				350	7.90		
1%Co/$BaZrO_3$				275	2.52		
				300	6.01		
				325	10.50		
				350	13.70		
0.2%Pt 1%Co/$BaZrO_3$				250	3.06		
				275	7.33		
				300	11.80		
				325	16.90		

Ce – CeO_2; Zr – ZrO_2; Si – SiO_2; Al – Al_2O_3.

Table A5. Catalytic performance in CO_2 hydrogenation (continuation).

Catalyst	H_2: CO_2	P (bar)	CO_2 initial (%)	T_{react} (°C)	Activity*10^{-3} (molCO_2/molMe/s)	Ref. Fig. A15	Ref.
40% Co/Gd	9	1	10	210	0.49	[5]	[22]
				225	0.63		
				240	0.76		
				255	0.85		
				270	0.90		
				285	0.91		
				300	0.92		
40% Co/Zr				210	0.34		
				225	0.48		
				240	0.54		
				255	0.54		
				270	0.56		
				285	0.60		
				300	0.70		
40% Co/Ce				210	0.31		
				225	0.46		
				240	0.70		
				255	0.90		
				270	1.06		
				285	1.14		
				300	1.19		
40% Co/ZnO				210	0.06		
				225	0.11		
				240	0.18		
				255	0.25		
				270	0.34		
				285	0.58		
				300	0.74		
10% Co/Zr	4	30	20	400	12.00	[6]	[22]
10% Co/Al				400	16.00		
Co/Si	4	1	22.2	200	0.08	[7]	[23]
		6		200	0.25		
Co/Pt/Si		1		200	0.46		
		6		200	1.08		
Co/Si 10nm	4	6	22.2	200	0.59	[8]	[24]
				250	10.10		
				300	27.50		
Co/Si 7 nm				200	1.54		
				250	8.99		
				300	26.30		

Ce – CeO_2; Zr – ZrO_2; Si – SiO_2; Al – Al_2O_3; Gd -Gd_2O_3

Table A5. Catalytic performance in CO_2 hydrogenation (continuation)

Catalyst	H_2: CO_2	P (bar)	CO_2 initial (%)	T_{react} (°C)	Acti-vity*10^{-3} (molCO_2/molMe/s)	Ref. Fig. A15	Ref.
Co/Si 3nm				200	1.40		
				250	6.48		
				300	36.60		
Co/Ti (ox 5bar)	4	5	25	250	3.20	[9]	[25]
Co/Si (red 5bar)				250	1.30		
10CoCZ 700 (red 500 °C)	4	1	5	200	1.46	[10]	[26]
				225	3.35		
				250	6.22		
				275	9.19		
				300	11.30		
				325	12.80		
1CoCZ 300	4	1	5	250	14.65	[11]	[27]
2.5CoCZ 300				250	10.23		
5CoCZ 300				250	7.37		
10CoCZ 300				250	4.78		
20CoCZ 300				250	2.53		
10wt.%Co /Ce (55)	4	1	10	200	0.31	[12]	[28]
				220	0.69		
				250	2.36		
				270	3.88		
				300	4.30		
10wt.%Co /Ce(19)				200	0.23		
				220	0.41		
				250	1.42		
				270	3.23		
				300	4.22		
Co_3O_4				200	0.07		
				220	0.18		
				250	0.38		
				270	0.44		
				300	0.44		
Co0.3 Ce0.7				200	0.03		
				220	0.40		
				250	2.37		
				270	3.29		
				300	3.41		

Ce – CeO_2; Si – SiO_2. CZ – CeO_2-ZrO_2; Ti – TiO_2; Si – SiO_2; Al – Al_2O_3; Zr – ZrO_2

Table A5. Catalytic performance in CO_2 hydrogenation (continuation)

Catalyst	H_2: CO_2	P (bar)	CO_2 initial (%)	T_{react} (°C)	Activity$*10^{-3}$ (molCO_2/molMe/s)	Ref. Fig. A15	Ref.
Co0.5 Ce0.5				200	0.04	[12]	[28]
				220	0.29		
				250	1.26		
				270	1.70		
				300	1.72		
Co0.6 Ce0.4				200	0.21		
				220	0.49		
				250	1.08		
				270	1.28		
				300	1.29		
Co0.7 Ce0.3				200	0.25		
				220	0.54		
				250	0.99		
				270	1.02		
				300	1.02		
Co0.8 Ce0.2				200	0.19		
				220	0.63		
				250	1.02		
				270	1.02		
				300	1.02		
Co0.9 Ce0.1	4	1	10	200	0.27	[12]	[28]
				220	0.50		
				250	0.58		
				270	0.58		
				300	0.58		
10wt.% Co/Zr	50	1	1	200	0.62		
				220	1.24		
				250	2.60		
				270	3.77		
				300	4.27		
10wt.% Co/Si				200	0.42		
				220	1.24		
				250	3.26		
				270	4.07		
				300	4.38		
10wt.% Co/Ti				200	0.05		
				220	0.11		
				250	0.39		
				270	0.92		
				300	1.39		
10Co/gamma-Al				200	0.06		
				220	0.24		
				250	0.64		
				270	1.47		
				300	2.16		
10wt.% Co/Ce (230)				200	0.91		
				220	1.81		
				250	3.63		
				270	4.41		
				300	4.38		

Table A5. Catalytic performance in CO_2 hydrogenation (continuation)

Catalyst	H_2: CO_2	P (bar)	CO_2 initial (%)	T_{react} (°C)	Acti-vity*10^{-3} (molCO_2/ molMe/s)	Ref. Fig. A15	Ref.
10wt.% Co/Ce (140)				200	0.72		
				220	1.58		
				250	3.57		
				270	4.39		
				300	4.39		
1Co-Zr	4	30	0.1667	340	0.02	[13]	[29]
5Co-Zr				340	0.08		
10Co-Zr				340	0.10		
15Co-Zr				340	0.10		
50Co-Zr				340	0.40		
10Co/Zr				340	0.45		
10Co-Zr				280	0.01		
10Co-Zr				300	0.01		
1wt.% Co/Ce	4	1	0.1	220	0.11	[14]	[30]
				240	0.11		
				260	0.11		
				280	0.11		
				300	0.33		
3wt.% Co/Ce				220	0.04		
				240	0.04		
				260	0.11		
				280	0.26		
				300	0.33		
5wt.% Co/Ce				220	0.00		
				240	0.02		
				260	0.09		
				280	0.18		
				300	0.24		
8wt.% Co/Ce				220	0.03		
				240	0.05		
				260	0.10		
				280	0.16		
				300	0.21		
10wt.% Co/Ce				220	0.02		
				240	0.05		
				260	0.10		
				280	0.14		
				300	0.18		
12wt.% Co/Ce				220	0.03		
				240	0.06		
				260	0.10		
				280	0.14		
				300	0.16		
15wt.% Co/Ce				220	0.03		
				240	0.06		
				260	0.10		
				280	0.12		
				300	0.13		

Ce – CeO_2; Si – SiO_2. CZ – CeO_2-ZrO_2; Ti – TiO_2; Si – SiO_2; Al – Al_2O_3; Zr – ZrO_2

Table A5. Catalytic performance in CO_2 hydrogenation (continuation)

Catalyst	H_2: CO_2	P (bar)	CO_2 initial (%)	T_{react} (°C)	Activity*10^{-3} (molCO_2/ molMe/s)	Ref. Fig. A15	Ref.
Co/Si ox [14-17 nm]	3	20	24	250	0.22	[15]	[31]
Co/Al ox [14-17 nm]				250	0.23		
Co/Ti ox [14-17 nm]				250	0.95		
Co/Ce ox [>37nm]				250	0.57		
Co/Si red [14-17 nm]				250	0.58		
Co/Al red [14-17 nm]				250	0.27		
Co/Ti red [14-17 nm]				250	0.75		
Co/Ce red [>37nm]				250	0.70		
20mol.% Co/Ce	4	1		220	0.84	[16]	[32]
				240	1.53		
				260	3.73		
				280	8.03		
				300	12.66		
25mol.% Co/Ce				220	0.33		
				240	1.51		
				260	2.88		
				280	5.23		
				300	9.98		
33mol.% Co/Ce				220	0.14		
				240	0.38		
				260	2.04		
				280	4.81		
				300	8.27		
50mol.% Co/Ce				220	0.42		
				240	1.43		
				260	2.82		
				280	4.79		
				300	6.51		

Table A5. Catalytic performance in CO_2 hydrogenation (continuation)

Catalyst	H_2: CO_2	P (bar)	CO_2 initial (%)	T_{react} (°C)	Acti-vity*10^{-3} ($molCO_2$/ molMe/s)	Ref. Fig. A15	Ref.
66.7mol.% Co/Ce				220	0.81		
				240	1.58		
				260	2.77		
				280	3.90		
				300	4.70		
43wt.%Co-Si 0.52	2	20	25	320	0.22	[17]	[33]
43wt.%Co-Si 0.95				320	0.21		
43wt.%Co-Si 1.48				320	0.20		
43wt.%Co-Si 1.87				320	0.17		
43wt.%Co/ Si				320	0.18		
CoOx				320	0.31		
2.5CoCe (Ce/Co=4)	4	1	1	260	0.01	[18]	[34]
				280	0.07		
				300	0.16		
1CoCe	5	1	14.28	250	0.0013	[19]	[35]
2CoCe				250	0.0012		
4CoCe				250	0.0007		

Ce – CeO_2; Si – SiO_2. CZ – CeO_2-ZrO_2; Ti – TiO_2; Si – SiO_2; Al – Al_2O_3; Zr – ZrO_2

References. Appendix A.

1. Meunier, F. C. On the contamination with nickel and nickel tetracarbonyl during FT-IR investigation of catalysts under CO-containing gases. J Catal 372, 388 (2019).

2. Paredes-Nunez, A., Jbir, I., Bianchi, D. & Meunier, F. C. Spectrum baseline artefacts and correction of gas-phase species signal during diffuse reflectance FT-IR analyses of catalysts at variable temperatures. Appl Catal A Gen 495, 17–22 (2015).

3. Chen, W., Zijlstra, B., Filot, I. A. W., Pestman, R. & Hensen, E. J. M. Mechanism of Carbon Monoxide Dissociation on a Cobalt Fischer–Tropsch Catalyst. ChemCatChem 10, 136–140 (2018).

4. Binet, C., Badri, A., Boutonnet-Kizling, M. & Lavalley, J. C. FTIR study of carbon monoxide adsorption on ceria: CO_{2-2} carbonite dianion adsorbed species. Journal of the Chemical Society, Faraday Transactions 90, 1023–1028 (1994).

5. Binet, C., Daturi, M. & Lavalley, J. C. IR study of polycrystalline ceria properties in oxidised and reduced states. Catal Today 50, 207–225 (1999).

6. Lustemberg, P. G., Bosco, M. V., Bonivardi, A., Busnengo, H. F. & Ganduglia-Pirovano, M. V. Insights into the Nature of Formate Species in the Decomposition and Reaction of Methanol over Cerium Oxide Surfaces: A Combined Infrared Spectroscopy and Density Functional Theory Study. Journal of Physical Chemistry C 119, 21452–21464 (2015).

7. Vayssilov, G. N., Mihaylov, M., Petkov, P. S., Hadjiivanov, K. I. & Neyman, K. M. Reassignment of the vibrational spectra of carbonates, formates, and related surface species on ceria: A combined density functional and infrared spectroscopy investigation. Journal of Physical Chemistry C 115, 23435–23454 (2011).

8. Li, C. et al. Adsorption of carbon monoxide and carbon dioxide on cerium oxide studied by Fourier-transform infrared spectroscopy. Part 2.—Formation of formate species on partially reduced CeO_2 at room temperature. Journal of the Chemical Society, Faraday Transactions 1: Physical Chemistry in Condensed Phases 85, 1451–1461 (1989).

9. Aguirre, A. & Collins, S. E. Selective detection of reaction intermediates using concentration-modulation excitation DRIFT spectroscopy. Catal Today 205, 34–40 (2013).

10. Vrijburg, W. L. et al. Efficient Base-Metal NiMn/TiO_2 Catalyst for CO_2 Methanation. ACS Catal 9, 7823–7839 (2019).

11. Pozdnyakova, O. et al. Preferential CO oxidation in hydrogen (PROX) on ceria-supported catalysts, part II: Oxidation states and surface species on Pd/CeO_2 under reaction conditions, suggested reaction mechanism. J Catal 237, 17–28 (2006).

12. Mehl, S. et al. Thermal evolution of cobalt deposits on Co_3O_4 (111): atomically dispersed cobalt, two-dimensional CoO islands, and metallic Co nanoparticles. Physical Chemistry Chemical Physics 17, 23538–23546 (2015).

13. Busca, G., Guidetti, R. & Lorenzelli, V. Fourier-transform Infrared Study of the Surface Properties of Cobalt Oxides. 86, 989–994 (1990).

14. Ferstl, P. et al. Adsorption and Activation of CO on Co_3O_4(111) Thin Films. Journal of Physical Chemistry C 119, 16688–16699 (2015).

15. Zijlstra, B. et al. Coverage Effects in CO Dissociation on Metallic Cobalt Nanoparticles. ACS Catal 9, 7365–7372 (2019).

16. Weststrate, C. J., van de Loosdrecht, J. & Niemantsverdriet, J. W. Spectroscopic insights into cobalt-catalyzed Fischer-Tropsch synthesis: A review of the carbon monoxide interaction with single crystalline surfaces of cobalt. J Catal 342, 1–16 (2016).

17. Paredes-Nunez, A. et al. CO Hydrogenation on Cobalt-Based Catalysts: Tin Poisoning Unravels CO in Hollow Sites as a Main Surface Intermediate. Angewandte Chemie 130, 556–559 (2018).

18. Oh, R. et al. Insights into CeO_2 Particle Size Dependent Selectivity Control for CO_2 Hydrogenation Using Co/CeO_2 Catalysts. ACS Catal 897–906 (2024).

19. Franken, T., Terreni, J., Borgschulte, A. & Heel, A. Solid solutions in reductive environment – A case study on improved CO_2 hydrogenation to methane on cobalt based catalysts derived from ternary mixed metal oxides by modified reducibility. J Catal 382, 385–394 (2020).

20. Zhou, G. et al. CO_2 hydrogenation to methane over mesoporous Co/SiO_2 catalysts: Effect of structure. Journal of CO_2 Utilization 26, 221–229 (2018).

21. Shin, H. H., Lu, L., Yang, Z., Kiely, C. J. & McIntosh, S. Cobalt Catalysts Decorated with Platinum Atoms Supported on Barium Zirconate Provide Enhanced Activity and Selectivity for CO_2 Methanation. ACS Catal 6, 2811–2818 (2016).

22. Díez-Ramírez, J. et al. Effect of support nature on the cobalt-catalyzed CO_2 hydrogenation. Journal of CO_2 Utilization 21, 562–571 (2017).

23. Beaumont, S. K. et al. Combining in situ NEXAFS spectroscopy and CO_2 methanation kinetics to study Pt and Co nanoparticle catalysts reveals key insights into the role of platinum in promoted cobalt catalysis. J Am Chem Soc 136, 9898–9901 (2014).

24. Iablokov, V. et al. Size-controlled model Co nanoparticle catalysts for CO_2 hydrogenation: Synthesis, characterization, and catalytic reactions. Nano Lett 12, 3091–3096 (2012).

25. Melaet, G. et al. Evidence of highly active cobalt oxide catalyst for the Fischer-Tropsch synthesis and CO_2 hydrogenation. J Am Chem Soc 136, 2260–2263 (2014).

26. Parastaev, A. et al. Boosting CO_2 hydrogenation via size-dependent metal–support interactions in cobalt/ceria-based catalysts. Nat Catal 3, 526–533 (2020).

27. Parastaev, A. et al. Breaking structure sensitivity in CO_2 hydrogenation by tuning metal–oxide interfaces in supported cobalt nanoparticles. Nat Catal 5, 1051–1060 (2022).

28. Nguyen, T. H., Kim, H. B. & Park, E. D. CO and CO_2 Methanation over CeO_2-Supported Cobalt Catalysts. Catalysts 12, 212 (2022).

29. Dostagir, N. H. M. et al. Co Single Atoms in ZrO_2 with Inherent Oxygen Vacancies for Selective Hydrogenation of CO_2 to CO. ACS Catal 11, 9450–9461 (2021).

30. Zhou, G., Zhao, S., Xie, F., Chen, S. & Xie, H. Construction of surface active centers on the mesoporous Co/$CeO_{2-\delta}$ catalysts for CO_2 hydrogenation. Int J Hydrogen Energy (2023).

31. Have, I. C. ten et al. Uncovering the reaction mechanism behind CoO as active phase for CO_2 hydrogenation. Nature Communications 2022 13:1 13, 1–11 (2022).

32. Xu, S., Xie, F., Xie, H., Zhou, G. & Liu, X. Effect of structure and composition on the CO_2 hydrogenation properties over bimodal mesoporous CeCo composite catalyst. Chemical Engineering Journal 375, 122023 (2019).

33. Wang, L. et al. Silica accelerates the selective hydrogenation of CO_2 to methanol on cobalt catalysts. Nature Communications 2020 11:1 11, 1–9 (2020).

34. Dai, B. et al. CO_2 reverse water-gas shift reaction on mesoporous M-CeO_2 catalysts. Can J Chem Eng 95, 634–642 (2017).

35. Deng, K. et al. Studies of CO_2 hydrogenation over cobalt/ceria catalysts with in situ characterization: the effect of cobalt loading and metal–support interactions on the catalytic activity. Catal Sci Technol 10, 6468–6482 (2020).

Chapter 3

CO_2 methanation of Co/CeO_2 prepared by wetness impregnation of Co on flame-synthesized CeO_2

Abstract

A set of Co/CeO_2 catalysts with varying Co loading was prepared by wet impregnation of Co on flame-synthesized CeO_2 and compared for their structure and catalytic performance in CO_2 methanation to an earlier set of FSP-prepared Co-CeO_2 composites. At low Co loading (2.5 mol.%), Co is mostly highly dispersed as Co^{2+} ions in strong interaction with CeO_2, which can not be reduced at 300 °C. The amount of these highly dispersed Co^{2+} species (~2.5 mol.%) was consistent across all catalysts. Higher Co content (5 and 10 mol.%) led to segregated Co_3O_4 nanoparticles (~2 – 2.5 nm), which partially reduced to metallic Co nanoparticles (2.5 – 3 nm) at 300 °C. At low Co content, the impregnated catalysts mainly produced CO at a low CO_2 conversion. With increasing Co content above 5 mol.%, the Co nanoparticles obtained upon reduction hydrogenated CO_2 to CH_4, with only small amounts of CO and C_2H_6 by-products. CO hydrogenation on these samples yielded olefins and oxygenates (86% selectivity) with low CH_4. The highest activity in CO hydrogenation (8.1 ± 0.5 $mmol_{CO}/mol_{Co}/s$ at 250 °C) was obtained for 5CoWI. Despite differences in product selectivity, all Co/CeO_2 catalysts deactivate under CO and CO_2 hydrogenation. Characterization revealed that the deactivation of Co/CeO_2 catalysts is accompanied by carbon deposition on Co nanoparticles. The very small Co clusters and highly dispersed Co^{2+} interacting strongly with CeO_2 in Co/CeO_2 were selective for CO production and less prone to deactivation. Finally, regeneration in artificial air could remove the deposited carbon species and restore the initial performance of Co/CeO_2 in CO_2 hydrogenation.

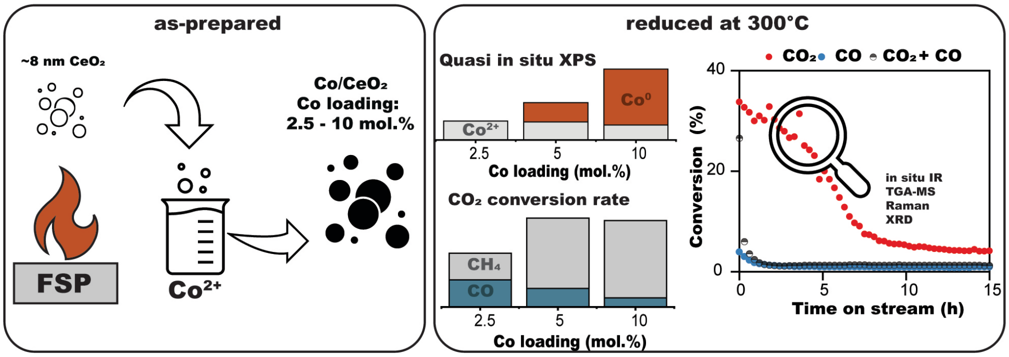

Introduction

CO_2 hydrogenation to chemicals is promising for storing renewable H_2.[1–3] Among the various reaction products, catalytic CO_2 hydrogenation to CH_4 (synthetic natural gas, SNG) is of significant interest because SNG can be easily transported in existing infrastructure to a large market.[4,5]

Base transition metals have been extensively studied as active CO and CO_2 hydrogenation catalysts due to their lower cost than noble metals (Ru, Rh, Pt, Pd). Ni is widely studied for CO_2 methanation.[6,7] Co has been widely investigated for Fischer-Tropsch (FT) synthesis, the conversion of synthesis gas to long-chain hydrocarbons.[8–10] Given its high activity, it is worthwhile exploring the use of Co as a metal for CO_2 methanation.

Nonreducible oxide supports, such as SiO_2 and Al_2O_3, are typically used to disperse the active phase as metal nanoparticles.[11–17] Recently, there has been growing interest in reducible supports, such as TiO_2 and CeO_2, which can improve the catalytic performance of metal nanoparticles due to their redox properties and strong interaction with metals.[18–25] The possibility of stabilizing several oxidation states of Co can affect the activity and product distribution in CO_2 hydrogenation.[26,27] For example, Co on reducible CeO_2 exhibits high activity and methane selectivity in CO_2 hydrogenation.[19–21,27,28] H_2 spillover in Co/CeO_2 catalysts results in the reduction of the CeO_2 surface, the resulting oxygen vacancies assisting in CO_2 adsorption and activation.[29,30] Generally, metallic Co is considered the active phase for CO_2 conversion to hydrocarbons.[31,32] Recently, it has been mentioned that Co-oxides can be active in CO_2 hydrogenation.[22,33,34] It has also been shown that increasing the metal-support interface in Co-CeO_2 catalysts results in high activity in the reverse water-gas shift (rWGS) reaction, favoring CO and minimizing CH_4 formation.[19,35–37] Parastaev et al. showed that small Co clusters dispersed on the surface of CoO nanoparticles, which are stabilized by a CeO_2-ZrO_2 support after reduction at 300 °C, are much more active in CO_2 methanation than metallic Co particles formed at higher reduction temperatures [38].

Despite their promising performance, the stability of Co/CeO_2 catalysts in CO_2 hydrogenation has only been investigated scarcely.[39–41] Deactivation of Co catalysts in CO_x hydrogenation can occur due to metal sintering [42], carbon deposition [41], active phase transformation, e.g., oxidation of metallic Co [43,44], and poisoning of the active sites.[45,46] Like CO hydrogenation, their propensity to deactivation in CO_2 hydrogenation has been linked to the Co particle size. [47–49] For example, small metallic Co Co particles (4–5 nm) are easily oxidized by H_2O during the FT synthesis reaction, unlike larger particles.[50]

Herein, we investigated the activity, product distribution, and stability of Co/CeO_2 catalysts in CO and CO_2 methanation. The preparation of the CeO_2 support by flame spray pyrolysis (FSP) results in much smaller CeO_2 crystallites than typical (precipitated) CeO_2 supports. Besides the higher surface area, the small CeO_2 crystallites are more reducible, resulting in stronger interactions with transition metals, Different from the inclusion of Co in the FSP step in **Chapter 2**, Co was introduced here by wetness impregnation. We investigated the influence of the Co loading on the catalytic performance in CO and CO_2 methanation. Based on earlier works showing the benefit of a lower reduction temperature where not all Co is reduced [38], we reduced the catalysts at a relatively low temperature of 300 °C. Combined with catalyst characterization, we discuss the role of Co particle size and Co-CeO_2 interactions on the catalytic performance.

Experimental Section

Materials

Co(II) acetate tetrahydrate ($Co(CH_3CO_2)_2 \cdot 4H_2O$, 99%, Merck), glacial acetic acid (99% Sigma-Aldrich) and 2-ethylhexanoic acid (99% Fisher Scientific), cerium(III) acetate hydrate ($Ce(CH_3CO_2)_3 \cdot 1H_2O$, 98%, TCI Europe NV), ammonia solution (28 wt.%, Thermo Fisher) were used as received without further purification.

Catalyst Preparation

Flame Spray Pyrolysis

Flame spray pyrolysis (FSP) of CeO_2 was performed in a Tethis NPS10 apparatus. The Tethis NPS10 apparatus was placed in a standard chemical laboratory fume hood modified to comply with EN 14172, EN 1822, and ISO 45H standards (modifications realized by Interflow). The air inflow of the fume hood was kept at a minimum of 0.7 m/s using active control systems. The exhaust flow to the (external) ventilation was equipped with HEPA H14 and ULPA U17 filters. The experiments were conducted after assessing all safety aspects, including those related to working with nanomaterials, in a risk-inventory and evaluation (RI&E) procedure, as required by the Dutch labor law. Appropriate amounts of $Ce(CH_3CO_2)_3 \cdot H_2O$ were dissolved in a 1:1 (v/v) solvent mixture of acetic acid and 2-ethylhexanoic acid. The Ce concentration was 0.15 M. This solution was stirred at 80 °C for approximately 1 h until the metal precursors were completely dissolved. The precursor solution was fed by a syringe pump with an injection rate of 5 mL/min to the center of a methane/oxygen flame to form a fine spray. The pressure drop at the capillary tip was maintained at 2.5 bar by adjusting the orifice gap area at the nozzle. The flow rates of methane and oxygen were respectively 1.5 L/min, and 3.0 L/min. Solid samples were collected on a glass microfiber filter (Whatman) using a vacuum pump. The as-prepared CeO_2 is denoted as CeFSP.

Wet Impregnation

A series of catalysts with intended Co loadings of 2.5, 5, and 10 mol.% with respect to Ce was prepared by wet impregnation. For this purpose, the desired amount of Co (II) acetate was dissolved in 40 ml of aqueous ammonia (28 wt.%). About 2 g of synthesized CeFSP was added to the solution, followed by stirring for 2 h, after which water was removed by evaporation. The catalysts were dried in air at 110°C overnight and calcined at 350 °C for 4 h. The samples are denoted as xCoWI, where x indicates the atomic percentage of Co with respect to Ce (100 × Co/(Co + Ce)).

Catalyst Characterization

Inductively Coupled Plasma Optical Emission Spectroscopy (ICP-OES)

The chemical composition of the as-prepared catalysts was determined by ICP-OES analysis (Spectro CIROS CCD Spectrometer). Before the ICP-OES measurements, the catalyst samples were dissolved in 5 mL concentrated sulfuric acid (H_2SO_4) at a temperature of 200 °C under stirring for at least 30 min, followed by dilution in water.

N_2 Physisorption

The textural properties of the as-prepared catalysts were determined by N_2 physisorption. at a temperature of −196 °C using a Micrometrics TriStar II 3020 instrument. Prior to physisorption measurements, the samples were heated to 160 °C in a N_2 flow for 4 h. The specific surface area (SSA) was determined by the Brunauer–Emmett–Teller (BET) method.

X-ray diffraction (XRD)

Synchrotron X-ray diffraction patterns were collected at the ID15A beamline of the ESRF (Grenoble, France). The in situ measurements were carried out in transmission mode using an incident X-ray energy of 100 keV (λ = 0.124 Å). A Pilatus3X CdTe 2M detector was used to collect the scattered signal. About 20 mg of sieved catalyst (125-250 μm) was loaded into quartz capillaries (2 mm o.d., wall thickness 0.1 mm) between two glass wool layers. The capillary was sealed with PTFE ferrules in a home-built Clausen-type flow cell. The sample was heated using a gas blower (Cyberstar). The temperature control was performed by a thin (0.25 mm) K-type thermocouple placed inside the catalyst bed. Typically, the temperature was raised from 50 °C to 300 °C at a rate of 8.5 °C/min in a flow of 50 mL/min of 20 vol.% H_2 in Ar, followed by an isothermal dwell of 0.5 h at 300 °C. Then, the system was cooled to 250 °C in the same mixture. After reaching this temperature, the reduction mixture was replaced by a reaction mixture consisting of 5 vol.% CO2 and 20 vol.% H2 balanced by Ar fed at a 50 mL/min flow rate for 0.5 h. The detector distance, energy, and tilt were calibrated using a standard CeO_2 powder obtained from NIST. The CeO_2 phase in the XRD data was analyzed by Rietveld refinement as implemented in the GSAS software. PDF data up to q = 28 Å^{-1} were reduced using the pdfgetX3 software [36]. Real-space refinement was performed with the PDFgui software [52]. The PDF is described using the G(r) formalism, which reflects the probability of finding a pair of atoms separated by a distance r with an integrated intensity dependent on the pair multiplicity and the scattering factors of the elements involved. G(r) is experimentally determined by the Fourier transform of the total scattering function F(Q), corresponding to the coherent scattering coming from the sample (Bragg peaks and diffuse scattering) after normalization.

Ultraviolet-visible diffuse reflectance spectroscopy (UV-Vis DRS)

UV-Vis DRS spectra were collected at room temperature with a Shimadzu UV-2401PC spectrometer equipped with an integrating sphere coated with $BaSO_4$ as the standard. Samples were diluted with $BaSO_4$ (30 mg sample mixed with 120 mg $BaSO_4$).

Transmission Electron Microscopy (TEM)

The morphology and particle size distributions of as-prepared and reduced catalysts were investigated by TEM using an FEI Titan Cryo-TEM instrument operating at an acceleration voltage of 300 kV. An appropriate amount of finely ground material was ultrasonically dispersed in analytical-grade absolute ethanol, before deposition on holey Cu TEM grids. Additional TEM measurements to determine the nanoscale elemental distribution involved scanning transmission electron microscopy - energy dispersive X-ray analysis (STEM-EDX). Measurements were carried out on a FEI-cubed Cs-corrected Titan instrument operating at an acceleration voltage of 300 kV. Co-CeO_2 catalysts were reduced at 300 °C in a flow of 20 vol.% H_2 in He for 4 h, followed by passivation at room temperature in a flow of 2 vol.% O_2 in He for 1 h. The as-prepared and passivated samples were crushed, sonicated analytical-grade absolute ethanol, before deposition on holey Cu TEM grids.

Temperature-Programmed Reduction (H_2-TPR)

The reducibility of the samples was studied by H_2-TPR with a Micromeritics AutoChem II instrument. Typically, about 100 mg sample was loaded into a quartz U-tube between two quartz wool layers. Prior to H_2-TPR, the sample was treated at 350 °C for 1 h in a flow of 50 mL/min of 5 vol.% O_2 in He. TPR profiles were recorded under heating the sample from 40 to 700 °C at a rate of 10 °C/min in a 50 mL/min flow of 4 vol.% H_2 in He. H_2 consumption was measured by a thermal conductivity detector (TCD), which was calibrated using an AgO reference.

H_2 and CO Chemisorption

H_2 and CO chemisorption measurements were performed with a Micromeritics ASAP2010C instrument. Typically, about 100 mg sample was loaded into a quartz

U-tube between two quartz wool layers. Before chemisorption measurements, the catalyst was reduced in an H_2 flow at 300 °C by heating to this temperature at a rate of 10°C/min, followed by an isothermal dwell of 4 h. After evacuation at 320 °C for 1 h, CO and H_2 adsorption isotherms were recorded at 35 °C and 150 °C, respectively.

Thermogravimetric-Mass Spectrometry Analysis (TGA-MS)

TGA-MS was used to determine the amount of carbonaceous deposits retained on the catalysts after the reaction. A Mettler Toledo TGA/DSC 1 instrument was connected to a mass spectrometer (MS, Pfeiffer Omnistar). Around 15-25 mg of spent catalyst was placed in an alumina crucible and pre-treated in a 50 mL/mi flow of 20 vol.% O_2 in He at 50 °C (rate 10 °C/min) for 0.5 h to remove contaminants. TG analysis was performed from 50 °C till 950 °C in the same flow using a rate of 10°C/min.

Raman Spectroscopy

Raman spectroscopy was carried out using a WITec UHTS300 spectrometer equipped with a WITec WMT50 confocal Raman microscope. Raman spectra of powder samples were collected using a 532 nm laser (0.5 mW) and an acquisition time of 30 s. The Project FIVE software (version 5.1) was used for data treatment.

IR Spectroscopy

IR spectra were recorded on a Bruker Vertex 70v FTIR spectrometer equipped with a DTGS detector. The experiments were performed in situ using a home-built environmental transmission IR cell. Self-supporting pellets were made by pressing approximately 10 mg sample in a disc with a diameter of 13 mm. Each spectrum was collected by averaging 32 scans with a resolution of 2 cm^{-1} in the 4000–1000 cm^{-1} range.

For CO IR measurements, the sample was first reduced in a flow of 20 vol.% H_2 in He at 300 °C (rate 10 °C/min) for 4 h. After outgassing at 300 °C in vacuum and cooling to 50 °C, IR spectra were recorded as a function of the CO partial pressure in the 0–10 mbar range. Additional CO IR measurements were carried out at liquid N_2 temperature. For these measurements, the same reduction procedure was followed. After outgassing, the sample was cooled by liquid N_2. The sample temperature was approximately -168 °C. IR spectra were recorded as a function of CO partial pressure in the 0–10 mbar range. As-prepared samples were also investigated by CO IR spectroscopy at liquid N_2 temperature. For this purpose, the samples were evacuated at 50 °C for 1 h, prior to cooling to liquid N_2 temperature. CO_2 IR spectra were recorded after reduction of the samples as described above. IR spectra were obtained as a function of CO_2 partial pressure in the 0–10 mbar range at 50 °C. Operando IR spectra during CO_2 methanation were recorded in a flow of 4 vol.% CO_2 and 16 vol.% H_2 balanced by N_2 at temperatures in the 200 – 300 °C range. Spectra were recorded first at 200 °C and then at higher temperature up to at

300 °C at intervals of 25 °C using a rate of 5 °C/min. All IR spectra were background subtracted, and the intensity was normalized to the weight of the pellet.

X-ray Photoelectron Spectroscopy (XPS)

The surface chemical properties of the as-prepared catalysts were studied with a K-Alpha XPS apparatus (Thermo Scientific) equipped with an aluminum anode (Al Kα = 1486.68 eV) monochromatized X-ray source. Finely ground samples were placed on double-sided carbon tape. All spectra were acquired using a flood-gun to reduce surface charging. A pass energy of 40 eV was used for region scans with a step size of 0.1 eV and a dwell time of 0.5 s. The U''' (Ce^{4+}) component of the Ce 3d line with a characteristic position of 916.7 eV was used to correct the binding energies of the Co $2p_{3/2}$ and Ce 3d regions.[53,54] A standard procedure involving Shirley background subtraction and atomic sensitivity factors was applied for data processing. Spectral lines were fitted with the CasaXPS software (version 3.2.23) using a symmetric pseudo-Voigt function, referred to as GL (30), except for the main metallic component of Co, which was fitted by the asymmetric LA (1.2,5,5) line shape. The Ce 3d line was fitted according to a model described in the literature.[32, 33]

Quasi-in situ X-ray photoelectron spectroscopy (XPS)

The surface chemical properties of the reduced and deactivated catalysts were studied using a Kratos AXIS Ultra 600 equipped with a monochromatic X-ray source (Al Kα = 1486.68 eV). Self-supporting pellets were made by pressing approximately 40 mg of a sample in a disk with a diameter of 13 mm. Pretreatment of catalysts were carried out in a high-temperature reaction cell (Kratos, WX-530), allowing in vacuum sample transfer into the analysis chamber. The samples were reduced in 20 vol.% H_2 in Ar at a flow rate of 50 mL/min at 300 °C for 4 h at a rate of 10 °C/min and ambient pressure. Then, the sample was cooled to 100 °C in the pretreatment mixture and the reaction cell was evacuated to a pressure below 10^{-8} mbar, followed by transfer of the sample to the XPS analysis chamber. A pass energy of 40 eV was typically used for region scans with a step size of 0.1 eV and a dwell time of 0.5 s. Energy calibration and fitting of Ce 3d and Co2p were performed using the same procedure as described in the XPS description above.

Catalytic Activity Measurements

CO_x hydrogenation

The catalytic performance of CeO_2 and Co/CeO_2 samples in CO_2 hydrogenation was evaluated in a down-flow stainless-steel reactor with an internal diameter of 4 mm. The reaction was performed at atmosphere pressure and the temperature was varied in the range of 200–300 °C. The samples were pressed, crushed, and sieved to a fraction of 125–250 μm. Typically, the reactor was filled with 50 mg catalyst diluted with 200 mg of SiC. Before the reaction, the catalyst was reduced in a flow of 100 mL/min of 20 vol.% H_2 in He, whilst ramping from room temperature to 300 °C at a rate of 10 °C/min, followed by an isothermal dwell at 300 °C for 4 h. The reduced catalyst was cooled in the same gas mixture to the initial reaction temperature of 200 °C. The reaction was started by replacing the reduction gas mixture with a flow of 50 mL/min of 60 vol.% H_2, 15 vol.% CO_2 and 25 vol.% Ar. The temperature was increased in steps of 25 °C at a rate of 5 °C/min. At each isothermal dwell of 170 min, the effluent gas was sampled and analyzed by an online gas chromatograph (Shimadzu, GC-2014) equipped with RT-Q-Bond (FID), and Shincarbon ST 80/100 (TCD) analysis sections. The CO_2 conversion and carbon-based product selectivity were calculated as follows:

$$X(CO_2) = 1 - \frac{F(CO_2)_{out}}{F(CO_2)_{out} + F(CO)_{out} + F(CH_4)_{out} + F(CH_3OH)_{out} + xF\left(C_xH_y\right)_{out}} \quad (1)$$

$$S(product) = \frac{F(product)_{out}}{F(CO)_{out} + F(CH_4)_{out} + F(CH_3OH)_{out} + xF\left(C_xH_y\right)_{out}} \quad (2)$$

where C_xH_y represents hydrocarbons with more than one carbon atom formed during the reaction. *F* stands for the volumetric flow rate determined from the concentration measured by gas chromatography, using Ar as an internal standard and appropriate FID and TCD response factors determined using gas calibration mixtures.

The reaction rate (r_{CO2} in $mol_{CO2} \cdot mol_{Co}^{-1} \cdot s^{-1}$) was calculated and normalized to the Co loading in the following manner:

$$r_{CO2} = \frac{X(CO_2) * F(CO_2)_{in}}{n_{Co} * V_m} \quad (3)$$

where $F\,(CO_2)_{in}$ is the known CO_2 volumetric flow rate at the reactor inlet. V_m is the molar volume of an ideal gas at standard temperature and pressure. The rates of CH_4 and CO were calculated in a similar manner.

CO hydrogenation was performed in the same reactor used for CO_2 hydrogenation. The reaction was started by replacing the reduction gas mixture with a flow of 50 mL/min (18.8 vol.% CO, 56.2 vol.% H_2, 25 vol.% Ar) at 1 bar. The CO conversion and carbon-based product selectivity were calculated in a similar manner:

$$X(CO) = 1 - \frac{F(CO)_{out}}{F(CO_2)_{out} + F(CO)_{out} + F(CH_4)_{out} + F(CH_3OH)_{out} + xF\left(C_xH_y\right)_{out}} \quad (4)$$

The reaction rate (r_{CO} in $mol_{CO} \cdot molCo^{-1} \cdot s^{-1}$) was normalized by the Co loading in the following manner:

$$r_{CO} = \frac{X(CO) * F(CO)_{in}}{n_{Co} * V_m} \quad (5)$$

where $F(CO)_{in}$ is the known CO volumetric flow rate at the reactor inlet. V_m is the molar volume of an ideal gas at standard temperature and pressure. The product selectivity and product formation rates were calculated in the same way as described above.

Some reaction experiments involved the hydrogenation of mixtures of CO_2 and CO. The reaction was started by replacing the reduction gas mixture with a flow of 50 mL/min (3.6 vol.% CO, 11.4 vol.% CO_2, 60 vol.% H_2, 25 vol.% Ar, 50 mL/min) at 1 bar. The total C (CO+CO_2) conversion was calculated as follows:

$$X(CO + CO_2) = 1 - \frac{F(CO_2)_{out} + F(CO)_{out}}{F(CO_2)_{out} + F(CO)_{out} + F(CH_4)_{out} + F(CH_3OH)_{out} + xF\left(C_xH_y\right)_{out}} \quad (6)$$

The product selectivity and product formation rates were calculated in the same way as described above.

Results and discussion

Catalyst Characterization

The most important physicochemical properties of the CeFSP and CoWI catalysts are listed in **Table 3.1**. The Co loadings determined by ICP-OES analysis are close to the intended values. The XRD patterns of as-prepared CoWI catalysts and the CeFSP support shown in **Figure 3.1a** mainly feature peaks of the fluorite structure belonging to CeO_2. Reflections due to Co_3O_4 are only observed in the 10CoWI catalyst (**Figure 3.1b**). Thus, Co is well dispersed in all CoWI catalysts. Rietveld refinement shows that the CeO_2 unit cell is slightly contracted in all CoWI samples in comparison with the CeFSP one, which points to the partial substitution of Ce^{4+} (ionic radius of 0.92 Å) with the smaller Co^{2+} ion (ionic radius of 0.72 Å).[57,58] As Co is introduced by incipient wetness impregnation, it is most likely that Co ends up in the surface region of the CeO_2 crystallites. The crystallite size of CeO_2 estimated by Rietveld refinement increases slightly from 9.5 nm (CeFSP) to ~10 nm for the samples containing Co (**Table 3.1**). The specific surface area of the samples between 155 and 180 m^2/g decreases with increasing Co loading. This is probably caused by Co-oxide particles blocking some of the interparticle voids. All N_2 physisorption isotherms can be categorized as type IV with an H2 hysteresis loop due to mesopores. As XRD did not show any peaks related to ordered mesopores, the hysteresis loop likely originates from the voids between aggregated nanocrystallites. The surface area of these supported CeO_2 catalysts is much higher than that of typical commercial CeO_2 samples, which have a typical surface area below 50 m^2/g.

UV-Vis spectra of CeFSP and as-prepared CoWI catalysts (**Figure 3.1c**) contain bands in the 260 – 280 nm range, which can be assigned to CeO_2.[59] The UV-Vis spectra of the as-prepared 2.5CoWI and 5CoWI catalysts contain a broad band in the 400 – 600 nm range, likely due to Co in close interaction with CeO_2.[60] The 10CoWI sample with the highest Co loading presents two characteristic bands in the 400 – 480 nm and 700 – 760 nm ranges due to Co_3O_4, assigned to O^{2-} – Co^{2+} and O^{2-} – $Co^{3,}$ ligand to metal transfer bands, respectively.[61]

Bright-field TEM was used to study the morphology and average particle size of the as-prepared catalysts. All samples exhibit an octahedral shape, irrespective of the

Co loading (**Figure B1**). The average particle sizes for the catalysts are 5.5 ± 2.4 nm for 2.5CoWI, 6.2 ± 2.5 nm for 5CoWI, and 5.7 ± 2.2 nm for 10CoWI. The poor contrast between Co and Ce makes distinguishing the Co-containing phases from the CeFSP support in the CoWI samples challenging.

Table 3.1. Physicochemical properties of as-prepared CeFSP and CoWI catalysts.

Catalyst	Co (mol.%)^a	S_{BET} (m^2/g)^b	d_{CeO2} (nm)^c	d_{Co3O4} (nm)^c	a_{CeO2} (Å)^c	d_{CeO2} (nm)^d	Co/Ce (at.%/at.%)^e
CeFSP	0	181	9.5 ± 0.06	-	5.411	5.0 ± 2.0	-
2.5CoWI	2.5	156	9.9 ± 0.05	-	5.407	5.5 ± 2.4	0.026
5CoWI	4.9	155	9.6 ± 0.05	-	5.405	6.2 ± 2.5	0.048
10CoWI	9.3	135	9.7 ± 0.05	3.5 ± 0.3	5.408	5.7 ± 2.2	0.082

a – determined from ICP analysis, b -determined by N_2 physisorption on as-prepared samples, c –lattice parameter of CeO_2, determined by Rietveld refinement of synchrotron XRD on as-prepared samples (a_{CeO2}), d – determined by TEM for as-prepared samples, e – determined by XPS for as-prepared samples

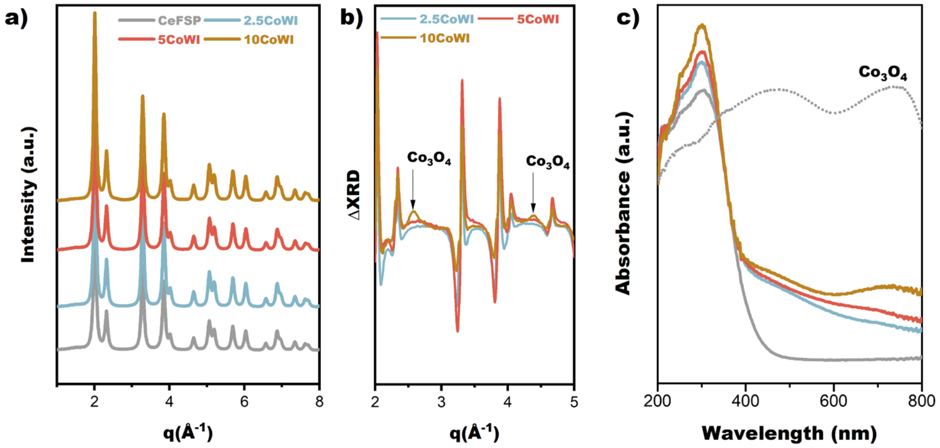

Figure 3.1. (a) Synchrotron XRD patterns (λ = 0.124 Å) of CoWI and CeFSP, (b) Synchrotron ΔXRD of as-prepared CoWI (ΔXRD obtained by subtraction of the diffractogram of as-prepared CeFSP sample from corresponding CoWI diffractograms). (c) UV-Vis spectra of CeFSP, CoWI, and the Co_3O_4 reference.

To determine the average Co particle size in the as-prepared CoWI catalysts, we utilized high-angle annular dark-field scanning TEM (HAADF-STEM) combined with energy-dispersive X-ray (EDX) mapping. **Figure 3.2** presents the elemental maps of Co and Ce in the as-prepared CoWI catalysts. In the sample with the lowest Co loading (2.5CoWI), Co is mostly highly dispersed on the CeO_2 support particles. Only a few aggregated Co particles can be observed with a size of ~1.5 nm. Co aggregation is significant in the 5CoWI and 10CoWI catalysts, although both samples also contain highly dispersed Co. The 10CoWI catalyst contained sufficient nanoparticles to determine their average size, being 2.5 ± 0.8 nm.

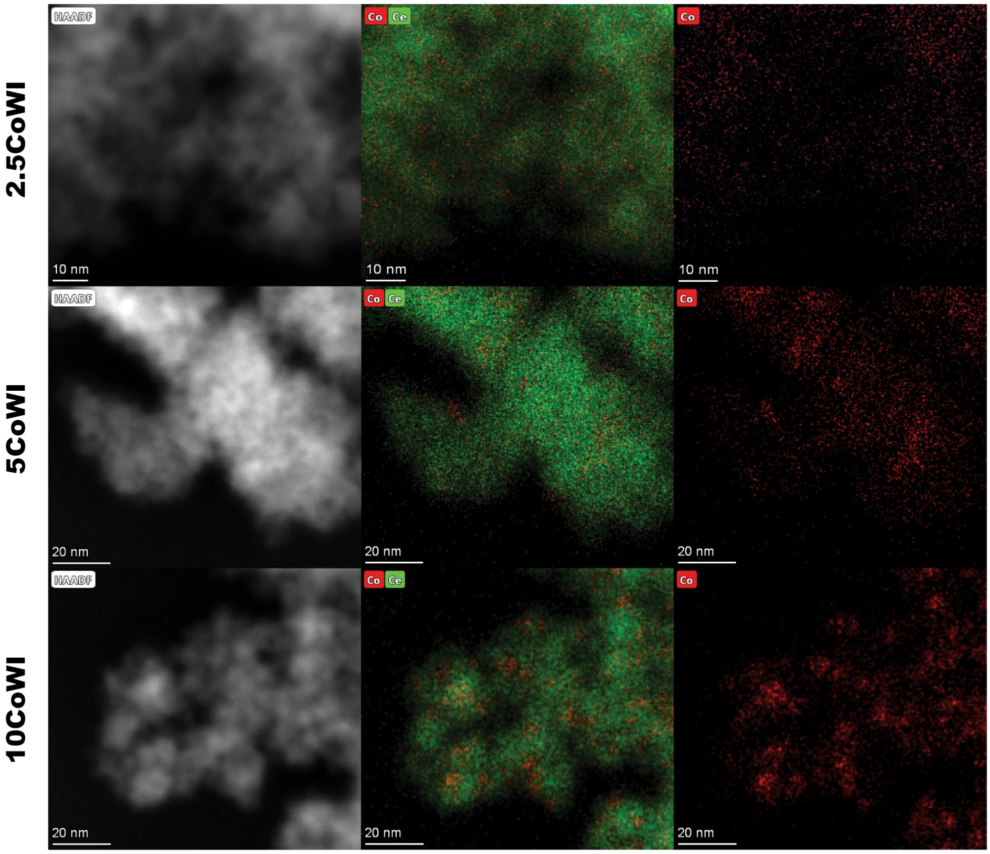

Figure 3.2. STEM-EDX images: (left) HAADF-STEM images and corresponding EDX elemental maps of (middle) Co and Ce and (right) Co for as-prepared CoWI catalysts.

The surface of the as-prepared samples was probed by XPS and CO IR spectroscopy. The Co $2p_{3/2}$ XP spectra were fitted using a literature model.[62] The fitted XP spectra are shown in **Figure B2**. The corresponding Co/Ce surface ratios are listed in **Table 3.1**. The XP spectrum of 2.5CoWI can be fitted with one Co^{2+} component with a Co $2p_{3/2}$ binding energy of 781.0 eV and an accompanying satellite peak at 786.5 eV. At Co loadings of 5 mol.% and 10 mol.%, the formation of Co_3O_4 on the surface was evident from the $2p_{3/2}$ contribution of Co^{3+} at 778.8 eV, along with two Co^{2+} contributions at 780.6 eV and 782.4 eV.[63] The Co^{3+} fractions for 5CoWi and 10CoWi of 28% and 36%, respectively, are significantly lower than the Co^{3+} fraction in Co_3O_4. This indicates that the surface of the samples also contains highly dispersed CoO or a Co-CeO_2 solid solution[19], confirming the interpretation of the UV-Vis and STEM-EDX results. As expected, the amount of Co_3O_4 increases with the Co loading.

The presence of Co^{2+} is also evident from the low-temperature CO IR spectra. In addition to narrow bands at 2150 – 2155 cm^{-1} due to CO adsorption on Ce^{4+} [64–66], the IR spectra of the CoWI catalysts contain a sharp band at 2090 – 2100 cm^{-1} due to CO adsorption on Co^{2+}.[67,68] A band due to CO adsorption on Co^{3+}, expected at 2180 cm^{-1} [67], is not observed.

Overall, the XRD, UV-Vis, XPS, STEM-EDX, and CO IR results indicate that all CoWI catalysts contain uniformly distributed and, most likely, isolated Co^{2+}. Some CoO clusters and nanoparticles with a size of ca. 1 nm were visible for the 2.5CoWI catalyst. The catalysts with a higher Co loading contain more aggregated forms of Co as CoO and Co_3O_4.

Metal-support interactions

To evaluate the interactions between Co and CeO_2, we compared H_2-TPR profiles of the CoWI catalysts to that of the bare CeFSP. The weight-normalized reduction profiles are shown in **Figure 3.3a**. The H_2-TPR profile of CeFSP is characterized by a single reduction peak at 580 °C, attributed to the reduction of surface Ce^{4+} to Ce^{3+}.[69] The profiles of 5CoWI and 10CoWI show two peaks at 300 °C and 425 °C, owing to the reduction Co_3O_4 to CoO and CoO to Co, respectively.[70–72] The 2.5CoWI sample contains a low-temperature peak at 200 °C, likely due to the reduction of surface-adsorbed oxygen species[73,74], and a main reduction peak at 350 °C due to the reduction of CoO in strong interaction with CeO_2 or Co in a Co-CeO_2 solid solution.[75] The peak due to metallic Co formation for 2.5CoWI is very small. Overall, this interpretation is consistent with the XRD and XPS findings, indicating the predominance of Co^{2+} species at low Co loading and a growing amount of Co_3O_4, which can be reduced to metallic Co at elevated temperatures, with increasing Co loading. The excess amount of H_2, i.e., the difference between the total H_2 consumed and H_2 required to reduce CoO/Co_3O_4 completely (**Figure 3.3b**), stems from the reduction of the CeO_2 surface by spillover hydrogen from metallic Co particles. This also explains the lower onset temperature of CeO_2 surface reduction [31]. As the CeO_2 surface area is similar for the three CoWI catalysts, the excess amount of consumed H_2 does not strongly vary with Co loading. In the following, we employed a reduction temperature of 300 °C using a heating rate of 10 °C and a dwell of 4 h in 20 vol.% H_2 in He to partially reduce Co in the CoWI catalysts, which can benefit the CO_2 hydrogenation performance of Co supported on CeO_2-containing supports.

H_2 chemisorption measurements on the reduced catalysts (**Table 3.2, Figure 3.3c**) indicate irreversible H_2 chemisorption on all CoWI samples (**Figure B3**). The amount of chemisorbed H_2 increases with the Co loading, reaching the highest value for 5CoWI. CO chemisorption also revealed irreversible CO chemisorption for CoWI catalysts and CeFSP (**Figure B3**). The observation that the CeFSP also chemisorbed CO points to oxygen vacancies formed during the reduction.[76,77] The presence of metallic Co led to higher CO chemisorption values.[78–80] Due to the involvement of the CeO_2 support, H_2 and CO chemisorption cannot be used to determine the amount of metallic Co sites.

The reduced and passivated catalysts were also examined using XPS depth profiling to verify that CeO_2 did not encapsulate Co after reduction. The surface Co/Ce ratios showed a significant decrease with every Ar etching step, indicating a higher concentration of Co at the surface (**Figure B4**). These results suggest that the reduction treatment did not lead to a Ce-containing oxide layer on the metallic Co particles.

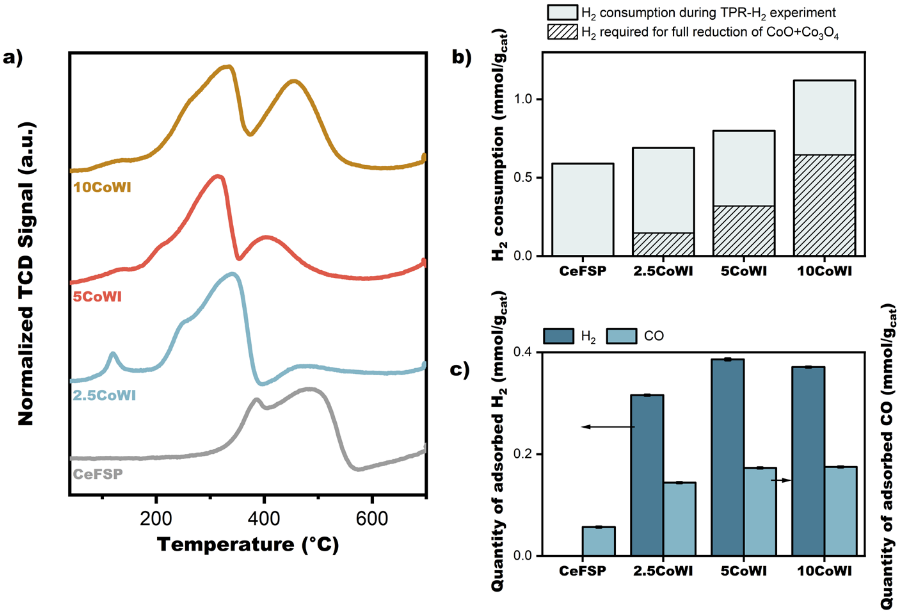

Figure 3.3. (a) Weight-normalized H_2-TPR profiles of CeFSP and CoWI (conditions: 4 vol.% H_2, 50 mL/min). (b) Quantification of H_2 consumption during TPR experiments (light grey – excess of H_2; dashed bar – the amount required for complete $CoO+Co_3O_4$ reduction; the ratio of CoO and Co_3O_4 was estimated by XPS of as-prepared samples). (c) Amount of H_2 and CO chemisorbed during chemisorption experiments.

We also used quasi-in situ XPS to study the surface composition and degree of Co and CeO_2 reduction of the reduced CoWI catalysts. The samples were reduced at 300 °C at atmospheric pressure in a flow of 20 vol.% H_2 in inert for 4 h in a reaction chamber connected to the analysis chamber of a Kratos XPS system, followed by evacuation and transfer to the XPS analysis chamber. The resulting Co $2p_{3/2}$ and Ce 3d XP spectra and their fits are shown in **Figure 3.4**, and the fit results are given in **Table 3.2**. The fraction of metallic Co in the reduced catalysts was 52% for 5CoWI and 79% for 10CoWI. The reduced 2.5CoWI catalyst only contained a contribution of Co^{2+} at a $2p_{3/2}$ binding energy of 780.6 eV, indicating that the amount of metallic Co is very low in this sample. Based on the remaining Co^{2+} fraction and the Co loading, the catalysts contain a nearly constant amount of Co^{2+} after reduction, i.e., 2.5 mol.% for 2.5CoWI, 2.4 mol.% for 5CoWI, and 2.0 mol.% for 10CoWI. This almost constant Co^{2+} amount likely represents highly dispersed Co^{2+} ions in strong interaction with the CeO_2 support. These species cannot be reduced at 300 °C, although CO IR spectroscopy shows that the surface of reduced 2.5CoWI contains a small amount of metallic Co clusters. The decrease in the Co^{2+} amount at higher Co loading might be due to the increasing surface coverage by Co metal particles. As the reduced Co particles are small, we can assume that XPS probes nearly all Co. Thus, the amount of metallic Co can be estimated to increase from 2.6 mol.% for 5CoWI to 7.3 mol.% for 10CoWI. The deconvolution of the Ce 3d XP spectra showed that the presence of Co led to a higher Ce^{3+} contribution of ~37% for all reduced CoWI catalysts than the Ce^{3+} contribution of ~7% in the as-prepared catalysts. The XPS Co/Ce surface ratios of the reduced catalysts are lower than those of the as-prepared catalysts (**Table 3.1** and **Table 3.2**). The slight decrease in the Co/Ce ratio upon reduction of the 2.5CoWI catalyst can be explained by the very low Co reduction degree. In contrast, the reduction of 5CoWI and 10CoWI results in a substantial decrease in the Co/Ce ratio, which aligns with the sintering of Co during Co-oxide transformation into metallic Co particles.

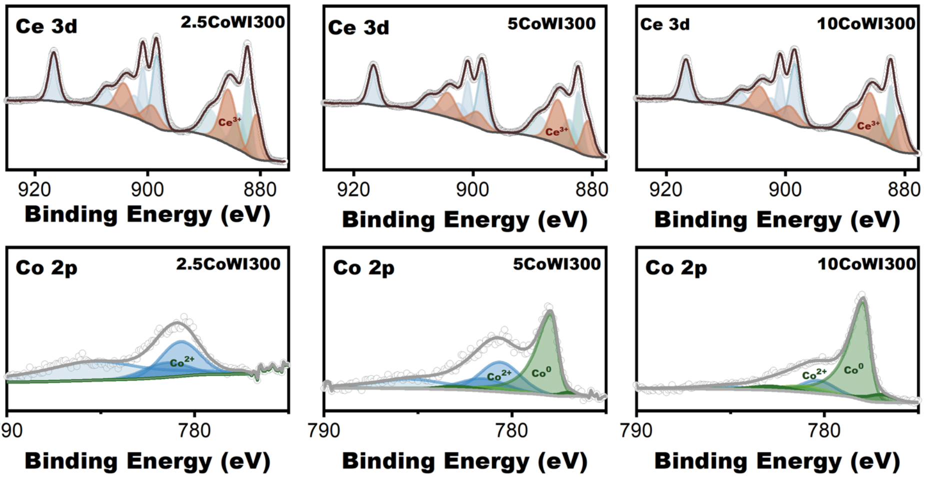

Figure 3.4. Deconvolution of Ce 3d (top) and Co $2p_{3/2}$ (bottom) XP spectra of reduced CoWI catalysts (reduction conditions: 20 vol.% H2 in Ar, 50 mL/min, 300 °C, 4 h).

The Co particle size in the reduced and passivated CoWI catalysts was estimated from HAADF-STEM-EDX maps (**Figure 3.5**). At low Co loading (2.5CoWI), Co remains highly dispersed on CeO_2, with only a few Co particles visible with sizes ~2 nm. The average Co particle sizes in the reduced 5CoWI and 10CoWI catalysts were 2.5 ± 0.4 nm and 3.0 ± 0.7 nm for 5CoWI and 10CoWI, respectively. Both catalysts also contained highly dispersed Co.

The theoretical amount of chemisorbed H_2 was estimated, assuming a spherical shape of the particles and a H/Co adsorption stoichiometry of unity and considering for 5CoWI and 10CoWI, the Co particle sizes determined from STEM-EDX maps and Co reduction degrees from the quasi-in situ XPS measurements. The resulting values of 0.03 mmol/g for 5CoWI and 0.08 mmol/g 10CoWI are substantially lower than the experimental H_2 chemisorption values, i.e., 0.32 mmol/g for 2.5CoWI, 0.39 mmol/g for 5CoWI and 0.37 mmol/g for 10CoWI. The difference is caused by hydrogen spill-over from Co to CeO_2, typical for CeO_2-supported metal catalysts.[81,82]

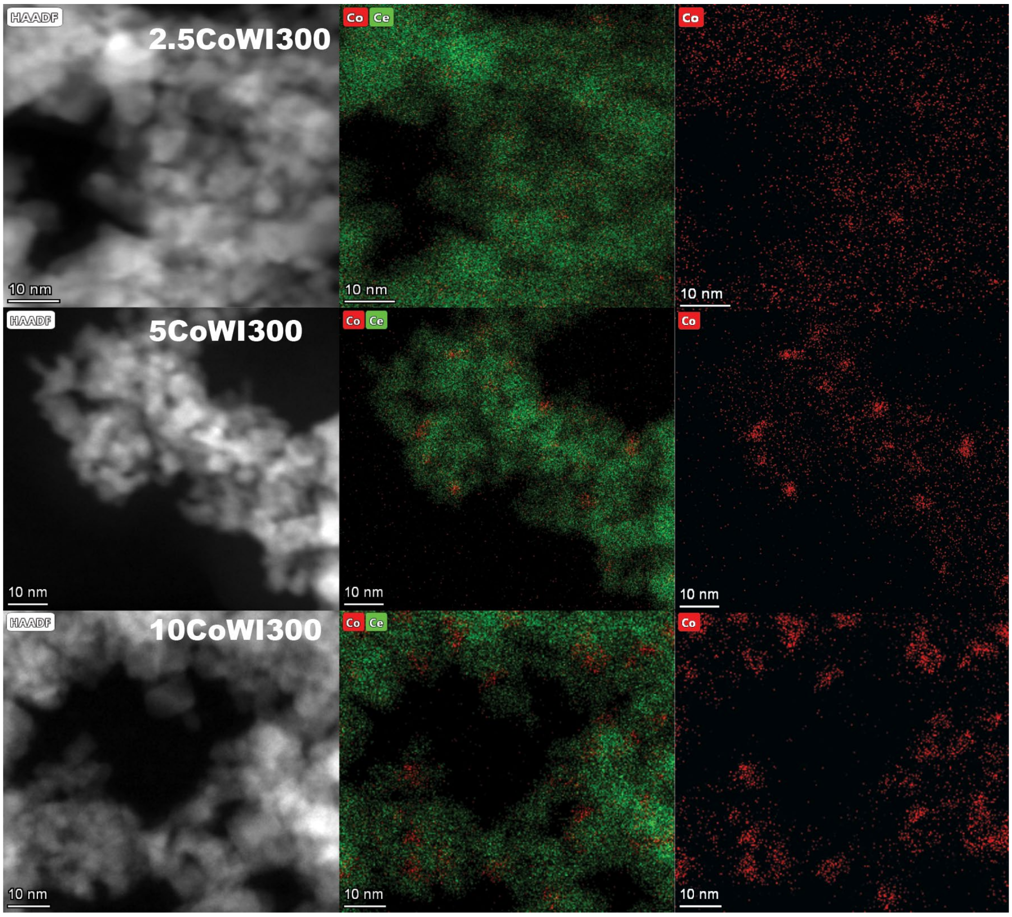

Figure 3.5. STEM-EDX images: (left) HAADF-STEM images and corresponding EDX elemental maps of (middle) Co and Ce and (right) Co for reduced and passivated CoWI catalysts.

The structural changes of the CoWI catalysts and the bare CeFSP support during reduction and subsequent CO_2 hydrogenation were investigated in more detail by in situ synchrotron XRD. XRD data were recorded up to $q = 14$ Å^{-1} and PDF data up to $q = 28$ Å^{-1}. The synchrotron XRD patterns of the CoWI catalysts can be described well by CeO_2 (**Figure B5**). The patterns for the 2.5CoWi and 5CoWINo catalysts did not contain reflections due to Co-containing phases, implying that the reduced Co particles are very small. The 10CoWI catalyst shows a stepwise reduction of Co_3O_4 to Co metal, following the sequence $Co_3O_4 \rightarrow CoO \rightarrow Co$, the transitions taking place at 175 °C and 225 °C, respectively (**Figure B6**). Subtracted XRD patterns (ΔXRD plots, referenced to the as-prepared state) emphasize that, with increasing Co loading, the contribution at q = 2.96 Å^{-1} due to metallic Co becomes stronger (**Figure 3.6a**). The negative features at q = 2.58 and 4.36 Å^{-1} of the 10CoWI catalyst point to the disappearance of the Co_3O_4 phase.

Table 3.2. H_2-TPR of as-prepared catalysts and physicochemical properties of reduced at 300 °C CoWI and CeFSP samples.

Catalyst	CeFSP	2.5CoWI	5CoWI	10CoWI
H_2 (mmol/g)[a]	0.59	0.69	0.8	1.12
Excess H_2 (mmol/g)[b]	-	0.54	0.48	0.47
d_{Co} (nm)[c]		1.6 ± 0.3	2.5 ± 0.4	3.0 ± 0.7
H_2 (mmol/g)[d]	0.00	0.32	0.39	0.37
Theoretical H_2 (mmol/g)[e]	-	0	0.03	0.08
CO (mmol/g)[f]	0.057	0.16	0.23	0.21
Co reduction degree[g]	-	0	0.52	0.79
Ce^{3+} (%)[g]	-	36	36	38
Co/Ce (at.%/at.%)[g]	-	0.02	0.02	0.03

a – determined from H_2-TPR in 100 – 650 °C range, b – estimated from the difference between total H_2 consumption during H_2-TPR and H_2 required to reduce CoO and Co_3O_4 completely, c – estimated from HAADF-STEM-EDX maps of reduced and passivated catalysts (reduction treatment: 300 °C), d – determined by H_2 chemisorption at 150 °C on catalysts reduced at 300 °C, e – estimated assuming a spherical shape of the Co particles and a H/Co adsorption stoichiometry of 1, the Co reduction degree, derived from XPS of reduced CoFSP catalysts, f – determined by CO chemisorption at 35 °C on pre-reduced samples at 300 °C, g – Co reduction degree $Co^0/(Co^0+Co^{2+})$ and Ce^{3+} fraction determined by quasi-in situ XPS on samples reduced at 300 °C.

Rietveld refinement of the XRD patterns revealed an increase in the CeO_2 unit cell parameter during reduction for all catalysts and the CeFSP sample (**Figure 3.6b**), along with a minor increase in the CeO_2 crystallite size from 10 nm to 12 nm (**Figure B7**). In addition to gradual thermal expansion, a more abrupt increase in the CeO_2 unit cell parameter from 5.405 to 5.444 Å is observed in the 100 – 250 °C temperature range for all CoWI catalysts and the CeFSP support (**Figure 3.6b**). The expansion of the CeFSP unit cell is more gradual, and the change in the unit cell parameter is less pronounced than that of the CoWI catalysts (**Figure 3.6b**). The reduction of Ce^{4+} to the larger Ce^{3+} ion and the electrostatic repulsion between oxygen vacancies and the surrounding cations cause this abrupt increase of the unit cell parameter.[83]

The G(r) derived from the PDF of CoWI and CeFSP before and after reduction are shown in **Figure B8**. The observed peaks at distances *r* = 3.8, 4.5, 5.4, 5.9, and 6.6 Å are characteristic of the CeO_2 structure. The refined lattice parameters of as-prepared CeFSP 2.5CoWI, 5CoWI, and 10CoWI catalysts are 5.408 Å, 5.402 Å, 5.406 Å, and 5.406 Å, respectively (**Table B1**). The decrease of unit cell parameter for 2.5CoWI can be explained by shortening of the average distance between Ce-Ce atom pairs due to Co insertion in the CeO_2 lattice, which is in good agreement with the other characterization results.[84] The change in the unit cell parameter is less pronounced for the catalysts containing more Co. The experimental PDF curves were also fitted by a Gaussian peak corresponding to the Ce-Ce distance of ~3.8 Å in the CeO_2 fluorite structure. The resulting CeO_2 peaks of as-prepared CoWI catalysts exhibit shorter interatomic distances than in CeFSP, which further confirms the insertion of Co in the CeO_2 structure (**Table B1**). To identify small changes due to Co, we determined ΔG(r) by subtracting G(r) of CeFSP from the G(r) of the CoWI catalysts (**Figure B9**). Following a procedure developed for Ni-ZrO_2-CeO_2 samples[85], the PDFs of Co_3O_4, CoO, Co, and Co doped in CeO_2 were modeled. Their comparison indicated that the ΔG(r) of the as-prepared 10CoWI catalyst contains features of Co_3O_4 (**Figure B9**), while the ΔG(r) of the 2.5CoWI and 5CoWI shows peaks that match those of Co doped in the CeO_2 lattice (r = 3.8 and 4.5 Å).

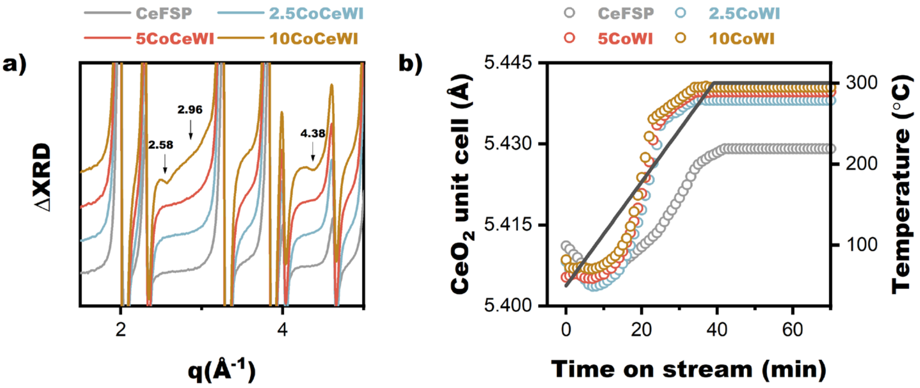

Figure 3.6. (a) Synchrotron ΔXRD (λ = 0.124 Å) of CeFSP and CoWI before and after reductive pretreatment. ΔXRD difference is obtained by subtraction of the diffractogram of the as-prepared sample from the diffractogram of the reduced catalyst. (b) Refined unit cell parameter of CeO_2 for CeFSP and CoWI during the reductive treatment (conditions: 20% H_2 in Ar, 50 mL/min, 50 – 300 °C, 1 bar).

The direct G(r) analysis and Rietveld refinement of the PDF data of the reduced catalysts show an increase in the interatomic distances, implying an expansion of the CeO_2 lattice. This can be attributed to thermal expansion and the formation of Ce^{3+} ions. The likely random distribution of Ce^{3+} in the reduced catalysts and the increased thermal motion at higher temperatures can explain the broader peaks in the PDF (**Figure B8**). The ΔG(r) of the reduced CoWI catalysts shows features of metallic Co (r = 2.5; 4.3 and 5.6 Å) and Co doped into the CeO_2 lattice (r = 3.8 and 4.5 Å) (**Figure B9**). The latter implies that not all Co^{2+} ions were reduced under these conditions, which is consistent with the STEM-EDX results of the reduced catalysts.

To estimate the degree of CeO_2 reduction, the change in the unit cell parameter of CeO_2 (Δa) was determined by subtracting the unit cell of the as-prepared sample from the unit cell of the sample after reduction. **Figure B10** shows that Δa increases with the Co loading, indicating that the presence of Co leads to a deeper reduction of CeO_2.[38]

The nature of the Co species in the reduced CoWI catalysts was also investigated by CO IR spectroscopy at 50 °C and liquid N_2 temperature (**Figure 3.7 and B11**). The assignment of the observed bands is shown in **Table A2**. All spectra recorded at 50 °C are dominated by linear and bridged carbonyl bands in the 2060 – 2000 cm^{-1} and 1970 – 1840 cm^{-1} range, respectively.[86] At low Co loading (2.5CoWI), the carbonyl band at 2020 – 2040 cm^{-1} is relatively narrow, indicating the presence of highly dispersed Co.[38,86,87] The spectra of the reduced 5CoWI and 10CoWI catalysts contain a significantly broader carbonyl band around 2000 cm^{-1} at low CO coverage, indicative of CO adsorption on metallic Co nanoparticles. Increasing the CO coverage leads to a blue shift of the carbonyl band from 2000 cm^{-1} to 2040 cm^{-1} due to lateral (dipole) interactions between adsorbed CO molecules on these larger metallic Co particles.[88,89] The spectra of the reduced CoWI catalysts also contain bands due to formate species (formate-I at 2838, 1584, and 1565 cm^{-1}; formate-II at 2838, 1565 and 1359 cm^{-1}; formate-III at 1550, 1371 cm^{-1}) and weaker bands due to carbonate and bicarbonate species (1635, 1425, 1222 cm^{-1}) (**Figure B12**).[90] These results confirm the high reactivity of the CeO_2 surface towards CO, which affects the CO chemisorption results. The negative band around 2090 cm^{-1} of the IR spectra suggests that CO partially reoxidized the CeO_2 support for all CoWI catalysts.

The corresponding CO IR spectra recorded at liquid N_2 temperature contain narrower carbonyl bands for 2.5CoWI than for the other catalysts (**Figure B11**). This further supports the conclusion that this catalyst contains very small Co clusters. The relatively narrow band at ~1933 cm^{-1}, which is likely due to bridged carbonyls on Co clusters, was only observed for the reduced 2.5CoWI catalyst. The carbonyl bands related to small Co clusters in 2.5CoWI are much broader in the IR spectra recorded at liquid N_2 temperature than those obtained at 50 °C. This is most likely due to lateral interactions of these carbonyls with CO adsorbed on proximate Co^{2+} sites or physically absorbed CO. The presence of larger Co nanoparticles in the reduced 5CoWI and 10CoWI catalysts is evident from the broader and shifting carbonyl band with Co loading. This may be linked to the increased density of highly undercoordinated Co sites, such as step-edges, on larger particles.[91] A broad band in the 2110 – 2135 cm^{-1} region in the reduced CeFSP and CoWI catalysts corresponds to the Ce^{3+} $^2F5/2 \rightarrow {}^2F7/2$ spin-orbit electronic transition.[64] This band evidences the partial reduction of CeO_2 in CeFSP and CoWI catalysts.[31] The highest intensity of this band for 2.5CoWI suggests that the CeO_2 surface is more reduced than for the other samples.

The reduced catalysts were also studied by IR spectroscopy of adsorbed CO_2 at 50 °C (**Figure B13-14**). Pronounced carbonyl bands in all IR spectra indicate that CO_2 can dissociate on the reduced catalysts at 50 °C without H_2. Similar to the CO IR spectra, the carbonyl bands for 2.5CoWI are narrower than those for the other catalysts. The negative band around 2090 cm^{-1} suggests that the CeO_2 support was partially reoxidized by CO_2 in all CoWI catalysts. Earlier, Parastaev et al. concluded that CO_2 activation in partially reduced Co/CeO_2-ZrO_2 catalysts occurs at sites at the interface between metallic Co and reducible components in the catalysts, namely CoO and CeO_2.[38]

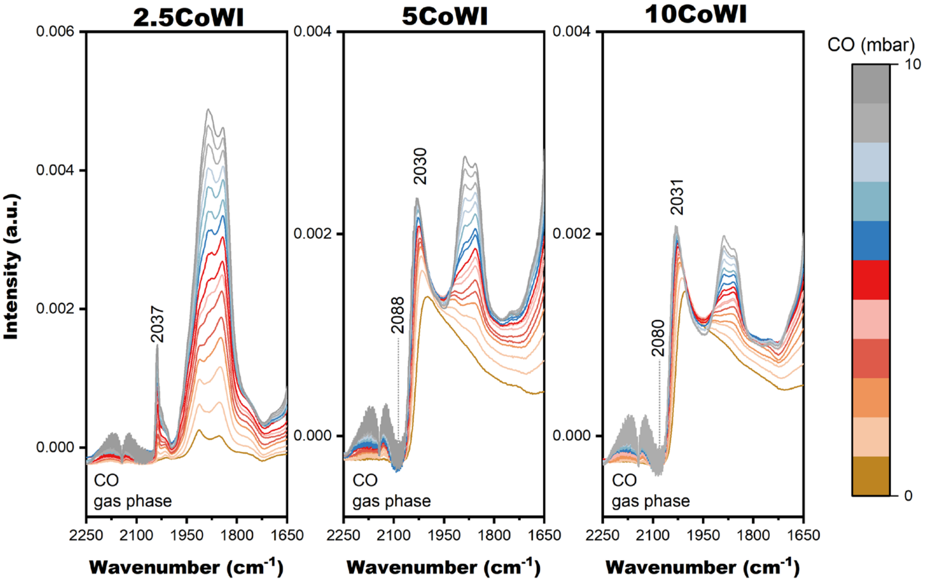

Figure 3.7. IR spectra of the CoWI reduced at 300 °C after CO adsorption at 50 °C (conditions: 1 – 10 mbar CO).

Overall, the XRD, XRD-PDF, STEM-EDX, and IR results showed that a small amount of tiny Co clusters were formed in the 2.5CoWI catalyst upon reduction at 300 °C. Reduction of the 5CoWI and 10CoWI led to larger Co nanoparticles. XPS analysis shows that the Co reduction degree of 2.5CoWI is very low, implying that the surface predominantly comprises highly dispersed Co^{2+} in strong interaction with CeO_2, resisting reduction at 300 °C. In addition to a nearly similar amount of such difficult-to-reduce Co^{2+} species, the reduced 5CoWI and 10CoWI catalysts contain metallic Co particles in amounts of 2.6 mol.% and 7.3 mol.% in 5CoWI and 10CoWI, respectively. HAADF-STEM-EDX maps of the reduced and passivated CoWI catalysts revealed that Co remains highly dispersed on CeO_2, with only a few Co particles visible with sizes ~ 2 nm for 2.5CoWI, while the average Co particle size in the reduced 5CoWI and 10CoWI catalysts was ~2.5 nm and ~3.0 nm, respectively. XPS also confirmed the presence of Ce^{3+} species due to CeO_2 surface reduction, implying the presence of oxygen vacancies. The partially reduced state of the surface is confirmed by in situ XRD, PDF, and IR spectroscopy. All reduced CoWI catalysts strongly chemisorb H_2, the H atoms generated on metallic Co spilling over to the CeO_2 support. CO adsorbed stronger on the metallic Co nanoparticles in the reduced 5CoWI and 10CoWI catalysts than the small amount of reduced Co in 2.5CoWI.

CO_2 hydrogenation

The catalytic performance of the reduced CoWI catalysts and the reduced bare CeFSP support was evaluated at atmospheric pressure in the temperature range of 200 – 300 °C. While CeFSP did not convert CO_2 under these conditions, the reduced CoWI catalysts hydrogenated CO_2 to CO and CH_4 (**Figure B15**). At 200 °C, the highest CO_2 conversion (2%) and CH_4 selectivity (84%) were obtained with the 10CoWI catalyst. The CO selectivity increased at the expense of the CH_4 selectivity with decreasing Co loading. The 2.5CoWI catalyst exhibited a CO selectivity of 78%, a CH_4 selectivity (20%), and a small amount of CH_3OH (~2%). Increasing the reaction temperature increased the CH_4 selectivity (**Figure B15**), suggesting that $CO_2 \rightarrow CO \rightarrow CH_4$ is the main pathway for CO_2 hydrogenation for the CoWI catalysts.[92]

We compared the product distribution among the catalysts at a similar conversion of ~4% at 250 °C by varying the space velocity (i.e., using 50 mg 2.5CoWI, 25 mg 5CoWI, and 15 mg 10CoWI, **Figure 3.8**). These results show that the 10CoWI catalyst exhibited the highest CH_4 selectivity (59%), while the 2.5CoWI exhibits the highest CO selectivity of 78%. The 5CoWI catalyst produced nearly equal amounts of CO and CH_4 under these conditions.

The notable differences in the product distribution can point to different structures of the active sites, which may be linked to the difference in Co particle size. Small clusters and single metal atoms possess catalytic properties distinct from metal nanoparticles.[93] The formation of CH_4 during CO_2 hydrogenation has been associated with step-edge sites on large enough metal nanoparticles[38,94], whereas very small clusters, which lack such sites needed for CO dissociation and Co-O-Ce interfaces preferentially convert CO_2 to CO via the rWGS reaction.[19,95]

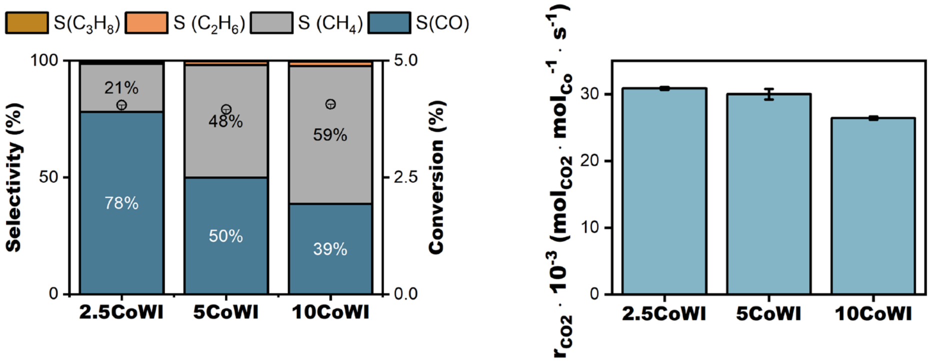

Figure 3.8. Catalytic performance of CoWI catalysts reduced at 300 °C: CO_2 conversion and product distribution at a reaction temperature 250 °C (left). CO_2 methanation reaction rate at 250 °C, normalized to the total Co loading (right) (conditions: 250 °C, 50 mg of 2.5CoWI, 25 mg of 5CoWI, 15 mg of 10CoWI, 15 vol.% CO_2, 60 vol.% H_2, 25 vol.% Ar, 50 mL/min, 1 bar).

Figure 3.8 shows the CO_2 conversion rates (r_{CO2}) normalized to the Co loading determined at the same low conversion. The highest r_{CO2} was observed for the 2.5CoWI catalyst ((3.1 ± 0.2 $mmol_{CO2}/mol_{Co}/s$). The rCO_2 decreased with increasing Co loading. As discussed above, normalizing the reaction rates to the number of metallic Co sites based on H_2 and CO chemisorption is not possible.

To compare the performance of CoWI and CoFSP catalysts (**Chapter 2**), r_{CO2} normalized to the Co loading was determined at 200 °C (**Table B2**). The reduced 2.5CoWI and 5CoWI samples displayed higher metal-weight normalized activity at 200 °C than the CoFSP catalysts. The 10CoWI (r_{CO2} of $3.8 \pm 0.8 \times 10^{-3}$ $mol_{CO2} \cdot mol_{Co}^{-1} \cdot s^{-1}$; CH_4 selectivity of 78%) exhibited a performance close to that of 10CoFSP ($3.9 \pm 0.2 \times 10^{-3}$ $mol_{CO2} \cdot mol_{Co}^{-1} \cdot s^{-1}$ and CH_4 selectivity of 86%). likely due to the formation Co nanoparticle size ~3.5 – 4.5 nm in both samples, although to the Co reduction degree for 10CoWI(79%) is higher than for 10CoFSP (52%). Highly dispersed Co in 2.5CoWI displayed substantially higher r_{CO2} ($5.3 \pm 0.3 \times 10^{-3}$ $mol_{CO2} \cdot mol_{Co}^{-1} \cdot s^{-1}$) than 2.5CoFSP ($r_{CO2}$ of $1.2 \pm 0.2 \times 10^{-3}$ $mol_{CO2} \cdot mol_{Co}^{-1} \cdot s^{-1}$) with a comparably high CO selectivity (75 – 79%). Thus, even though both samples contain highly dispersed Co in close interaction with CeO_2, it is likely that more Co is at the surface in 2.5CoWI, resulting in more metallic Co clusters upon reduction. Nevertheless, the high CO selectivity for both samples indicates that CH_4 formation is limited on these small Co clusters, while highly dispersed Co^{2+} at the Co–O–Ce interface are also likely selective in CO_2 hydrogenation to CO.

The data in **Figure B16, Table B2, and Table A5** can be used to compare the activity of the CoWI catalysts to literature data. In brief, the 2.5CoWI and 5CoWI catalysts show higher catalytic activity in CO_2 methanation in the 200 – 275 °C range compared to a wide range of Co/CeO_2 and Co/TiO_2 catalysts.

Stability in CO_2 hydrogenation

We evaluated the performance of the CoWI catalysts in CO_2 hydrogenation reaction for 65 h at a temperature of 300 °C (**Figure 3.9a-c**). The conversion levels are expressed as a ratio of the conversion at a given time and the conversion at the start of the reaction. The three CoWI catalysts show strong deactivation during the first 20 h, followed by a semi-steady state. The initial strong deactivation is accompanied by an increase in the CO selectivity at the expense of CH_4. The increased CO selectivity goes together with an increase in the selectivity of C_{2+} hydrocarbons (**Figure B17**). A higher CO intermediate partial pressure might lead to more C growth monomer formation on the Co surface, resulting in a higher chain-growth probability.[88]

To understand the initial rapid deactivation, the surface of the catalysts was studied by in situ IR spectroscopy using a CO_2 methanation feed with a H_2/CO_2 ratio of 4 at temperatures in the range of 200 – 300 °C. CH_4 formation was already evident at 200 °C for all CoWI catalysts from the characteristic gas-phase CH_4 bands at 3017 and

1306 cm^{-1} (**Figure B18**).[96] The spectra also contain bands due to gaseous CO, indicating that CO is a reaction intermediate in CO_2 hydrogenation on the CoWI catalysts. The formation of CO also explains the carbonyl bands due to CO on metallic Co in the 1800 – 2050 cm^{-1} range for the 5CoWI and 10CoWI catalysts. The absence of atop carbonyl for 2.5CoWI differs from the earlier discussed CO and CO_2 IR experiments for the 2.5CoWI catalyst (**Figure 3.10 and 3.6**), suggesting weaker CO adsorption on 2.5CoWI compared to 5CoWI and 10CoWI. All spectra contain bands in the 1970 – 1840 cm^{-1} range due to bridged carbonyls, which become more intense with increasing temperature.

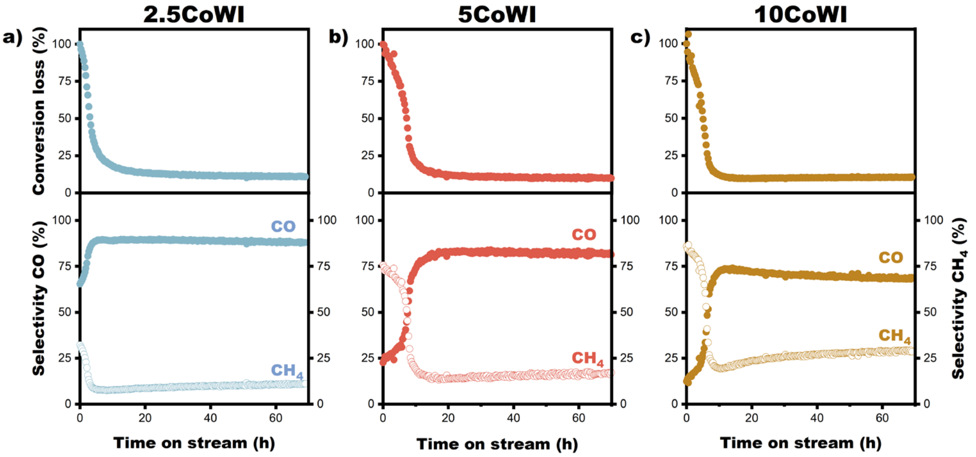

Figure 3.9. CO_2 conversion as a function of time on stream for CoWI catalysts reduced at 300 °C (a-c) (conditions: 300°C, 1 bar, 50 mg of sample, 15 vol.% CO_2, 60 vol.% H_2, 25 vol.% Ar, 50 mL/min).

Figure 3.10 shows that all CoWI catalysts feature pronounced broad IR bands in the carbonate region (1000 – 1700 cm^{-1}), which can be assigned to mono-, bi-, and polydentate carbonate and bicarbonate species.[66,90] They are formed upon the reaction of CO_2 with basic sites of the CeO_2 support. The surface also contains formate species, which follow from the C-H stretching band at 2841 cm^{-1}.[90] Various formate species are present (formate-I at 1584 and 1565 cm^{-1}; formate-II at 1565 and 1359 cm^{-1}; formate-III at 1550, 1371 cm^{-1}). The 2.5CoWI spectra show an increasing intensity of formate (2839 cm^{-1}) and CH_4 bands with increasing temperature. On the other hand, the spectra of 5CoWI and 10CoWI show a decreasing intensity of the formate and atop carbonyl bands with increasing temperature, while the intensity of CH_4 increased (**Figure B19**).

The higher intensity of the formate bands for 2.5CoWI combined with the absence of Co carbonyls may indicate the dominant rWGS reaction takes place on highly dispersed Co^{2+} species (2.5CoWI), whereas Co nanoparticles convert CO_2 to CO and CH_4 via conventional metal-catalyzed reactions on 5CoWI and 10CoWI.

IR spectroscopy was used to study catalyst stability in a flow of 4 vol.% CO_2 and 16 vol.% H_2 balanced by N_2 during 11.5 h (**Figure B20-21**). Normalized MS data recorded during these operando IR measurements for CoWI catalysts demonstrated that 2.5CoWI is more stable and produces less CH_4 than 5CoWI and 10CoWI under CO_2 methanation conditions for 11.5 h on stream. IR spectra of 2.5CoWI showed an intense band at 2841 cm^{-1} due to formate, while the carbonate/bicarbonate bands became slightly more intense during the first 1.5 h on stream and then remained stable. Normalized MS signals for 5CoWI and 10CoWI demonstrated a gradual decrease in the CH_4 signal during 1.5 h and 2.5 h, respectively. The fact that the CH_4 MS signal, the intensity of CH_4-related and atop carbonyl IR bands for 5CoWI and 10CoWI follow a similar trend (**Figure B20-21**) suggests that CO plays an important role in CH_4 formation on Co nanoparticles. The contribution of bridged carbonyls in 1970 – 1840 cm^{-1} range remains the same for all CoWI catalysts.

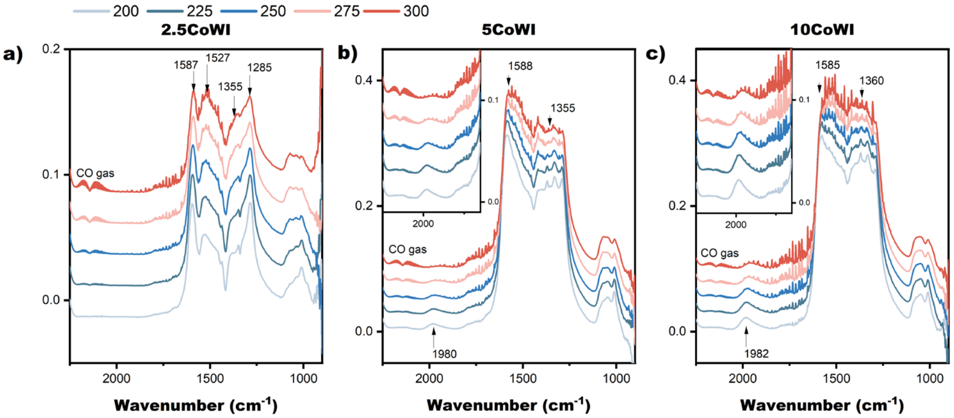

Figure 3.10. Background-subtracted operando IR spectra in a flow of 4 vol.% CO_2, 16 vol.% H_2 balanced by N_2 at 200 – 300 °C for 2.5CoWI (a), 5CoWI (b), and 10CoWI (c) samples reduced at 300 °C (conditions: 200 – 300 °C, 1 bar, 9 mg of sample).

We also investigated the reduced-passivated and used catalysts (i.e., catalysts after 65 h CO_2 hydrogenation) by Raman spectroscopy (**Figure B22**). All spectra show an intense band at 466 cm^{-1} due to the F_{2g} mode of CeO_2.[97] The reduced-passivated catalysts contain a broad band in the 560 – 610 cm^{-1} range due to oxygen vacancies.[98] Raman spectra of 5CoWI and 10CoWI showed a feature at 690 cm^{-1}, which can be assigned to the A_{1g} vibration of Co_3O_4.[99] The intensity of this band increases with the Co loading, pointing to the formation of Co_3O_4 nanoparticles, likely due to oxidation of the active phase during the passivation treatment. The Raman spectra did not contain bands at 455 and 675 cm^{-1} characteristic of CoO.[99] The Raman spectra of the used catalysts contain characteristic features of graphite with the G band around 1600 cm^{-1} [100] and the D band at 1350 cm^{-1} [101]. The D-band is related to disorder in the sp^2 carbon network of graphite and amorphous carbon. The spectra indicate the presence of graphitic coke on the used CoWI catalysts. **Figure B22** shows that the intensity of these graphite-related peaks increases with Co loading. Therefore, it is likely that the formation of graphitic coke on Co nanoparticles is the cause of the deactivation observed during CO_2 hydrogenation.

Thermogravimetric analysis (TGA-MS) was used to distinguish polymeric and graphitic carbon deposits (**Figures 11 a-c**). This analysis revealed that significant mass losses start at 175 °C for all used CoWI catalysts. The combustion temperature derived from the DTG curves exhibits a maximum at 275 °C, pointing to the "soft coke formation.[102] The MS signal shows an additional CO_2 feature at 650 °C for 5CoWI and 10CoWI (**Figure B23**), which might be explained by the decomposition of carbonate species from the catalyst surface.[103] The amount of carbon deposits increases with the Co loading, indicating that these deposits are formed on the Co metal nanoparticles.

Ex-situ synchrotron XRD of used catalysts after CO_2 hydrogenation did not provide evidence of Co-carbide phases (**Figure B24**). Moreover, no large Co nanoparticles were observed in the synchrotron XRD patterns of the used catalyst, indicating the absence of sintering under reaction conditions.

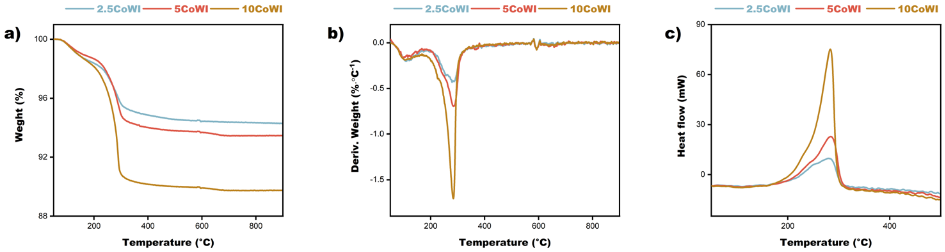

Figure 3.11. TG (a) and DTG (b) analysis, heat flow (c) of spent CoWI catalysts. Deactivated samples were obtained at the following reaction conditions: 300 °C – 50 mg of catalyst, 15 vol.% CO_2, 60 vol.% H_2, 25 vol.% Ar, 50 mL/min, 1 bar, 65 h. TG analysis conditions: 40 – 900 °C, 25 mg of catalyst, 20 vol.% O_2 in He, 50 mL/min, 10 °C/min.

We studied the regeneration of the CoWI catalysts by exploring reaction-regeneration experiments for the 10CoWI catalyst (**Figure B25). Figure 3.12** shows the activity and product distribution of the 10CoWI catalyst, following various reaction-regeneration cycles. Regeneration was carried out for 1 h in a mixture of 20 vol.% O_2 in He, followed by reduction at 300 °C for 4 h min and evaluation of the CO_2 hydrogenation activity at 300 °C. This experiment shows that the deactivation of the 10CoWI catalyst in CO_2 hydrogenation can be reversed by oxidation of the coke deposits. Despite this, we observe that the stability of the 10CoWi catalyst improved after each regeneration, whilst the activity and product distribution remained unchanged. It has been suggested that roughening of the Co surface and subsequent changing of morphology during reaction-regeneration cycles may result in the formation of more active/defect sites within the same Co particle.[39,40] Consecutive reduction-oxidation-reduction (ROR) treatments substantially increased the Fischer-

Tropsch activity of Co supported on reducible TiO_2 and Nb_2O_5 by changing the Co–support interactions rather than redispersion of Co.[104] In line with this, it was observed that CO chemisorption of 10CoWI upon reduction-oxidation-reduction cycles did not increase, excluding redispersion of Co as an explanation also in this study (**Figure B26**).

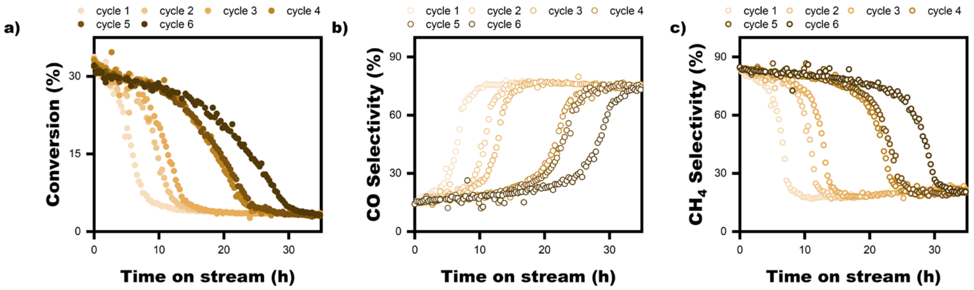

Figure 3.12. CO_2 conversion (a), CO (b), and CH_4 (c) selectivity as a function of time on stream for 10CoWI reduced at 300 °C (a-c) (conditions: 300 °C – 50 mg of catalyst, 15 vol.% CO_2, 60 vol.% H_2, 25 vol.% Ar, 50 mL/min, 1 bar).

Deactivation due to CO

The possible role of CO in catalyst deactivation during CO_2 hydrogenation was studied by determining catalyst stability in CO hydrogenation (H_2/CO ratio = 3) at atmospheric pressure and 200 – 300 °C for the CoWI catalysts. CeFSP was inactive during these catalytic tests. The WGS activity of the CoWI samples was negligible, as no CO_2 was detected during the CO methanation reaction. **Figure 3.13** shows that the main reaction products were olefins and oxygenate (86% selectivity), with CH_4 as a minor product (14 – 20% selectivity). This starkly contrasts the predominance of CO and CH_4 formed during CO_2 hydrogenation, with only a small amount of paraffins with two or more C atoms (**Figure 3.8**). The CO conversion of all catalysts at 200 – 300 °C increased with the Co loading (**Figure B27**). The highest conversion was reached at 275 °C (**Figure B27**). In general, all catalysts showed a lower activity in CO hydrogenation than in CO_2 hydrogenation. **Figure 3.8** shows reaction rates (rCO) normalized to the Co loading and determined at 250 °C under differential conditions. The highest r_{CO} was observed for the 5CoWI catalyst (8.1 ± 0.5 $mmol_{CO}/mol_{Co}/s$) (**Figure 3.8**). The r_{CO} decreased with increasing Co loading. As mentioned above, reporting turnover frequencies based on the number of metallic Co sites using H_2 and CO chemisorption data is not reasonable.

Despite the substantial difference in product distribution, the deactivation curves demonstrated a similar trend for CO and CO_2 hydrogenation (**Figure 3.13 and 3.8**). Deactivation in CO hydrogenation occurred much faster (~3 h) than in CO_2 hydrogenation (~10 h). The 2.5CoWI catalyst was slightly more resistant to deactivation in CO hydrogenation (**Figure 3.13c**). These results suggest that Co clusters (2.5CoWI) are less susceptible to deactivation than Co nanoparticles (5CoWI and 10CoWI).

Deactivation of the catalysts in CO hydrogenation was accompanied by an increase in CH_4 selectivity and a significant decrease in olefins and oxygenates products selectivity (**Figure B28**). The selectivity towards C_2H_4 and C_3H_6 hydrocarbons declined more gradually and plateaued at ~9% and ~15%, respectively. A decrease in the overall CO conversion rate and a lower rate of C-C coupling is expected, when Co step-edge sites are poisoned , where CO dissociation occurs.[88] Consequently, C hydrogenation on less reactive facets becomes more significant, shifting the product distribution towards CH_4.

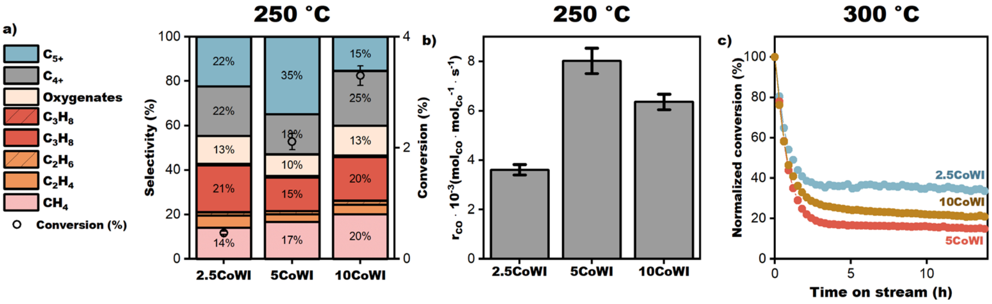

Figure 3.13. (a) Catalytic performance of CoWI catalysts reduced at 300 °C: CO conversion and product distribution at a reaction temperature 250 °C. (b) CO reaction rate at 250 °C, normalized to the total Co loading (conditions: 250 °C, 50 mg of sample, 19.6 vol.% CO, 56.2 vol.% H_2, 25 vol.% Ar, 50 mL/min). (c) Normalized CO conversion as a function of time on stream for CoWI catalysts, reduced at 300 °C (conditions: 1 bar, 50 mg of sample, 18.8 vol.% CO, 56.2 vol.% H_2, 25 vol.% Ar, 50 mL/min).

At high reaction temperatures, a higher CO conversion facilitates the formation of coke, as C hydrogenation cannot keep up with C formation.[42,105] To distinguish the type of carbon deposits (e.g., graphitic, aliphatic, or aromatic) formed during the reaction, thermogravimetric analysis coupled with mass spectrometry (TGA-MS) was used to study the used samples (**Figures B29-30**). Significant mass losses occurred above 200 °C for all CoWI catalysts. The combustion temperature derived from DTG shows a maximum of 275 – 300 °C, similar to the one observed after deactivation in CO_2. The amount of carbon deposits increases with the Co loading. The highest amount of deposits (13%) was obtained with 5CoWI. Together with C deposition on the surface, metallic Co particles may also transform into Co-carbide, e.g., Co2C, under particular conditions, also causing catalyst deactivation.[106] Several studies demonstrates that CoC_2 formation goes together with a high selectivity toward lower olefins and oxygenates.[107,108] Ex-situ synchrotron XRD of the catalysts used in CO hydrogenation did not show evidence for the formation of Co-carbide phases (**Figure B31**). Moreover, the XRD data did not point to significant sintering of the Co nanoparticles.

Therefore, the results show the deactivation of CoWI catalysts in CO_2 and CO hydrogenation is caused by the formation of carbon deposits. The formation of such carbon deposits at step-edge sites of Co nanoparticles has been mentioned.[89,106,109] To further study the impact of CO on the activity and stability of 10CoWI in CO_2 hydrogenation, reaction experiments were carried out with a mixture of CO and CO_2 and H_2 (H_2/(CO+CO_2) ratio = 4) at 300 °C (**Figure B30**). The initial conversion was highest (33%) when the feed was free from CO. Adding 3.6 vol.% CO to 11.4 vol.% CO_2 and 60 vol.% H_2 in Ar feed led to a decrease of the CO_2 conversion to 27%. The lowest initial conversion (4%) was found in CO hydrogenation (18.8 vol.% CO, 56.2 vol.% H_2, 25 vol.% Ar). Deactivation of the catalysts in CO hydrogenation and mixture of CO and CO_2 is much faster (3 h) than in CO_2 hydrogenation (10 h). The conversion stabilized at approximately 5% after deactivation when the feed did not contain CO. The initial rapid deactivation in mixtures of CO and CO_2 led to higher selectivity to C_{2+} hydrocarbons at the expense of the CH_4 selectivity during the first hour on stream, similar to reaction carried out with only CO in the feed (**Figure B32-33**). After 1 h on stream, the CH_4 selectivity increased at the expense of the C_{2+} selectivity, which was also noted during CO hydrogenation. Instead, during CO_2 hydrogenation, deactivation was accompanied by an increase in the CO selectivity at the expense of the CH_4 selectivity (**Figure B33**). These results suggest that the active Co sites for CO dissociation are blocked by carbon deposition during deactivation originating from CO. While active centers for rWGS seems rather stable during CO_2 hydrogenation which is likely due to the formation of very small Co nanoparticles (< 2 nm).[35] However, we cannot exclude that the highly dispersed Co – O – Ce species also contribute to CO formation.[18,95,110]

Conclusions

A series of catalysts with varying Co loading (2.5 – 10 mol.%) were evaluated in CO_2 and CO methanation at atmospheric pressure. FSP preparation of CeO_2 resulted in small CeO_2 nanoparticles of ~8 nm with a higher surface area than conventional CeO_2. Impregnated and calcination led to Co/CeO_2 samples comprised of small CeO_2 nanoparticles (10 nm), highly dispersed Co, and, with increasing Co content, segregated Co-oxide particles. A relatively large fraction of Co in 2.5CoWI is present as Co^{2+} ions in strong interaction with CeO_2 and they cannot be reduced at 300 °C. The amount of such stable highly dispersed Co^{2+} species is nearly the same in all Co/CeO_2 catalysts, i.e., ~2.5 mol.%. Catalysts containing 5 mol.% and 10 mol.% Co contain segregated Co_3O_4 nanoparticles of ~2 nm and ~2.5 nm. These particles are partially reduced to metallic Co nanoparticles of 2.5 nm (5 mol.% Co) and 3 nm (10 mol.% Co) upon reduction at 300 °C. The highest Co-weight-normalized activity in CO_2 hydrogenation of 3.1 ± 0.2 $mmol_{CO2}/mol_{Co}/s$ was observed for the 2.5CoWI catalyst at 250 °C. The low Co reduction degree of this sample and the presence of very small metal Co clusters led to predominant formation of CO (78%) in addition to CH_4 (21%). Catalysts containing more and larger Co nanoparticles mainly yield CH_4, small amounts of CO and C_2H_6. CO hydrogenation on these samples mostly yielded olefins and oxygenate products (86% selectivity) with a relatively low amount of CH_4. The highest Co-weight-normalized activity in CO hydrogenation at 250 °C of 8.1 ± 0.5 $mmol_{CO}/mol_{Co}/s$ was obtained for the 5CoWI sample. Despite the differences in product selectivity, all Co/CeO_2 catalysts deactivated under CO and CO_2 hydrogenation conditions. Characterization shows that catalyst deactivation is caused by deposition of carbon from CO dissociation, which occurs most easily on nanometer-sized Co particles. CO hydrogenation results in faster deactivation than CO_2 hydrogenation. Catalyst regeneration in 20 vol.% O_2 in He fully restores and even improves the performance of Co/CeO_2 catalysts in CO_2 hydrogenation.

References

1. Guo, L., Guo, X., He, Y. & Tsubaki, N. CO_2 heterogeneous hydrogenation to carbon-based fuels: recent key developments and perspectives. J Mater Chem A Mater 11, 11637–11669 (2023).

2. Ashok, J. et al. A review of recent catalyst advances in CO_2 methanation processes. Catal Today 356, 471–489 (2020).

3. Kondratenko, E. V., Mul, G., Baltrusaitis, J., Larrazábal, G. O. & Pérez-Ramírez, J. Status and perspectives of CO_2 conversion into fuels and chemicals by catalytic, photocatalytic and electrocatalytic processes. Energy Environ Sci 6, 3112–3135 (2013).

4. Ren, J. et al. Methanation of CO/CO_2 for power to methane process: Fundamentals, status, and perspectives. Journal of Energy Chemistry 80, 182–206 (2023).

5. Rönsch, S. et al. Review on methanation – From fundamentals to current projects. Fuel 166, 276–296 (2016).

6. Wang, W., Wang, S., Ma, X. & Gong, J. Recent advances in catalytic hydrogenation of carbon dioxide. Chem Soc Rev 40, 3703–3727 (2011).

7. Zhang, Z. et al. Advances in studies of the structural effects of supported Ni catalysts for CO_2 hydrogenation: from nanoparticle to single atom catalyst. J Mater Chem A Mater 10, 5792–5812 (2022).

8. Suppiah, D. D., Daud, W. M. A. W. & Johan, M. R. Supported metal oxide catalysts for CO_2 Fischer−Tropsch conversion to liquid fuels - A review. Energy and Fuels 35, 17261–17278 (2021).

9. Diehl, F. & Khodakov, A. Y. Promotion of Cobalt Fischer-Tropsch catalysts with noble metals: A review. Oil and Gas Science and Technology 64, 11–24 (2009).

10. Suo, Y., Yao, Y., Zhang, Y., Xing, S. & Yuan, Z. Y. Recent advances in cobalt-based Fischer-Tropsch synthesis catalysts. Journal of Industrial and Engineering Chemistry 115, 92–119 (2022).

11. Mehrabi, M., Ashjari, M. & Meshkani, F. Cobalt supported on silica–alumina nanocomposite for use in CO_2 methanation process: effects of Si/Al molar ratio and Co loading on catalytic activity. Research on Chemical Intermediates 50, 219–238 (2024).

12. Ilsemann, J. et al. Cobalt@Silica Core-Shell Catalysts for Hydrogenation of CO/CO_2 Mixtures to Methane. ChemCatChem 11, 4884–4893 (2019).

13. Schubert, M. et al. Highly active Co–Al_2O_3 -based catalysts for CO_2 methanation with very low platinum promotion prepared by double flame spray pyrolysis. Catal Sci Technol 6, 7449–7460 (2016).

14. Zhou, G. et al. CO_2 hydrogenation to methane over mesoporous Co/SiO_2 catalysts: Effect of structure. Journal of CO_2 Utilization 26, 221–229 (2018).

15. Iablokov, V. et al. Size-controlled model Co nanoparticle catalysts for CO_2 hydrogenation: Synthesis, characterization, and catalytic reactions. Nano Lett 12, 3091–3096 (2012).

16. Zhou, G. et al. CO_2 hydrogenation to methane over mesoporous Co/SiO_2 catalysts: Effect of structure. Journal of CO_2 Utilization 26, 221–229 (2018).

17. Ho, S. W. Effects of ethanol impregnation on the properties of thoria-promoted Co/SiO_2 catalyst. J Catal 175, 139–151 (1998).

18. Oh, R. et al. Insights into CeO_2 Particle Size Dependent Selectivity Control for CO_2 Hydrogenation Using Co/CeO_2 Catalysts. ACS Catal 897–906 (2024)

19. Deng, K. et al. Studies of CO_2 hydrogenation over cobalt/ceria catalysts with in situ characterization: the effect of cobalt loading and metal–support interactions on the catalytic activity. Catal Sci Technol 10, 6468–6482 (2020).

20. Díez-Ramírez, J. et al. Effect of support nature on the cobalt-catalyzed CO_2 hydrogenation. Journal of CO_2 Utilization 21, 562–571 (2017).

21. Das, T. & Deo, G. Effects of metal loading and support for supported cobalt catalyst. Catal Today 198, 116–124 (2012).

22. Wang, M. et al. Unraveling the tunable selectivity on cobalt oxide and metallic cobalt sites for CO_2 hydrogenation. Chemical Engineering Journal 446, (2022).

23. Zou, X. et al. Boosting CO_2 methanation on ceria supported transition metal catalysts via chelation coupled wetness impregnation. J Colloid Interface Sci 620, 77–85 (2022).

24. Scarfiello, C. et al. Modified Co/TiO_2 catalysts for CO_2 hydrogenation to fuels. J Catal 428, 115202 (2023).

25. Bertella, F., Concepción, P. & Martínez, A. TiO_2 polymorph dependent SMSI effect in Co-Ru/TiO_2 catalysts and its relevance to Fischer-Tropsch synthesis. Catal Today 289, 181–191 (2017).

26. Liu, S. et al. Hetero-site cobalt catalysts for higher alcohols synthesis by CO_2 hydrogenation: A review. Journal of CO_2 Utilization 67, 102322 (2023).

27. Scarfiello, C., Pham Minh, D., Soulantica, K. & Serp, P. Oxide Supported Cobalt Catalysts for CO_2 Hydrogenation to Hydrocarbons: Recent Progress. Adv Mater Interfaces 10, 2202516 (2023).

28. Le, T. A., Kim, M. S., Lee, S. H. & Park, E. D. CO and CO_2 Methanation Over Supported Cobalt Catalysts. Top Catal 60, 714–720 (2017).

29. Hussain, I. et al. A review of the indispensable role of oxygen vacancies for enhanced CO_2 methanation activity over CeO_2-based catalysts: Uncovering, influencing, and tuning strategies. Int J Hydrogen Energy 48, 24663–24696 (2023).

30. Boaro, M., Colussi, S. & Trovarelli, A. Ceria-based materials in hydrogenation and reforming reactions for CO_2 valorization. Front Chem 7, 426236 (2019).

31. Parastaev, A. et al. Boosting CO_2 hydrogenation via size-dependent metal–support interactions in cobalt/ceria-based catalysts. Nat Catal 3, 526–533 (2020).

32. Kattel, S. et al. CO_2 Hydrogenation over Oxide-Supported PtCo Catalysts: The Role of the Oxide Support in Determining the Product Selectivity. Angewandte Chemie International Edition 55, 7968–7973 (2016).

33. Xu, S., Xie, F., Xie, H., Zhou, G. & Liu, X. Effect of structure and composition

on the CO_2 hydrogenation properties over bimodal mesoporous CeCo composite catalyst. Chemical Engineering Journal 375, 122023 (2019).

34. Have, I. C. ten et al. Uncovering the reaction mechanism behind CoO as active phase for CO_2 hydrogenation. Nature Communications 2022 13:1 13, 1–11 (2022).

35. Zhou, X., Price, G. A., Sunley, G. J. & Copéret, C. Small Cobalt Nanoparticles Favor Reverse Water-Gas Shift Reaction Over Methanation Under CO_2 Hydrogenation Conditions. Angewandte Chemie - International Edition 62, (2023).

36. Li, B. et al. CeO_2-supported Fe, Co and Ni toward CO_2 hydrogenation: Tuning catalytic performance via metal-support interaction. Journal of Rare Earths 41, 926–932 (2023).

37. Fu, X. P. et al. Boosting reactivity of water-gas shift reaction by synergistic function over CeO_2-x/CoO_{1-x}/Co dual interfacial structures. Nature Communications 2023 14:1 14, 1–11 (2023).

38. Parastaev, A. et al. Breaking structure sensitivity in CO_2 hydrogenation by tuning metal–oxide interfaces in supported cobalt nanoparticles. Nat Catal 5, 1051–1060 (2022).

39. Klingenberg, B. et al. Structural aspects of activation and deactivation of cobalt catalysts in hydrogenation of carbon dioxide. Stud Surf Sci Catal 101, 961–969 (1996).

40. Fröhlich, G. et al. Activation and deactivation of cobalt catalysts in the hydrogenation of carbon dioxide. Appl Catal A Gen 134, 1–19 (1996).

41. Lojewska, J. & Dziembaj, R. Deactivation of cobalt hydrogenation catalyst induced by carbonaceous deposits. A model and its experimental verification. Stud Surf Sci Catal 126, 121–128 (1999).

42. van Koppen, L. M., Iulian Dugulan, A., Leendert Bezemer, G. & Hensen, E. J. M. Elucidating deactivation of titania-supported cobalt Fischer-Tropsch catalysts under simulated high conversion conditions. J Catal 420, 44–57 (2023).t

43. Khangale, P. R., Meijboom, R. & Kalala Jalama, ·. Catalyst Deactivation Rate During Hydrogenation of CO_2 to Longer-Chained Hydrocarbons Over 6 wt.% Potassium-Promoted Co/Al_2O_3 Catalyst. Catal Letters 151, 3396–3403 (1234).

44. Van Berge, P. J., Van De Loosdrecht, J., Barradas, S. & Van Der Kraan, A. M. Oxidation of cobalt based Fischer-Tropsch catalysts as a deactivation mechanism. Catal Today 58, 321–334 (2000).

45. Tsakoumis, N. E., Rønning, M., Borg, Ø., Rytter, E. & Holmen, A. Deactivation of cobalt based Fischer–Tropsch catalysts: A review. Catal Today 154, 162–182 (2010).

46. Shen L., Xu J., Zhu M., Han Y.F. Essential role of the support for nickel-based CO_2 methanation catalysts, ACS Catal. 10, (2020).

47. Wolf, M., Kotzé, H., Fischer, N. & Claeys, M. Size dependent stability of cobalt nanoparticles on silica under high conversion Fischer–Tropsch environment. Faraday Discuss 197, 243–268 (2017).

48. Bezemer, G. L. et al. Cobalt particle size effects in the Fischer-Tropsch reaction

studied with carbon nanofiber supported catalysts. J Am Chem Soc 128, 3956–3964 (2006).

49. Den Breejen, J. P. et al. On the origin of the cobalt particle size effects in Fischer-Tropsch catalysis. J Am Chem Soc 131, 7197–7203 (2009).

50. Van Steen, E. et al. Stability of nanocrystals: Thermodynamic analysis of oxidation and re-reduction of cobalt in water/hydrogen mixtures. Journal of Physical Chemistry B 109, 3575–3577 (2005).

51. Juhás, P., Davis, T., Farrow, C. L. & Billinge, S. J. L. PDFgetX3: a rapid and highly automatable program for processing powder diffraction data into total scattering pair distribution functions. urn:issn:0021-8898 46, 560–566 (2013).

52. Farrow, C. L. et al. PDFfit2 and PDFgui: computer programs for studying nanostructure in crystals. Journal of Physics: Condensed Matter 19, 335219 (2007).

53. Stadnichenko, A. I. et al. Study of active surface centers of Pt/CeO_2 catalysts prepared using radio-frequency plasma sputtering technique. Surf Sci 679, 273–283 (2019).

54. Larachi, F., Pierre, J., Adnot, A. & Bernis, A. Ce 3d XPS study of composite $Ce_xMn_{1-x}O_{2-y}$ wet oxidation catalysts. Appl Surf Sci 195, 236–250 (2002).

55. Kato, S. et al. Quantitative depth profiling of Ce^{3+} in Pt/CeO_2 by in situ high-energy XPS in a hydrogen atmosphere. Physical Chemistry Chemical Physics 17, 5078–5083 (2015).

56. Skála, T., Šutara, F., Prince, K. C. & Matolín, V. Cerium oxide stoichiometry alteration via Sn deposition: Influence of temperature. J Electron Spectros Relat Phenomena 169, 20–25 (2009).

57. Yang, Z. et al. Effect of Co substitution and magnetic field on the morphologies and magnetic properties of CeO_2 nanoparticles. Ceram Int 45, 11927–11933 (2019).

58. Abbas, F. et al. Differential cytotoxicity of ferromagnetic Co doped CeO_2 nanoparticles against human neuroblastoma cancer cells. J Alloys Compd 648, 1060–1066 (2015).

59. Hagfeldt, A. & Grätzel, M. Light-Induced Redox Reactions in Nanocrystalline Systems. Chem Rev 95, 49–68 (1995).

60. Wu, T. S. et al. Dramatic band gap reduction incurred by dopant coordination rearrangement in Co-doped nanocrystals of CeO_2. Scientific Reports 2017 7:1 7, 1–7 (2017).

61. Khodakov, A. Y., Chu, W. & Fongarland, P. Advances in the development of novel cobalt Fischer-Tropsch catalysts for synthesis of long-chain hydrocarbons and clean fuels. Chem Rev 107, 1692–1744 (2007).

62. Cabrera-German, D., Gomez-Sosa, G. & Herrera-Gomez, A. Accurate peak fitting and subsequent quantitative composition analysis of the spectrum of Co 2p obtained with Al Kα radiation: I: cobalt spinel. Surface and Interface Analysis 48, 252–256 (2016).

63. Lykhach, Y. et al. Quantitative Analysis of the Oxidation State of Cobalt Oxides by Resonant Photoemission Spectroscopy. Journal of Physical Chemistry Letters 10,

6129–6136 (2019).

64. Binet, C., Badri, A., Boutonnet-Kizling, M. & Lavalley, J. C. FTIR study of carbon monoxide adsorption on ceria: CO_{2-2} carbonite dianion adsorbed species. Journal of the Chemical Society, Faraday Transactions 90, 1023–1028 (1994).

65. Wu, W., Savereide, L. M., Notestein, J. & Weitz, E. In-situ IR spectroscopy as a probe of oxidation/reduction of Ce in nanostructured CeO_2. Appl Surf Sci 445, 548–554 (2018).

66. Binet, C., Daturi, M. & Lavalley, J. C. IR study of polycrystalline ceria properties in oxidized and reduced states. Catal Today 50, 207–225 (1999).

67. Busca, G., Guidetti, R. & Lorenzelli, V. Fourier-transform Infrared Study of the Surface Properties of Cobalt Oxides. 86, 989–994 (1990).

68. Ferstl, P. et al. Adsorption and Activation of CO on Co_3O_4(111) Thin Films. Journal of Physical Chemistry C 119, 16688–16699 (2015).

69. Ocampo, F., Louis, B. & Roger, A. C. Methanation of carbon dioxide over nickel-based $Ce_{0.72}Zr_{0.28}O_2$ mixed oxide catalysts prepared by sol–gel method. Appl Catal A Gen 369, 90–96 (2009).

70. Karaca, H. et al. In situ XRD investigation of the evolution of alumina -supported cobalt catalysts under realistic conditions of Fischer-Tropsch synthesis. Chemical Communications 46, 788–790 (2010).

71. Castner, D. G., Watson, P. R. & Chan, I. Y. (A). X-ray Absorption Spectroscopy, X-ray Photoelectron Spectroscopy, and Analytical Electron Microscopy Studies of Cobalt Catalysts. 2. Hydrogen Reduction Properties. J. Phys. Chem 94, 819–828 (1990).

72. Khodakov, A. Y., Griboval-Constant, A., Bechara, R. & Villain, F. Pore-size control of cobalt dispersion and reducibility in mesoporous silicas. Journal of Physical Chemistry B 105, 9805–9811 (2001).

73. Zhang, F. et al. In Situ Elucidation of the Active State of Co-CeO_x Catalysts in the Dry Reforming of Methane: The Important Role of the Reducible Oxide Support and Interactions with Cobalt. ACS Catal 8, 3550–3560 (2018).

74. Luo, J. Y. et al. Mesoporous Co_3O_4–CeO_2 and Pd/Co_3O_4–CeO_2 catalysts: Synthesis, characterization and mechanistic study of their catalytic properties for low-temperature CO oxidation. J Catal 254, 310–324 (2008).

75. Carvalho, F. L. S., Asencios, Y. J. O., Bellido, J. D. A. & Assaf, E. M. Bio-ethanol steam reforming for hydrogen production over Co_3O_4/CeO_2 catalysts synthesized by one-step polymerization method. Fuel Processing Technology 142, 182–191 (2016).

76. Chen, S. et al. Probing surface structures of CeO_2, TiO_2, and Cu_2O nanocrystals with CO and CO_2 chemisorption. Journal of Physical Chemistry C 120, 21472–21485 (2016).

77. Yang, Z., He, B., Lu, Z. & Hermansson, K. Physisorbed, chemisorbed, and oxidized CO on highly active Cu-CeO_2(111). Journal of Physical Chemistry C 114, 4486–4494 (2010).

78. Bridge, M. E., Comrie, C. M. & Lambert, R. M. Hydrogen chemisorption and the carbon monoxide-hydrogen interaction on cobalt (0001). J Catal 58, 28–33 (1979).

79. Weststrate, C. J., van de Loosdrecht, J. & Niemantsverdriet, J. W. Spectroscopic insights into cobalt-catalyzed Fischer-Tropsch synthesis: A review of the carbon monoxide interaction with single crystalline surfaces of cobalt. J Catal 342, 1–16 (2016).

80. Yang, J., Frøseth, V., Chen, D. & Holmen, A. Particle size effect for cobalt Fischer–Tropsch catalysts based on in situ CO chemisorption. Surf Sci 648, 67–73 (2016).

81. Zhang, S. et al. Boosting selective hydrogenation through hydrogen spillover on supported-metal catalysts at room temperature. Appl Catal B 297, 120418 (2021).

82. Ghogia, A. C. et al. Hydrogen Spillover in the Fischer-Tropsch Synthesis on Carbon-supported Cobalt Catalysts. ChemCatChem 12, 1117–1128 (2020).

83. Marrocchelli, D., Bishop, S. R., Tuller, H. L. & Yildiz, B. Understanding Chemical Expansion in Non-Stoichiometric Oxides: Ceria and Zirconia Case Studies. Adv Funct Mater 22, 1958–1965 (2012).

84. Coduri, M., Scavini, M., Allieta, M., Brunelli, M. & Ferrero, C. Defect structure of Y-doped ceria on different length scales. Chemistry of Materials 25, 4278–4289 (2013).

85. Pakharukova, V. P. et al. Investigation of the Structure and Interface Features of Ni/$Ce_{1-x}Zr_xO_2$ Catalysts for CO and CO_2 Methanation. Journal of Physical Chemistry C 125, 20538–20550 (2021).

86. Weststrate, C. J., van de Loosdrecht, J. & Niemantsverdriet, J. W. Spectroscopic insights into cobalt-catalyzed Fischer-Tropsch synthesis: A review of the carbon monoxide interaction with single crystalline surfaces of cobalt. J Catal 342, 1–16 (2016).

87. Matsubu, J. C., Yang, V. N. & Christopher, P. Isolated metal active site concentration and stability control catalytic CO_2 reduction selectivity. J Am Chem Soc 137, 3076–3084 (2015).

88. Chen, W., Zijlstra, B., Filot, I. A. W., Pestman, R. & Hensen, E. J. M. Mechanism of Carbon Monoxide Dissociation on a Cobalt Fischer–Tropsch Catalyst. ChemCatChem 10, 136–140 (2018).

89. Zijlstra, B. et al. Coverage Effects in CO Dissociation on Metallic Cobalt Nanoparticles. ACS Catal 9, 7365–7372 (2019).

90. Daturi, M., Binet, C., Lavalley, J. C. & Blanchard, G. Surface FTIR investigations on $Ce_xZr_{1-x}O_2$ system. Surf. Interface Anal 30, 273–277 (2000).

91. Van Helden, P., Ciobîcə, I. M. & Coetzer, R. L. J. The size-dependent site composition of FCC cobalt nanocrystals. Catal Today 261, 48–59 (2016).

92. Kattel, S., Liu, P. & Chen, J. G. Tuning Selectivity of CO_2 Hydrogenation Reactions at the Metal/Oxide Interface. J Am Chem Soc 139, 9739–9754 (2017).

93. Li, S. et al. Tuning the Selectivity of Catalytic Carbon Dioxide Hydrogenation over Iridium/Cerium Oxide Catalysts with a Strong Metal–Support Interaction.

Angewandte Chemie International Edition 56, 10761–10765 (2017).

94. Bezemer, G. L. et al. Cobalt particle size effects in the Fischer-Tropsch reaction studied with carbon nanofiber supported catalysts. J Am Chem Soc 128, 3956–3964 (2006).

95. Dostagir, N. H. M. et al. Co Single Atoms in ZrO_2 with Inherent Oxygen Vacancies for Selective Hydrogenation of CO_2 to CO. ACS Catal 11, 9450–9461 (2021).

96. Feron, O., Langlais, F. & Naslain, R. In-situ analysis of gas phase decomposition and kinetic study during carbon deposition from mixtures of carbon tetrachloride and methane. Carbon N Y 37, 1355–1361 (1999).

97. Wu, Z., Li, M., Howe, J., Meyer, H. M. & Overbury, S. H. Probing defect sites on CeO_2 nanocrystals with well-defined surface planes by raman spectroscopy and O_2 adsorption. Langmuir 26, 16595–16606 (2010).

98. Xu, Y. et al. Resolving a Decade-Long Question of Oxygen Defects in Raman Spectra of Ceria-Based Catalysts at Atomic Level. Journal of Physical Chemistry C 123, 18889–18894 (2019).

99. Tang, C. W., Wang, C. Bin & Chien, S. H. Characterization of cobalt oxides studied by FT-IR, Raman, TPR and TG-MS. Thermochim Acta 473, 68–73 (2008).

100. Robertson, J. Diamond-like amorphous carbon. Materials Science and Engineering: R: Reports 37, 129–281 (2002).

101. Souza, N. et al. Upcycling spent petroleum cracking catalyst: pulsed laser deposition of single-wall carbon nanotubes and silica nanowires. RSC Adv 6, 72596–72606 (2016).

102. Vogt, E. T. C., Fu, D. & Weckhuysen, B. M. Carbon Deposit Analysis in Catalyst Deactivation, Regeneration, and Rejuvenation. Angewandte Chemie International Edition 62, e202300319 (2023).

103. Janoš, P. et al. Recovery of Cerium Dioxide from Spent Glass-Polishing Slurry and Its Utilization as a Reactive Sorbent for Fast Degradation of Toxic Organophosphates. Advances in Materials Science and Engineering 2015, 241421 (2015).

104. Hernández Mejía, C., van Deelen, T. W. & de Jong, K. P. Activity enhancement of cobalt catalysts by tuning metal-support interactions. Nature Communications 2018 9:1 9, 1–8 (2018).

105. Niemelä, M. K. & Krause, A. O. I. The long-term performance of Co/SiO_2 catalysts in CO hydrogenation. Catal Letters 42, 161–166 (1996).

106. Carvalho, A. et al. Elucidation of deactivation phenomena in cobalt catalyst for Fischer-Tropsch synthesis using SSITKA. J Catal 344, 669–679 (2016).

107. Lin, T. et al. Fischer-Tropsch Synthesis to Olefins: Catalytic Performance and Structure Evolution of Co_2C-Based Catalysts under a CO_2 Environment. ACS Catal 9, 9554–9567 (2019).

108. Xiang, Y. & Kruse, N. Tuning the catalytic CO hydrogenation to straight- and long-chain aldehydes/alcohols and olefins/paraffins. Nature Communications 2016 7:1 7, 1–6 (2016).

109. Petersen, M. A., Van Den Berg, J. A., Ciobîcă, I. M. & Van Helden, P. Revisiting CO Activation on Co Catalysts: Impact of Step and Kink Sites from DFT. ACS Catal 7, 1984–1992 (2017).

110. Qiu, N., Zhang, J. & Wu, Z. Peculiar surface-interface properties of nanocrystalline ceria-cobalt oxides with enhanced oxygen storage capacity. Physical Chemistry Chemical Physics 16, 22659–22664 (2014).

Appendix B

Figures.

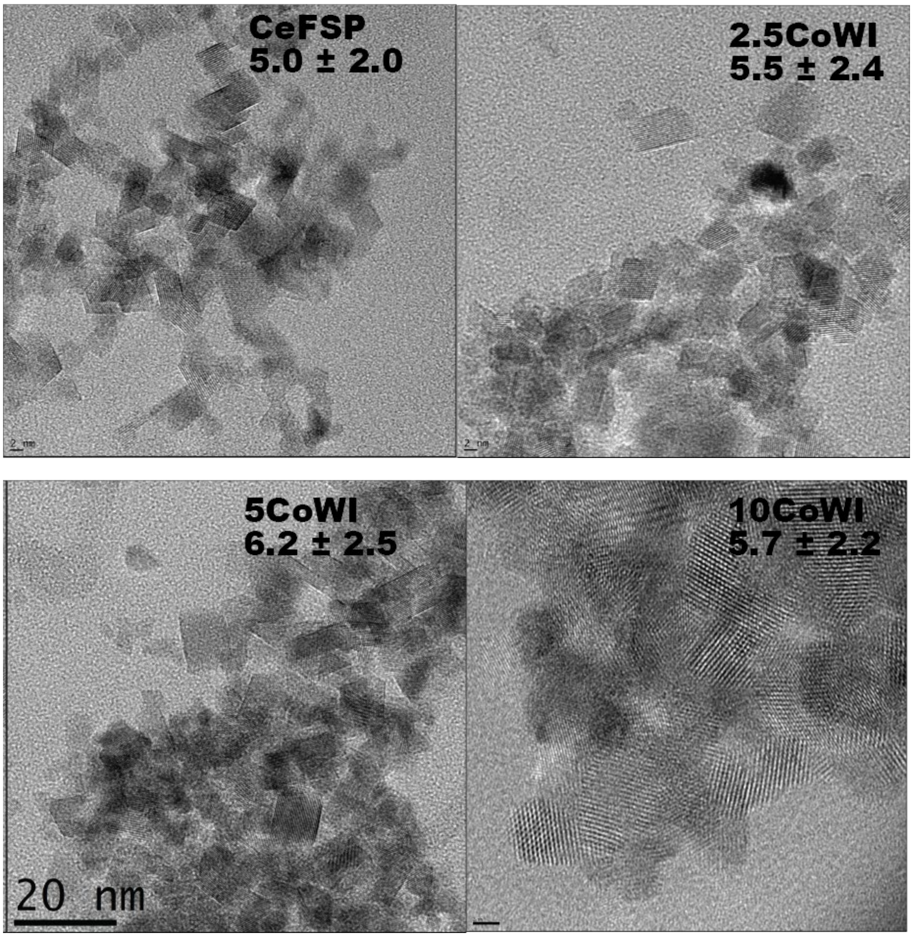

Figure B1.TEM images of as-prepared CeFSP and CoWI catalyst with corresponding particle size estimations.

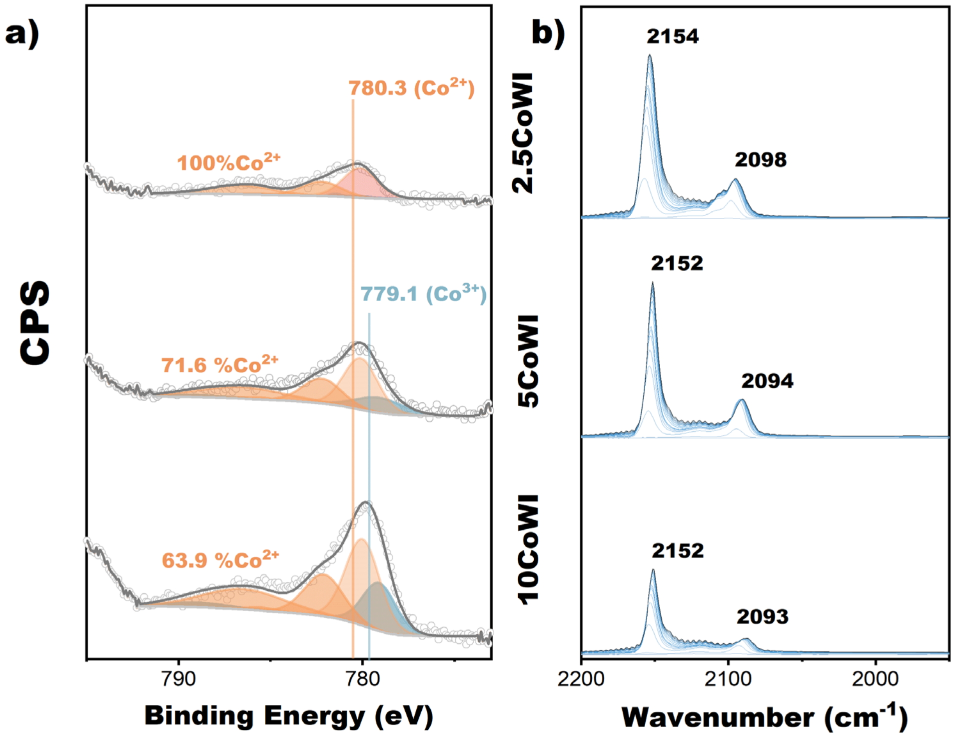

Figure B2. (a) Deconvolution of Co 2p of as-prepared CoWI catalysts. (b) IR spectra of CO adsorbed on as-prepared CoWI at liquid N_2 temperature(T_{ads} = -168 °C with increasing CO partial pressure from light blue to dark blue with a maximum CO partial pressure of 10 mbar).

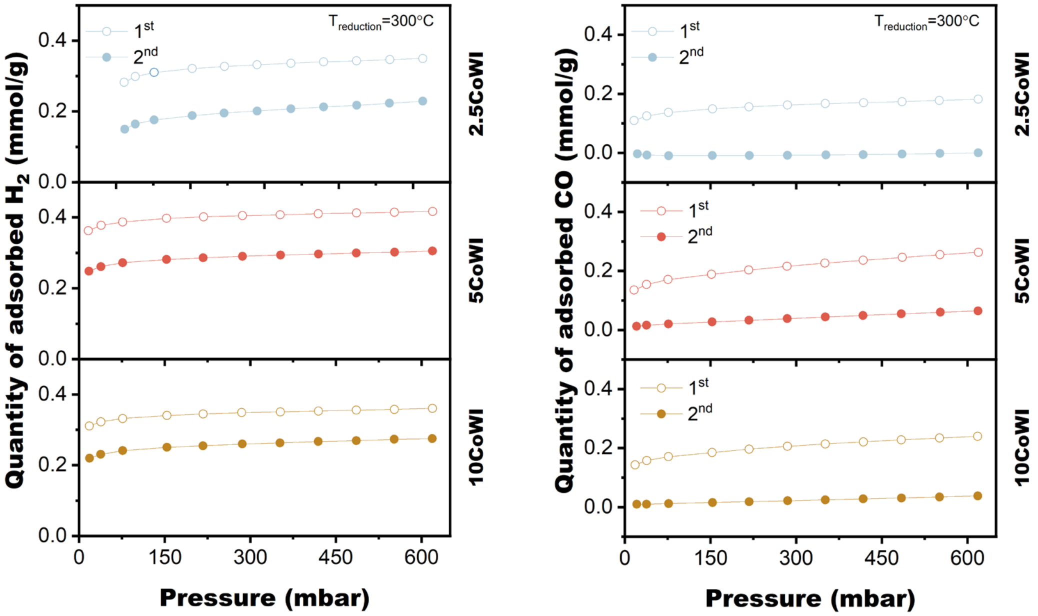

Figure B3. H_2 chemisorption isotherms at 150 °C of CoWI samples reduced at 300 °C (left). CO chemisorption isotherms at 35 °C of CoWI samples reduced at 300 °C (right).

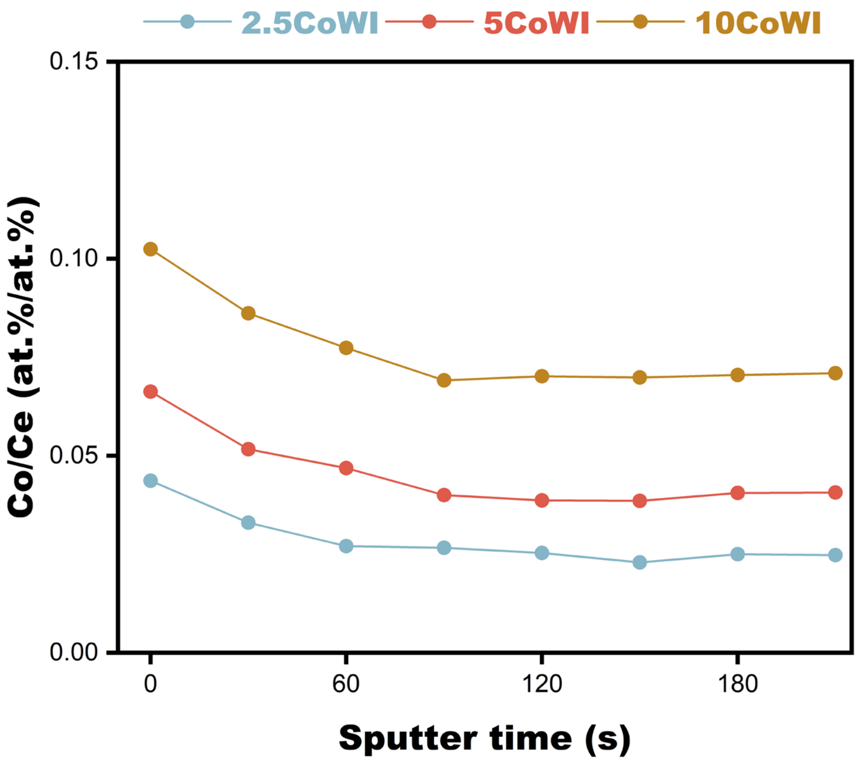

Figure B4. Depth profile of CoWI derived from Co/Ce surface ratios measured by XPS. Catalysts were exposed to 8 iterations of Ar+ sputtering (30 s each) to obtain a depth profile.

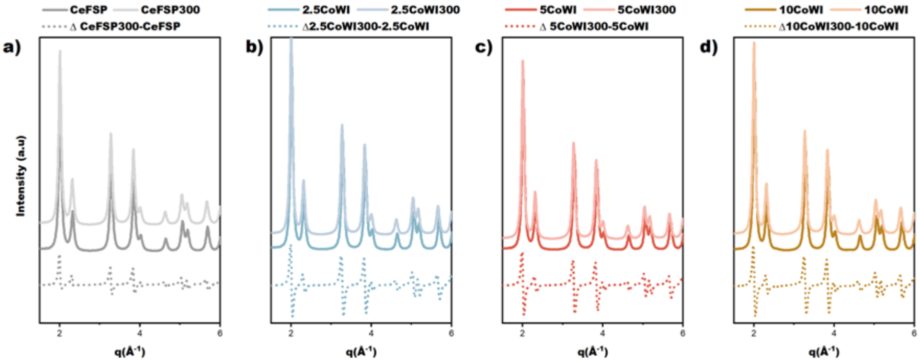

Figure B5. Synchrotron XRD (λ = 0.124 Å) and ΔXRD patterns of CeFSP(a), 2.5CoWI (b), 5CoWI (c) and 10CoWI (d) before and after reductive pretreatment. ΔXRD difference is obtained by subtraction of the diffractogram of as-prepared sample from the reduced diffractogram of the same sample.

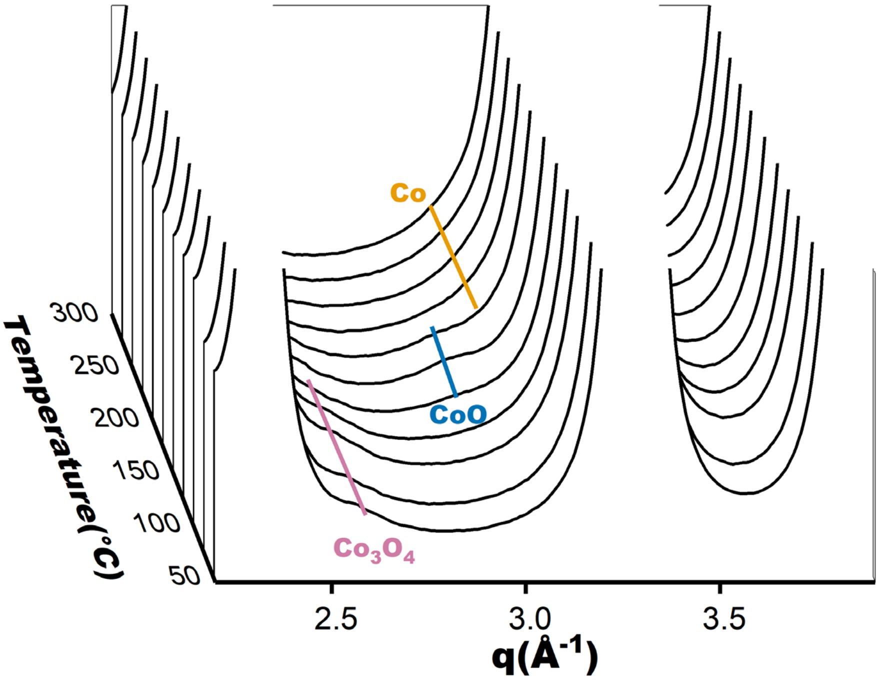

Figure B6. Synchrotron XRD (λ = 0.124 Å) patterns of 10CoWI during reductive pretreatment (conditions: 20% H_2 in Ar, 50 mL/min, 1 bar, 50 – 300 °C).

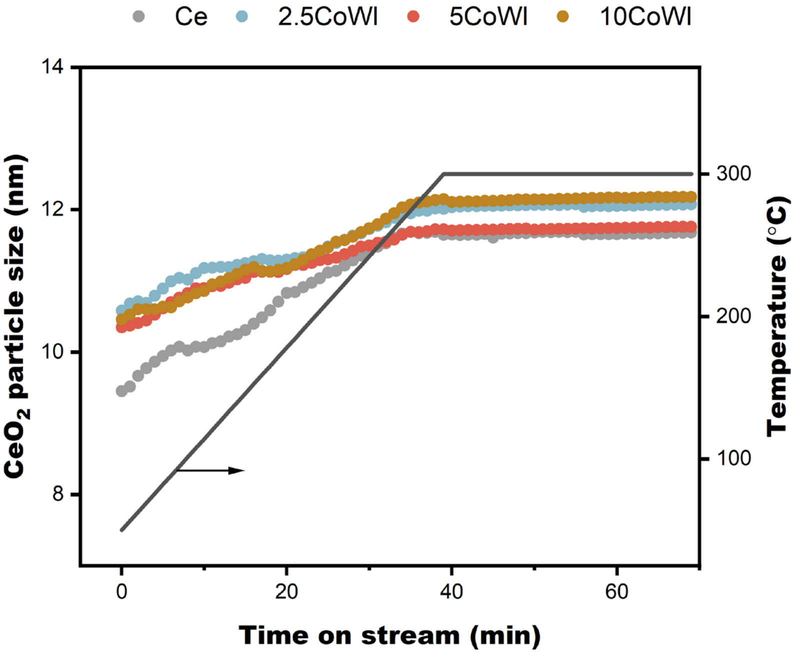

Figure B7. Refined CeO_2 particle size of CeFSP and CoWI during pretreatment (conditions: 20 vol.% H_2 in Ar, 50 mL/min, 50 – 300 °C, 1 bar).

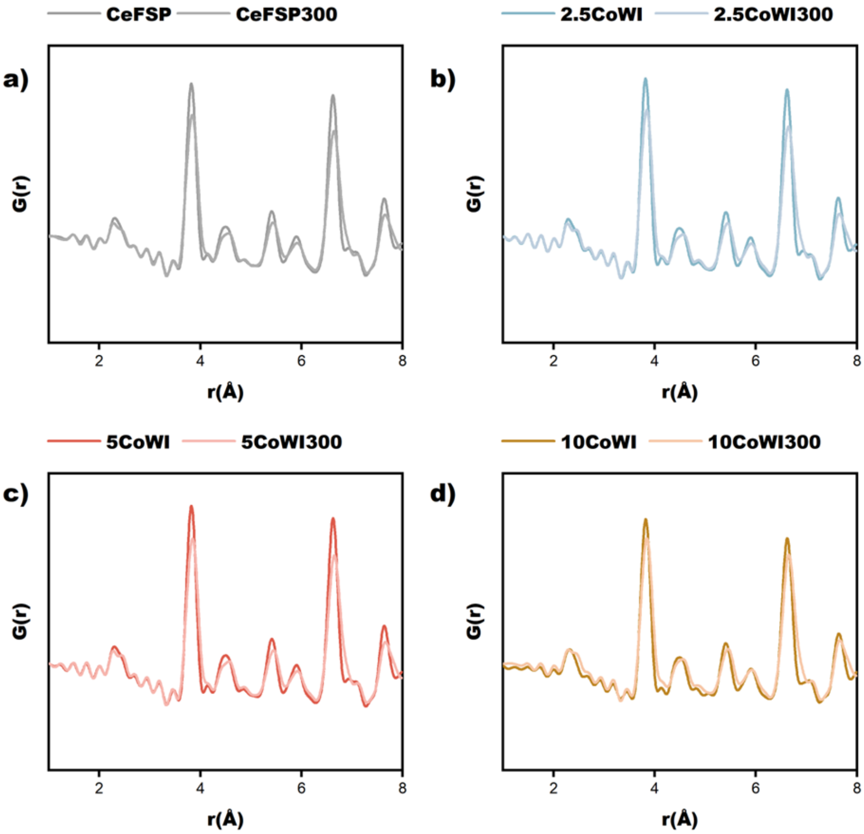

Figure B8. Experimental G(r) of CeFSP(a) and CoWI(c-d) before and after reduction at 300°C (conditions: 20 vol.% H_2 in Ar, 50 mL/min, 1 bar).

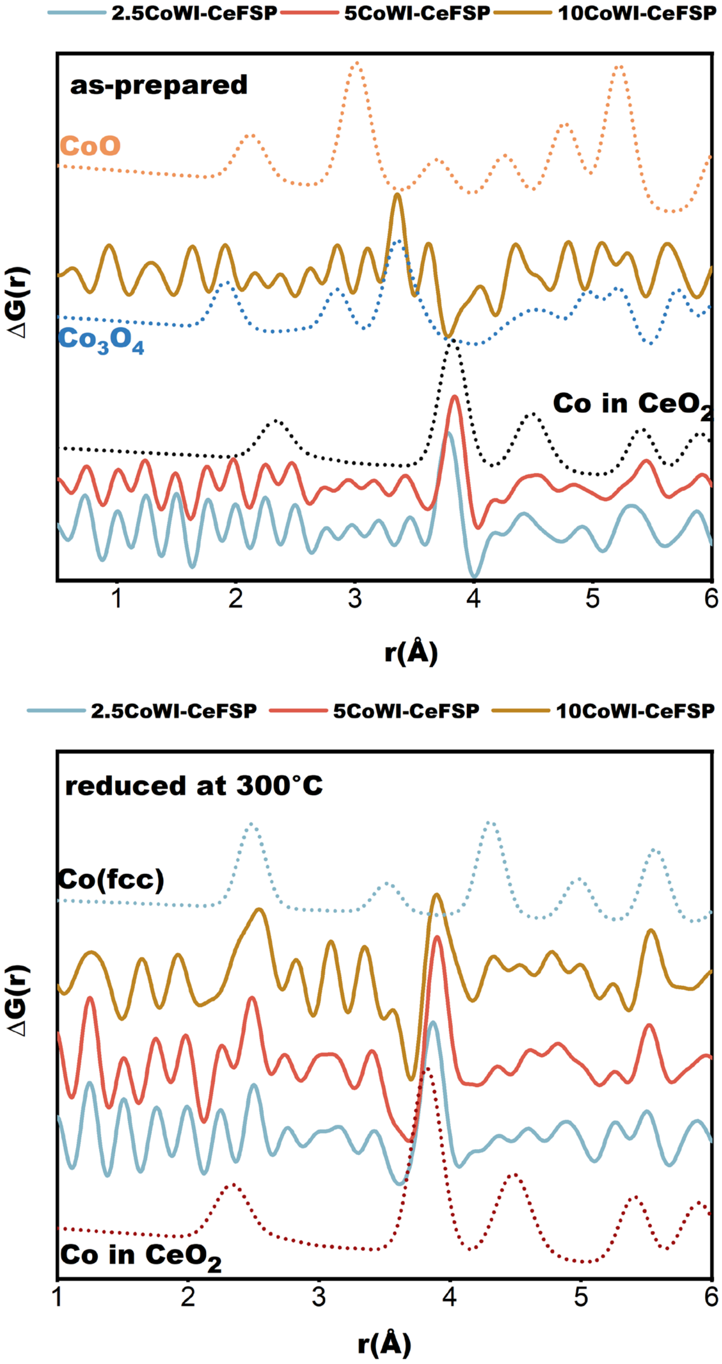

Figure B9. ΔG(r) of CoWI catalysts and calculated G(r)of Co_3O_4, CoO, Co metal and Co incorporated into CeO_2. ΔG(r) is obtained by subtraction of G(r) curve of CeFSP from G(r) curve of CoWI under the same conditions (conditions: 20 vol.% H_2 in Ar, 50 mL/min, 1 bar).

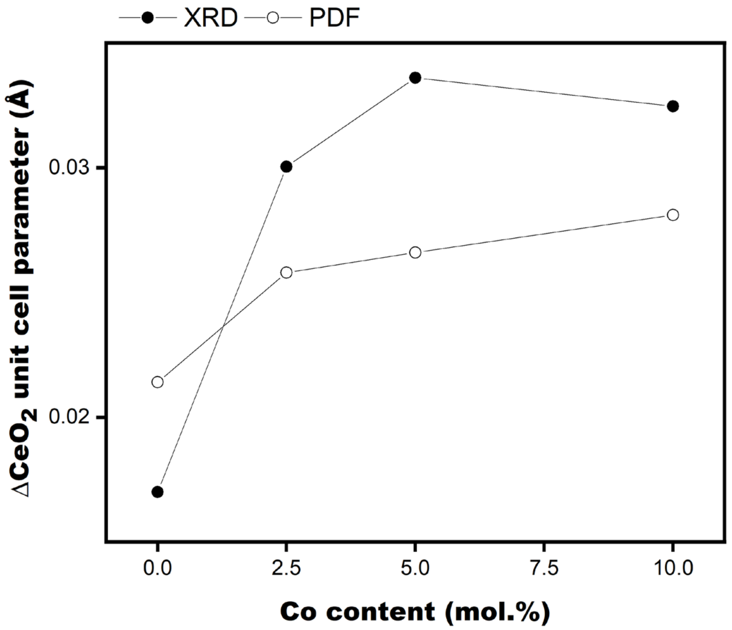

Figure B10. ΔCeO_2 unit cell parameter and Quantity of adsorbed hydrogen from H_2 chemisorption results of CeFSP and CoWI. ΔCeO_2 unit cell parameter was obtained by substruction of CeO_2 unit cell parameter of as-prepared sample from CeO_2 unit cell parameter of the same sample after reduction.

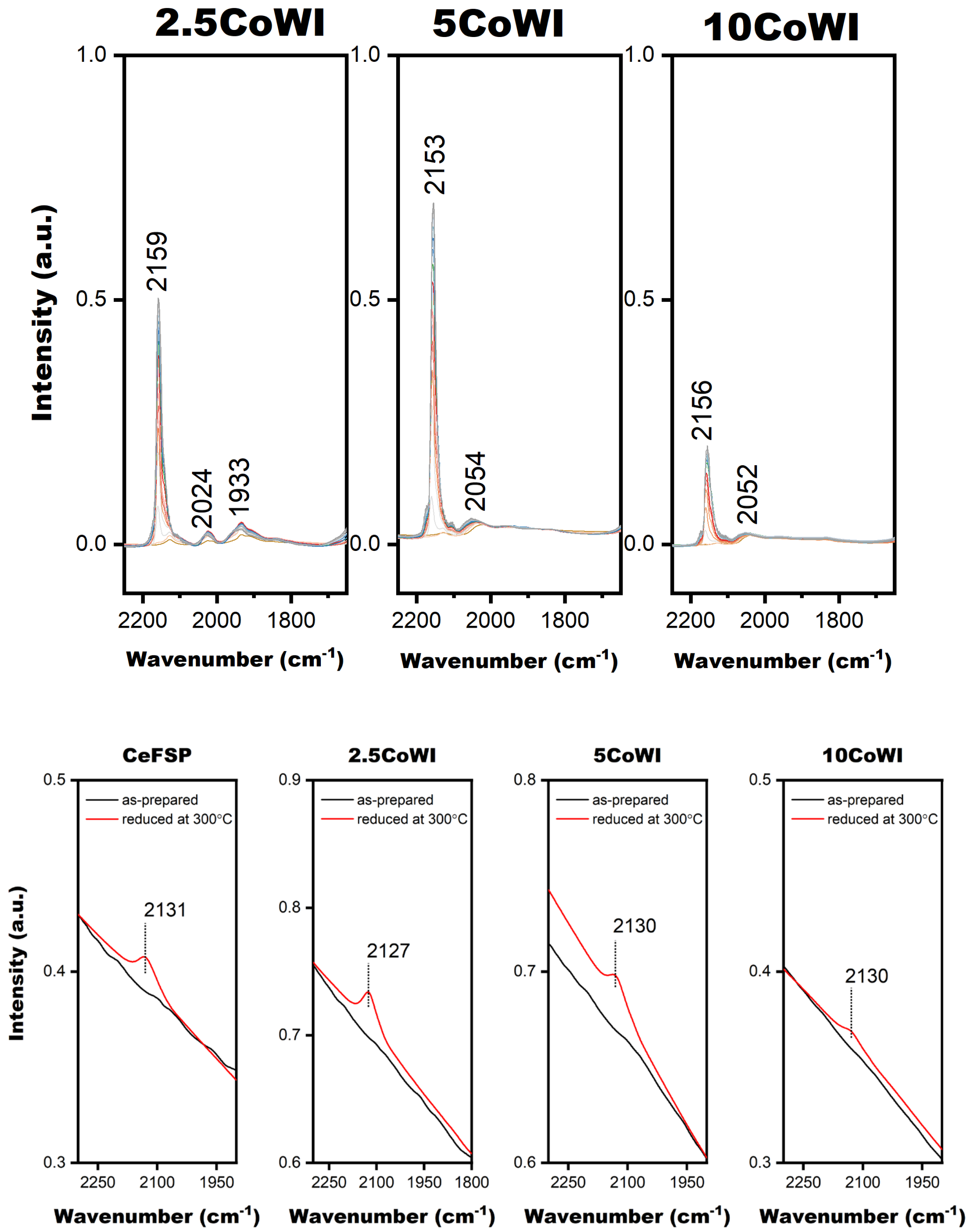

Figure B11. Background subtracted IR spectra of the CoWI reduced at 300 °C after CO adsorption at liquid N_2 temperature (top) (conditions: 1 – 10 mbar CO). IR spectra of the as-prepared CeFSP and CoWI catalysts and CeFSP and CoWI catalyst reduced at 300 °C before CO adsorption at liquid N_2 temperature (bottom).

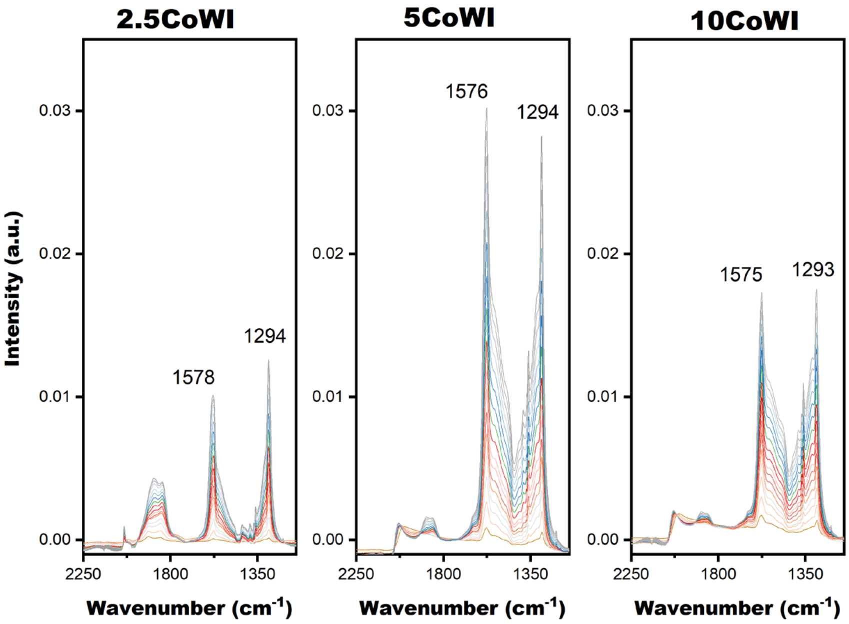

Figure B12 The carbonate region of IR spectra of the CoWI reduced at 300 °C after CO adsorption at 50 °C (conditions: 1 – 10 mbar CO).

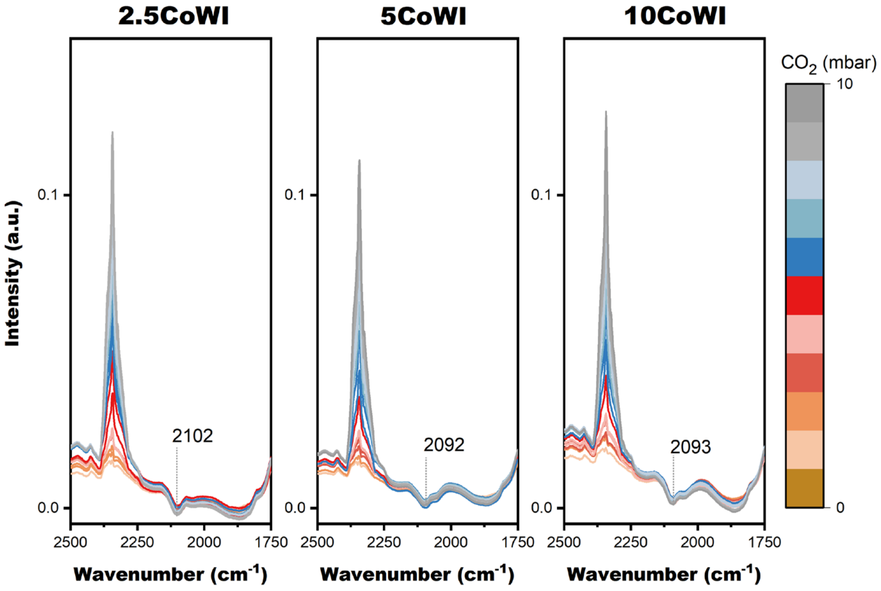

Figure B13. IR spectra of the CoWI reduced at 300 °C after CO_2 adsorption at 50 °C (conditions: 1 – 10 mbar CO_2).

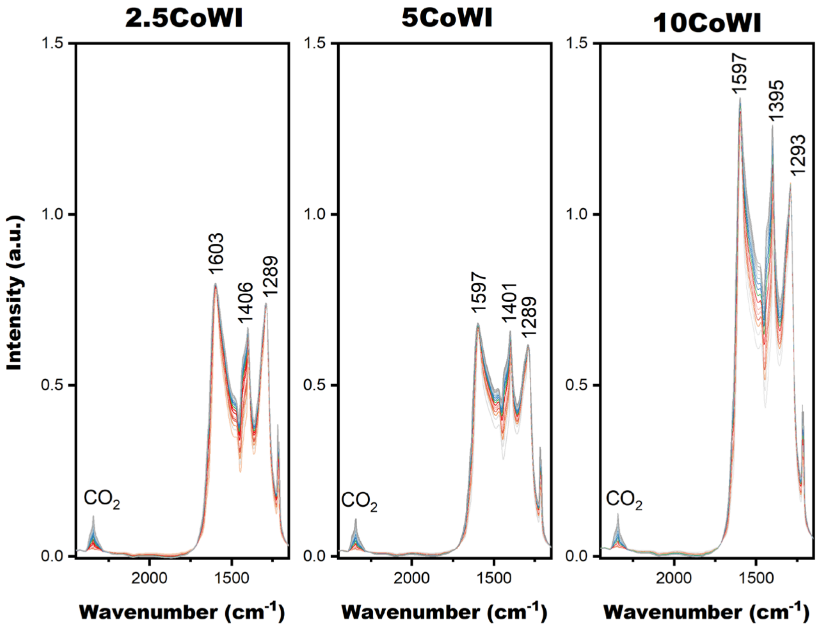

Figure B14.The carbonate region of IR spectra of the CoWI reduced at 300 °C after CO_2 adsorption at 50 °C (conditions: 1 – 10 mbar CO_2).

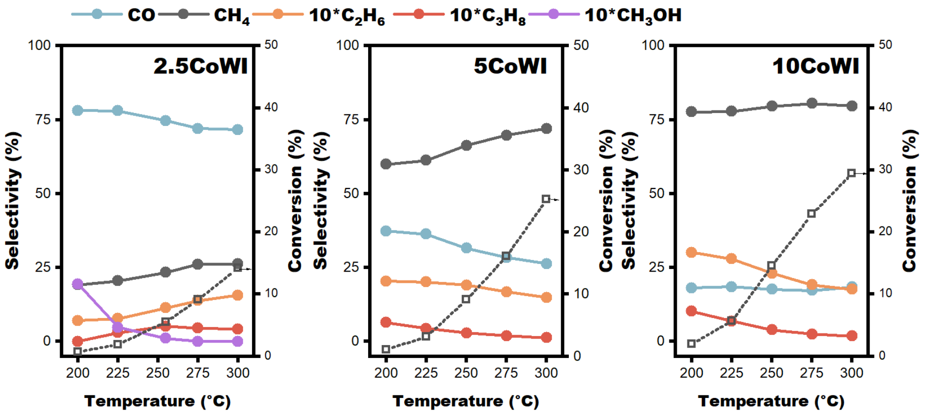

Figure B15. Catalytic performance of CoWI catalysts reduced at 300 °C in CO_2 hydrogenation as a function of temperature (conditions: 200 – 300 °C, 50 mg of catalyst, 15 vol.% CO_2, 60 vol.% H_2, 25 vol.% Ar, 50 mL/min, 1 bar).

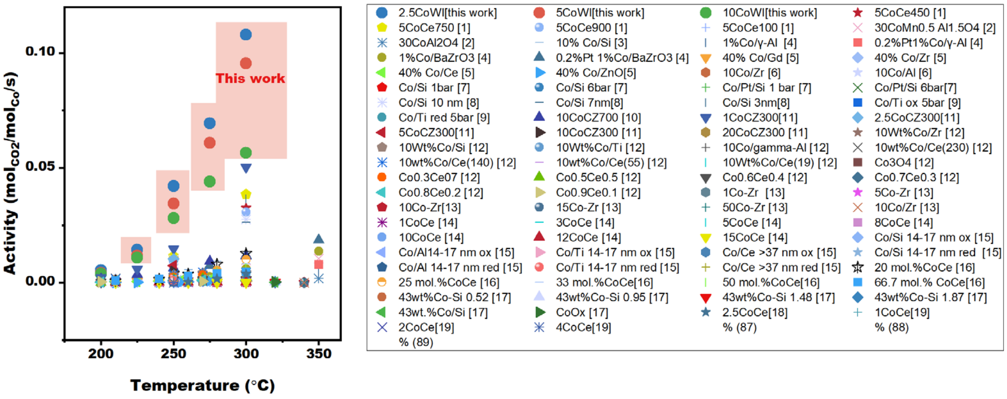

Figure B16. Catalytic activity of CoWI catalysts in comparison to Co-based catalysts reported in literature.

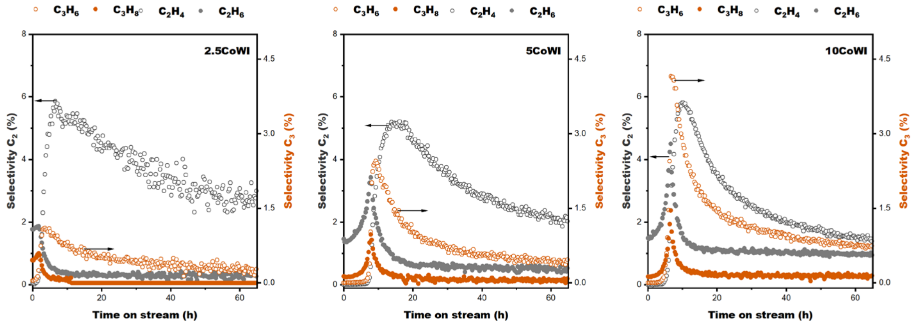

Figure B17. C_2 and C_3 product selectivity as a function of the time on stream of 2.5CoWI, 5CoWI, and 10CoWI reduced at 300 °C (conditions: 300 °C, 50 mg of catalyst, 15 vol.% CO_2, 60 vol.% H_2, 25 vol.% Ar, 50 mL/min, 1 bar, 65 h).

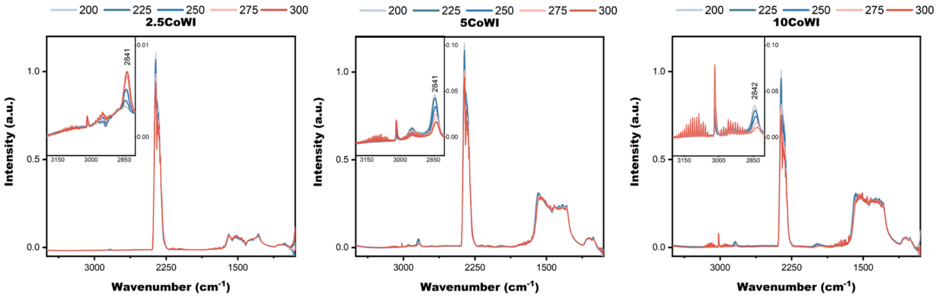

Figure B18. Background-subtracted operando IR spectra in a flow of 4% CO_2, 16% H_2 balanced by N_2 at 200 – 300 °C for 2.5CoWI, 5CoWI, and 10CoWI samples reduced at 300 °C (conditions: 300 °C, 1 bar, 9 mg of sample).

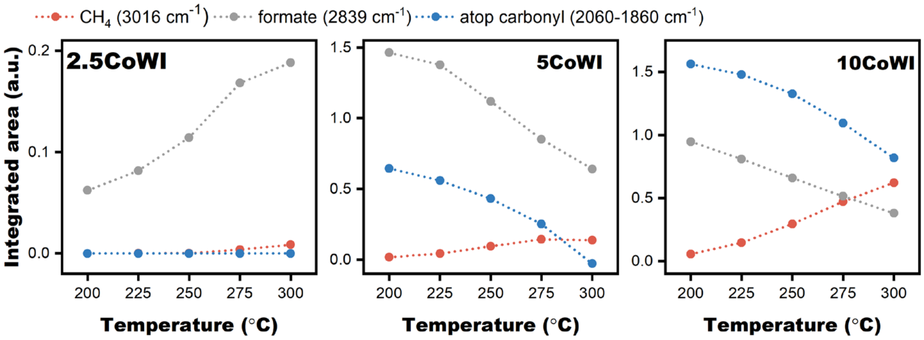

Figure B19. The integrated area of CH_4, formate, and carbonyl bands of CoWI samples reduced at 300 °C as a function of temperature (conditions: 200 – 300°C, 1 bar, 4% CO_2, 16% H_2 balanced by N_2, 9 mg of sample).

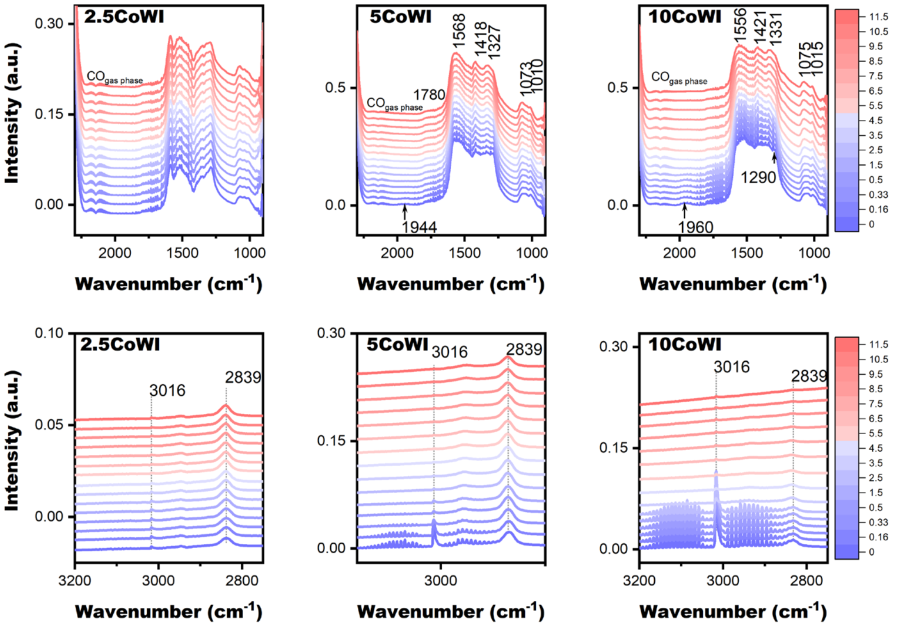

Figure B20. Background-subtracted operando IR spectra in a flow of 4 vol.% CO_2, 16 vol.% H_2 balanced by N_2 at 300 °C for 2.5CoWI, 5CoWI, and 10CoWI samples reduced at 300 °C during 11.5 h on stream: carbonyl/carbonate regions (top) and CH_4 and formate regions (bottom) (conditions: 300 °C, 1 bar, 9 mg of sample).

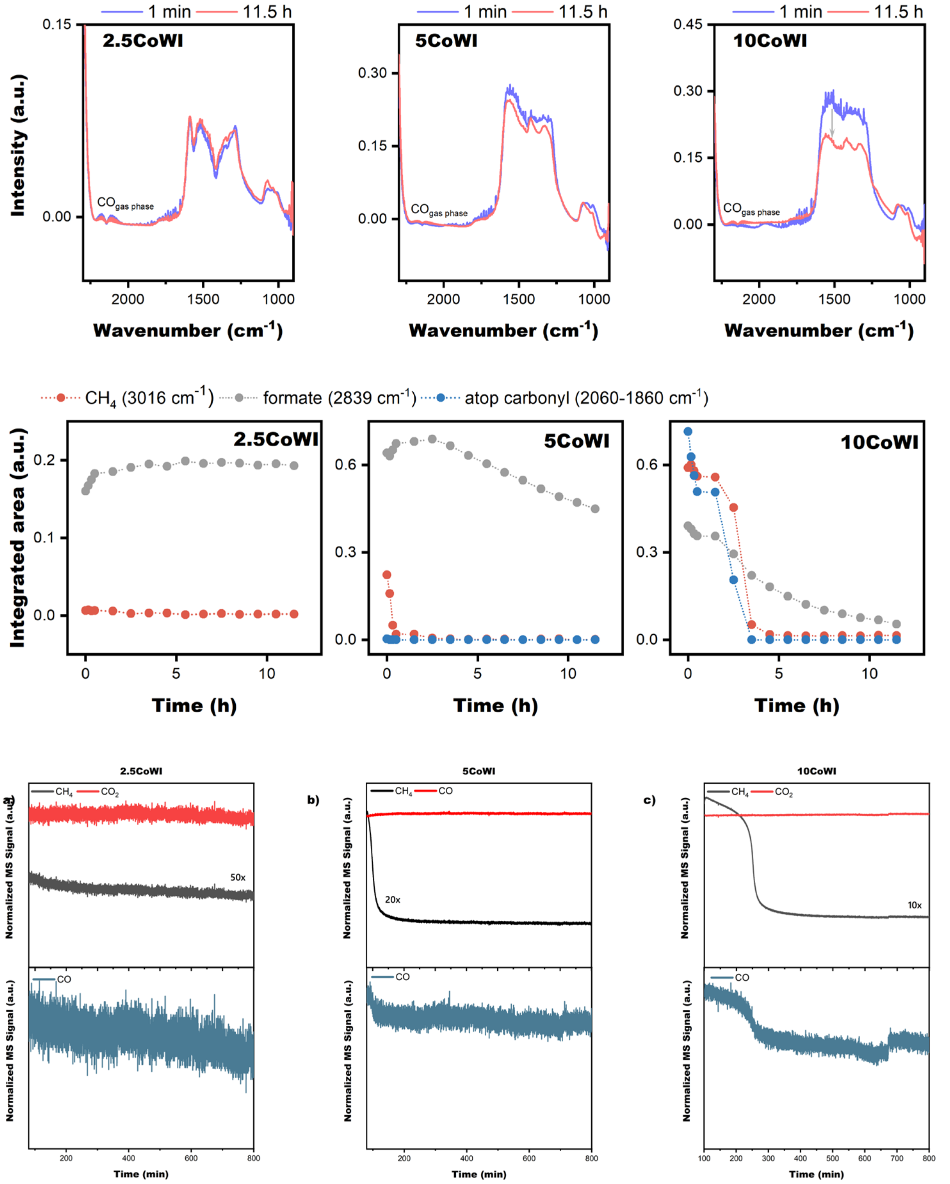

Figure B21. Background-subtracted operando IR spectra in a flow of 4% CO_2, 16% H_2 balanced by N_2 at 300 °C for CoWI samples reduced at 300 °C after 10 min and 11 h on stream (top). The integrated area of CH_4, formate, and carbonyl bands of CoWI samples reduced at 300 °C as a function of time (middle). Normalized MS signal of CO_2 (m/z = 44), CH_4 (m/z = 15), and CO (m/z = 28) during deactivation experiments in IR CoWI samples reduced at 300 °C (bottom) (conditions: 300°C, 1 bar, 4% CO_2, 16% H_2 balanced by N_2).

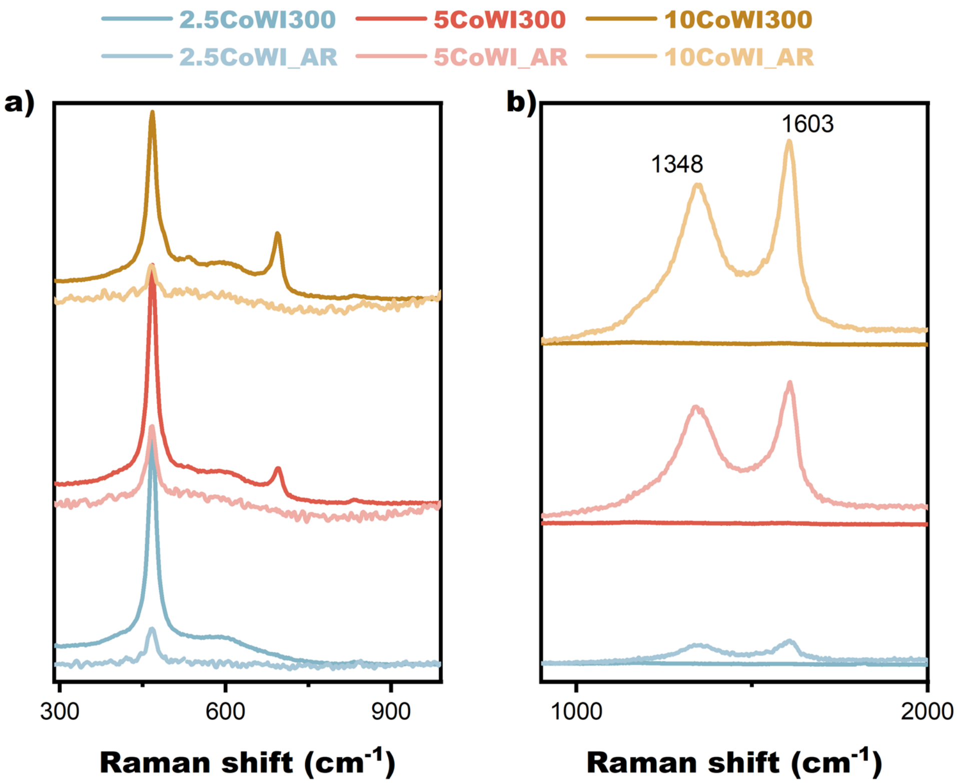

Figure B22. Raman spectra of reduced at 300 °C and spent CoWI catalysts. Deactivated samples were obtained at the following reaction conditions: 300 °C – 50 mg of catalyst, 15 vol.% CO_2, 60 vol.% H_2, 25 vol.% Ar, 50 mL/min, 1 bar, 65 h.

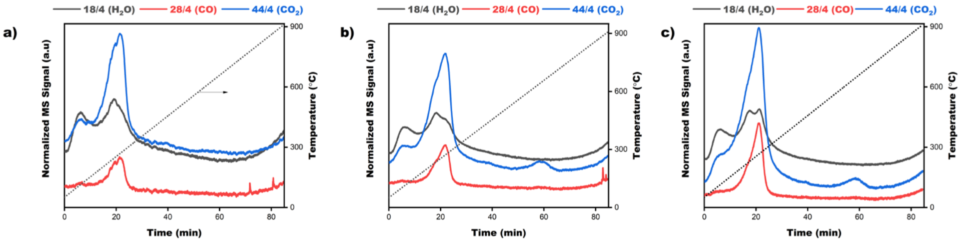

Figure B23. Normalized MS profiles of m/z = 18/4 (H_2O/He), 28/4 (CO/He), 44/4 (CO_2/He) signals were recorded simultaneously with TG profiles in **Figure 3.11 (main text)** (TG analysis conditions: 40 – 900 °C, 25 mg of catalyst, 20 vol.% O_2 in He, 50 mL/min, 10 °C/min).

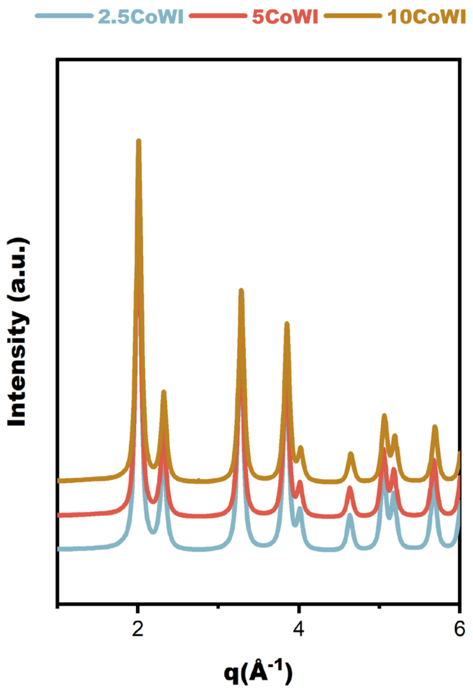

Figure B24. Synchrotron XRD patterns (λ = 0.124 Å) of used CoWI. Deactivated samples were obtained at the following reaction conditions: 300 °C – 50 mg of catalyst, 15 vol.% CO_2, 60 vol.% H_2, 25 vol.% Ar, 50 mL/min, 1 bar, 65 h.

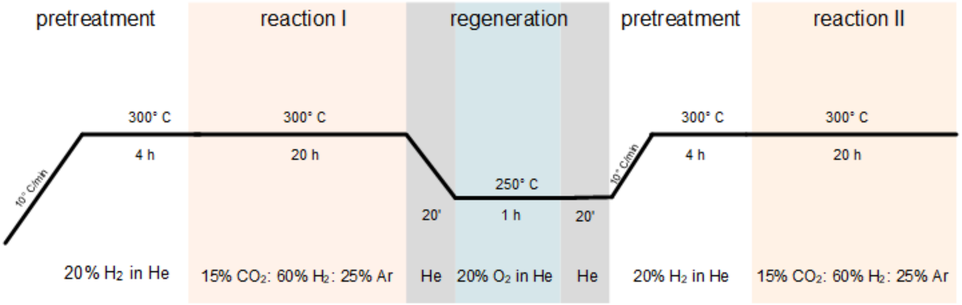

Figure B25. Experimental procedure during regeneration tests (reduction-oxidation-reduction).

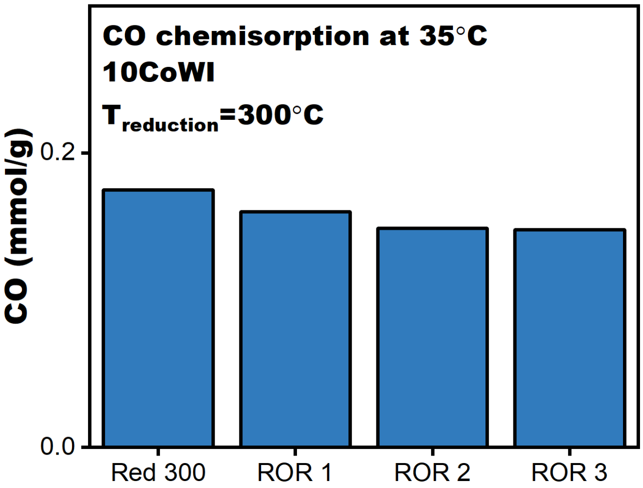

Figure B26. CO chemisorption results at 35 °C of 10CoWI upon reduction-oxidation-reduction (ROR) cycles.

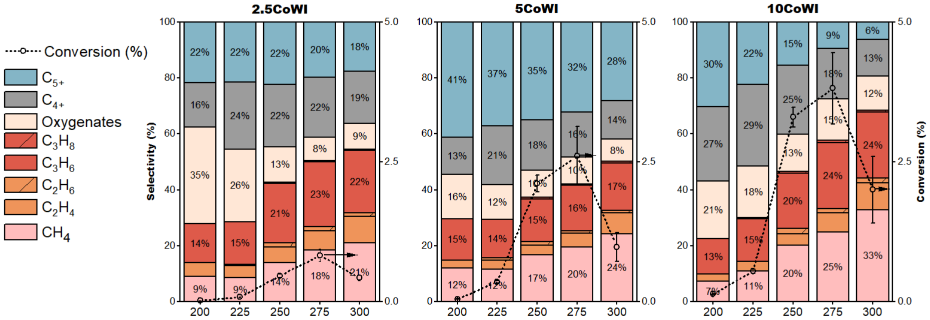

Figure B27. Conversion and product selectivity as a function of the temperature of 2.5CoWI, 5CoWI, and 10CoWI reduced at 300 °C during CO hydrogenation (conditions: 200 – 300 °C, 1 bar, 50 mg of sample, 18.8 vol.% CO, 56.2 vol.% H_2, 25 vol.% Ar, 50 mL/min).

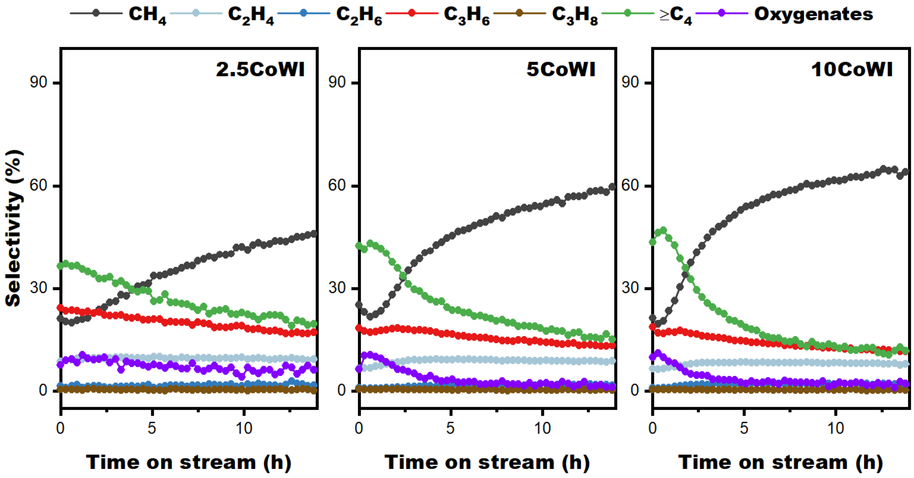

Figure B28. Product selectivity as a function of time of CoWI catalysts, reduced at 300 °C (conditions: 300 °C – 50 mg of catalyst, 18.8 vol.% CO, 56.2 vol.% H_2, 25 vol.% Ar, 50 mL/min, 1 bar, 14 h).

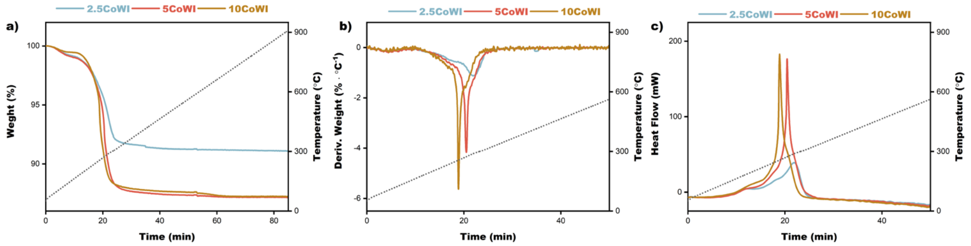

Figure B29. TG (a) and DTG (b) analysis, heat flow (c) of used CoWI catalysts. Deactivated samples were obtained at the following reaction conditions: 300 °C – 50 mg of catalyst, 18.8 vol.% CO, 56.2 vol.% H_2, 25 vol.% Ar, 50 mL/min, 1 bar, 14 h (TG analysis conditions: 40 – 900 °C, 25 mg of catalyst, 20 vol.% O_2 in He, 50 mL/min, 10 °C/min).

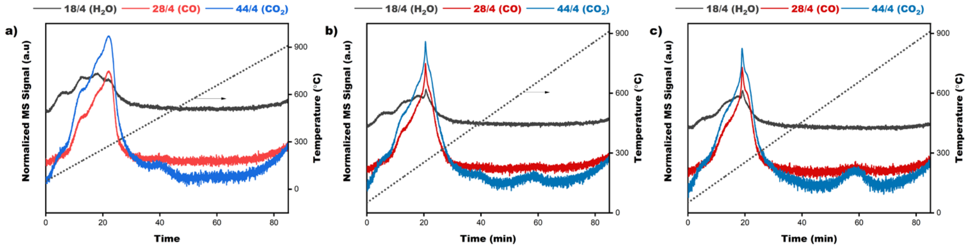

Figure B30. Normalized MS profiles of m/z = 18/4 (H_2O/He), 28/4 (CO/He), 44/4 (CO_2/He) signals recorded simultaneously with TG profiles in Figure B26. TG analysis conditions: 40 – 900 °C, 25 mg of catalyst, 20 vol.% O_2 in He, 50 mL/min, 10 °C/min.

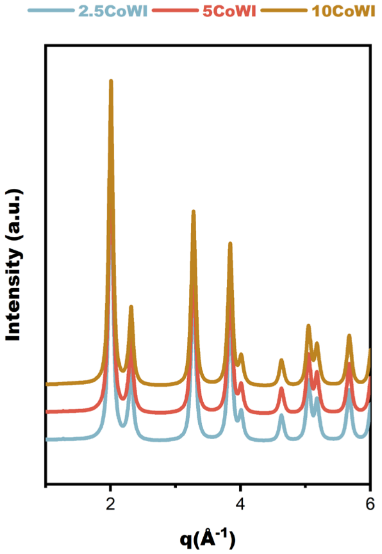

Figure B31. Synchrotron XRD patterns (λ = 0.124 Å) of spent CoWI. Deactivated samples were obtained at the following reaction conditions: 300 °C – 50 mg of catalyst, 18.8 vol.% CO, 56.2 vol.% H_2, 25 vol.% Ar, 50 mL/min, 1 bar, 14 h.

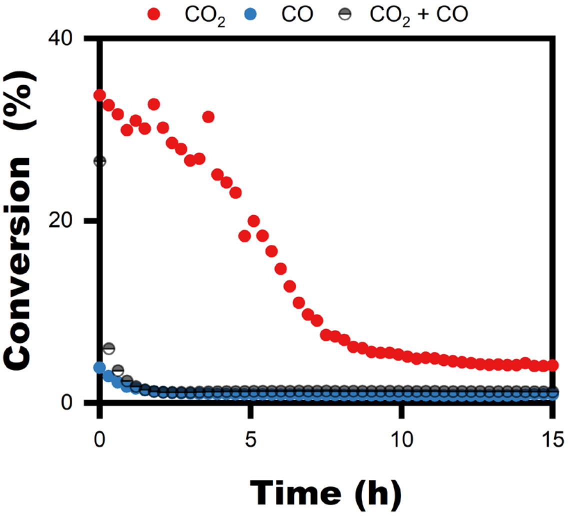

Figure B32. CO_2 (red), CO (blue), CO_2+CO (black) conversions at 300 °C as a function of time on stream for 10CoWI catalyst, reduced at 300°C (conditions CO hydrogenation: 1 bar, 50 mg of sample, 18.8 vol.% CO, 56.2 vol.% H_2, 25 vol.% Ar, 50 mL/min; conditions CO_2 hydrogenation: 300°C, 1 bar, 50 mg of sample, 15 vol.% CO_2, 60 vol.% H_2 , 25 vol.% Ar, 50 mL/min; conditions CO_2+CO hydrogenation: 300°C, 1 bar, 50 mg of sample, 3.6 vol.% CO, 11.4 vol.% CO_2, 60 vol.% H_2, 25 vol.% Ar, 50 mL/min).

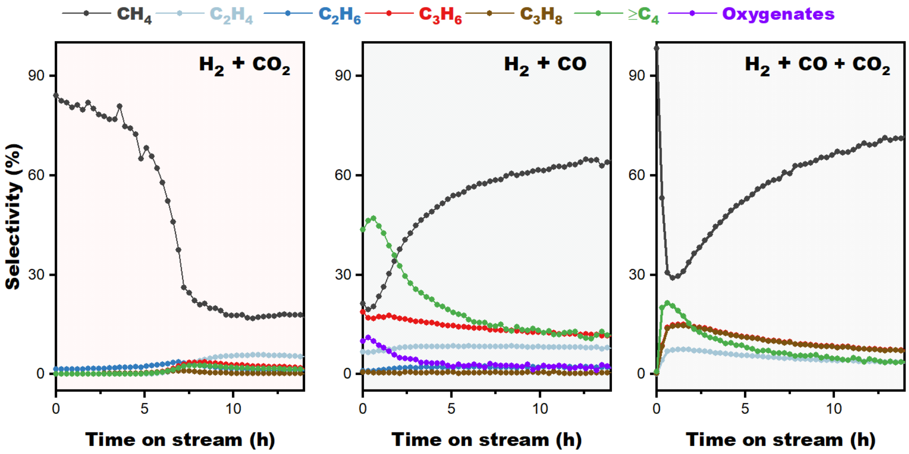

Figure B33. Product selectivity conversions as a function of time on stream for 10CoWI catalyst reduced at 300 °C during CO, CO_2 and (CO_2 + CO) mixture hydrogenation (conditions CO hydrogenation: 1 bar, 50 mg of sample, 18.8 vol.% CO, 56.2 vol.% H_2, 25 vol.% Ar, 50 mL/min; conditions CO_2 hydrogenation: 300°C, 1 bar, 50 mg of sample, 15 vol.% CO_2, 60 vol.% H_2 , 25 vol.% Ar, 50 mL/min; conditions CO_2+CO hydrogenation: 300°C, 1 bar, 50 mg of sample, 3.6 vol.% CO, 11.4 vol.% CO_2, 60 vol.% H_2, 25 vol.% Ar, 50 mL/min).

Tables.

Table B1. The analysis of experimental PDF of as-prepared and reduced at 300 °C CeFSP and CoWI (error margins are reported in brackets).

Sample	Direct analysis			Refined PDF		
	FWHM (A) Gauss function	Position	Area (a.u.)	a(Å)	d_{CeO2} (nm)	Rw
CeFSP	0.113	3.821	2.62665	5.4081 (0.0006)	6.0 (0.3)	0.14
CeFSP300	0.145	3.838	2.73816	5.429 (0.001)	6.8 (0.4)	0.15
2.5CoWI	0.107	3.817	2.61368	5.402 (0.001)	5.3 (0.7)	0.14
2.5CoWI300	0.137	3.834	2.70837	5.423 (0.002)	5.6 (0.7)	0.14
5CoWI	0.109	3.818	2.67597	5.406 (0.001)	5.2 (0.7)	0.14
5CoWI300	0.140	3.842	2.75536	5.435 (0.002)	5.1 (0.7)	0.14
10CoWI	0.107	3.819	2.70749	5.406 (0.001)	4.9 (0.5)	0.14
10CoWI300	0.141	3.843	2.41137	5.436 (0.002)	5.1 (0.7)	0.14

Table B2. Catalytic activity of CoWI catalysts in CO_2 hydrogenation (conditions: 200 – 300 °C, 50 mg of catalyst, 15 vol.% CO_2, 60 vol.% H_2, 25 vol.% Ar, 50 mL/min, 1 bar).

Catalyst	H_2: CO_2	P (bar)	CO_2 initial (%)	T_{react} (°C)	Activity*10^{-3} ($molCO_2$/molCo/s)	Ref. Fig. B16	Ref.
2.5CoWI	4	1	15	200	5.35	This work	This work
				225	14.32		
				250	41.93		
				275	69.36		
				300	107.82		
5CoWI				200	4.06		
				225	11.78		
				250	34.44		
				275	60.87		
				300	95.49		
10CoWI				200	3.81		
				225	10.86		
				250	28.03		
				275	43.94		
				300	56.51		

Chapter 4

Flame-synthesized Ni–CeO_2 Catalysts for CO_2 hydrogenation

Abstract

Catalytic hydrogenation of CO_2 with renewable H_2 to valuable chemicals, such as CO, CH_4, and CH_3OH, is considered an approach to close carbon cycles and mitigate climate change. Herein, we obtained Ni-CeO_2 composite catalyst precursors in a single step by flame spray pyrolysis, aiming at correlating the impact of the strong interactions between Ni and CeO_2 on the structure and performance of reduced catalysts in CO_2 hydrogenation. The high-surface-area flame-synthesized catalysts are made up of small CeO_2 crystallites containing highly dispersed Ni in their lattice and at their surface. Upon reduction, the catalysts contain Ni nanoparticles with a high activity in CO_2 methanation, outperforming most catalyst formulations in literature. The Ni-weight-normalized activity does not vary much with Ni content (~4.4 $\text{mmol}_{CO2}/\text{mol}_{Ni}$/s at 200 °C), but product distribution shifted towards higher CH_4 selectivity with increasing Ni content. The reduced sample with the lowest Ni content of 1 mol.% contains a highly dispersed Ni^{2+} in strong interaction with CeO_2 and very small Ni clusters resulting predominantly in CO formation (CO selectivity 71% at 200 °C). The small amount of CH_3OH among the reaction products at low Ni content is associated with CO_2 hydrogenation on oxygen vacancies assisted by H_2 dissociation on very small Ni clusters. Catalysts containing more and larger Ni nanoparticles mainly yield CH_4, small amounts of CO and no CH_3OH. The high CO_2 methanation activity of FSP-prepared Ni-CeO_2 catalysts is linked to the synergy between relatively small metallic Ni nanoparticles and Ni^{2+}-O-Ce sites, involving oxygen vacancies. We also found that small Ni clusters in 1 mol.% Ni-CeO_2 have a tendency for coke-induced deactivation, while small Ni nanoparticles in 10 mol.%Ni-CeO_2 are stable under reaction conditions and yield mostly CH_4 (CH_4 selectivity of 98% at 300 °C).

Introduction

Fossil fuels are currently the main energy source, leading to the emission of large amounts of carbon dioxide (CO_2) into the atmosphere.[1] Over the past decades, the emission of this greenhouse gas has led to various environmental concerns such as global warming and ocean acidification.[2–4] Catalytic hydrogenation of CO_2 is receiving considerable attention due to its potential to convert CO_2 into valuable chemicals (CO, CH_4, and CH_3OH) or fuels.[5–10] Future scenarios involving capture of CO_2 from the atmosphere and the use of green H_2 from renewable energy sources can close the carbon cycle.

CO_2 methanation, i.e., the Sabatier reaction, is generally considered a structure-sensitive reaction.[11–15] Previous research has shown that the size of transition metal particles in supported metal catalysts significantly affects the catalytic performance due to the presence of different exposed active sites (edge, corner, terrace, and step-edge sites).[16–18] Small clusters and single (metal) atom (SA) catalysts exhibit a high selectivity to CO in CO_2 hydrogenation, owing to the lack of specific ensembles of surface atoms (e.g., step-edge sites) with an electronic structure conducive to facile C-O bond dissociation.[19–22] Typically, supported Ni catalysts are preferred for the Sabatier reaction due to the relatively low cost of Ni and the high selectivity to CH_4.[23–26] Co- and Ru-based catalysts have also been widely investigated due to their high activity at low reaction temperatures below 300 °C, although their application is impeded by their cost.[20,27–30] The exact reaction mechanism and structure-activity relationships for the various supported transition metal catalysts are still debated.

The support can also influence the structure and the chemical state of the catalytically active metal.[31,32] In particular, CeO_2 has attracted attention as a promising support due to strong metal-support interactions resulting in a high dispersion of transition metals[33–35] and its ability to form oxygen vacancies, which can assist in CO_2 activation.[36–38] Ni-CeO_2, in particular, has been considered a promising catalyst in CO_2 hydrogenation.[11,25,39–42] Compared to traditional Ni supported on SiO_2 and Al_2O_2, Ni/CeO_2 offers several advantages, such as high Ni dispersion due to the strong metal-support interactions[11,15], increased CO_2 hydrogenation activity through the formation of specific active sites at the metal-support interface[43,44], which derives from CeO_2's unique redox properties providing oxygen vacancies for CO_2 adsorption and activation.[36–38]

In this work, we used flame spray pyrolysis to prepare a set of Ni-CeO_2 catalysts for CO_2 methanation. It has been shown that flame spray pyrolysis (FSP) yields nanocrystalline CeO_2 with unusual redox properties, beneficial to several important catalytic reactions.[34,45] We introduced Ni in the FSP preparation step of the NiO–CeO_2 catalyst precursors to study the synergy between Ni and CeO_2. We evaluated the catalytic performance in the 200–300 °C range at atmospheric pressure. It was observed that catalysts with a low Ni content resulted in high CO selectivity at low CO_2

conversion. A high Ni content led to high productivity with CH_4 as the dominant product. To establish structure-activity relationships, various techniques, including N_2 physisorption, transmission electron microscopy (TEM), X-ray diffraction (XRD), H_2-TPR, Raman spectroscopy, quasi in situ X-ray photoelectron spectroscopy (XPS) were used to characterize the Ni-CeO_2 samples before and after reduction. Most importantly, at Ni contents above 5 mol.%, reduction leads to small Ni metal nanoparticles, which can explain the high activity of these catalysts.

Experimental Section

Materials

Ni (II) acetylacetonate ($Ni(C_5H_7O_2)_3$, 95%, Sigma-Aldrich), Ni (II) nitrate ($Ni(NO_3)_2$, 99%, Sigma-Aldrich), glacial acetic acid (99% Sigma-Aldrich) and 2-ethylhexanoic acid (99% Fisher Scientific), cerium (III) acetate hydrate ($Ce(CH_3CO_2)_3 \cdot 1H_2O$, 98%, TCI Europe NV), cerium (IV) dioxide (CeO_2, 99%, Sigma-Aldrich), citric acid ($HOC(COOH)(CH_2COOH)_2 \cdot 1H_2O$, Merck, >99.5%), silicon dioxide (SiO_2, X-080, CRI Catalyst Company, 280 m^2 /g) were used as received.

Catalyst Preparation

Flame Spray Pyrolysis

Flame spray pyrolysis (FSP) of CeO_2 and Ni-CeO_2 samples was performed with a Tethis NPS10 setup. The Tethis NPS10 apparatus was placed in a standard chemical laboratory fume hood modified to comply with EN 14172, EN 1822, and ISO 45H standards (modifications realized by Interflow). The air inflow of the fume hood was kept at a minimum of 0.7 m/s using active control systems. The exhaust flow to the (external) ventilation was equipped with HEPA H14 and ULPA U17 filters. The experiments were conducted after assessing all safety aspects, including those related to working with nanomaterials, in a risk-inventory and evaluation (RI&E) procedure, as required by the Dutch labor law. Appropriate amounts of Ni $(C_5H_7O_2)_3$ and Ce $(CH_3CO_2)_3 \cdot H_2O$ were dissolved in an 1:1 (v/v) solvent mixture of acetic acid and 2-ethylhexanoic acid. The Ni and Ce concentrations were 0.15 M. This solution was stirred at 80 °C for approximately 1 h until complete dissolution of the metal precursors. The precursor solution (25 mL) was fed into the center of a methane/oxygen flame by a syringe pump with an injection rate of 5 mL/min to form a fine spray. The pressure drop at the capillary tip was maintained constant at 2.5 bar by adjusting the orifice gap area at the nozzle. The flame was kept constant with a flow of 1.5 L/min methane and 3.0 L/min oxygen. Solid samples were collected on a glass microfiber filter (Whatman) with the aid of a vacuum pump. The as-prepared CeO_2 and Ni–CeO_2 catalysts are denoted as CeFSP and xNiFSP, where x stands for Ni content (mol.%) with respect to the support (Ni/ (Ni + Ce)).

Impregnation

A reference catalyst with an intended Ni loading of 10 mol.% was prepared by wet impregnation. For this purpose, the desired amount of $Ni(NO_3)_2$ was dissolved in 60 mL of an aqueous ammonia solution (28 wt.%). About 3 g of commercially available CeO_2 or synthesized CeFSP was added to the solution followed by stirring the suspension for 2 h. Then, water was removed by evaporation. The catalyst was dried in air at 110°C overnight and calcined at 400 °C for 4 h. These samples were denoted as $10Ni/CeO_2$ and 10NiCeFSP(WI).

Another reference catalyst with an intended Ni loading of 10 mol.% was prepared by incipient wetness impregnation using citric acid to control the dispersion of the Ni nanoparticles (citric acid/Ni ratio of 0.13).[12] The SiO_2 support was dried in air at 110 °C overnight before impregnation. The desired amounts of $Ni(NO_3)_2$ and citric acid were dissolved in deionized water. The resulting solution was used for impregnation. The catalyst was dried in air at 110 °C overnight and calcined at 400 °C for 4 h. This sample is denoted as $10Ni/SiO_2$.

Catalyst Characterization

Inductively Coupled Plasma Optical Emission Spectroscopy (ICP-OES)

The chemical composition (Ni and Ce) of the as-prepared catalysts was determined by ICP-OES analysis (Spectro CIROS CCD Spectrometer). Prior to these measurements, the catalysts were dissolved in 5 mL of concentrated sulfuric acid (H_2SO_4) at a temperature of 200 °C under stirring for at least 30 min, followed by dilution in water.

N_2 Physisorption

The textural properties of the as-prepared catalysts were determined by N_2 physisorption at a temperature −196 °C using a Micrometrics TriStar II 3020 instrument. Prior to physisorption measurements, the samples were heated to 160 °C in an N_2 flow for 4 h. The specific surface area (SSA) was determined by the Brunauer–Emmett–Teller (BET) method.

X-ray diffraction (XRD)

In situ synchrotron X-ray diffraction patterns were collected at the ID15A beamline of the ESRF. The measurements were carried out in Debye-Scherrer geometry at an incident X-ray energy of 100 keV. A Pilatus3X CdTe 2M detector was used to collect the scattered signal. About 20 mg of sieved catalyst (125 - 250 μm) was loaded into quartz capillaries (1.5 mm o.d. wall thickness 0.15 mm) between two glass wool layers. The capillary was sealed with PTFE ferrules in a home-built Clausen-type flow cell. The sample was heated using a prototype synchrotron oven, developed at the ESRF.

Temperature calibration was performed by a thin (0.25 mm) K-type thermocouple placed inside the catalyst bed. Typically, the temperature was raised from 50 °C to 300 °C at a rate of 10 °C/min in a 50 mL/min flow of a mixture of 20 vol.% H_2 in Ar, followed by an isothermal dwell of 1 h at 300 °C. The reduction mixture was replaced by a reaction mixture consisting of 15 vol.% CO_2, 60 vol.% H_2 balanced by Ar fed at a total flow of 50 mL/min for 1 h. The NiO, Ni, and CeO_2 phases were analyzed in the GSAS software (version 5720) using Rietveld refinement.

Ultraviolet-visible diffuse reflectance spectroscopy (UV-Vis DRS)

UV-Vis DRS spectra were collected at room temperature with a Shimadzu UV-2401PC spectrometer equipped with an integrating sphere coated with $BaSO_4$ as standard. Samples were diluted with $BaSO_4$ (30 mg sample mixed with 120 mg $BaSO_4$).

Raman spectroscopy

Raman spectroscopy was carried out using a WITec WMT50 confocal Raman microscope with a WITec UHTS300 spectrometer. Raman spectra were directly collected for powder samples, and a 532 nm laser was used. The Project FIVE 5.1 software was used for data treatment.

Transmission Electron Microscopy (TEM)

The morphology and particle size distribution of as-prepared and reduced catalysts were investigated by TEM using an FEI Titan Cryo-TEM instrument operating at an acceleration voltage of 300 kV. An appropriate amount of finely ground material was ultrasonically dispersed in analytical-grade absolute ethanol before deposition on holey Cu TEM grids.

Additional TEM measurements to determine the nanoscale elemental distribution involved scanning transmission electron microscopy - energy dispersive X-ray analysis (STEM-EDX). Measurements were carried out on a FEI-cubed Cs-corrected Titan instrument operating at an acceleration voltage of 300 kV. Ni-CeO_2 catalysts were reduced at 300 °C in a flow of 20 vol.% H_2 in He for 4 h, followed by passivation at room temperature in a flow of 2 vol.% O_2 in He for 1 h. The as-prepared and passivated samples were crushed and sonicated in analytical-grade absolute ethanol before deposition on holey Au TEM grids.

Temperature-Programmed Reduction (H_2-TPR)

H_2-TPR was used to study the reducibility of the samples with a Micromeritics AutoChem II instrument. Typically, about 100 mg sample was loaded into a quartz U-tube between two quartz wool layers. Prior to H_2-TPR, the sample was treated at 350 °C for 1 h in a flow of 50 mL/min of 5 vol.% O_2 in He. TPR profiles were recorded under heating the sample from 40 to 700 °C at a 10 °C/min rate in a 50 mL/min flow of 4 vol.% H_2 in He. H_2 consumption was measured by a thermal conductivity detector (TCD) and calibrated using AgO reference.

H_2 Chemisorption

H_2 chemisorption measurements were performed with a Micromeritics ASAP2010C instrument. Typically, about 100 mg sample was loaded into a quartz U-tube between two quartz wool layers. Before chemisorption measurements, the catalyst was reduced in a H_2 flow at 300 °C by heating to this temperature at a rate of 10 °C/min, followed by an isothermal dwell of 4 h. After evacuation at 320 °C for 1 h, H_2 adsorption isotherms were recorded at 150 °C.

Infrared (IR) Spectroscopy

IR spectra were recorded on a Bruker Vertex 70v FTIR spectrometer equipped with a DTGS detector. The experiments were performed in situ using a home-built environmental transmission IR cell. Self-supporting pellets were made by pressing approximately 10 mg sample in a disc with a diameter of 13 mm. Each spectrum was collected by averaging 32 scans with a 2 cm^{-1} resolution in the 4000–1000 cm^{-1} range.

For CO IR measurements, the sample was first reduced in a flow of 20 vol.% H_2 in He at 300 °C (heating rate 10 °C/min) for 4 h. After outgassing at 300 °C in a vacuum and cooling to 50 °C, IR spectra were recorded as a function of the CO partial pressure in the 0–10 mbar range. CO IR measurements were also carried out at liquid N_2 temperatures. For these measurements, the same reduction procedure was followed. After outgassing, the sample was then cooled by liquid N_2. The sample temperature was approximately -168 °C. IR spectra were recorded as a function of CO partial pressure in the 0 – 10 mbar range. As-prepared samples were also investigated by CO IR spectroscopy at liquid N_2 temperature. For this purpose, the samples were evacuated at 50 °C for 1 h, before cooling to liquid N_2 temperature. CO_2 IR measurements were also carried out after the reduction of the samples as described above. CO_2 adsorption was carried out at 50 °C, and IR spectra were obtained as a function of CO_2 partial pressure in the 0–10 mbar range. For in situ methanation measurements, the spectra were recorded on pre-reduced at 300 °C catalysts in a flow of 4% CO_2, 16% H_2 balanced by N_2 at 200 – 300 °C. The sample was then heated to 300 °C at a rate of 5 °C/min, while recording IR spectra at intervals of 25 °C. All samples were background subtracted, and the intensity was normalized to the weight of the pellet.

X-ray Photoelectron Spectroscopy (XPS)

The surface chemical properties of the as-prepared catalysts were studied with a K-Alpha XPS instrument (Thermo Scientific) equipped with an aluminum anode (Al Kα = 1486.68 eV) monochromatized X-ray source. Finely ground samples were placed on double-sided carbon tape. All spectra were acquired using a flood gun to reduce surface charging. A pass energy of 40 eV was used for region scans with a step size of 0.1 eV and a dwell time of 0.5 s. The U”’ (Ce^{4+}) component of the Ce 3d line with a characteristic position of 916.7 eV was used to correct the binding energies of the Ni

$2p_{3/2}$ and Ce 3d regions.[46,47] A standard procedure involving Shirley background subtraction and atomic sensitivity factors was applied for data processing. Spectral lines were fitted with the CasaXPS software (version 3.2.23) using a symmetric pseudo-Voigt function, referred to as GL (30). Only the main metallic component of Co was fitted by the asymmetric LA (1.2,5,5) line shape in the CasaXPS software (version 3.2.23). The Ce 3d line was fitted according to a model described in the literature.[32, 33]

Quasi-in situ X-ray photoelectron spectroscopy (XPS)

The surface chemical properties of the reduced and deactivated catalysts were studied using a Kratos AXIS Ultra 600 equipped with a monochromatic X-ray source (Al Kα = 1486.68 eV). Self-supporting pellets were made by pressing approximately 40 mg of a sample in a disk with a diameter of 13 mm. Pretreatment and deactivation of catalysts were carried out in a high-temperature reaction cell (Kratos, WX-530), allowing vacuum sample transfer into the analysis chamber. The samples were reduced in a mixture of 20 vol.% H_2 in Ar at a 50 mL/min flow at 300 °C for 4 h at a heating rate of 10 °C/min and ambient pressure. After that, the sample was cooled to 100 °C in a pretreatment mixture, and the reaction cell was evacuated to a pressure below 10^{-8} mbar for transferring to the analysis chamber. A deactivation test was performed in 15 vol.% CO_2, 60 vol.% H_2 balanced by Ar fed at a total flow of 50 mL/min at ambient pressure and 300 °C for 24 h. Then, the sample was cooled to 100 C in a reaction mixture, and the reaction cell was evacuated to a pressure below 10^{-8} mbar for transfer to the analysis chamber.

A pass energy of 40 eV was typically used for region scans with a step size of 0.1 eV and a dwell time of 0.5 s. Energy calibration and fitting of Ce 3d and Ni 2p were performed using the same procedure as described in the XPS description above. The main metallic component of Ni was fitted by the asymmetric LA (1.2,5,5) line shape in the CasaXPS software (version 3.2.23).

In situ thermal gravimetric analysis (TGA)

In situ TG measurements were carried out using an in-house designed ReactorTGA system, which consists of a Discovery HP-TGA75 instrument (TA Instruments) with a top-loading magnetic suspension balance and a home-built gas dosing system. An amount of 25 mg of NiFSP catalyst (125 – 250 µm) was loaded into a 100 µL Al_2O_3 crucible. The TGA experiments were performed in a flow of 50 mL/min 4 vol.% H_2 in Ar at 1.5 bar, whilst increasing the temperature to 300 °C at a rate of 10 °C/min, followed by a dwell at this temperature of 4 h. Then the flow was changed to 50 mL/min of pure Ar for 20 min. The deactivation experiments were performed in a 50 mL/min flow of 0.8 vol.% CO_2, 3.2 vol.%H_2 in Ar at 300 °C (1.5 bar). Temperature-programmed oxidation of postreaction catalysts was carried out in a flow of 20 vol.% O_2 in N_2 at 1.5 bar whilst increasing the temperature from 50 °C to 900 °C at a rate of 10 °C/min, followed by a dwell at this temperature of 1 h. The buoyancy effect was accounted for by measuring an empty crucible under the same conditions.

Catalytic Activity Measurements

CO_2 hydrogenation

The catalytic performance of CeO_2 and Ni-CeO_2 samples in CO_2 hydrogenation was carried out in a down-flow stainless-steel reactor with an internal diameter of 4 mm. The reaction was performed at atmospheric pressure, and the temperature varied in the range of 200–300 °C. The samples were pressed, crushed, and sieved to a fraction of 125 – 250 µm. Typically, the reactor was filled with 50 mg catalyst diluted with 200 mg of SiC of the same sieve fraction. Before the reaction, the catalyst was reduced in a 100 mL/min flow of 20 vol.% H_2 in He, heating from room temperature to 300 °C at a rate of 10 °C/min, followed by an isothermal dwell for 4 h. The reduced catalyst was cooled in the same gas mixture to the initial reaction temperature of 200 °C. The reaction was started by replacing the reduction gas mixture with a flow of 50 mL/min of 60 vol.% H_2, 15 vol.% CO_2, and 25 vol.% Ar (CO_2: H_2 = 1:4). The temperature was increased in steps of 25 °C using a rate of 5 °C/min. At each isothermal dwell of 36 min, the effluent gas was sampled and analyzed by an online gas chromatograph (Shimadzu, GC-2014) equipped with RT-Q-Bond (FID), and Shincarbon ST 80/100 (TCD) analysis stions. The measurements were taken after ca. 2 h time-on-stream and CO_2 conversion, carbon product selectivity, and product formation rates were calculated as follows:

$$X(CO_2) = 1 - \frac{F(CO_2)_{out}}{F(CO_2)_{out} + F(CO)_{out} + F(CH_4)_{out} + F(CH_3OH)_{out} + xF\left(C_xH_y\right)_{out}} \quad (1)$$

$$S(product) = \frac{F(product)_{out}}{F(CO)_{out} + F(CH_4)_{out} + F(CH_3OH)_{out} + xF\left(C_xH_y\right)_{out}} \quad (2)$$

$$r(product) = \frac{F(product)_{out}}{V_m * n_{Ni}} \quad (3)$$

where *F* stands for the volumetric flow rate determined from the concentration measured by gas chromatography using Ar as an internal standard and FID and TCD response factors determined by using gas calibration mixtures. V_m is the molar volume of an ideal gas at standard temperature and pressure. n_{Ni} is Ni content in the sample in mol_{Ni}.

The reaction rate (r_{CO2} with the unit $mol_{CO2} \cdot mol_{Ni}^{-1} \cdot s^{-1}$) was normalized by the Ni content in the following manner:

$$r_{CO2} = \frac{X\,(CO_2) * F(CO_2)_{in}}{n_{Ni} * V_m} \quad (4)$$

The stability of the catalyst was tested at 300 °C for 72 h with the same gas feed composition. Activation energies of NiFSP catalysts were evaluated at 248 – 255 °C in a flow of 50 mL/min of 60 vol.% H_2, 15 vol.% CO_2, and 25 vol.% Ar (CO_2/H_2 = 1/4). The catalyst amount was adjusted by dilution with SiC (1NiFSP 50 mg; 10NiFSP 10 mg) to ensure conversion levels below 5%.

Results and discussion

Catalyst Characterization

The relevant physicochemical properties of the flame-synthesized CeFSP and NiFSP samples are listed in **Table 4.1**. The Ni contents determined by ICP-OES analysis are close to the targeted values. Synchrotron XRD patterns of the as-prepared CeFSP and NiFSP samples are shown in **Figure 4.1a-b**. The dominant crystalline phase is fluorite CeO_2. At a Ni content above 10 mol.%, diffraction lines belong to NiO are also observed (**Figure 4.1b**). The CeO_2 lattice parameter of the NiFSP catalysts is similar to the one for CeFSP. The average CeO_2 particle size determined from the XRD data is around 9 nm. The variations in the average CeO_2 particle size does not correlate with the Ni content. The specific surface areas determined by N_2 physisorption vary between 120 and 180 m^2/g and without a noticeable trend with the Ni content. For the samples containing NiO diffraction peaks, the Rietveld refinement showed that the NiO particle size increased from 5.8 nm for 20NiFSP to 6.0 nm for 30NiFSP.

The morphological properties of the NiFSP catalyst and CeFSP were investigated by TEM (**Figure C1**). The average size of the CeO_2 particles is in the 5 – 7 nm range without any noticeable trend with the Ni content.[34] Due to the poor contrast between Ni and Ce, no Ni-oxide particles could be distinguished. The surface Ni/Ce ratios determined by XPS increase with the Ni content and are slightly higher than the bulk values, suggesting the enrichment of Ni in the surface region of the CeO_2 crystallites.

UV-Vis spectra of CeFSP and as-prepared NiFSP catalysts are characterized by bands at 260 – 280 nm, which are related to CeO_2.[50] The spectra of the as-prepared NiFSP catalysts also contain broad bands 400 – 600 nm (**Figure 4.1c**), indicative of Ni doping.[51–53] No characteristic signals of NiO, expected at 345 nm and 720 nm were observed for any NiFSP catalysts.[54,55] Characteristic bands of NiO at 345 nm are evident for $10Ni/CeO_2$.

Table 4.1. Physicochemical properties of as-prepared CeFSP and NiFSP

Catalysts	Ni (mol.%)[a]	S_{BET} (m^2/g)[b]	a_{CeO2} (Å)[c]	d_{CeO2} (nm)[c]	d_{NiO} (nm)[c]	d_{CeO2} (nm)[d]	Ni/Ce (at.%/at.%)[e]
CeFSP	0	181	5.411	8.5	-	5.0 (2)	n.a.
1NiFSP	1.0	132	5.410	10.1	-	5.7 (2)	0.03
2.5NiFSP	2.6	137	5.411	10.2	-	5.6 (2)	0.06
5NiFSP	5.1	145	5.409	9.2	-	5.6 (2)	0.10
10NiFSP	10.1	128	5.411	8.1	-	5.5 (2)	0.18
20NiFSP	19.9	137	5.410	8.9	5.8 (0.2)	5.8 (2)	0.36
30NiFSP	29.5	132	5.409	8.9	6.0 (0.2)	5.6 (2)	0.49

a – determined from ICP analysis, b -determined by N_2 physisorption on as-prepared samples, c – determined by Rietveld refinement of synchrotron XRD on as-prepared samples (error margins), d – determined by TEM for as-prepared samples (error margins), e – determined by XPS for as-prepared samples

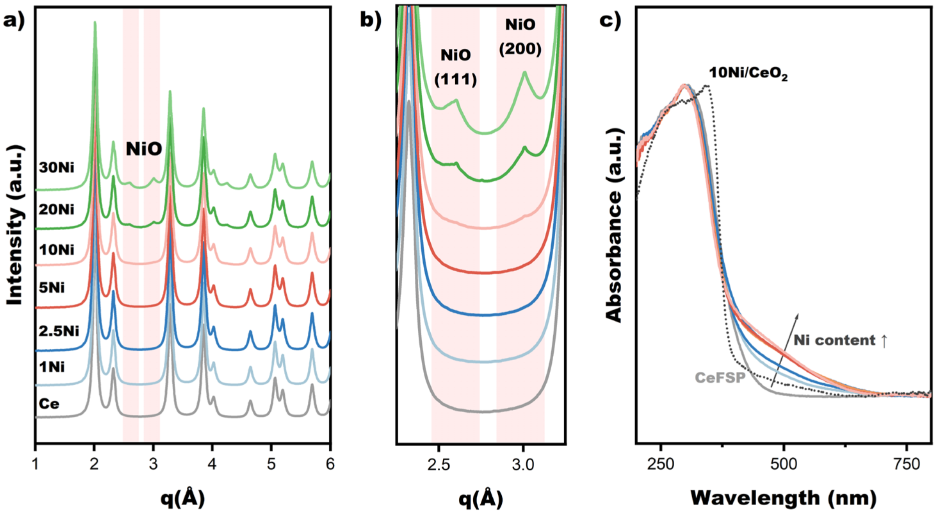

Figure 4.1. (a) Synchrotron XRD patterns (100 keV, λ = 0.124 Å) of NiFSP and CeFSP. (b) a zoom in the q = 2.25–3.25 $Å^{-1}$ region, highlighting the NiO (111) and NiO (200) diffraction lines. (c) UV-Vis spectra of CeFSP and NiFSP, 10Ni/CeO_2.

The Raman spectra of NiFSP catalysts and the CeFSP support are shown in **Figure C2**. The intense peak at ~460 cm^{-1} is assigned to the F_{2g} mode of the CeO_2 fluorite structure.[56] The broad band at 588 cm^{-1} is typically associated with a defect-induced D band due to the formation of oxygen vacancies.[28,56] However, the shift of Raman peak to lower wavenumbers (635 cm^{-1}) has also been linked to a Ni-CeO_2 solid solution.[57,58] An additional band at 225 cm^{-1} is attributed to NiO nanoparticle formation.[59] This band increases with the Ni content.

Overall, the XRD, UV-Vis, Raman, and XPS results indicate that all NiFSP catalysts contained uniformly distributed and, most likely, isolated Ni^{2+} species. In addition, there are indications for the presence of NiO particles for samples with a Ni content of 10 mol.% and above.

Ni-CeO_2 interactions

Next, we studied the reduction behavior of these samples (**Figure 4.2**). CeFSP exhibits a single reduction peak at 580 °C, attributed to the reduction of surface Ce^{4+} to Ce^{3+}.[60–62] At low Ni content (1NiFSP), the reduction profile of the NiFSP samples contains a broad reduction feature between 200 and 400 °C, which can be attributed to highly dispersed Ni ions, likely included in the surface forming a Ni – O – Ce solid solution.[53,63] Increasing the Ni content shifts this reduction peak to lower temperatures. This shift is likely due to the reduction of NiO species to Ni particles, which facilitate the further reduction of the Ni^{2+} ions on the surface. At a Ni content of 5 mol.% and higher, the H_2-TPR profiles contain two peaks at 300 °C and 425 °C. The peak at 300 °C is due to the reduction of NiO particles that are weakly bound to CeO_2.[64] The high-temperature peak at 425 °C is considered to be a superposition of the reduction of

NiO in strong interaction with CeO_2 [65] and the partial reduction of the CeO_2 surface. The excess amount of consumed H_2 (**Figure 4.2b**), i.e., the difference between the total H_2 consumed and H_2 required to reduce NiO completely, stems from the surface reduction of CeO_2 by spillover hydrogen from metallic Ni particles. This also explains the lower onset temperature of CeO_2 reduction.[66] Hydrogen spillover due to metals that can dissociate H_2 results in reduction of the CeO_2 surface at lower temperatures. As the surface areas are similar for all NiFSP catalysts, the excess amount of consumed H_2 does not strongly vary with Ni content. In the following, we employed a reduction temperature of 300 °C using a heating rate of 10 °C and a dwell of 4 h in 20 vol.% H_2 in He to reduce the NiFSP catalysts.

H_2 chemisorption measurements on the reduced catalysts (**Table 4.2, Figure 4.2c, Figure C3**) show irreversible H_2 chemisorption on all NiFSP catalysts. The amount of chemisorbed H_2 increased with Ni content, reaching the highest value for 30NiFSP. The Ni particle size in the reduced and passivated NiFSP catalysts was estimated from HAADF-STEM-EDX maps (**Figure 4.3a and Table 4.2**). At low Ni content (1NiFSP), Ni remains highly dispersed on CeO_2. At a higher Ni content (5NiFSP), several small Ni-containing particles with a size of ~1 nm are visible. The presence of Ni nanoparticles is even more evident for 10NiFSP and 20NiFSP with average particle sizes of ~2.5 nm and ~4.4 nm, respectively. All these catalysts also contained highly dispersed Ni.

Table 4.2. H_2-TPR of as-prepared samples and physicochemical properties of samples reduced at 300 °C.

Catalysts	H_2 (mmol/g)[a]	Excess H_2 (mmol/g)[b]	H_2 (mmol/g)[c]	Theoretical H_2 (mmol/g)[d]	d_{Ni} (nm)[e]	d_{Ni} (nm)[f]
CeFSP	0.60	-	0	0	n.a.	n.a.
1NiFSP	0.69	0.63	0.352	0.03	-	-
2.5NiFSP	0.71	0.52	0.400	0.08	n.a.	-
5NiFSP	0.89	0.59	0.405	0.15	~1	-
10NiFSP	1.19	0.56	0.423	0.13	2.5 ± 1	-
20NiFSP	1.95	0.61	0.465	0.20	4.4 ± 1.5	3.5 (0.2)
30NiFSP	2.84	0.67	0.506	0.30	n.a.	3.5 (0.2)

a – determined from H_2-TPR in 100 – 650 ℃ range, b - estimated from the difference between total H_2 consumption and H_2 required to reduce NiO completely during H_2-TPR, c- determined by H_2 chemisorption at 150 ℃ on pre-reduced samples at 300 ℃, d – estimated assuming a spherical shape of the Ni particles and a H/Ni adsorption stoichiometry of 1, the Ni reduction degree of 1, Ni particle sizes derived from XRD(30NiFSP) and HAADF-STEM-EDX maps(for 5NiFSP; 10NiFSP and 20NiFSP) of reduced NiFSP catalysts (the dispersion of 1NiFSP and 2.5NiFSP was assumed 100%), e – estimated from HAADF-STEM-EDX maps of reduced and passivated catalysts (reduction treatment: 300 ℃), f – determined by Rietveld refinement of XRD of the catalysts after reduction at 300 ℃ (error margin).

The structural changes of the NiFSP catalysts and the bare CeFSP support during reduction were investigated in more detail by in situ synchrotron XRD. The synchrotron XRD patterns of the NiFSP catalysts can be described well by CeO_2 (**Figure C4**). The patterns for the reduced 1NiFSP, 2.5NiFSP, and 5NiFSP catalysts did not contain reflections of Ni-containing phases, implying that the reduced Ni particles are very small in agreement with the HAADF-STEM-EDX maps of the reduced NiFSP catalysts (**Figure 4.3a**). The XRD patterns of the 10NiFSP, 20NiFSP and 30NiFSP samples show indications of the NiO → Ni reduction at ~200 °C (**Figure C4**). Subtracted XRD patterns (ΔXRD plots, referenced to the as-prepared state) emphasize that, with increasing Ni content, the contributions at $q = 3.1$ $Å^{-1}$ and 3.5 $Å^{-1}$ due to metallic Ni become stronger (**Figure 4.3b and Figure C5-6**). The negative features at $q = 2.6$, 2.9, and 4.2 $Å^{-1}$ of the 10NiFSP, 20NiFSP, and 30NIfSP catalysts point to the disappearance of the NiO phase.

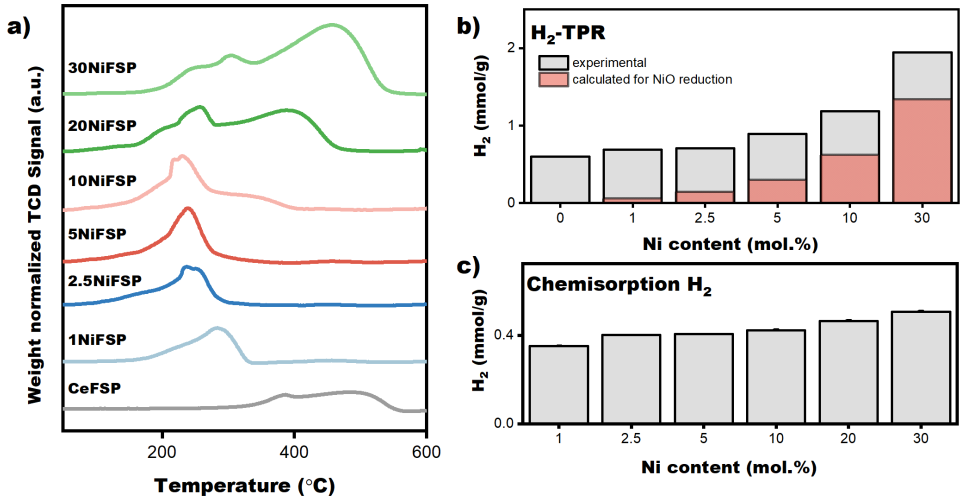

Figure 4.2. (a) Weight-normalized H_2-TPR profiles of CeFSP and NiFSP catalysts (conditions: 4 vol.% H_2, 50 mL/min). (b) Quantification of hydrogen consumption during TPR experiments (light grey – excess of H_2; orange – the amount required for complete NiO reduction). (c) Amount of H_2 chemisorbed during chemisorption experiments.

Rietveld refinement of the XRD patterns revealed an increase in the CeO_2 unit cell parameter during reduction for all catalysts and the CeFSP sample (**Figure 4.3c-d, Figure C7**), along with a small increase of the CeO_2 crystallite size from 8 nm to 12 nm. In addition to gradual thermal expansion, a more abrupt expansion of the CeO_2 unit cell parameter from 5.405 to 5.437 Å is noted in the 125 – 225 °C temperature range for all NiFSP catalysts and the CeFSP support (**Figure 4.3c**). The expansion of the CeFSP unit cell is more gradual, and the change in the unit cell parameter is less pronounced than that of the NiFSP catalysts (**Figure 4.3c**). The reduction of Ce^{4+} to the larger Ce^{3+} ion and the electrostatic repulsion between oxygen vacancies and the surrounding cations cause this abrupt increase of the unit cell parameter.[67]

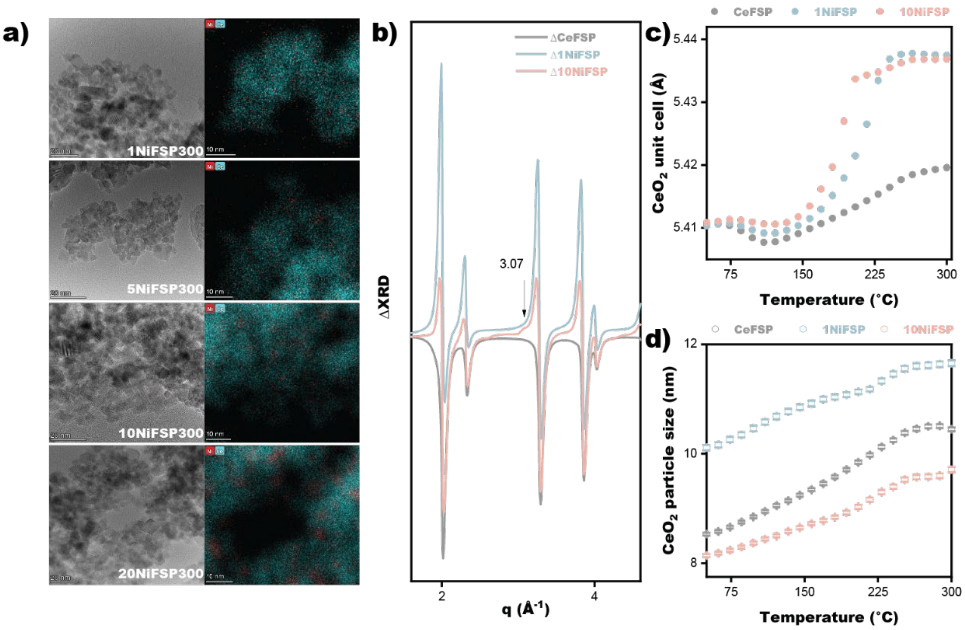

Figure 4.3. (a) STEM-EDX images: (left) TEM images and corresponding EDX elemental maps of mixed Ni and Ce (right) for NiFSP after reduction at 300 °C. (b) Synchrotron ΔXRD ($\lambda = 0.124$ Å) patterns of CeFSP, 1NiFSP, and 10NiFSP before and after reductive pretreatment. ΔXRD difference is obtained by subtraction of the diffractogram of the as-prepared sample from the reduced diffractogram of the same sample. (c) Refined unit cell of CeO_2 for CeFSP, 1NiFSP and 10NiFSP during reductive pretreatment. (d) Refined CeO_2 particle size of CeFSP, 1NiFSP, and 10NiFSP during pretreatment. (conditions: 20% H_2 in Ar, 50 mL/min, 50 – 300 °C, 1 bar).

The theoretical amount of chemisorbed H_2 was estimated from the Ni particle size estimated by STEM-EDX mapping (XRD Scherrer equation for reduced 30NiFSP) and assuming spherical particles and a H/Ni adsorption stoichiometry of unity. The Ni dispersion of 1NiFSP and 2.5NiFSP was assumed to be 100%. The resulting theoretical estimates of NiFSP catalysts listed in **Table 4.2** are substantially lower than the experimental H_2 chemisorption values. The difference is caused by hydrogen spillover to CeO_2 in supported metal nanoparticle catalysts.[70,71] Due to the involvement of the CeO_2 support, H_2 chemisorption can therefore not be used to determine the amount of metallic Ni sites.

The nature of the Ni species in the reduced NiFSP catalysts was further investigated by CO IR spectroscopy at liquid N_2 temperature (**Figure C9**). All spectra recorded at liquid N_2 temperature are dominated by linear and bridged carbonyl bands in the 2060 – 2000 cm^{-1} and 1970 – 1840 cm^{-1} range, respectively.[72] At low Ni content (1NiFSP), the carbonyl band at 2064 cm^{-1} indicates the presence of low coordinated/isolated Ni centers.[73] The spectra of the reduced 5NiFSP and 10NiFSP catalysts contain a significantly broader carbonyl band at 2050 cm^{-1} at low CO coverage, indicative of CO adsorption on metallic Ni nanoparticles.[74,75] Increasing the CO coverage leads to a blue shift of the carbonyl band from 2000 cm^{-1} to 2080 cm^{-1} due to lateral (dipole) interactions between adsorbed CO molecules on these larger metallic Ni particles.[76,77] The spectrum of all samples contains narrow bands at 2150 – 2160 cm^{-1} and 2125 – 2145 cm^{-1}, assigned to CO adsorption on Ce^{4+} and Ce^{3+}, respectively.[78–80] A broad band in the 2110 – 2135 cm^{-1} region in the reduced CeFSP and NiFSP catalysts corresponds to the Ce^{3+} ^{2}F5/2 → ^{2}F7/2 spin-orbit electronic transition.[81] This band evidences the partial reduction of CeO$_2$ in CeFSP and NiFSP catalysts.[66]

The combined XRD, STEM-EDX, and CO IR spectroscopy results show that a small amount of very small Ni clusters were formed in the 1NiFSP catalyst after reduction at 300 °C. Reduction of the catalysts with a Ni content of 5 mol.% and above led to larger Ni nanoparticles. XPS analysis shows that the reduction degree of Ni in reduced 10NiFSP catalyst is 59%, meaning that a significWe employed quasi-in situ XPS to study the surface composition and reduction degree of the reduced 1NiFSP and 10NiFSP catalysts. The samples were reduced in the reactor chamber of a Kratos XPS system. The reduction was carried out at 300 °C for 4 h at atmospheric pressure in a flow of 20 vol.% H$_2$ in He. The resulting Ni 2p$_{3/2}$ and Ce 3d XP spectra and their fits are shown in **Figure C8**, and the fit results are given in **Table C1**. The low Ni 2p$_{3/2}$ signal does not allow reliable quantification of the Ni oxidation state in 1NiFSP. The Ni 2p$_{3/2}$ spectrum of the reduced 10NiFSP catalyst shows a metallic Ni component at 852.6 eV and a Ni^{2+} component at 583.7 eV.[68] The Ni reduction degree was 59%. The amount of highly dispersed Ni^{2+} in the reduced sample was ~4 mol.%, which is very similar to the amount of highly dispersed and difficult-to-reduce Co^{2+} in Co-CeO$_2$ prepared by FSP (**Table C1 and Table 2.3**). The presence of such Ni^{2+} species in CeO$_2$ is likely due to the inclusion of Ni^{2+} in the bulk and surface of CeO$_2$ during flame synthesis. Deconvolution of the Ce 3d XP spectra shows that the reduction step led to an increase of the Ce^{3+} fraction from ~8% in the as-prepared samples to ~29% in the reduced catalysts.[47,48,69] The XPS Ni/Ce surface ratio in the reduced 10NiFSP catalyst is lower than the corresponding ratio in the as-prepared catalyst (**Table 4.2 and Table C1**). This points to the sintering of Ni species during reduction, assuming that encapsulation of Ni by CeO$_2$ will not occur at the low reduction temperature employed.

ant fraction of highly dispersed Ni^{2+} remains unreduced due to their strong interaction with CeO$_2$. The amount of such difficult-to-reduce Ni^{2+} species is ~4 mol.%. HAADF-STEM-EDX maps of the reduced and passivated NiFSP catalysts revealed that Ni remains highly dispersed on CeO$_2$, with only a few Ni particles of ~ 1 nm visible for 5NiFSP, while the average Ni particle size in the reduced 10NiFSP and 20NiFSP catalysts was ~2.5 nm and ~4.4 nm, respectively. XPS revealed the presence of Ce^{3+} species due to CeO$_2$ surface reduction, implying the presence of oxygen vacancies. The partially reduced state of the surface is also confirmed by in situ XRD and IR spectroscopy. All reduced NiFSP catalysts strongly chemisorb H$_2$, the H atoms generated on metallic Ni spilling over to the CeO$_2$ support. CO adsorbed stronger on the metallic Ni nanoparticles in the reduced 5NiFSP and 10CoNiFSP catalysts than the small amount of reduced low coordinated Ni in 1NiFSP. The influence of different Ni structures after reduction was further investigated in CO_2 hydrogenation.

CO_2 hydrogenation over NiFSP and CeFSP

The catalytic performance of reduced NiFSP catalysts and the reduced bare CeFSP was evaluated in the 200 – 300 °C temperature range and atmospheric pressure. While CeFSP displayed negligible catalytic activity under these conditions, the reduced NiFSP catalysts hydrogenated CO_2 to CO and CH_4 (**Figure 4.4** and **Figure C10**). Ni-normalized reaction rates were obtained at 200 °C and differential conditions (CO_2 conversion below 10%) as a function of the Ni content (**Figure 4.4**). The reaction rate does not vary strongly with the Ni content as it did for Co-CeO_2 catalysts (**Figure 2.5**). There is, however, a strong shift in the product distribution: an increase in the CH_4 selectivity at the expense of CO formation. Besides CH_4 and CO, a small amount of CH_3OH was observed at low Ni content (1 – 5 mol.%), which disappears for Ni contents of 10 mol.% and above due to the presence of Ni nanoparticles. For such a high Ni content, higher CH_4 selectivity coincides with decreasing C_2H_6 and C_3H_8 selectivity (**Figure C4**). This suggests that the C-C coupling on the Ni surface competes with the hydrogenation process, leading to methane formation.[82]

The CO_2 conversion rate and the CH_4 selectivity increase with the Ni content. The 1NiFSP catalyst shows a high selectivity towards CO (~71%) at 200 °C at a low CO_2 conversion of 0.2%., while the 30NiFSP sample achieved a CH_4 selectivity of 96% at a CO_2 conversion of 7.3% at 200 °C. Increasing the reaction temperature led to a higher CO_2 conversion and CH_4 selectivity: a CH_4 selectivity of 99% at a CO_2 conversion of 89% at 300 °C was noted for 30NiFSP and a CH_4 selectivity of 53% at a CO_2 conversion of 8% at 300 °C for 1NiFSP (**Figure C10**). This suggests that CO_2 methanation follows the $CO_2 \rightarrow CO \rightarrow CH_4$ pathway.[12]

We compared the product distribution among the 1NiFSP and 10NiFSP catalysts at the same conversion at 250 °C. This was achieved by varying the space velocity (50 mg 1NiFSP and 10 mg 10NiFSP), resulting in a CO_2 conversion of ca. 3% (**Figure 4.4**). The results show that 10NiFSP exhibits a much higher CH_4 selectivity of 67% than the value of 12% achieved with 1NiFSP. The apparent activation energies based on CH_4 formation rates (**Figure C11**) are similar for 1NiFSP (65 $kJ \cdot mol^{-1}$) and 10NiFSP (64 $kJ \cdot mol^{-1}$), indicating that CH_4 formation occurs on similar active sites. These values for the apparent activation energy are consistent with values reported for CO_2 methanation on Ni catalysts.[42,83]

The notable differences in the product distribution can point to different structures of the active sites, which may be linked to the difference in particle size. Typically, catalysts containing small clusters and/or single atoms have distinct catalytic properties as compared to metal nanoparticle catalysts.[28,84] In CO_2 hydrogenation reaction, it is generally accepted that metal nanoparticles are necessary for CH_4 production, while the single atom/small clusters are apt to produce CO.[12,22,41,82] It has been shown that the Ni particle size can affect selectivity as very small particles (<2 nm) are inefficient at catalyzing the intermediate CO methanation reaction due to the lack of step-edge sites for C-O dissociation.[12,15] Sub-nanometer clusters or isolated Ni atoms on the support can catalyze the rWGS reaction without significantly contributing to methanation.[15] With increasing Ni content, the reduced catalysts contain an increasing amount of metallic Ni nanoparticles and some highly dispersed Ni^{2+} (~ 4mol.% for 10NiFSP). The metallic Ni nanoparticles provide sites for the conventional hydrogenation of CO_2 to CH_4 via CO intermediate. The decomposition of CH_3OH will likely happen on metallic Ni, which reasonably explains the absence of CH_3OH among the reaction products for the catalysts with high Ni content. While the CO formation rate decreases with an increasing amount of metallic Ni, the CH_4 formation rate increases in line with our explanations. 1NiFSP and 10NiFSP catalysts were selected to investigate structure and stability under reaction conditions further.

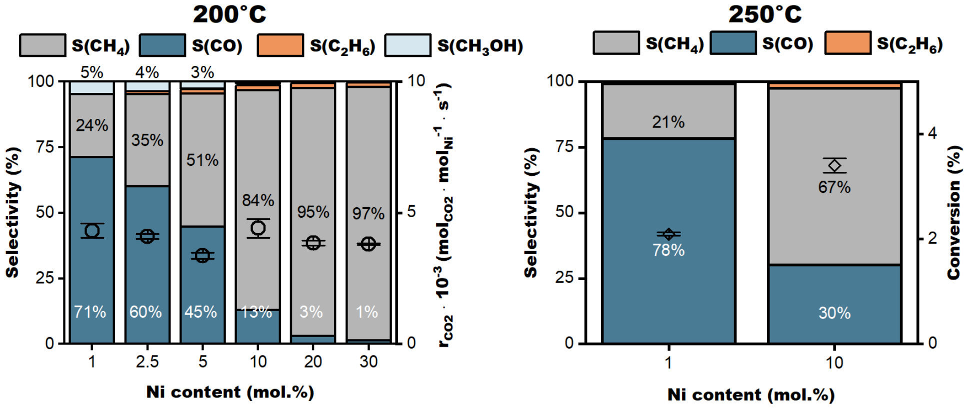

Figure 4.4. Catalytic activity and product distribution of the NiFSP catalysts reduced at 300 °C in CO_2 hydrogenation at 200 °C. The reaction rate was normalized to the total Ni content (conditions: 200 °C, 50 mg of catalyst, 15 vol.% CO_2, 60 vol.% H_2, 25 vol.% Ar, 50 mL/min, 1 bar) (left). Catalytic performance of 1NiFSP and 10NiFSP catalysts reduced at 300 °C: CO_2 conversion and product distribution at a reaction temperature 250 °C (conditions: 250 °C, 50 mg of 1NiFSP, 10 mg of 10NiFSP, 15 vol.% CO_2, 60 vol.% H_2, 25 vol.% Ar, 50 mL/min, 1 bar) (right).

The performance of these catalysts was compared to Ni/CeO_2 catalysts prepared by conventional wet impregnation and incipient wetness impregnation using CeFSP, a conventional CeO_2 support and SiO_2 (10Ni/CeO_2, 10NiCeFSP(WI), and 10Ni/SiO_2) .When reduced at 300 °C, these catalysts displayed a lower activity in CO_2 hydrogenation and lower CH_4 selectivity than 10NiFSP (**Figure C12**). The support can affect the dispersion and the reducibility of the active metal, and the nature of active sites.[85] Several studies studied the influence of the CeO_2 particle size and morphology on the catalytic activity and product distribution of supported transition metal catalysts.[86–88]

Oh et al. showed that the CO selectivity on a 5 wt.% Co/CeO_2 in CO_2 hydrogenation can be tuned by changing the CeO_2 particle size.[89] In another study, enhanced activity of the Ni catalyst supported on CeO_2 nanopolyhedrons in CO_2 hydrogenation was attributed to CeO_2 nanoparticles of ~7 nm.[88]

The high CO selectivity for the NiFSP correlates well with the fact that highly dispersed Ni^{2+} is present in 1NiFSP and 10NiFSP catalysts after reduction at 300 °C. While CH_4 formation mostly happens on step-edges of Ni nanoparticles from CO, possibly formed on highly dispersed Ni centers. The lower amount of highly dispersed Ni centers and bigger Ni nanoparticles ~3 nm formed upon reduction of 10NiCeFSP(WI) can contribute to lower activity of 10NiCeFSP(WI) compared to 10NiFSP. However further research on the influence of CeO_2 particle sizes on the structure of Ni sites, Ni dispersion, and CeO_2 reducibility is necessary. A lower surface area of 10Ni/CeO_2 (~50 m^2/g) results in the formation of big Ni nanoparticles ~33 nm and a lower amount of highly dispersed Ni center, which might result in lower activity and CH_4 selectivity.

Compared to the activity and product distribution of CoFSP catalysts, discussed in **Chapter 2** (**Figure 2.5**), NiFSP samples, containing ~2.5 nm Ni nanoparticles, displayed slightly higher metal-weight normalized activity at 200 °C of $4.4 \pm 0.3 \times 10^{-3}$ $mol_{CO2} \cdot mol_{Ni}^{-1} \cdot s^{-1}$ compared to 10CoFSP catalyst ($3.9 \pm 0.2 \times 10^{-3}$ $mol_{CO2} \cdot mol_{Co}^{-1} \cdot s^{-1}$) with ~4.5 nm Co nanoparticles. Interestingly, highly dispersed Ni in 1NiFSP displayed relatively close r_{CO2} ($4.3 \pm 0.3 \times 10^{-3}$ $mol_{CO2} \cdot mol_{Ni}^{-1} \cdot s^{-1}$) to 10NiFSP and 10CoFSP with high CO selectivity (75%), while highly dispersed Co in reduced 2.5CoFSP demonstrated higher CO selectivity of 79% at lower r_{CO2} (1.2 ± 0.4 10^{-3} $mol_{CO2} \cdot mol_{Co}^{-1} \cdot s^{-1}$). The improved CH_4 selectivity in NiFSP might originate from higher Ni dispersion and therefore enhanced H_2 dissociation, as Ni particle size in reduced NiFSP is smaller than Co particle size in CoFSP upon reduction at the same metal content. Despite the difference in activity, the selectivity trends remain the same, suggesting that CH_4 formation required metal nanoparticles with exposed step-edge sites, while CO production most likely takes place on small metal clusters and/or highly dispersed Ni^{2+}/Co^{2+} in Ni–O–Ce or Co–O–Ce interfaces.

A comparison of the catalytic performance of the NiFSP in CO_2 hydrogenation to literature values of Ni-based catalysts is shown in **Figure C13** and **Table C2**. Thus, the 10NiFSP catalyst shows a higher catalytic activity in CO_2 methanation in the 200 – 275 °C range than Ni supported on CeO_2 and TiO_2 supports.

Structure sensitivity CO_2 hydrogenation

Although CO_2 methanation has been extensively studied, the reaction mechanism remains under debate. While some argue that CO_2 hydrogenation follows the $CO_2 \rightarrow CO \rightarrow CH_4$ pathway [12], others report that formate is a key intermediate.[90–92] It should be mentioned that the reaction mechanism can depend on the metal, the support, and their interactions.[84]

We first investigated the activation of CO_2 on the surface of the reduced catalysts by IR spectroscopy of adsorbed CO_2 at a temperature of 50 °C (**Figure C14**). All IR spectra contain a strong band due to the asymmetric stretching vibration of gaseous CO_2 at ~2346 cm^{-1}.[76] A minor carbonyl band in the IR spectra indicates that CO_2 can dissociate on the freshly reduced catalysts already at 50 °C.[74,75,93–95] Similar to the CO IR spectra, the carbonyl bands for 1NiFSP are at 2064 cm^{-1}, indicating di- or tricarbonyls on highly under-coordinated Ni, likely Ni^{2+}. The carbonyl bands on the small Ni clusters and nanoparticles in 5NiFSP and 10NiFSP are broad and located in the range 2020 – 2070 cm^{-1}, which is likely due to CO adsorption on Ni nanoparticles and CO adsorbed on highly dispersed low coordinated Ni^{2+} sites. The negative band at 2090 cm^{-1} in the IR spectra suggests that the reduced surface of CeO_2 can be reoxidized by CO_2. The spectra also contain intense signals of formate species at 2845, 1597, and 1374 cm^{-1}.[92] Bands at 1413 and 1288 cm^{-1} are typically assigned to multiple carbonate and bicarbonate species originating from CO_2 adsorption on CeO_2.[96,97]

Then, we investigated the surface of the reduced 1NiFSP and 10NiFSP catalysts by operando IR spectroscopy during CO_2 methanation in a flow of 4 vol.% CO_2 and 16 vol.% H_2 balance by N_2 in the 200 – 300 °C range and using MS for gas-phase analysis (**Figure 4.5 and Figure C15).** Normalized MS data for 1NiFSP and 10NiFSP catalysts confirmed that 1NiFSP produces less CH_4 than 10NiFSP under these conditions (**Figure C16**). CH_4 formation already takes place at 200 °C in 10NiFSP and increases with temperature, as follows from the characteristic gas-phase CH_4 bands at 3017 and 1306 cm^{-1} [98] and the MS data (**Figure C15-16**). The CH_4 IR bands are weaker for 1NiFSP, confirming the lower CH_4 reaction rate for 1NiFSP (**Figure C15-16**). The IR spectra also contain clear signatures of gaseous CO for 1NiFSP and 10NiFSP, indicating CO_2 dissociation to CO. These CO species also adsorb on metallic Ni, giving rise to carbonyl bands in the 1800 – 2100 cm^{-1} range for 10NiFSP. In contrast, no carbonyl bands were observed for 1NiFSP. The spectra of 10NiFSP show a decreasing intensity of the atop carbonyl bands with increasing temperature, indicating lower CO coverage. **Figure 4.5** shows that both NiFSP catalysts feature pronounced broad IR bands in the carbonate region (1000 – 1700 cm^{-1}), which can be assigned to mono-, bi- and polydentate carbonate and bicarbonate species.[79,96] Their formation relates to the basicity of the CeO_2 support. The surface also contained formate groups, which followed from the C-H stretching band at 2841 cm^{-1}.[96] The several bands can be assigned to different formate species (formate-I at 1584, and 1565 cm^{-1}; formate-II at 1565 and 1359 cm^{-1}; formate-III at 1550, 1371 cm^{-1}). IR spectra of 1NiFSP contain formate bands at 2948 cm^{-1}, 2843 cm^{-1}, 1584 cm^{-1} and 1373 cm^{-1} for 1NiFSP, while formate bands for 10NiFSP located at 1578 cm^{-1} with minor contribution at 2843 cm^{-1}. The higher intensity of the formate band at 1584 cm^{-1} for 1NiFSP than that at 1578 cm^{-1} for 10NiFSP indicates a higher coverage with formate on the former catalyst. This slight shift in the location of this band can indicate a difference in Ni-CeO_2 interactions.[90]

The intensity of the formate bands decreases with temperature for 1NiFSP and 10NiFSP, whereas the intensity of the CO gas phase increases. Although not conclusive, these data indicate that formate species can be involved in CO_2 conversion to CO on these catalysts.

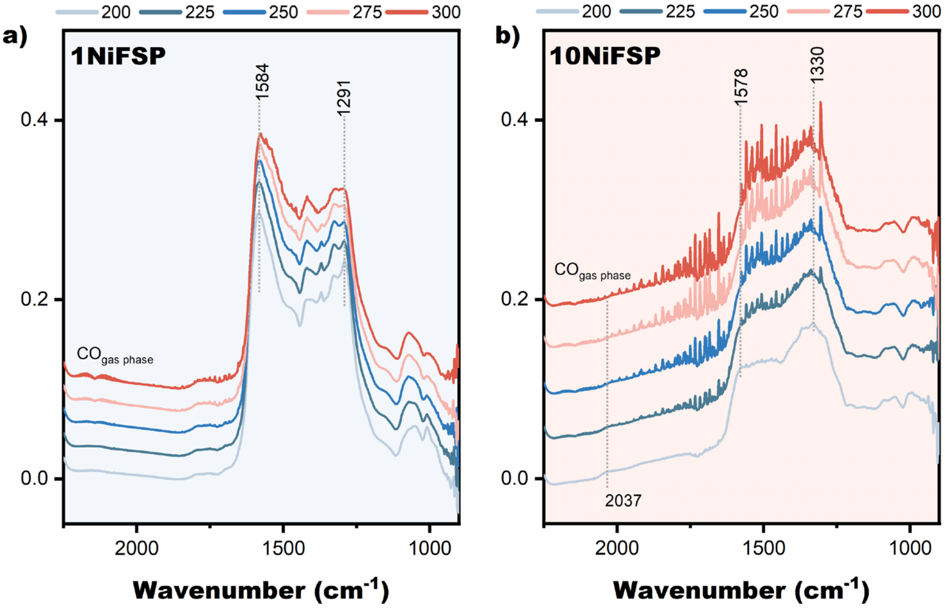

Figure 4.5. Background-subtracted IR spectra in a flow of 4 vol.% CO_2, 16 vol.% H_2 balanced by N_2 at 200 – 300 °C for (a) 1NiFSP, and (b) 10NiFSP samples reduced at 300 °C (conditions: 200 – 300 °C, 1 bar, 9 mg of sample).

Overall, IR spectroscopy shows that 1NiFSP and 10NiFSP contain two different structures of Ni after reduction: under-coordinated Ni atoms are formed at 1 mol.% Ni, while at 10 mol.% Ni formation of Ni nanoparticles with the small contribution of highly dispersed Ni is evident. Both catalysts can efficiently dissociate CO_2 to CO. Partial reduction of CeO_2 accompanied by the formation of oxygen vacancies is evident for both catalysts independent of Ni content. The decrease in the intensity of formate bands of 1NiFSP and 10NiFSP correlates with the increase in the intensity of CO gas phase, suggesting that a mechanism involving formate surface species plays a role in in rWGS activity.

Stability CO_2 hydrogenation

The stability of 1NiFSP and 10NiFSP was evaluated at 300 °C for 60 h (**Figure 4.6a**). The 10NiFSP catalyst is stable is over 60 h of reaction time and remains selective toward CH_4. In contrast, the 1NiFSP catalyst shows severe deactivation during 60 h on stream. The deactivation of 1NiFSP is accompanied by an increase in the CO selectivity at the expense of the CH_4 selectivity.

In situ TG analysis (**Figure 4.6b, Figure C17**) reveals a more significant weight gain for 1NiFSP in comparison with 10NiFSP during CO_2 hydrogenation at 300 °C in a flow of 50 mL/min of 0.8 vol.% CO_2, 3.2 vol.% H_2 in Ar for 70 h. The MS signal shows that the 10NiFSP catalyst is stable over 60 h of reaction time and remains selective toward CH_4. In comparison, the 1NiFSP shows severe deactivation during 60 h on stream, accompanied by an increase in the CO selectivity at the expense of the CH_4 selectivity (**Figure C17**). The significant difference in product distribution between 1NiFSP and 10NiFSP remains in line with the stability tests (**Figure 4.6a**). Likely, the 10NiFSP sample deactivates less due to enhanced H_2 dissociation on Ni nanoparticles. In contrast, the small Ni clusters are prone to deactivation as carbon deposited by CO dissociation cannot be removed fast enough. After deactivation, the 1NiFSP catalyst produces mainly CO, which is likely due to Ni-O-Ce sites, involving oxygen vacancies.

Temperature-programmed oxidation of the used catalysts revealed that significant mass losses start above 100 °C for both catalysts (**Figure 4.6c and C18**). The combustion temperature derived from the DTG curves exhibits a maximum at 127 °C for 1NiFSP and 135 °C for 10NiFSP. The MS signal shows CO_2 formation between 100 and 500 °C (**Figure C18**), pointing to the removal of soft coke[99], although we cannot exclude that CO_2 originates from formate species accumulated on the surface. Such formate species are typically removed by oxidation in the 70 – 330 °C temperature range[100,101], while carbonates decompose at much higher temperatures, typically above 600 °C.[102] The carbon deposit content is 2.6% for 1NiFSP and 2.2% for 10NiFSP (**Figure C18**). The “soft coke” formation is likely the cause of the deactivation of the very small clusters in 1NiFSP, blockage of the of active sites by formate/carbonate species cannot be excluded.

We employed quasi-in situ XPS to study the surface composition and reduction degree of the 1NiFSP and 10NiFSP catalysts after the reaction. The samples were reduced in the reactor chamber of a Kratos XPS system. The reduction was carried out at 300 °C for 4 h at atmospheric pressure in a flow of 20 vol.% H_2 in Ar. The reaction stability tests were carried out at 300 °C in a flow of 15 vol.% CO_2, 60 vol.% H_2, 25 vol.% Ar for 24 h. The resulting Ni $2p_{3/2}$ and Ce 3d XP spectra and their fits are shown in **Figure C19**, and the fit results are given in **Table C1**.

The low Ni signal does not allow reliable quantification of the Ni oxidation states in 1NiFSP. After reduction and reaction, the Ni $2p_{3/2}$ spectra of the 10NiFSP catalyst can be fitted with a Ni^0 component at 852.6 eV and a Ni^{2+} component at 583.7 eV (**Figure C8 and Figure C19**). A slight increase in the Ni^{2+} fraction is noted for 10NiFSP, when the spectra after reduction (41%) and after reaction (43%) are compared (**Table C1**). The fraction of Ce^{3+} of 10NiFSP slightly decreased from 29% after reduction to 26% after reaction (**Table C1**), which might be attributed to the reaction of surface oxygen vacancies in CeO_2 with CO_2. The fraction of Ce^{3+} in 1NiFSP slightly increases from 30% after reduction to 32% after reaction. The Ni/Ce surface ratios in the 10NiFSP decreased from 0.11 after reduction to 0.09 after the reaction, which can point to some sintering during the reaction, considering that the encapsulation of Ni by CeO_2 is not likely to occur at the low reaction temperature.

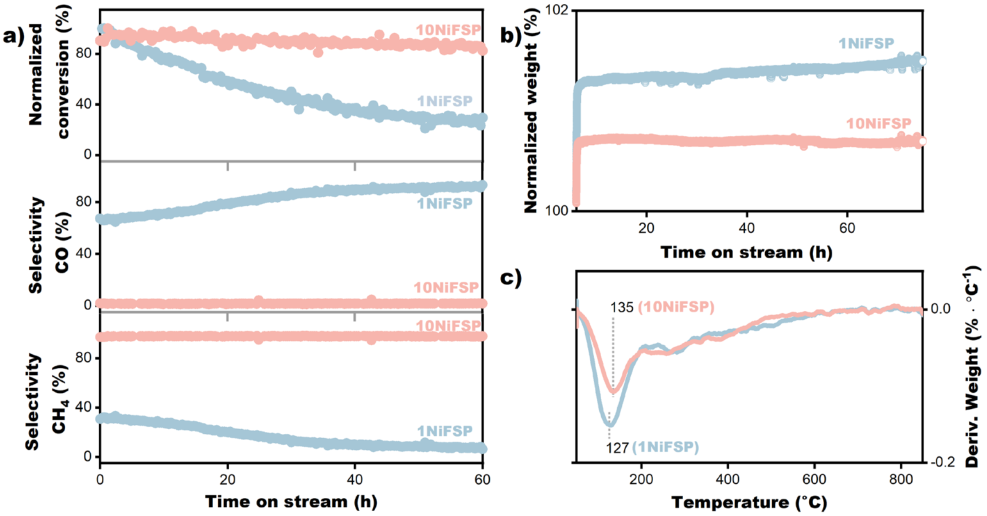

Figure 4.6. (a) Conversion and product selectivity as a function of the time on stream of 1NiFSP and 10NiFSP reduced at 300 °C (conditions: 300 °C, 50 mg of catalyst, 15 vol.% CO_2, 60 vol.% H_2, 25 vol.% Ar, 50 mL/min, 1 bar, ,). (b) TG analysis during deactivation over 1NiFSP and 10NiFSP catalysts (reaction conditions: 300 °C – 25 mg of catalyst, 0.8 vol.% CO_2, 3.2 vol.% H_2 in Ar, 50 mL/min, 1.5 bar, 70 h). (c) DTG analysis of temperature-programmed oxidation of spent 1NiFSP and 10NiFSP (TG analysis conditions: 50 – 900 °C, 25 mg of catalyst, 20 vol.% O_2 in He, 50 mL/min, 10 °C/min).

Fitting of the C 1s spectra of CeO_2-based samples with many overlapping components is challenging.[103] The component at 285 eV is assigned to C–C/C–H bonds due to carbon deposits (**Figure C20**).[103,104] The spectra of both samples contain a component around 290 eV, indicating the formation of carbonates on the catalyst surface after reduction and reaction[104,105], although it could also be due to formates, which typically appear at 288.0 eV.[106–109] Exposing the catalysts to the reaction mixture leads to a significant increase in the intensity of carbonates and/or formates, which is in line with observed IR results under CO_2 hydrogenation conditions (**Figure C15**).

The structural changes of the reduced NiFSP catalysts and the CeFSP support were investigated in more detail by in situ synchrotron XRD after reduction at 300 °C for 1 h and further exposure to CO_2 hydrogenation conditions at 300 °C for 1 h. The synchrotron XRD patterns of the NiFSP catalysts can be described well by CeO_2 and metallic Ni nanoparticles (**Figure C21-23**). The Ni nanoparticle size of the 20NiFSP and 30NiFSP catalysts increased from 3.5 nm after reduction to ~4.3 nm after CO_2 hydrogenation (**Figure C22**). The CeO_2 crystallite size of the NiFSP and CeFSP samples also increased slightly from ~ 10.5 nm after reduction to ~12.5 nm after reaction (**Figure 4.3c, Figure C21**).

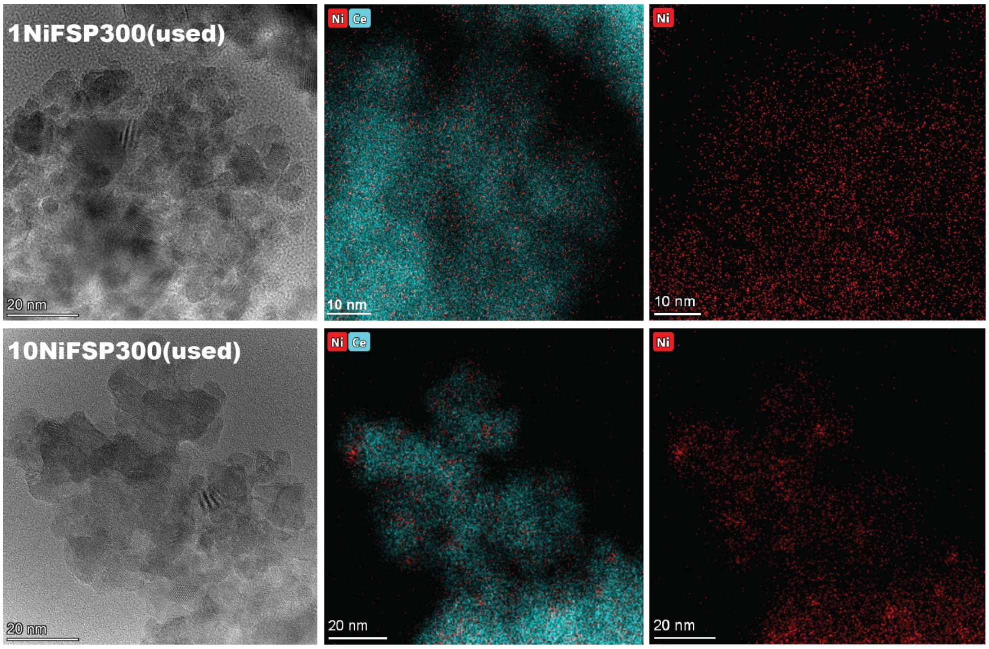

Figure 4.7. HAADF-STEM-EDX of used 1NiFSP (top) and 10NiFSP (bottom): HAADF-STEM images (left), Ni and Ce EDX maps (middle), and Ni EDX maps (right) (conditions: 300 °C, 1 bar, 50 mg of sample, 15 vol.% CO_2, 60 vol.% H_2, 25 vol.% Ar, 50 mL/min, 60 h).

Characterization of the used 10NiFSP catalyst by HAADF-STEM-EDX shows that the Ni metal crystallite size increased slightly from 3.4 ± 1.1 to 4.5 ± 1.9 nm (**Figure 4.7**). In contrast, the Ni phase in 1NiFSP remains uniformly distributed over the CeO_2 surface after reduction and the reaction stability test. the interaction between highly dispersed Ni^{2+} and CeO_2 in the 1NiFSP sample suppresses Ni sintering.[22,110–112]

Conclusions

Flame-made catalysts with varied Ni content (1 – 30 mol.%) were tested in CO_2 hydrogenation at atmospheric pressure. FSP preparation of Ni-CeO_2 catalysts resulted in small CeO_2 nanoparticles of ~8 nm with a higher surface area than conventional CeO_2, highly dispersed Ni, and, with increasing Ni content, segregated NiO particles. A relatively large fraction of Ni in 1NiFSP and 2.5NiFSP is present as Ni^{2+} ions in strong interaction with CeO_2 and they cannot be reduced at 300 °C. The amount of such stable highly dispersed Ni^{2+} species in the 10NiFSP catalyst was ~4 mol.%. Catalysts containing 20 mol.% Ni and 30 mol.% Ni contain segregated NiO nanoparticles of ~6 nm. These particles are partially reduced to metallic Ni nanoparticles of 2.5 nm (10 mol.% Ni) and 3.5 nm (20 mol.% Ni and 30 mol.% Ni) upon reduction at 300 °C. The Ni-weight-normalized activity does not vary strongly with the Ni content and was found ~4.4 $mmol_{CO2}/mol_{Ni}/s$ at 200 °C. There is, however, a strong shift in the product distribution: a very low Ni reduction degree with small metal Ni clusters in 1NiFSP led to the predominant formation of CO (71%) and less CH_4 (21%). A small amount of CH_3OH among the reaction products is associated with the hydrogenation of CO_2 on oxygen vacancies assisted by H_2 dissociation on very small Ni clusters. Catalysts containing more and larger Ni nanoparticles mainly yield CH_4 and small amounts of CO, while no CH_3OH was observed. The outstanding CO_2 methanation activity of FSP-prepared Ni-CeO_2 catalysts is linked to the synergy between relatively small metallic Ni nanoparticles and Ni^{2+}-O-Ce sites, involving oxygen vacancies. The Ni nanoparticles resulted in stable catalytic performance and high CH_4 selectivity. In contrast, the catalytic activity and CH_4 selectivity of highly dispersed Ni declined with reaction time, leading to increased CO selectivity. Most likely, these small Ni clusters deactivate as the carbon is not hydrogenated fast enough, possibly due to slower H_2 dissociation than on Ni nanoparticles. CO is formed on Ni^{2+}-O-Ce interface sites via a mechanism involving oxygen vacancies. Characterization of the used catalysts revealed slight sintering of the CeO_2 crystallites and Ni nanoparticles in 10NiFSP, while Ni remained highly dispersed in the 1NiFSP sample.

References

1. Mulvaney, D. Energy and the Environment I: Fossil Fuels. Sustainable Energy Transitions 81–108 (2020).

2. Doney, S. C., Fabry, V. J., Feely, R. A. & Kleypas, J. A. Ocean acidification: The other CO_2 problem. Ann Rev Mar Sci 1, 169–192 (2009).

3. Cox, P. M., Betts, R. A., Jones, C. D., Spall, S. A. & Totterdell, I. J. Acceleration of global warming due to carbon-cycle feedbacks in a coupled climate model. Nature 408, 184–187 (2000).

4. Solomon, S., Plattner, G. K., Knutti, R. & Friedlingstein, P. Irreversible climate change due to carbon dioxide emissions. Proc Natl Acad Sci U S A 106, 1704–1709 (2009).

5. Wang, W., Wang, S., Ma, X. & Gong, J. Recent advances in catalytic hydrogenation of carbon dioxide. Chem Soc Rev 40, 3703–3727 (2011).

6. Guo, L., Guo, X., He, Y. & Tsubaki, N. CO_2 heterogeneous hydrogenation to carbon-based fuels: recent key developments and perspectives. J Mater Chem A Mater 11, 11637–11669 (2023).

7. Ronda-Lloret, M., Rothenberg, G. & Shiju, N. R. A Critical Look at Direct Catalytic Hydrogenation of Carbon Dioxide to Olefins. ChemSusChem 12, 3896–3914 (2019).

8. Kondratenko, E. V., Mul, G., Baltrusaitis, J., Larrazábal, G. O. & Pérez-Ramírez, J. Status and perspectives of CO_2 conversion into fuels and chemicals by catalytic, photocatalytic and electrocatalytic processes. Energy Environ Sci 6, 3112–3135 (2013).

9. Ashok, J. et al. A review of recent catalyst advances in CO_2 methanation processes. Catal Today 356, 471–489 (2020).

10. Lee, W. J. et al. Recent trend in thermal catalytic low temperature CO_2 methanation: A critical review. Catal Today 368, 2–19 (2021).

11. Marconi, E., Tuti, S. & Luisetto, I. Structure-Sensitivity of CO_2 Methanation over Nanostructured Ni Supported on CeO_2 Nanorods. Catalysts 2019, Vol. 9, Page 375 9, 375 (2019).

12. Simons, J. F. M. et al. Structure Sensitivity of CO_2 Hydrogenation on Ni Revisited. J Am Chem Soc 145, 20289–20301 (2023).

13. Van Santen, R. A. Complementary structure sensitive and insensitive catalytic relationships. Acc Chem Res 42, 57–66 (2009).

14. Boudart, M. Catalysis by Supported Metals. Advances in Catalysis 20, 153–166 (1969).

15. Adhikari, D., Whitcomb, C. A., Zhang, W., Zhang, S. & Davis, R. J. Revisiting the influence of Ni particle size on the hydrogenation of CO_2 to CH_4 over Ni/CeO_2. J Catal 438, 115708 (2024).

16. Sterk, E. B. et al. Structure Sensitivity of CO_2 Conversion over Nickel Metal Nanoparticles Explained by Micro-Kinetics Simulations. JACS Au 2, 2714–2730 (2022).

17. Silaghi, M. C., Comas-Vives, A. & Copéret, C. CO_2 Activation on Ni/γ-Al_2O_3 Catalysts by First-Principles Calculations: From Ideal Surfaces to Supported Nanoparticles. ACS Catal 6, 4501–4505 (2016).

18. Ke, Q., Kang, L., Chen, X. & Wu, Y. DFT study of CO_2 catalytic conversion by H_2 over Ni13 cluster. Journal of Chemical Sciences 132, 1–11 (2020).

19. Matsubu, J. C., Yang, V. N. & Christopher, P. Isolated metal active site concentration and stability control catalytic CO_2 reduction selectivity. J Am Chem Soc 137, 3076–3084 (2015).

20. Aitbekova, A. et al. Low-Temperature Restructuring of CeO_2-Supported Ru Nanoparticles Determines Selectivity in CO_2 Catalytic Reduction. J Am Chem Soc 140, 13736–13745 (2018).

21. Kwak, J. H., Kovarik, L. & Szanyi, J. CO_2 reduction on supported Ru/Al_2O_3 catalysts: Cluster size dependence of product selectivity. ACS Catal 3, 2449–2455 (2013).

22. Li, S. et al. Tuning the Selectivity of Catalytic Carbon Dioxide Hydrogenation over Iridium/Cerium Oxide Catalysts with a Strong Metal–Support Interaction. Angewandte Chemie International Edition 56, 10761–10765 (2017).

23. Guo, Y. et al. Low-Temperature CO_2 Methanation over CeO_2-Supported Ru Single Atoms, Nanoclusters, and Nanoparticles Competitively Tuned by Strong Metal−Support Interactions and H-Spillover Effect. (2018).

24. Vogt, C. et al. Unravelling structure sensitivity in CO_2 hydrogenation over nickel. Nature Catalysis 2017 1:2 1, 127–134 (2018).

25. Lin, L. et al. Effect of Ni particle size on the production of renewable methane from CO_2 over Ni/CeO_2 catalyst. Journal of Energy Chemistry 61, 602–611 (2021).

26. Barreau, M. et al. Ionic Nickel Embedded in Ceria with High Specific CO_2 Methanation Activity. Angewandte Chemie International Edition 62, e202302087 (2023).

27. Dreyer, J. A. H. et al. Influence of the oxide support reducibility on the CO_2 methanation over Ru-based catalysts. Appl Catal B 219, 715–726 (2017).

28. Guo, Y. et al. Low-Temperature CO_2 Methanation over CeO_2-Supported Ru Single Atoms, Nanoclusters, and Nanoparticles Competitively Tuned by Strong Metal-Support Interactions and H-Spillover Effect. ACS Catal 8, 6203–6215 (2018).

29. Dostagir, N. H. M. et al. Co Single Atoms in ZrO_2 with Inherent Oxygen Vacancies for Selective Hydrogenation of CO_2 to CO. ACS Catal 11, 9450–9461 (2021).

30. Le, T. A., Kim, M. S., Lee, S. H. & Park, E. D. CO and CO_2 Methanation Over Supported Cobalt Catalysts. Top Catal 60, 714–720 (2017).

31. Pan, C. J. et al. Tuning/exploiting Strong Metal-Support Interaction (SMSI) in Heterogeneous Catalysis. J Taiwan Inst Chem Eng 74, 154–186 (2017).

32. van Deelen, T. W., Hernández Mejía, C. & de Jong, K. P. Control of metal-support interactions in heterogeneous catalysts to enhance activity and selectivity. Nature Catalysis vol. 2 955–970 (2019).

33. Farmer, J. A. & Campbell, C. T. Ceria maintains smaller metal catalyst particles

by strong metal-support bonding. Science (1979) 329, 933–936 (2010).

34. Muravev, V. et al. Size of cerium dioxide support nanocrystals dictates reactivity of highly dispersed palladium catalysts. Science (1979) 380, 1174–1178 (2023).

35. Cargnello, M. et al. Control of metal nanocrystal size reveals metal-support interface role for ceria catalysts. Science (1979) 341, 771–773 (2013).

36. Boaro, M., Colussi, S. & Trovarelli, A. Ceria-based materials in hydrogenation and reforming reactions for CO_2 valorization. Front Chem 7, 426236 (2019).

37. Konsolakis, M. et al. Rational Design of Ceria-Based Nanocatalysts for CO_2 Hydrogenation to Value-Added Products.

38. Rodriguez, J. A., Grinter, D. C., Liu, Z., Palomino, R. M. & Senanayake, S. D. Ceria-based model catalysts: Fundamental studies on the importance of the metal-ceria interface in CO oxidation, the water-gas shift, CO_2 hydrogenation, and methane and alcohol reforming. Chemical Society Reviews vol. 46 1824–1841 (2017).

39. Tada, S., Shimizu, T., Kameyama, H., Haneda, T. & Kikuchi, R. Ni/CeO_2 catalysts with high CO_2 methanation activity and high CH_4 selectivity at low temperatures. Int J Hydrogen Energy 37, 5527–5531 (2012).

40. Xie, Y. et al. Frustrated Lewis Pairs Boosting Low-Temperature CO_2 Methanation Performance over Ni/CeO_2 Nanocatalysts. ACS Catalysis 12, 10587–10602 (2022).

41. Hao, Z. et al. Decoupling the effect of Ni particle size and surface oxygen deficiencies in CO_2 methanation over ceria supported Ni. Appl Catal B 286, 119922 (2021).

42. Vrijburg, W. L. et al. Ceria–zirconia encapsulated Ni nanoparticles for CO_2 methanation. Catal Sci Technol 9, 5001–5010 (2019).

43. Aldana, P. A. U. et al. Catalytic CO_2 valorization into CH_4 on Ni-based ceria-zirconia. Reaction mechanism by operando IR spectroscopy. Catal Today 215, 201–207 (2013).

44. Xu, J. et al. Influence of pretreatment temperature on catalytic performance of rutile TiO_2-supported ruthenium catalyst in CO_2 methanation. J Catal 333, 227–237 (2016).

45. Zhu, J. et al. Mechanism and Nature of Active Sites for Methanol Synthesis from CO/CO_2 on Cu/CeO_2. ACS Catal 10, 11532–11544 (2020).

46. Stadnichenko, A. I. et al. Study of active surface centers of Pt/CeO_2 catalysts prepared using radio-frequency plasma sputtering technique. Surf Sci 679, 273–283 (2019).

47. Larachi, F., Pierre, J., Adnot, A. & Bernis, A. Ce 3d XPS study of composite $Ce_xMn_{1-x}O_{2-y}$ wet oxidation catalysts. Appl Surf Sci 195, 236–250 (2002).

48. Kato, S. et al. Quantitative depth profiling of Ce^{3+} in Pt/CeO_2 by in situ high-energy XPS in a hydrogen atmosphere. Physical Chemistry Chemical Physics 17, 5078–5083 (2015).

49. Skála, T., Šutara, F., Prince, K. C. & Matolín, V. Cerium oxide stoichiometry alteration via Sn deposition: Influence of temperature. J Electron Spectros Relat

Phenomena 169, 20–25 (2009).

50. Hagfeldt, A. & Grätzel, M. Light-Induced Redox Reactions in Nanocrystalline Systems. Chem Rev 95, 49–68 (1995).

51. Wu, T. S. et al. Dramatic band gap reduction incurred by dopant coordination rearrangement in Co-doped nanocrystals of CeO_2. Scientific Reports 2017 7:1 7, 1–7 (2017).

52. Sajith, N. V. et al. Visible light active Ni^{2+} doped CeO_2 nanoparticles for the removal of methylene blue dye from water. Results in Engineering 16, 100664 (2022).

53. Mahammadunnisa, S., Manoj Kumar Reddy, P., Lingaiah, N. & Subrahmanyam, C. $NiO/Ce_{1-x}Ni_xO_{2-\delta}$ as an alternative to noble metal catalysts for CO oxidation. Catal Sci Technol 3, 730–736 (2013).

54. Rao, P. V. R., Kumar, V. P., Rao, G. S. & Chary, K. V. R. Vapor phase selective hydrogenation of acetone to methyl isobutyl ketone (MIBK) over Ni/CeO_2 catalysts. Catal Sci Technol 2, 1665–1673 (2012).

55. Rives, V. & Kannan, S. Layered double hydroxides with the hydrotalcite-type structure containing Cu^{2+}, Ni^{2+} and Al^{3+}. J Mater Chem 10, 489–495 (2000).

56. Wu, Z., Li, M., Howe, J., Meyer, H. M. & Overbury, S. H. Probing defect sites on CeO_2 nanocrystals with well-defined surface planes by raman spectroscopy and O_2 adsorption. Langmuir 26, 16595–16606 (2010).

57. Li, X. et al. Strong Metal-Support Interactions of Ni-CeO_2 Effectively Improve the Performance of a Molten Hydroxide Direct Carbon Fuel Cell. ACS Omega 7, 24646–24655 (2022).

58. Fang, W. et al. Room Temperature Hydrogen Production from Ethanol over $CeNi_XH_ZO_Y$ Nano-Oxyhydride Catalysts. ChemCatChem 5, 2207–2216 (2013).

59. Mironova-Ulmane, N., Kuzmin, A., Sildos, I., Puust, L. & Grabis, J. Magnon and Phonon Excitations in Nanosized NiO. Latvian Journal of Physics and Technical Sciences 56, 61–72 (2019).

60. Fornasiero, P. et al. Rh-Loaded CeO_2-ZrO_2 Solid-Solutions as Highly Efficient Oxygen Exchangers: Dependence of the Reduction Behavior and the Oxygen Storage Capacity on the Structural-Properties. J Catal 151, 168–177 (1995).

61. Wang, H., Ye, J. L., Liu, Y., Li, Y. D. & Qin, Y. N. Steam reforming of ethanol over Co_3O_4/CeO_2 catalysts prepared by different methods. Catal Today 129, 305–312 (2007).

62. Carvalho, F. L. S., Asencios, Y. J. O., Bellido, J. D. A. & Assaf, E. M. Bio-ethanol steam reforming for hydrogen production over Co_3O_4/CeO_2 catalysts synthesized by one-step polymerization method. Fuel Processing Technology 142, 182–191 (2016).

63. Tang, R., Ullah, N., Hui, Y., Li, X. & Li, Z. Enhanced CO_2 methanation activity over Ni/CeO_2 catalyst by one-pot method. Molecular Catalysis 508, 111602 (2021).

64. Vita, A. et al. Activity and stability of powder and monolith-coated Ni/GDC catalysts for CO_2 methanation. Appl Catal B 226, 384–395 (2018).

65. Luisetto, I., Tuti, S., Romano, C., Boaro, M. & Di Bartolomeo, E. Dry reforming of methane over Ni supported on doped CeO_2: New insight on the role of dopants for

CO_2 activation. Journal of CO_2 Utilization 30, 63–78 (2019).

66. Parastaev, A. et al. Boosting CO_2 hydrogenation via size-dependent metal–support interactions in cobalt/ceria-based catalysts. Nat Catal 3, 526–533 (2020).

67. Marrocchelli, D., Bishop, S. R., Tuller, H. L. & Yildiz, B. Understanding Chemical Expansion in Non-Stoichiometric Oxides: Ceria and Zirconia Case Studies. Adv Funct Mater 22, 1958–1965 (2012).

68. Biesinger, M. C. et al. Resolving surface chemical states in XPS analysis of first row transition metals, oxides and hydroxides: Cr, Mn, Fe, Co and Ni. Appl Surf Sci 257, 2717–2730 (2011).

69. Artiglia, L. et al. Introducing Time Resolution to Detect Ce^{3+} Catalytically Active Sites at the Pt/CeO_2 Interface through Ambient Pressure X-ray Photoelectron Spectroscopy. Journal of Physical Chemistry Letters 8, 102–108 (2017).

70. Zhang, S. et al. Boosting selective hydrogenation through hydrogen spillover on supported-metal catalysts at room temperature. Appl Catal B 297, 120418 (2021).

71. Ghogia, A. C. et al. Hydrogen Spillover in the Fischer-Tropsch Synthesis on Carbon-supported Cobalt Catalysts. ChemCatChem 12, 1117–1128 (2020).

72. Weststrate, C. J., van de Loosdrecht, J. & Niemantsverdriet, J. W. Spectroscopic insights into cobalt-catalyzed Fischer-Tropsch synthesis: A review of the carbon monoxide interaction with single crystalline surfaces of cobalt. J Catal 342, 1–16 (2016).

73. Wang, H., Hu, Y., Adogwa, A., Yang, M. & Lu, T.-B. The in situ growth of atomically dispersed Ni species on CeO_2 during low-temperature CH_4/CO_2 reforming. J Mater Chem A Mater (2024).

74. Meunier, F. C. On the contamination with nickel and nickel tetracarbonyl during FT-IR investigation of catalysts under CO-containing gases. J Catal 372, 388 (2019).

75. Cárdenas-Arenas, A. et al. Isotopic and in situ DRIFTS study of the CO_2 methanation mechanism using Ni/CeO_2 and Ni/Al_2O_3 catalysts. Appl Catal B 265, 118538 (2020).

76. Chen, W., Zijlstra, B., Filot, I. A. W., Pestman, R. & Hensen, E. J. M. Mechanism of Carbon Monoxide Dissociation on a Cobalt Fischer–Tropsch Catalyst. ChemCatChem 10, 136–140 (2018).

77. Zijlstra, B. et al. Coverage Effects in CO Dissociation on Metallic Cobalt Nanoparticles. ACS Catal 9, 7365–7372 (2019).

78. Li, C. et al. Adsorption of carbon monoxide and carbon dioxide on cerium oxide studied by Fourier-transform infrared spectroscopy. Part 2.—Formation of formate species on partially reduced CeO_2 at room temperature. Journal of the Chemical Society, Faraday Transactions 1: Physical Chemistry in Condensed Phases 85, 1451–1461 (1989).

79. Binet, C., Daturi, M. & Lavalley, J. C. IR study of polycrystalline ceria properties in oxidised and reduced states. Catal Today 50, 207–225 (1999).

80. Wu, W., Savereide, L. M., Notestein, J. & Weitz, E. In-situ IR spectroscopy as a probe of oxidation/reduction of Ce in nanostructured CeO_2. Appl Surf Sci 445, 548–554 (2018).

81. Binet, C., Badri, A., Boutonnet-Kizling, M. & Lavalley, J. C. FTIR study of carbon monoxide adsorption on ceria: CO_{2-2} carbonite dianion adsorbed species. Journal of the Chemical Society, Faraday Transactions 90, 1023–1028 (1994).

82. Vogt, C. et al. Understanding carbon dioxide activation and carbon–carbon coupling over nickel. Nature Communications 2019 10:1 10, 1–10 (2019).

83. Jalama, K. Carbon dioxide hydrogenation over nickel-, ruthenium-, and copper-based catalysts: Review of kinetics and mechanism. Catalysis Reviews 59, 95–164 (2017).

84. Zhang, Z. et al. Advances in studies of the structural effects of supported Ni catalysts for CO_2 hydrogenation: from nanoparticle to single atom catalyst. J Mater Chem A Mater 10, 5792–5812 (2022).

85. Gac, W. et al. Effects of support composition on the performance of nickel catalysts in CO_2 methanation reaction. Catal Today 357, 468–482 (2020).

86. Xie, F., Xu, S., Deng, L., Xie, H. & Zhou, G. CO_2 hydrogenation on $Co/CeO_{2-\delta}$ catalyst: Morphology effect from CeO_2 support. Int J Hydrogen Energy 45, 26938–26952 (2020).

87. Bian, Z., Chan, Y. M., Yu, Y. & Kawi, S. Morphology dependence of catalytic properties of Ni/CeO_2 for CO_2 methanation: A kinetic and mechanism study. Catal Today 347, 31–38 (2020).

88. Jomjaree, T. et al. Catalytic performance of Ni catalysts supported on CeO_2 with different morphologies for low-temperature CO_2 methanation. Catal Today 375, 234–244 (2021).

89. Oh, R. et al. Insights into CeO_2 Particle Size Dependent Selectivity Control for CO_2 Hydrogenation Using Co/CeO_2 Catalysts. ACS Catal 897–906 (2024).

90. Li, B. et al. CeO_2-supported Fe, Co and Ni toward CO_2 hydrogenation: Tuning catalytic performance via metal-support interaction. Journal of Rare Earths 41, 926–932 (2023).

91. Wang, S., Pan, Q., Peng, J. & Wang, S. In situ FTIR spectroscopic study of the CO_2 methanation mechanism on $Ni/Ce_{0.5}Zr_{0.5}O_2$. Catal Sci Technol 4, 502–509 (2014).

92. Konishcheva, M. V. et al. On the Mechanism of CO and CO_2 Methanation Over Ni/CeO_2 Catalysts. Top Catal 59, 1424–1430 (2016).

93. Sang, J. C. et al. Adsorbed Carbon Formation and Carbon Hydrogenation for CO_2 Methanation on the Ni(111) Surface: ASED-MO Study. Bull Korean Chem Soc 26, 1682–1688 (2005).

94. Ren, J. et al. Insights into the mechanisms of CO_2 methanation on Ni(111) surfaces by density functional theory. Appl Surf Sci 351, 504–516 (2015).

95. Heine, C., Lechner, B. A. J., Bluhm, H. & Salmeron, M. Recycling of CO_2: Probing the Chemical State of the Ni(111) Surface during the Methanation Reaction with Ambient-Pressure X-Ray Photoelectron Spectroscopy. J Am Chem Soc 138, 13246–13252 (2016).

96. Daturi, M., Binet, C., Lavalley, J. C. & Blanchard, G. Surface FTIR investigations on $Ce_xZr_{1-x}O_2$ system. Surf. Interface Anal 30, 273–277 (2000).

97. Saw, E. T. et al. Bimetallic Ni–Cu catalyst supported on CeO_2 for high-temperature water–gas shift reaction: Methane suppression via enhanced CO adsorption. J Catal 314, 32–46 (2014).

98. Feron, O., Langlais, F. & Naslain, R. In-situ analysis of gas phase decomposition and kinetic study during carbon deposition from mixtures of carbon tetrachloride and methane. Carbon N Y 37, 1355–1361 (1999).

99. Vogt, E. T. C., Fu, D. & Weckhuysen, B. M. Carbon Deposit Analysis in Catalyst Deactivation, Regeneration, and Rejuvenation. Angewandte Chemie International Edition 62, e202300319 (2023).

100. Senanayake, S. D. & Mullins, D. R. Redox pathways for HCOOH decomposition over CeO_2 surfaces. Journal of Physical Chemistry C 112, 9744–9752 (2008).

101. Li, C., Domen, K., Maruya, K. ichi & Onishi, T. Spectroscopic identification of adsorbed species derived from adsorption and decomposition of formic acid, methanol, and formaldehyde on cerium oxide. J Catal 125, 445–455 (1990).

102. Janoš, P. et al. Recovery of Cerium Dioxide from Spent Glass-Polishing Slurry and Its Utilization as a Reactive Sorbent for Fast Degradation of Toxic Organophosphates. Advances in Materials Science and Engineering 2015, 241421 (2015).

103. Gengenbach, T. R., Major, G. H., Linford, M. R. & Easton, C. D. Practical guides for x-ray photoelectron spectroscopy (XPS): Interpreting the carbon 1s spectrum. Journal of Vacuum Science & Technology A: Vacuum, Surfaces, and Films 39, (2021).

104. Liu, Z. et al. Dry Reforming of Methane on a Highly-Active Ni-CeO_2 Catalyst: Effects of Metal-Support Interactions on C−H Bond Breaking. Angewandte Chemie International Edition 55, 7455–7459 (2016).

105. Zhong, L. et al. Improving the Catalytic Performance of Cobalt for CO Preferential Oxidation by Stabilizing the Active Phase through Vanadium Promotion. ACS Catal 11, 5369–5385 (2021).

106. Senanayake, S. D. et al. Probing the reaction intermediates for the water–gas shift over inverse CeO_x/Au(1 1 1) catalysts. J Catal 271, 392–400 (2010).

107. Lykhach, Y. et al. Adsorption and decomposition of formic acid on model ceria and Pt/Ceria catalysts. Journal of Physical Chemistry C 117, 12483–12494 (2013).

108. Senanayake, S. D. & Mullins, D. R. Redox pathways for HCOOH decomposition over CeO_2 surfaces. Journal of Physical Chemistry C 112, 9744–9752 (2008).

109. Mudiyanselage, K., Baber, A. E., Liu, Z., Senanayake, S. D. & Stacchiola, D. J. Isolation and characterization of formates on CeO_x–Cu_yO/Cu(1 1 1). Catal Today 240, 190–200 (2015).

110. Farmer, J. A. & Campbell, C. T. Ceria maintains smaller metal catalyst particles by strong metal-support bonding. Science (1979) 329, 933–936 (2010).

111. Zhang, X. et al. Highly Dispersed Copper over β-Mo_2C as an Efficient and Stable Catalyst for the Reverse Water Gas Shift (RWGS) Reaction. ACS Catal 7, 912–918 (2017).

112. Chen, P. et al. Experimental and Theoretical Understanding of Nitrogen-Doping-Induced Strong Metal-Support Interactions in Pd/TiO_2 Catalysts for Nitrobenzene Hydrogenation. ACS Catal 7, 1197–1206 (2017).

Appendix C

Figures.

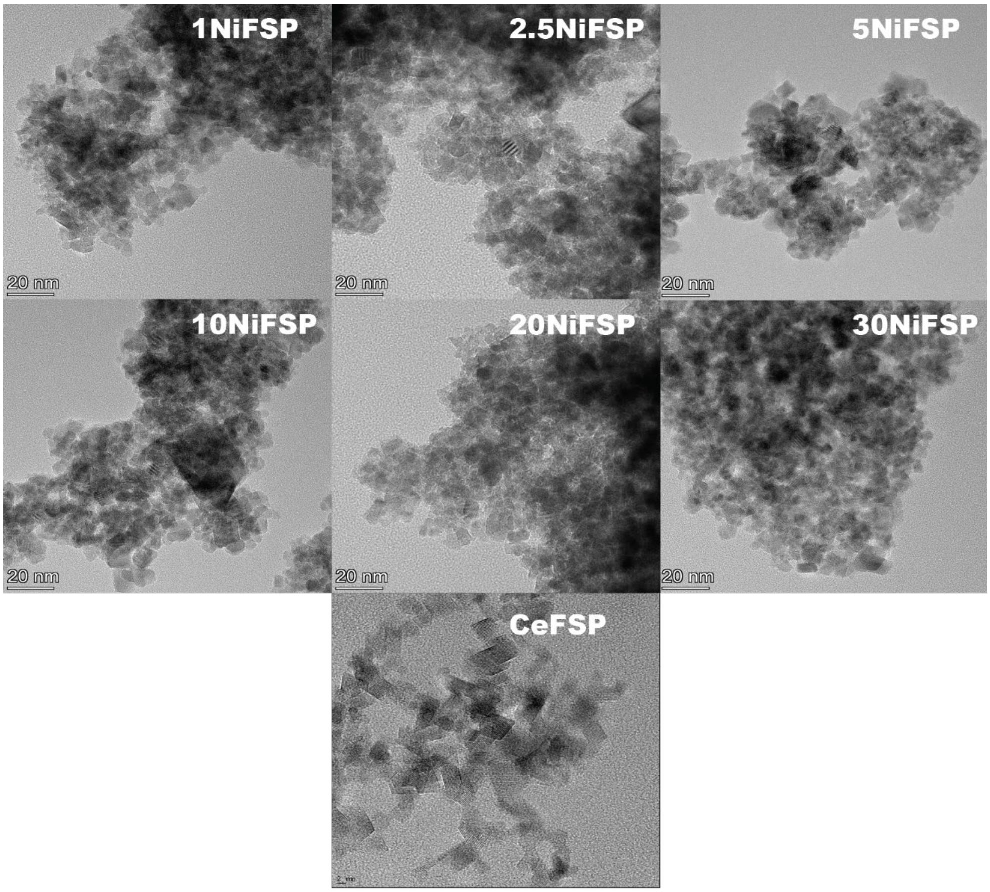

Figure C1. TEM images of as-prepared CeFSP and NiFSP catalysts. Corresponding particle size estimations are shown in Table 4.1.

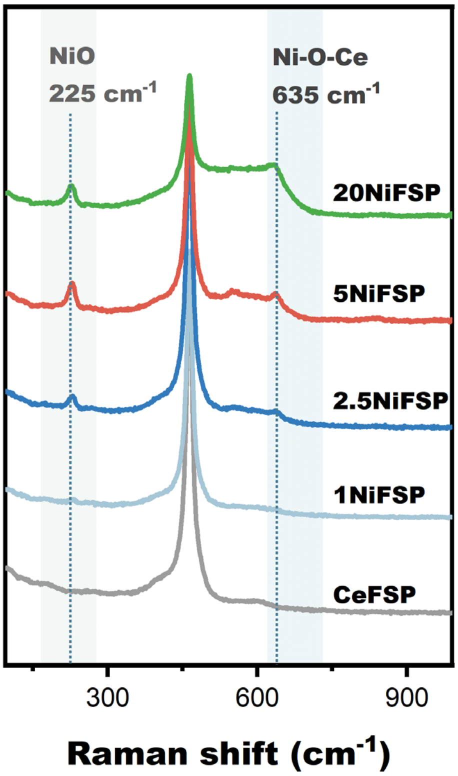

Figure C2. Raman spectra of as-prepared CeFSP and NiFSP catalysts (λ = 532 nm).

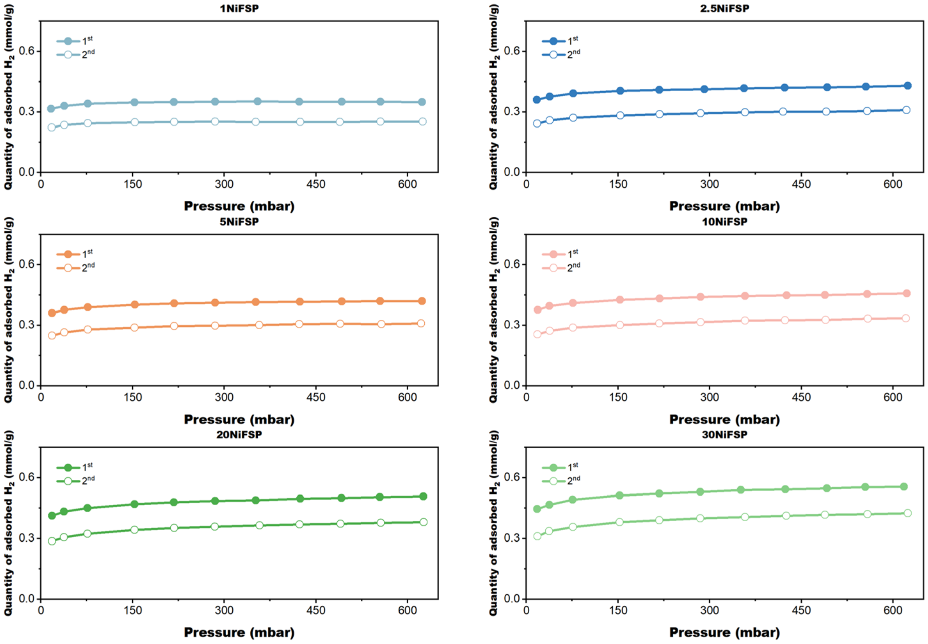

Figure C3. H_2 chemisorption isotherms over NiFSP reduced at 300 °C.

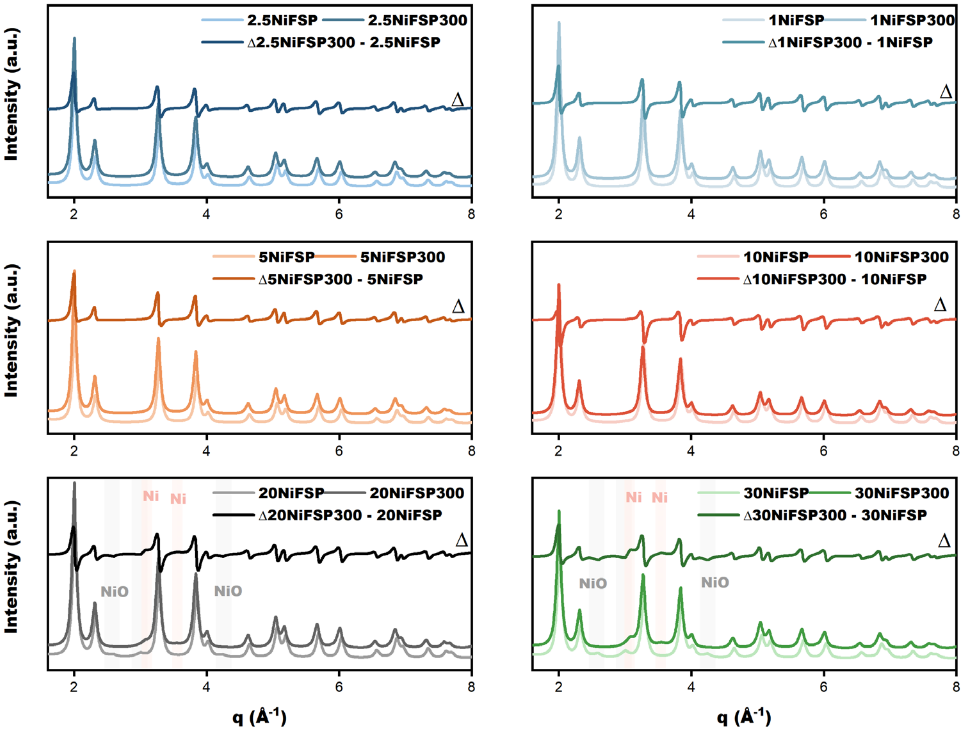

Figure C4. Synchrotron XRD (λ = 0.124 Å) patterns of NiFSP before and after reductive pretreatment (xNiFSP300). ΔXRD difference is obtained by subtraction of the diffractogram of as-prepared sample from reduced diffractogram of the same sample.

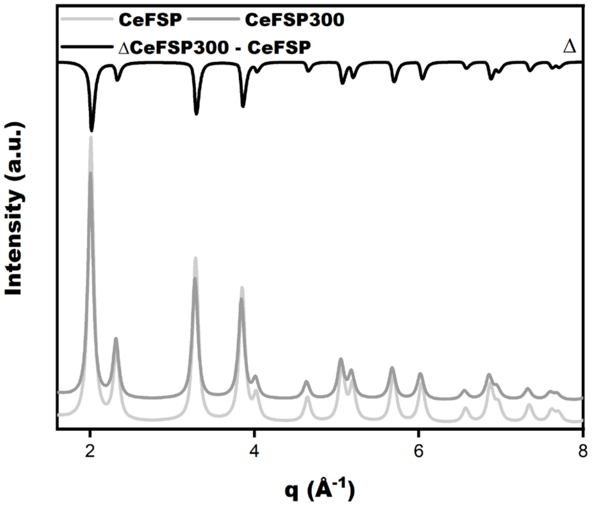

Figure C5. Synchrotron XRD (λ = 0.124 Å) patterns of as-prepared CeFSP and CeFSP after reductive pretreatment (CeFSP300). ΔXRD difference is obtained by subtraction of the diffractogram of the as-prepared sample from the reduced diffractogram of the same sample.

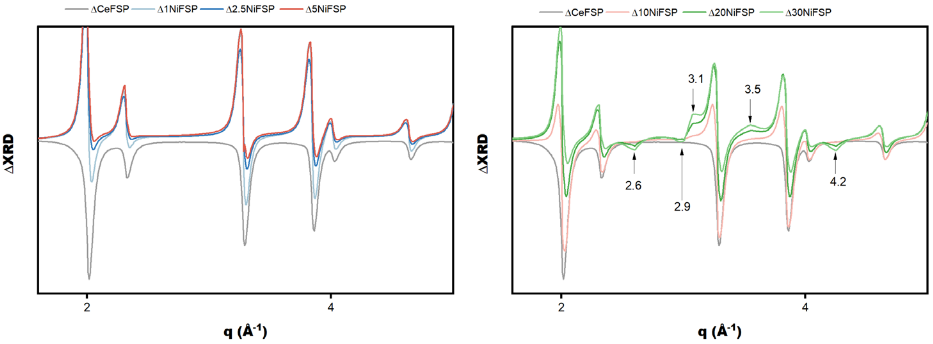

Figure C6. Synchrotron ΔXRD (λ = 0.124 Å) patterns of CeFSP and NiFSP before and after reductive pretreatment. ΔXRD difference is obtained by subtraction of the diffractogram of as-prepared sample from reduced diffractogram of the same sample.

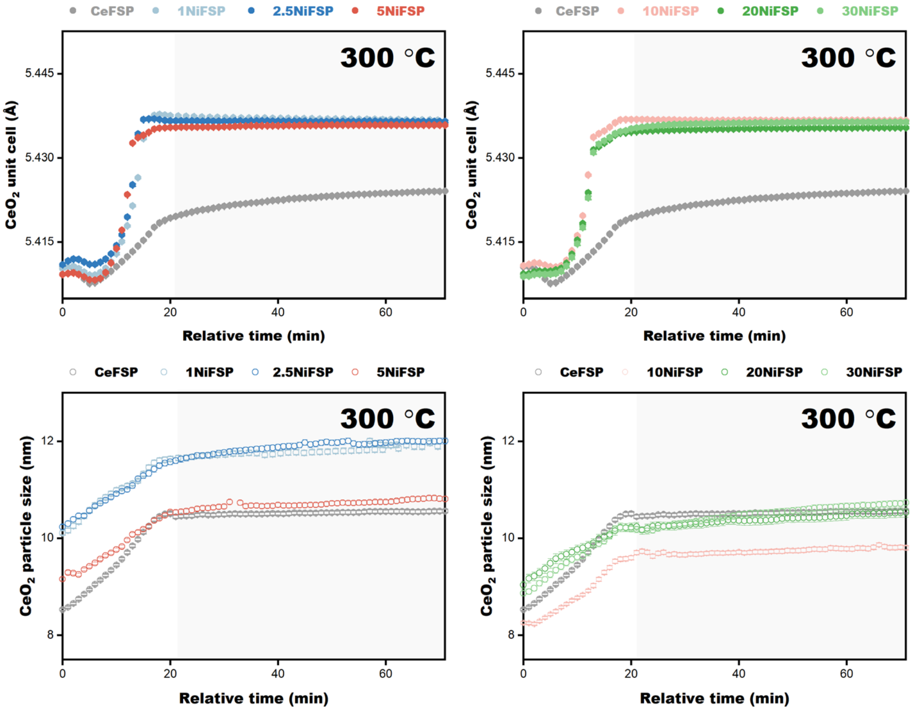

Figure C7. Refined unit cell parameters(top) and particle sizes(bottom) of CeO_2 for CeFSP and NiFSP catalysts during reductive pretreatment and dwell at 300 °C (grey area).

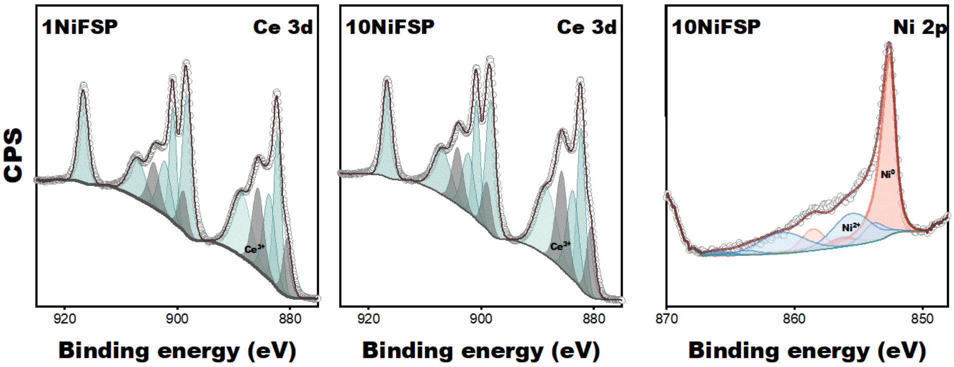

Figure C8. Deconvolution of Ce3d and Ni $2p_{3/2}$ of 1NiFSP and 10NiFSP, reduced at 300 °C for 4 h (conditions: 20 vol.% H_2 in Ar, 50 mL/min, 4 h)

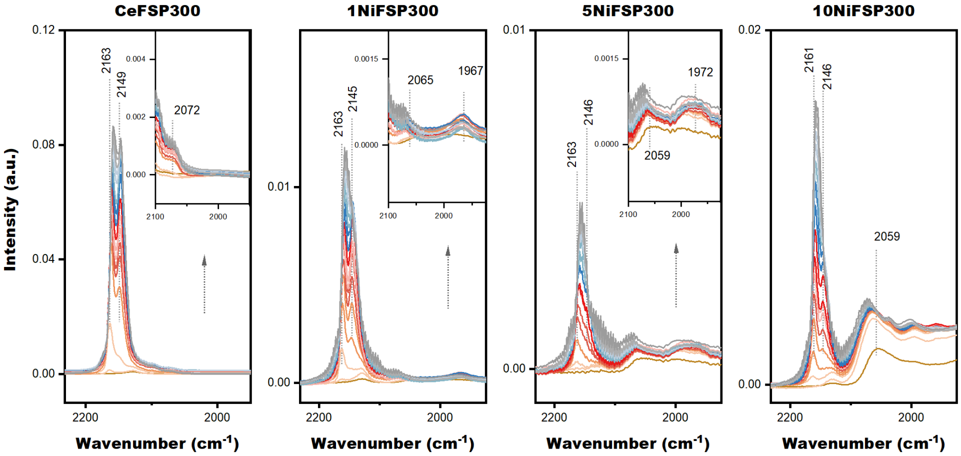

Figure C9. IR spectra of the CeFSP and NiFSP reduced at 300 °C after CO adsorption at liquid N_2 temperature (conditions: 1 – 10 mbar CO).

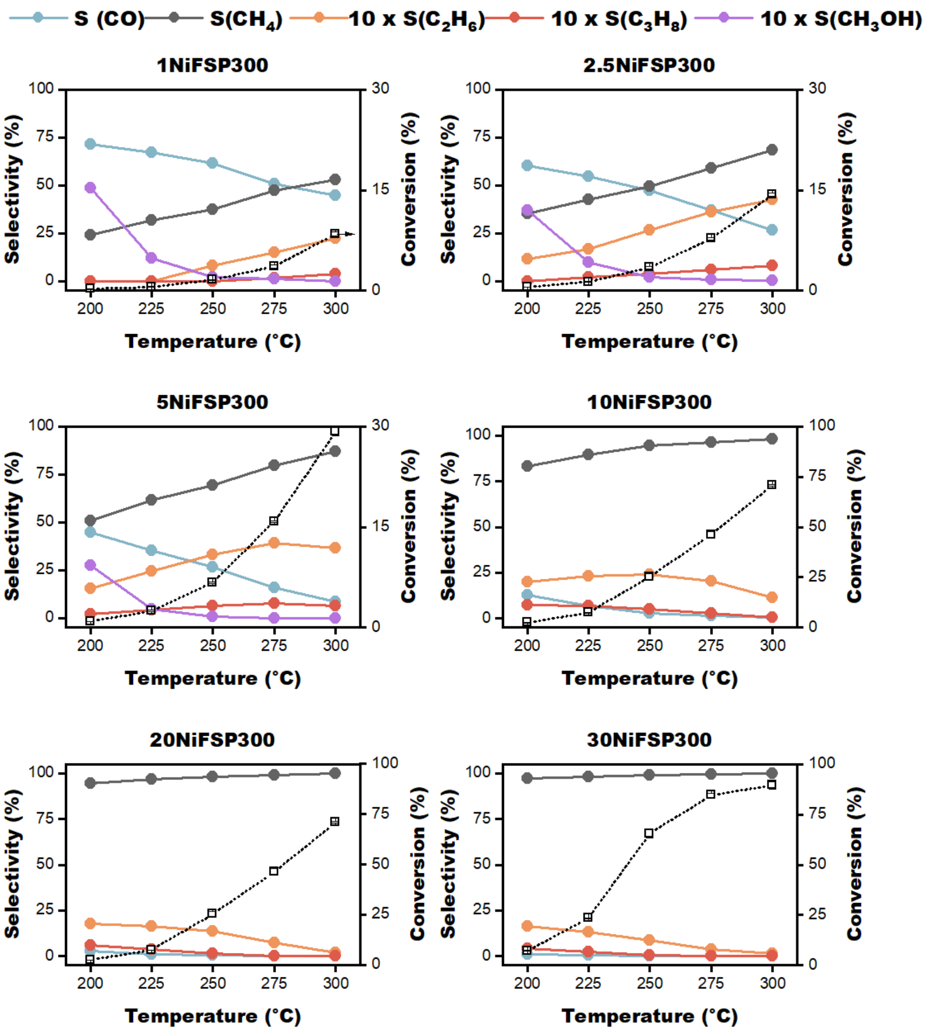

Figure C10. Catalytic performance of NiFSP catalysts reduced at 300°C in CO_2 hydrogenation as a function of temperature (conditions: 200 – 300 °C, 50 mg of catalyst, 15 vol.% CO_2, 60 vol.% H_2, 25 vol.% Ar, 50 mL/min, 1 bar).

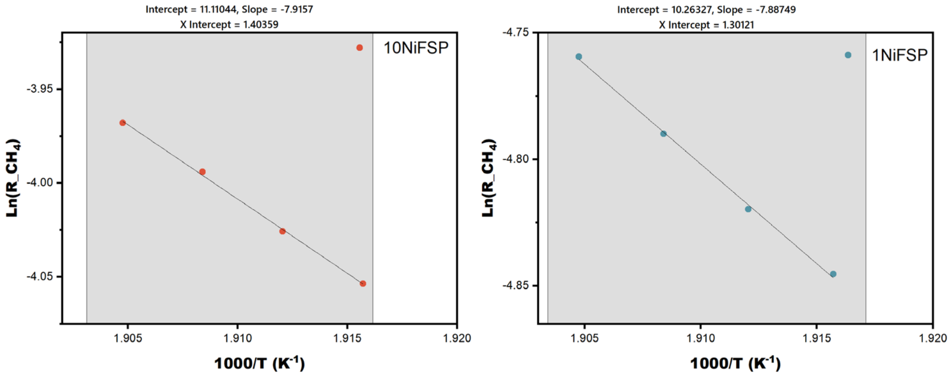

Figure C11. Arrhenius plots for activation energy calculated with respect to CH_4 formation (conditions: 248-252 °C, 50 mg of 1NiFSP, 10 mg of 10NiFSP, 15 vol.% CO_2, 60 vol.% H_2, 25 vol.% Ar, 50 mL/min, 1 bar).

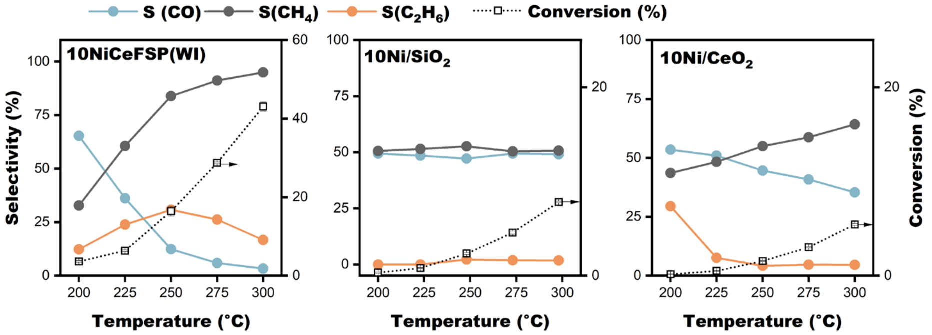

Figure C12. Catalytic performance of 10NiCeFSP(WI) (left), Ni/SiO2 (middle), and 10Ni/CeO2(right) catalysts reduced at 300 °C in CO_2 hydrogenation as a function of temperature (conditions: 200 – 300 °C, 50 mg of catalyst, 15 vol.% CO_2, 60 vol.% H_2, 25 vol.% Ar, 50 mL/min, 1 bar).

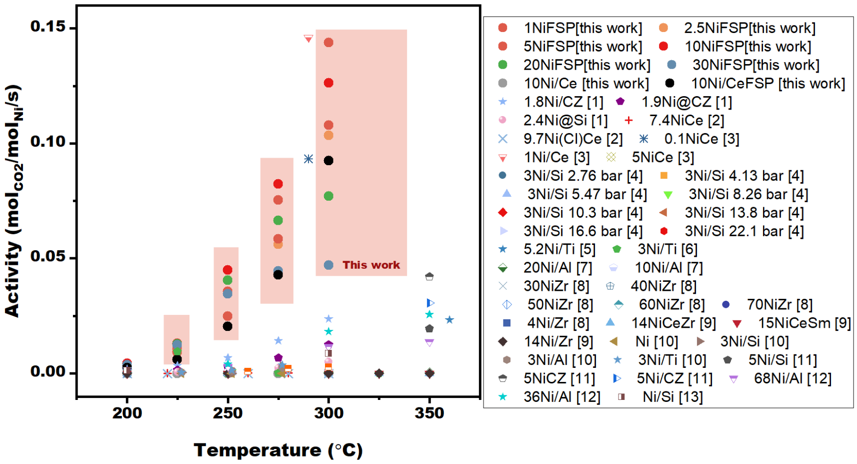

Figure C13. Activity as a function of the temperature of NiFSP catalysts and Ni-containing catalysts reported in the literature in CO_2 hydrogenation.

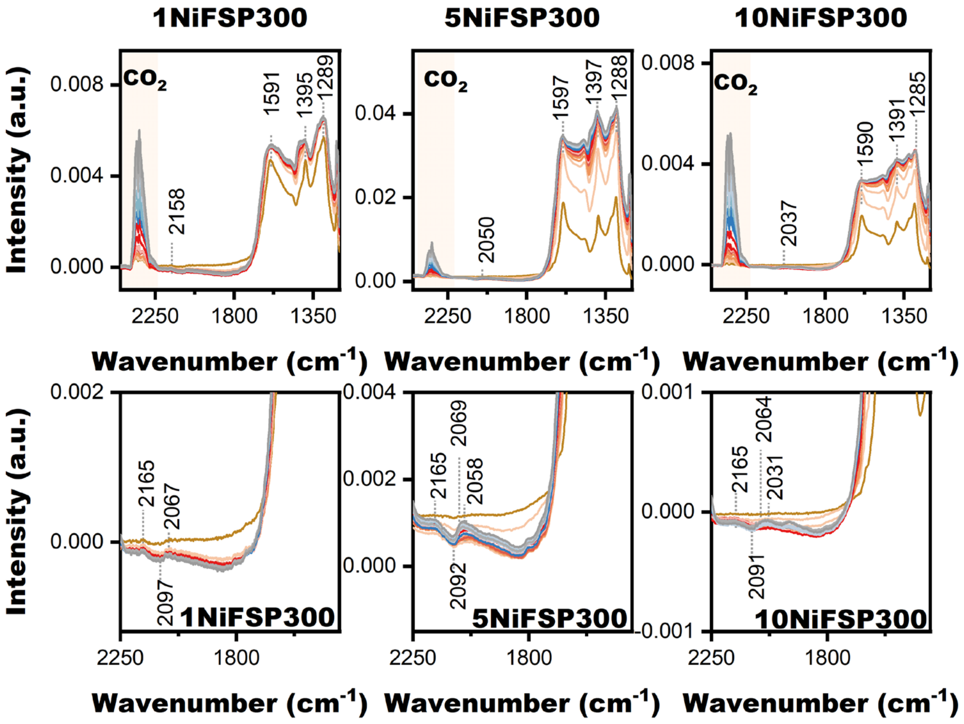

Figure C14. IR spectra (top) and in zoom in carbonyl region (bottom) of the CeFSP and NiFSP reduced at 300 °C after CO_2 adsorption at 50 °C. (conditions: 1 – 10 mbar CO_2).

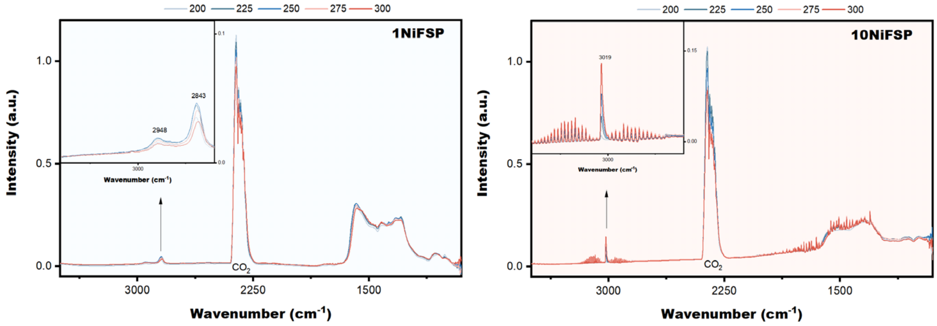

Figure C15. Background-subtracted operando IR spectra in a flow of 4%CO_2, 16% H_2 balanced by N_2 at 200 – 300 °C for 1NiFSP reduced at 300 °C (conditions: 200 – 300 °C, 1 bar, 9 mg of sample).

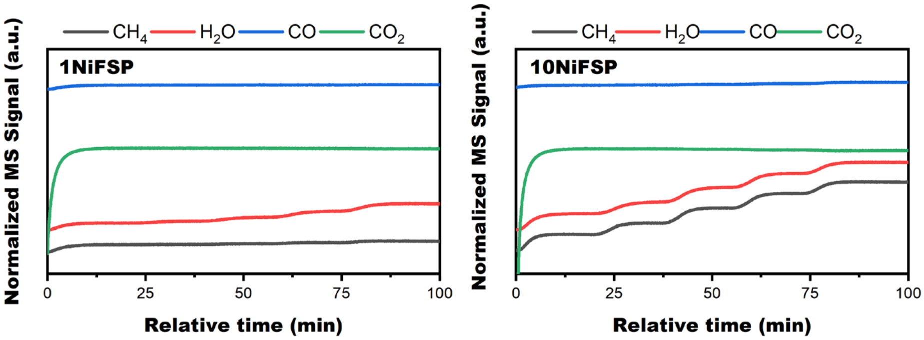

Figure C16.MS Signal during operando IR experiments in a flow of 4 vol.% CO_2, 16 vol.% H_2 balanced by N_2 at 200 – 300 °C for 1NiFSP and 10NiFSP reduced at 300 °C (conditions: 200 – 300 °C, 1 bar, 9 mg of sample).

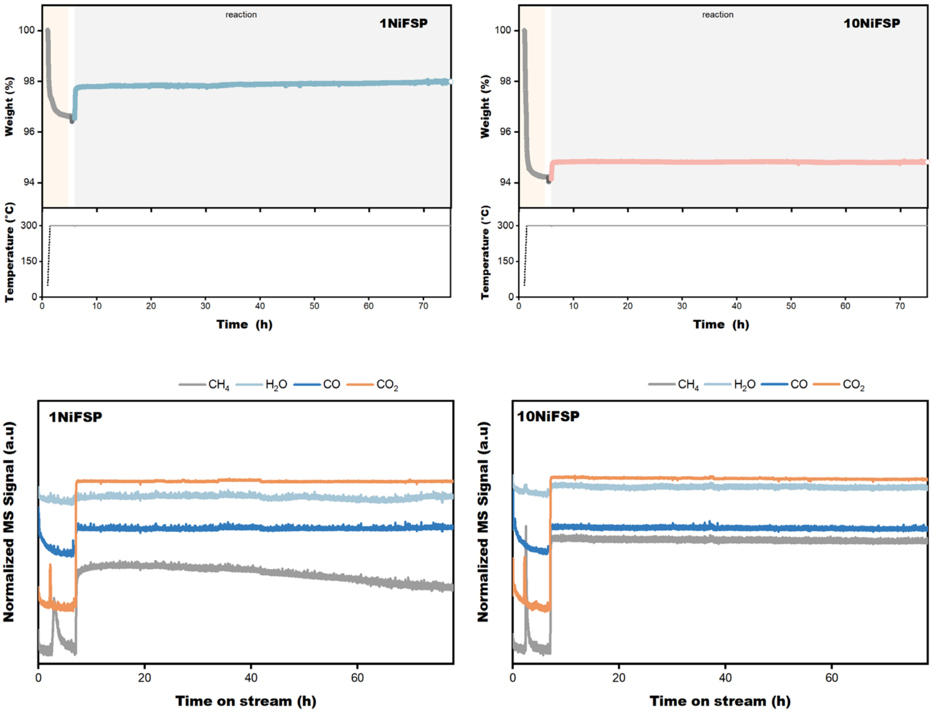

Figure C17. TG analysis and MS signal during pretreatment and deactivation over 1NiFSP and 10NiFSP catalysts (reaction conditions: 300 °C – 25 mg of catalyst, 0.8 vol.% CO_2, 3.2 vol.% H_2 in Ar, 50 mL/min, 1.5 bar, 70 h. Pretreatment conditions: 3.2 vol.% H_2 in Ar, 50 mL/min, 1.5 bar, 50 – 300 °C, 10 °C/min).

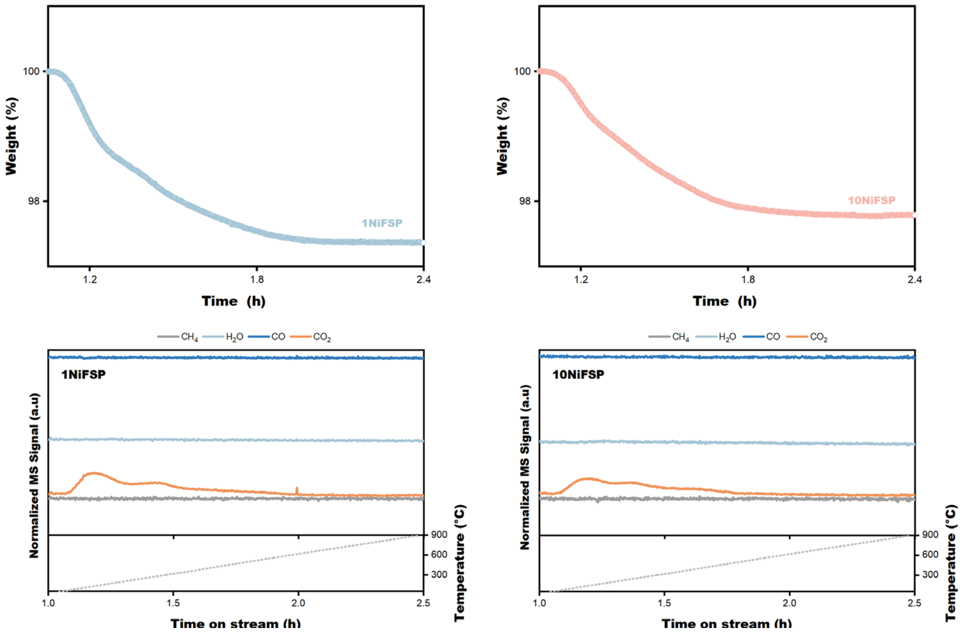

Figure C18. TG analysis and MS signal during temperature-programmed oxidation of spent 1NiFSP and 10NiFSP (TG analysis conditions: 50 – 900 °C, 25 mg of catalyst, 20 vol.% O_2 in He, 50 mL/min, 10 °C/min).

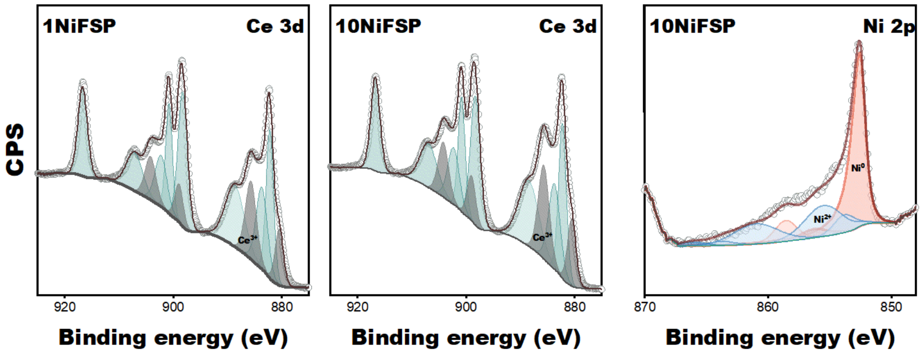

Figure C19. Deconvolution of Ce3d and Ni $2p_{3/2}$ of 1NiFSP and 10NIFSP, reduced at 300 °C, after CO_2 hydrogenation at 300 °C for 24 h (conditions: 300 °C, 30 mg of catalyst, 15 vol.% CO_2, 60 vol.% H_2, 25 vol.% Ar, 50 mL/min, 1 bar, 24 h).

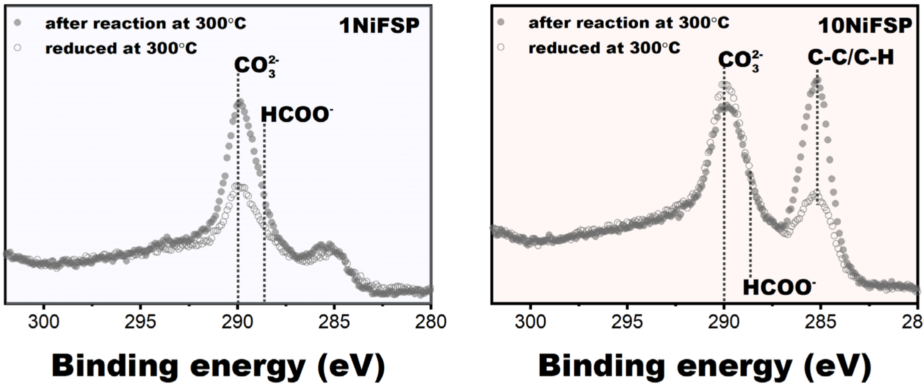

Figure C20. XP spectra of C 1s of 1NiFSP and 10NiFSP after pretreatment and reaction hydrogenation at 300 °C for 24 h (labeled as after reaction).

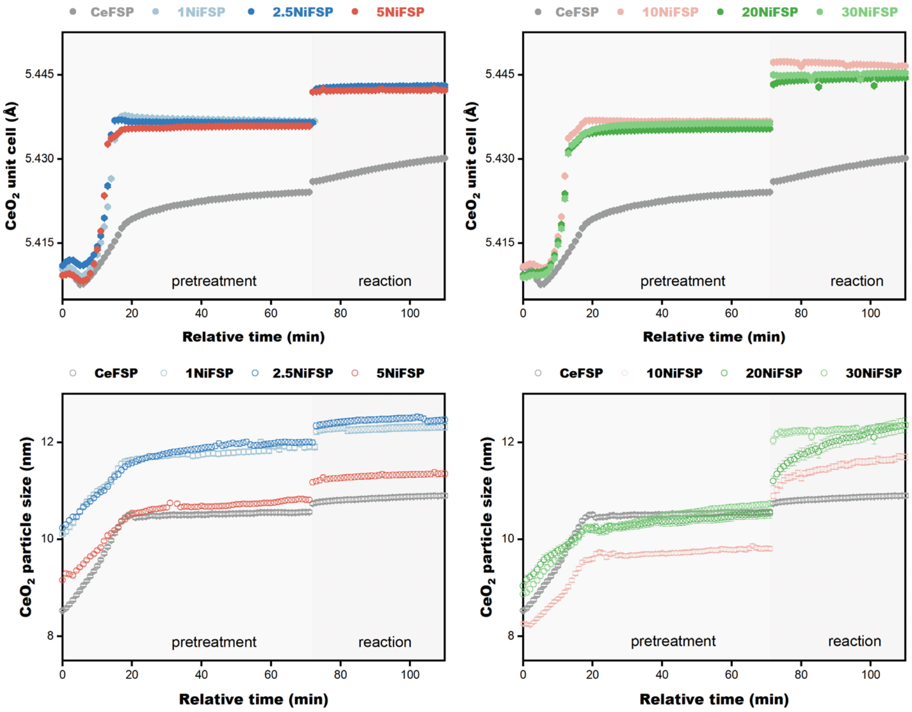

Figure C21. Refined unit cell parameters(top) and particle sizes(bottom) of CeO_2 for CeFSP and NiFSP catalysts during reductive pretreatment and CO_2 hydrogenation.

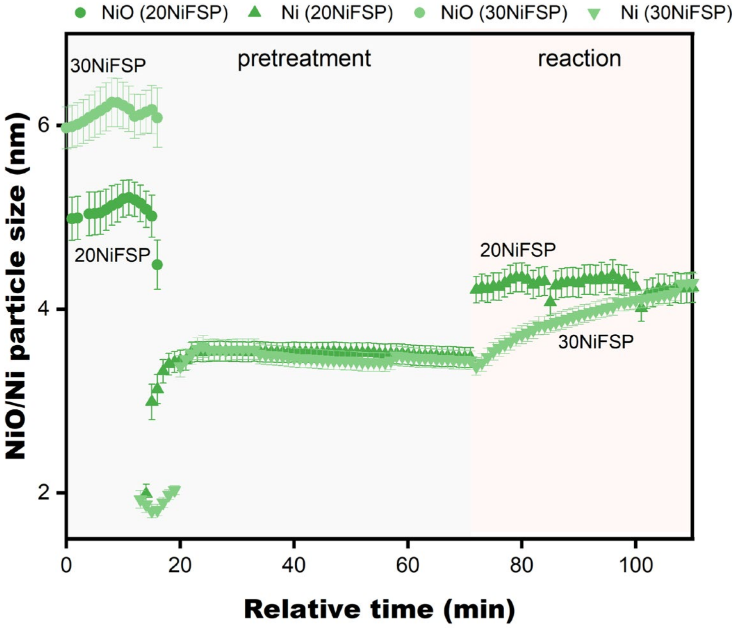

Figure C22. Refined particle size of NiO and Ni for 20NiFSP and 30NiFSP catalysts during reductive pretreatment and CO_2 hydrogenation.

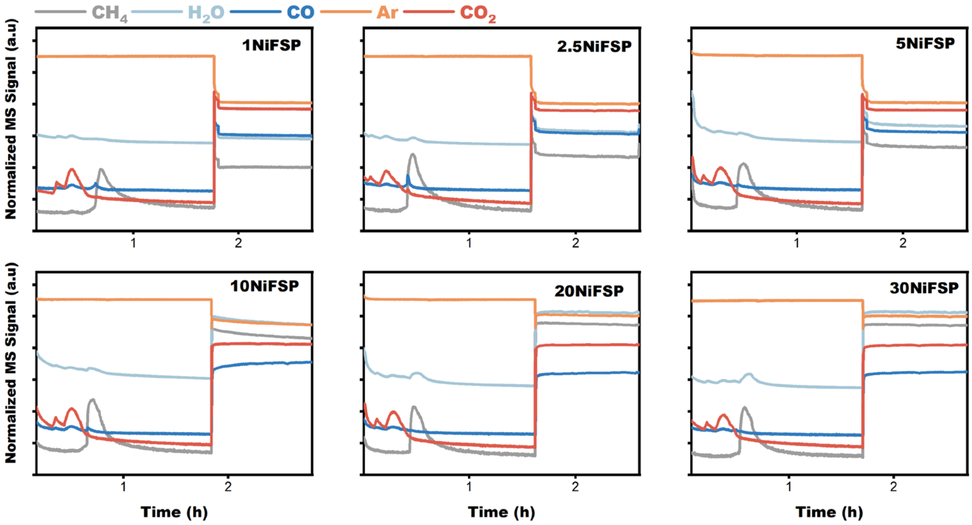

Figure C23.MS data of in situ synchrotron XRD experiments over NiFSP.

Tables.

Table C1. Atomic ratios derived from XPS analysis 1NiFSP and 10NiFSP after pre-treatment (xNiFSP300) and reaction (xNiFSP_used).

	1NiFSP300	1NiFSP_used	10NiFSP300	10NiFSP_used
Ni/Ce	-	-	0.11	0.09
C/Ce	0.85	1.26	1.23	1.59
O/Ce	3.60	3.97	3.96	4.15
Ce^{3+}/Ce	0.30	0.32	0.29	0.26
$Ni^{2+}/(Ni^{2+}+Ni^{0})$	-	-	0.41	0.43

Table C2. Catalytic performance in CO2 hydrogenation.

Catalyst	H_2: CO_2	P (bar)	CO_2 initial (%)	T_{react} (°C)	Activity (mmol$_{CO2}$/mol$_{Ni}$/s)	Ref. Fig. C6	Ref.
1NiFSP	4	1	15	200	3.720	This work	
				225	10.420		
				250	35.620		
				275	75.500		
				300	143.810		
2.5NiFSP				200	4.100		
				225	9.450		
				250	24.810		
				275	56.100		
				300	103.390		
5NiFSP				200	3.360		
				225	9.180		
				250	24.800		
				275	58.480		
				300	107.990		
10NiFSP				200	4.330		
				225	13.020		
				250	45.000		
				275	82.380		
				300	126.340		
20NiFSP				200	3.850		
				225	12.780		
				250	40.420		
				275	66.460		
				300	77.010		
30NiFSP				200	3.810		
				225	12.330		
				250	34.530		
				275	44.540		
				300	47.110		
10Ni/CeFSP				200	2.551		
				225	6.126		
				250	20.377		
				275	42.713		
				300	92.458		
10Ni/CeO_2				200	0.003		
				225	0.009		

Catalyst	H_2: CO_2	P (bar)	CO_2 initial (%)	T_{react} (°C)	Activity ($mmol_{CO2}/mol_{Ni}/s$)	Ref. Fig. C6	Ref.
				250	0.030		
				275	0.058		
				300	0.104		
1.8wt.%Ni/CZ	4	1	3	200	1.907	[1]	1
				225	3.362		
				250	6.914		
				275	14.127		
				300	23.770		
1.9wt.%Ni@ CZ				200	1.062		
				225	1.489		
				250	2.868		
				275	6.902		
				300	12.535		
2.4wt.%Ni@Si				200	0.655		
				225	0.671		
				250	0.710		
				275	2.440		
				300	5.126		
7.4Ni/Ce (10 nm)	65	1	1	200	0.030	[2]	2
				220	0.083		
				260	0.208		
				280	0.211		
				300	0.211		
9.7Ni (Cl)/Ce (100 nm)				200	0.000		
				220	0.000		
				260	0.002		
				280	0.004		
				300	0.006		
0.1wt.%Ni/Ce	4	1	13.3	290	93.333	[3]	3
1wt.%Ni/Ce				290	146.111		
5wt.%Ni/Ce				290	246.389		
3Ni/Si	4	2.76	4	252	0.462	[4]	4
3Ni/Si		4.13		252	0.510		
3Ni/Si		5.47		252	0.558		
3Ni/Si		8.26		252	0.608		
3Ni/Si		10.3		252	0.657		
3Ni/Si		13.8		252	0.690		
3Ni/Si		16.6		252	0.704		
3Ni/Si		22.1		252	0.740		
5.2Ni/a-Ti	4	1	19	360	23.200	[5]	5
3Ni/Ti	4	1	5	200	0.483	[6]	6
				225	9.660		
				250	0.181		
				275	0.338		
				300	0.604		
				325	0.110		
				350	0.186		
				375	0.257		
				400	0.290		
20% Ni/Al	3.5	1	-	200	0.533	[7]	7
				250	0.308		
				300	0.542		

Catalyst	H_2: CO_2	P (bar)	CO_2 initial (%)	T_{react} (°C)	Activity ($mmol_{CO2}/mol_{Ni}/s$)	Ref. Fig. C6	Ref.
				350	0.566		
				400	0.528		
				450	0.508		
				500	0.482		
10% Ni/Al				200	0.232		
				250	0.927		
				300	0.640		
				350	0.102		
				400	0.100		
				450	0.964		
				500	0.936		
				200	0.533		
Ni30Zr70				150	0.049	[8]	8
				200	0.045		
Ni40Zr60				150	0.002		
				200	0.071		
Ni50Zr50				150	0.016		
				200	0.102		
Ni60Zr40				150	0.008		
				200	0.072		
Ni70Zr30				150	0.008		
				200	0.003		
4%Ni/Zr				150	0.003		
				200	0.123		
14% Ni/CeZr	4	1	20	200	0.001	[9]	9
				250	0.008		
				300	0.001		
				325	0.002		
				350	0.002		
				375	0.002		
				400	0.002		
14% Ni/CeSm				150	0.000		
				200	0.001		
				250	0.009		
				300	0.015		
				325	0.016		
				350	0.016		
				375	0.016		
				400	0.017		
14% Ni/Zr				200	0.001		
				250	0.009		
				300	0.015		
				325	0.017		
				350	0.019		
				375	0.020		
				400	0.020		
Ni	4	1	3	227	0.002	[10]	10
				252	0.005		
				277	0.013		
3%Ni/Si				227	0.559		
				252	0.140		
				277	3.150		

Catalyst	H_2: CO_2	P (bar)	CO_2 initial (%)	T_{react} (°C)	Activity ($mmol_{CO2}/mol_{Ni}/s$)	Ref. Fig. C6	Ref.
3%Ni/Al				227	0.591		
				252	1.290		
				277	2.540		
3%Ni/Ti				227	0.573		
				252	1.440		
				277	3.580		
5% Ni/Si	4	1	16.4	350	19.400	[11]	[11]
5% NiCeZr				350	42.000		
5% Ni/CeZr				350	30.600		
68% Ni/Al	4	1	19	250	3.050	[12]	[12]
				300	11.700		
				350	13.800		
36% Ni/Al				250	4.110		
				300	18.200		
				350	25.700		
Ni/Si	4	5	10	200	1.250	[13]	[13]
				300	8.730		
				400	15.000		
7.8NiCe	4	1		260	0.938	[14]	[14]
				280	2.204		
				300	2.826		

Ce–CeO_2; Si – SiO_2; CZ – CeO_2-ZrO_2; Zr – ZrO_2; Al – Al_2O_3; Ti – TiO_2

References. Appendix C.

1. Vrijburg, W. L. et al. Ceria–zirconia encapsulated Ni nanoparticles for CO_2 methanation. Catal Sci Technol 9, 5001–5010 (2019).

2. Konishcheva, M. V. et al. On the Mechanism of CO and CO_2 Methanation Over Ni/CeO_2 Catalysts. Top Catal 59, 1424–1430 (2016).

3. Zheng, H. et al. Unveiling the Key Factors in Determining the Activity and Selectivity of CO_2 Hydrogenation over Ni/CeO_2 Catalysts. ACS Catal 12, 15451–15462 (2022).

4. Weatherbee, G. D. & Bartholomew, C. H. Hydrogenation of CO_2 on group VIII metals: II. Kinetics and mechanism of CO_2 hydrogenation on nickel. J Catal 77, 460–472 (1982).

5. Li, J. et al. Enhanced CO_2 Methanation Activity of Ni/Anatase Catalyst by Tuning Strong Metal-Support Interactions. ACS Catal 9, 6342–6348 (2019).

6. Vrijburg, W. L. et al. Efficient Base-Metal NiMn/TiO_2 Catalyst for CO_2 Methanation. ACS Catal 9, 7823–7839 (2019).

7. Rahmani, S., Rezaei, M. & Meshkani, F. Preparation of highly active nickel catalysts supported on mesoporous nanocrystalline γ-Al_2O_3 for CO_2 methanation. Journal of Industrial and Engineering Chemistry 20, 1346–1352 (2014).

8. Yamasaki, M., Habazaki, H., Asami, K., Izumiya, K. & Hashimoto, K. Effect of tetragonal ZrO_2 on the catalytic activity of Ni/ZrO_2 catalyst prepared from amorphous Ni–Zr alloys. Catal Commun 7, 24–28 (2006).

9. Perkas, N. et al. Methanation of carbon dioxide on ni catalysts on mesoporous ZrO_2 doped with rare earth oxides. Catal Letters 130, 455–462 (2009).

10. Vance, C. K. & Bartholomew, C. H. Hydrogenation of carbon dioxide on group viii metals: III, Effects of support on activity/selectivity and adsorption properties of nickel. Appl Catal 7, 169–177 (1983).

11. Aldana, P. A. U. et al. Catalytic CO_2 valorization into CH_4 on Ni-based ceria-zirconia. Reaction mechanism by operando IR spectroscopy. Catal Today 215, 201–207 (2013).

12. Beierlein, D. et al. Is the CO_2 methanation on highly loaded Ni-Al_2O_3 catalysts really structure-sensitive? Appl Catal B 247, 200–219 (2019).

13. Vogt, C. et al. Unravelling structure sensitivity in CO_2 hydrogenation over nickel. Nature Catalysis 2017 1:2 1, 127–134 (2018).

14. Dai, B. et al. CO_2 reverse water-gas shift reaction on mesoporous M-CeO_2 catalysts. Can J Chem Eng 95, 634–642 (2017).

Chapter 5

Flame-synthesized Co–TiO_2 catalysts for CO_2 hydrogenation

Abstract

A series of Co-TiO_2 catalysts with varying Co content (2.5 – 40 mol.%) were evaluated for CO_2 methanation. Flame spray pyrolysis (FSP) produced small TiO_2 nanoparticles (~8 nm) with higher surface area compared to conventional TiO_2 supports. Catalysts with low Co content contained highly dispersed Co^{2+} ions, which cannot be reduced at 500 °C. Catalysts with 10 mol.% or more Co also contained segregated $CoTiO_3$ particles, which reduced to metallic Co and rutile-TiO_2 nanoparticles at 500 °C. The highest Co-weight-normalized activity (4.9 ± 0.2 $mmol_{CO2}/mol_{Co}/s$ at 250°C with 91% CH_4 selectivity) was observed for the 20CoTi5 sample, which contains 14 nm rutile-TiO_2, ~4 nm hcp Co nanoparticles, and a small amount of fcc Co with Co reduction degree of 100%. Low Co reduction degree in 2.5CoTi5 and 5CoTi5 led to low CO_2 conversion and predominant CO formation (79%). Catalysts with higher Co content and larger Co nanoparticles mainly yielded CH_4, with small amounts of CO and C_2H_6. Further optimization revealed that despite structural differences in the particle sizes of as-prepared one-step flame-synthesized 20Co-TiO_2 catalysts, reduction led to 13 – 16 nm rutile-TiO_2 and metallic Co. The lower activity of the small particle 20CoTi2.5 sample in comparison with the 20CoTi5 and 20CoTi10 samples was attributed to incomplete Co reduction (69%), the predominance of larger fcc Co nanoparticles (~14 nm). The 20CoTi5 and 20CoTi10 catalyst perform better due to the higher Co dispersion (~4 nm hcp Co particles) ahd the complete Co reduction. The most active one-step flame-made 20Co-TiO_2 catalyst(20CoTi5) was compared to a conventional catalyst prepared by wet impregnation of Co on FSP-made TiO_2 (20Co/TiO_2). In situ synchrotron XRD and quasi-in situ XPS revealed Co metal formation upon reduction at 500 °C in both catalysts, with all Co being converted into similar-sized 4 – 5 nm hcp Co nanoparticles. Despite the similarities, the 20Co/TiO_2 catalyst exhibited a significantly lower CO_2 conversion than the flame-made 20CoTi5 one. The difference is likely due to the stabilization of small Co particles on rutile-TiO_2 in 20CoTi5, while the more reactive nature of anatase-TiO_2 in the wet-impregnated catalyst resulted in TiO_x overlayer formation on metallic Co.

Introduction

The rising levels of CO_2 in the atmosphere are regarded as the main cause of global climate change.[1–3] Considering CO_2 as a feedstock instead of waste is an approach to close carbon cycles and lower atmospheric CO_2 emissions on the condition that CO_2 is captured from the air and reduction is done by renewable energy sources. CO_2 hydrogenation into chemicals is a promising approach for obtaining renewable chemicals and fuels from green H_2.[4–6] Among the different hydrocarbon products, the catalytic CO_2 hydrogenation to CH_4 (synthetic natural gas, SNG) has gained significant attention because SNG can be easily transported in existing infrastructure.[7,8]

Catalysts play a crucial role in CO_2 methanation (the Sabatier reaction), with their composition and structure governing the CO_2 conversion and product distribution.[9–11] Irreducible oxide supports, such as SiO_2 and especially Al_2O_3, are commonly used to support the metallic nanoparticles that form the active phase for CO_2 hydrogenation.[12–15] Reducible oxides, in particular titanium dioxide (TiO_2), are also widely considered as catalyst support in CO_2 (and CO) hydrogenation reactions as its stronger interaction with transition metals can lead to highly dispersed metal particles.[16–20] Strong metal-support interactions (SMSI) can have a profound effect on catalyst structure and performance. Although nickel (Ni) is typically used for CO_2 methanation [20,21], cobalt (Co) has also been widely investigated for this purpose.[19,22–26] Co is generally regarded as a more active metal for C-O bond dissociation than Ni, explaining its preference in the Fischer-Tropsch (FT) reaction in which synthesis gas, a mixture of CO and H_2, is converted to long-chain hydrocarbons.[25,27,28] Co/TiO_2 catalysts are industrially important FT catalysts, the Co-TiO_2 interactions being critical to their performance.[27,29–32] A critical aspect of Co-based FT catalysts is structure sensitivity, which dictates that Co nanoparticles should have a size of at least 6 nm to exhibit a high CO dissociation activity.[33] The most common explanation is that step-edge sites for low barrier C-O bond dissociation disappear in smaller particles. Such optimum particle size has also been reported for Ru- and Ni-based catalysts for CO and CO_2 hydrogenation.[13,33–35] This structure sensitivity has led researchers to explore a variety of preparation methods to control the size and distribution of Co nanoparticles on metal-oxide supports.

Conventional wet methods to prepare TiO_2-supported metal catalysts lack control over the particle size.[36] It is often desirable to achieve a good Co dispersion at a high Co loading . Much effort has been devoted to the preparation of nanosized TiO_2, including sol-gel[37], homogeneous precipitation[38], hydrothermal[39], flame synthesis[40,41], and molten salt.[42] Commercially available P25 TiO_2 is widely adopted in catalysis studies. P25 is obtained by the Aerosil process, in which $TiCl_4$ is hydrolyzed in the vapor phase at very high temperatures (>1000 °C).[43] Developing methods to obtain high-surface area TiO_2 with controlled morphology, particle size and phase composition remains desirable.[41,44,45]

Flame spray pyrolysis (FSP) is a promising alternative approach to obtain well-defined nanosized materials, offering flexibility in terms of composition and scalability.[46,47] Gäßler and co-workers recently used two-nozzle spray pyrolysis to obtain Co/TiO_2, Co/SiO_2, and Co/Ti-SiO_2 catalysts with nearly identical Co particle size.[48] Co/TiO_2 displayed higher CO_2 activity and CH_4 selectivity than Co/SiO_2 and Co/Ti-SiO_2. Schubert et al. used double flame pyrolysis to prepare Co/Al_2O_3 catalysts promoted very small amounts of Pt, which facilitated Co reduction.[49]

The present study explores the use of flame synthesis of Co-TiO_2 composites for CO_2 hydrogenation. FSP was used to obtain Co-TiO_2 samples in a single preparation step. The impact of the Co content and the particle size, varied through changing the injection rate of the precursor solution into the flame, on the CO_2 hydrogenation of reduced samples was investigated. Detailed characterization of the samples before and after reduction and comparison to Co/TiO_2 samples prepared by conventional methods allowed the formulation of structure–performance relationships, highlighting the role of the TiO_2 (anatase vs. rutile) in obtaining active and stable Co/TiO_2 hydrogenation catalysts.

Experimental Section

Materials

Co (II) acetate tetrahydrate ($Co(CH_3CO_2)_2 \cdot 4H_2O$, 99%, Merck), glacial acetic acid (99% Sigma-Aldrich), and 2-ethylhexanoic acid (99% Fisher Scientific), Titanium (IV) isopropoxide ($Ti(OCH(CH_3)_2)_4$, 97% Sigma-Aldrich), ammonia solution ($NH_3 \cdot H_2O$, 28 wt.%, Thermo Fisher), P25 titania (Evonik Degussa, pore volume 0.3 mL/g, specific surface area 50 m^2/g, anatase-TiO_2/rutile-TiO_2 85%:15%) were used as received .

Catalysts Preparation

Flame Spray Pyrolysis

Flame spray pyrolysis (FSP) of TiO_2 and Co-TiO_2 catalysts was performed with a Tethis NPD10 setup. The Tethis NPS10 apparatus was placed in a standard chemical laboratory fume hood modified to comply with EN 14172, EN 1822, and ISO 45H standards (modifications realized by Interflow). The air inflow of the fume hood was kept at a minimum of 0.7 m/s using active control systems. The exhaust flow to the (external) ventilation was equipped with HEPA H14 and ULPA U17 filters. The experiments were conducted after assessing all safety aspects, including those related to working with nanomaterials, in a risk-inventory and evaluation (RI&E) procedure, as required by the Dutch labor law. Appropriate amounts of of $Co(C_5H_7O_2)_3$ and $Ti(OCH\ (CH_3)_2)_4$ were dissolved in an equivolumetric solvent mixture of acetic acid and 2-ethylhexanoic acid. The Co and Ti concentrations were 0.15 M. This solution was stirred at 80 °C for approximately 1 h until full dissolution of the metal precursors. The precursor solution was fed by a syringe pump at an injection rate of 2.5, 5, and

10 mL/min to the center of a methane/oxygen flame to form a fine spray. The pressure drop at the capillary tip was maintained at 2.5 bar by adjusting the orifice gap area at the nozzle. The flow rates of methane and oxygen were respectively 1.5 L/min, and 3.0 L/min. Solid samples were collected on a glass microfiber filter (Whatman) using a vacuum pump. The as-prepared TiO_2 and Co–TiO_2 catalysts are denoted as Tix and yCoTix, where x stands for the injection rate in mL/min, and y represents the intended Co content (mol.%) with respect to Ti (Co / (Ti + Co)).

Wet Impregnation

Reference catalysts with an intended Co loading of 20 mol.% were prepared by wet impregnation. For this purpose, the desired amount of $Co(CH_3CO_2)_2$ was dissolved in 40 ml of $NH_3 \cdot H_2O$ solution (28 wt.%). After adding 2 g of Ti5 or P25, the resulting suspension was stirred for 2 h. Then, water was removed by evaporation. The catalysts were dried in air at 110°C overnight and calcined at 350°C for 4 h. The resulting samples are denoted as 20CoTi5 (WI) and 20CoP25, respectively.

Catalyst Characterization

Inductively Coupled Plasma Optical Emission Spectroscopy (ICP-OES)

The chemical composition (Co and Ti) of the as-prepared catalysts was determined by ICP-OES analysis (Spectro CIROS CCD Spectrometer). Prior to these measurements, the catalysts were dissolved in a mixture of 2 mL of concentrated HNO_3 (65%) and 5 mL of concentrated H_2SO_4 (95-98%) at a temperature of 250 °C under stirring for at least 30 min, followed by dilution in water.

N_2 Physisorption

Textural properties were determined by N_2 physisorption at a temperature of −196 °C using a Micrometrics TriStar II 3020 instrument. Prior to physisorption measurements, the samples were heated to 160 °C in an N_2 flow for 4 h. The specific surface area (SSA) was determined by the Brunauer–Emmett–Teller (BET) method.

CO Chemisorption

CO chemisorption measurements were performed with a Micromeritics ASAP2010C instrument. Typically, about 100 mg sample was loaded into a quartz U-tube between two quartz wool layers. Before chemisorption measurements, the catalyst was reduced in an H_2 flow at 500 °C by heating to this temperature at a rate of 10°C/min, followed by an isothermal dwell of 4 h. After evacuation at 520 °C for 1 h, CO adsorption isotherms were recorded at 35 °C.

Temperature-Programmed Reduction (H_2-TPR)

The reducibility of the samples was studied by H_2-TPR with a Micromeritics AutoChem

II instrument. Typically, about 100 mg sample was loaded into a quartz U-tube between two quartz wool layers. Prior to H_2-TPR, the sample was treated at 350 °C for 1 h in a flow of 50 mL/min of 5 vol.% O_2 in He. TPR profiles were recorded under heating the sample from 40 to 700 °C at a rate of 10 °C/min in a 50 mL/min flow of 4 vol.% H_2 in He. H_2 consumption was measured by a thermal conductivity detector (TCD) and calibrated using an AgO reference.

X-ray diffraction (XRD)

In situ synchrotron X-ray diffraction patterns were collected at the ID15A beamline of the ESRF. The measurements were carried out in transmission mode using an incident X-ray energy of 100 keV. A PilatuD3X CdTe 2M detector was used to collect the scattered signal. About 20 mg of sieved catalyst (125 - 250 μm) was loaded into quartz capillaries (1.5 mm o.d. wall thickness 0.15 mm) between two glass wool layers. The capillary was sealed with PTFE ferrules in a home-built Clausen-type flow cell. The sample was heated using a prototype synchrotron oven, developed at ESRF. The temperature calibration was performed by a thin (0.25 mm) K-type thermocouple placed inside the catalyst bed. Typically, the temperature was raised from 50 °C to 500 °C at a rate of 10 °C/min in a flow of 50 mL/min of a mixture of 20 vol.% H_2 in Ar, followed by an isothermal dwell of 1 h at 500 °C and then cooled down to 300 °C in pretreatment mixture. The reduction mixture was replaced by a reaction mixture consisting of 15 vol.% CO_2, and 60 vol.% H_2 balanced by Ar fed at a total flow of 50 mL/min) for 1 h at 300 °C. The $CoTiO_3$, Co_3O_4, CoO, Co, and TiO_2 phases were analyzed by Rietveld refinement with GSAS software (version 5720).

Transmission Electron Microscopy (TEM)

The morphology and particle size distribution of as-prepared and reduced catalysts were investigated by TEM using an FEI Titan Cryo-TEM instrument operating at an acceleration voltage of 300 kV. An appropriate amount of finely ground material was ultrasonically dispersed in analytical-grade absolute ethanol before deposition on holey Cu TEM grids.

Ultraviolet-visible diffuse reflectance spectroscopy (UV-Vis DRS)

UV-Vis DRS spectra were collected at room temperature with a Shimadzu UV-2401PC spectrometer equipped with an integrating sphere coated with $BaSO_4$ as the standard. Samples were diluted with $BaSO_4$ (30 mg sample mixed with 120 mg $BaSO_4$).

Raman Spectroscopy

Raman spectroscopy was carried out using a WITec UHTD300 spectrometer equipped with a WITec WMT50 confocal Raman microscope. Raman spectra of powder samples were collected using a 532 nm laser (0.5 mW) and an acquisition time of 30 s. The Project FIVE software (version 5.1) was used for data treatment.

Infrared (IR) Spectroscopy

IR spectra were recorded on a Bruker Vertex 70v FTIR spectrometer equipped with a DTGS detector. The experiments were performed in situ using a home-built environmental transmission IR cell. Self-supporting pellets were made by pressing approximately 10 mg sample in a disc with a diameter of 13 mm. Each spectrum was collected by averaging 32 scans with a resolution of 2 cm^{-1} in the 4000–1000 cm^{-1} range.

For CO IR measurements, the sample was first reduced in a flow of 20 vol.% H_2 in He at 500 °C (rate 10 °C/min) for 4 h. After outgassing at 500 °C in vacuum and cooling to 50 °C, IR spectra were recorded as a function of the CO partial pressure in the 0–10 mbar range. CO_2 IR spectra were recorded after reduction of the samples as described above. IR spectra were obtained as a function of CO_2 partial pressure in the 0–10 mbar range at 50 °C. All IR spectra were background subtracted, and the intensity was normalized to the weight of the pellet.

X-ray Photoelectron Spectroscopy (XPS)

The surface chemical properties of the as-prepared catalysts were studied with a K-Alpha XPS instrument (Thermo Scientific) equipped with an aluminum anode (Al Kα = 1486.68 eV) monochromatized X-ray source. Finely ground samples were placed on double-sided carbon tape. All spectra were acquired using a flood gun to reduce surface charging. A pass energy of 40 eV was typically used for region scans with a step size of 0.1 eV and a dwell time of 0.5 s. The Ti $2p_{3/2}$ (Ti^{4+}) component at a characteristic binding energy of 458.6 eV was used to correct the binding energies of the Co 2p.[50,51] A standard procedure involving the use of Shirley background subtraction and atomic sensitivity factors was applied for data processing. Spectra were fitted by using the CasaXPS software (version 3.2.23). Spectral lines were fitted by a symmetric pseudo-Voigt function referred to as GL (30), except for the main metallic Co component, which was fitted by the asymmetric LA (1.2,5,5) line shape.[52–55]

Quasi-in situ X-ray photoelectron spectroscopy (XPS)

The surface chemical properties of the reduced and deactivated catalysts were studied using a Kratos AXIS Ultra 600 equipped with a monochromatic X-ray source (Al Kα = 1486.68 eV). Self-supporting pellets were made by pressing approximately 30 mg of a sample in a disk with a diameter of 13 mm. Pretreatment of catalysts were carried out in a high-temperature reaction cell (Kratos, WX-530), allowing in vacuum sample transfer into the analysis chamber. The samples were reduced in 20 vol.% H_2 in Ar at a flow rate of 50 mL/min at 500 °C for 4 h at a rate of 10 °C/min and ambient pressure. Then, the sample was cooled to 100 °C in the pretreatment mixture and the reaction cell was evacuated to a pressure below 10^{-8} mbar, followed by transfer of the sample to the XPS analysis chamber. A pass energy of 40 eV was typically used for region scans with a step size of 0.1 eV and a dwell time of 0.5 s. Energy calibration and fitting of Ti 2p and Co 2p were performed using the same procedure as described in the XPS section above.

Catalytic Activity Measurements

CO_2 hydrogenation

The catalytic performance of TiO_2 and Co/TiO_2 catalysts in CO_2 hydrogenation was evaluated in a down-flow stainless-steel reactor with an internal diameter of 4 mm. The reaction was performed at atmosphere pressure and 250 °C. The samples were pressed, crushed, and sieved to a fraction of 125 – 250 µm. Typically, the reactor was filled with 50 mg catalyst diluted with 200 mg of SiC. Before the reaction, the catalyst was reduced in a flow of 100 mL/min of 20 vol.% H_2 in He, whilst ramping from room temperature to 500 °C at a rate of 10 °C/min, followed by an isothermal dwell at 500 °C for 4 h. The reduced catalyst was cooled in the same flow to the initial reaction temperature of 250 °C. The reaction was started by replacing the reduction gas mixture with a flow of 50 mL/min of 60 vol.% H_2, 15 vol.% CO_2, and 25 vol.% Ar. During an isothermal dwell of 108 min, the effluent gas was sampled and analyzed by an online gas chromatograph (Shimadzu, GC-2014) equipped with RT-Q-Bond (FID), and Shincarbon ST 80/100 (TCD) analysis stions. CO_2 conversion, carbon product selectivity, and product formation rates were calculated as follows:

$$X(CO_2) = 1 - \frac{F(CO_2)_{out}}{F(CO_2)_{out} + F(CO)_{out} + F(CH_4)_{out} + F(CH_3OH)_{out} + xF\left(C_xH_y\right)_{out}} \quad (1)$$

$$S(product) = \frac{F(product)_{out}}{F(CO)_{out} + F(CH_4)_{out} + F(CH_3OH)_{out} + xF\left(C_xH_y\right)_{out}} \quad (2)$$

where *F* stands for the volumetric flow rate determined from the concentration measured by gas chromatography using Ar as an internal standard and FID and TCD response factors determined by using gas calibration mixtures.

The reaction rate (r_{CO2} with the unit $mol_{CO2} \cdot mol_{Co}^{-1} \cdot s^{-1}$) was normalized to the Co content (n_{Co}) in the following manner:

$$r_{CO2} = \frac{X\,(CO_2) * F(CO_2)_{in}}{n_{Co} * V_m} \quad (3)$$

, where V_m is the molar volume of an ideal gas at standard temperature and pressure.

Results and discussion

This work is organized in the following manner. First, a set of Co-TiO_2 samples prepared by FSP at a fixed injection rate (5 mL/min) and with varying Co content (2.5-40 mol.%) will be characterized in detail in their as-prepared and reduced states. Based on the catalytic performance of samples reduced sat 500 °C, the crystallite size of the samples containing 20 mol.% is varied by changing the FSP injection rate (2.5-10 mL/min). These samples will be contrasted with samples prepared by conventional wet impregnation of Co on FSP-derived TiO_2 and P25 TiO_2.

Impact of Co content in flame-synthesized Co-TiO_2 on CO_2 hydrogenation

FSP was used to prepare a set of Co-TiO_2 samples at an injection rate of 5 mL/min (xCoTi5) with a variable Co content. A TiO_2 support was prepared in the same way without Co in the preparation. The most important physicochemical properties of the resulting Ti5 and CoTi5 samples are listed in **Table 5.1**. The Co content determined by ICP-OES analysis is somewhat lower than intended for all CoTi5 samples.

The synchrotron XRD patterns of the as-prepared samples are shown in **Figure 5.1a**. Their Rietveld refinement shows the distribution of crystalline phases (**Table 5.2**). Ti5 contains predominantly a-TiO_2 (anatase-TiO_2) in an amount of 90 wt.% with an average crystallite size of ~14 nm and a small amount of r-TiO_2 (rutile-TiO_2) with an average crystallite size of ~15 nm. The addition of Co during FSP synthesis resulted in a larger contribution of r-TiO_2. **Table 5.2** shows that, with increasing Co content up to 20 mol.%, the a-TiO_2 contribution gradually decreased from 70% in 2.5CoTi5 (crystallite size ~14.5 nm) to 4.4% in 20CoTi5 (crystallite size ~7.5 nm). This goes together with the growing contributions of r-TiO_2, reaching the highest amount of 91% at 10CoTi5, and $CoTiO_3$ and Co_3O_4, making up most of the 40CoTi5 sample. Despite its increasing contribution, the crystallite size of r-TiO_2 did not change much as a function of the Co content. The 10CoTi5 and 20CoTi5 samples contain $CoTiO_3$ with average crystallite sizes of 2 and 8.8 nm. The sample with the highest Co content (40 mol.%) is made up of $CoTiO_3$ with a size of 15 nm and a large amount of Co_3O_4 with a size of 4 nm. The absence of diffraction lines of Co_3O_4 and $CoTiO_3$ in the samples with less than 10 mol.% Co is likely due to the small size of their crystalline domains. Most likely, the samples with a low Co content contain small particles of Co-oxide strongly interacting with the different crystalline TiO_2 and $CoTiO_3$ phases. The change in TiO_2 polymorph from anatase to rutile upon addition of Co is in line with literature.[56–58] The formation of $CoTiO_3$ has been frequently associated with the rutile phase of TiO_2.[56]

Raman spectroscopy was employed to study the structure of the samples (**Figure 5.1b**). Raman spectra of the as-prepared Ti5 and CoT5 samples contain typical a-TiO_2 bands at 144, 394, 514, and 636 cm^{-1}.[59–61] The intensity of these a-TiO_2 bands decreases with the Co content, which is in line with the decreasing a-TiO_2 content determined by XRD. While Ti5 does not exhibit the typical bands of r-TiO_2 at 446 and 609 cm^{-1} [60–62], all Co-containing samples contain these bands. Their intensity increases with the Co content, reaching a maximum for 20CoTi5. At a Co content of 5 mol.% and above, a broad band in the 550 – 750 cm^{-1} range can be attributed to $CoTiO_3$ (617 and 687 cm^{-1} [63,64] or Co_3O_4 at 690 cm^{-1} [65]. The absence of Raman bands at 455 and 675 cm^{-1} means that the samples do not contain CoO.[65]

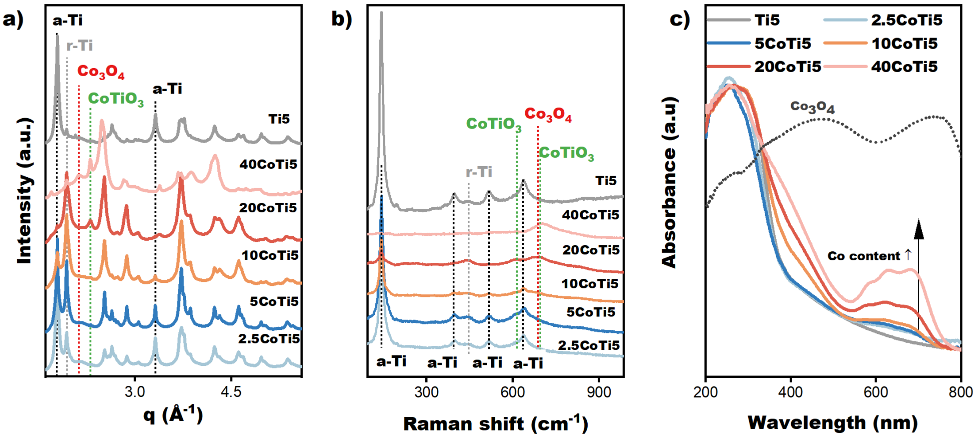

Figure 5.1. (a) Synchrotron XRD patterns (λ = 0.124 Å) of Ti5 and CoTi5 catalysts, highlighting the a-TiO_2, r-TiO_2, Co_3O_4, and $CoTiO_3$ diffraction lines. (b) Raman spectra (λ = 532 nm) and (c) UV-Vis spectra of the Ti5 and CoTi5 samples.

The UV-Vis spectra of Ti5 and the as-prepared 2.5CoTi5 catalyst (**Figure 5.1c**) contain a band at 250 nm, which can be assigned to a-TiO_2.[60,61] The formation of r-TiO_2 in CoTi5 samples containing 5 mol.% and more Co follows from the shift of the band from 250 nm to 270 nm.[61,62] All CoTi5 samples show a broad absorption band in the 520 – 770 range, characteristic of $CoTiO_3$. The absorption bands at 537 and 610 nm are typically associated with Co^{2+} → Ti^{4+} charge transfer in $CoTiO_3$.[63,64,66] The broad absorption edge at 543 nm is attributed to O^{2-} → Ti^{4+} charge transfer in $CoTiO_3$.[63,64,66] Notably, the bands in the 400 – 480 nm and 700 – 760 nm range, respectively characteristic of Co_3O_4 (O^{2-} → Co^{2+} and O^{2-} → $Co^{3,}$ charge-transfer bands[67], are absent in the UV-Vis spectra of the CoTi5 catalysts.

Representative TEM images show that the Ti5 and CoTi5 catalysts are made up of spherical nanoparticles (**Figure D1**). The number-averaged particle size is in the 7 – 9 nm range, showing no obvious trend with the Co content. The weight-averaged crystallite sizes of the phases in the Ti5 and CoTi5 samples determined by Rietveld refinement are in reasonable agreement with the particle sizes determined by TEM (**Table D1**). The specific surface area determined by N_2 physisorption decreases from ~ 200 m^2/g for Ti5 to 98 m^2/g for 20CoTi5 At a Co of 40 mol.%, the specific surface area was found to be higher at 161 m^2/g. The surface area of the FSP-made catalysts is substantially higher than that of P25 TiO_2 (~ 50 m^2/g). Due to the poor contrast, no clear Co-oxide particles could be distinguished. STEM-EDX maps of some of the as-prepared CoTi5 samples in **Figure 5.2** reflect the nanoscale distribution of Co. The maps of 2.5CoTi5 and 5CoTi5 indicate a homogeneous distribution of Co. At higher Co content (10CoTi5), some agglomeration of Co can be observed, resulting in particles of ~2 nm in addition to the highly dispersed Co.

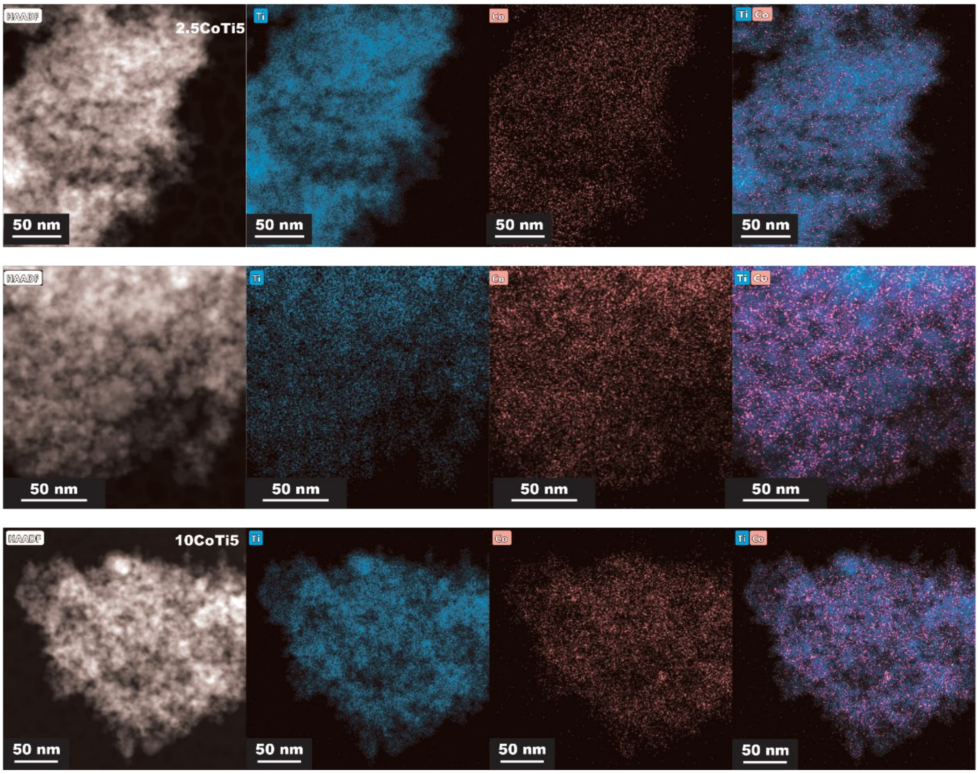

Figure 5.2. STEM-EDX images: (left) HAADF-STEM images and corresponding EDX elemental maps of Co and Ti for as-prepared 2.5CoTi5, 5CoTi5 and 10CoTi5.

Table 5.1. Physicochemical properties of as-prepared Ti5 and CoTi5 catalysts.

Catalyst	Co content (mol.%)[a]	S_{BET} (m^2/g)[b]	d_{TiO2} (nm)[c]	Co/Ti (at.%/at.%)[d]
Ti5	-	193	7 ± 3	-
2.5CoTi5	1.8	117	9 ± 5	0.05
5CoTi5	4.0	142	8 ± 3	0.11
10CoTi5	7.7	122	8 ± 3	0.19
20CoTi5	15.1	98	8 ± 3	0.33
40CoTi5	31.4	161	n.a.	0.77

a – determined from ICP analysis, b -determined by N_2 physisorption on as-prepared samples, c – determined by TEM for as-prepared samples, d – determined by XPS for as-prepared samples.

XPS was used to probe the surface composition of the as-prepared samples. Deconvoluted XP spectra are shown in **Figure D2**. The CoTi5 samples contain a single Co $2p_{3/2}$ state with a binding energy of 781.0 eV and an accompanying satellite at 786.5 eV, indicative of the predominance of Co^{2+}.[55] The XPS surface Co/Ti ratios increase with the Co content (**Table 5.1**) and are slightly higher than the bulk values, suggesting that most Co is located in the surface region. The Ti $2p_{3/2}$ region can be fitted by a feature with a binding energy of 458.7 eV due to Ti^{4+} with no significant contribution of Ti^{3+}.

Table 5.2. Rietveld refinement results of as-prepared Ti5 and CoTi5 catalysts (error margins reported in brackets).

Catalyst	a-TiO_2 (%)	$d_{a\text{-}TiO2}$ (nm)	r-TiO_2 (%)	$d_{r\text{-}TiO2}$ (nm)	$CoTiO_3$ (%)	d_{CoTiO3} (nm)	Co_3O_4 (%)	d_{Co3O4} (nm)
Ti5	89 (1)	14.4 (0.5)	11 (1)	15.1 (1)	-	-	-	-
2.5CoTi5	70 (1)	17.8 (0.6)	30 (1)	12.5 (0.8)	-	-	-	-
5CoTi5	60 (1)	14.5 (0.4)	40 (1)	15.2 (0.5)	-	-		-
10CoTi5	9 (1)	12.8 (0.8)	91 (1)	9.2 (0.1)	-	~ 2 *		-
20CoTi5	4	7.5 (1.3)	75 (1)	9.1 (0.2)	21 (1)	8.8 (0.4)		-
40CoTi5	0	-	8 (1)	6.4 (0.2)	43 (1)	8.0 (0.3)	49 (1)	3.9 (0.1)

** - estimated using Scherrer equation, K = 0.89.*

Overall, characterization shows that the Ti5 and CoTi5 samples contain different crystalline phases. The Ti5 sample is mainly made up of a-TiO_2. The introduction of Co leads to a growing contribution of r-TiO_2, which is likely present as $CoTiO_3$, the dominant form of Co in these samples. r-TiO_2 particles are most abundant in the samples containing 10 and 20 mol.% Co with relatively small crystallite sizes. A higher Co content leads to the segregation of Co_3O_4 next to $CoTiO_3$. The surface areas of the FSP-made catalysts, which vary in the 200 – 90 m^2/g range and typically decrease with the Co content, are much higher than that of P25 TiO_2 (~ 50 m^2/g).

Next, we studied the reduction behavior of these samples. **Figure 5.3a** shows the weight-normalized H_2-TPR profiles for the CoTi5 and Ti5 samples. Ti5 exhibits a very weak reduction feature at 500 °C, which can be attributed to the reduction of surface Ti^{4+} to Ti^{3+}.[68]

All CoTi5 catalysts exhibit a more intense yet broad H_2 uptake between 450 and 800 °C due to the reduction of Co species in strong interaction with TiO_2.[69,70] Based on the characterization results, it is likely that most of Co is present as $CoTiO_3$. An increase in Co content from 2.5 mol.% to 10 mol.% shifts the main reduction peak to lower temperatures, which is attributed to an increasing contribution of Co-oxides with a less strong interaction with TiO_2 than Co in $CoTiO_3$. The reduction of such Co species to metallic Co can facilitate the reduction of $CoTiO_3$ via spillover hydrogen. The reduction features in 20CoTi5 and 40CoTi5 shifted again to higher temperatures compared to 5CoTi5 and 10CoTi5, which may be due to the segregation of large Co_3O_4 crystallites from $CoTiO_3$.[71,72] This is most evident for the 40CoTi5 sample. The small reduction feature between 200 °C and 400 °C in its TPR profile is likely due to the reduction of Co_3O_4 to CoO [73,74], while the broad reduction peak between 450 and 800 °C should be due to the reduction of $CoTiO_3$ and CoO to Co.[73,74]

Figure 5.3b shows that the experimentally determined H_2 uptake corresponds well with the theoretical H_2 uptake for the reduction Co^{2+} to metallic Co. The slightly higher

H_2 uptake for the 40CoTi5 sample can be explained by the significant amount of Co_3O_4, which requires more H_2 for complete Co reduction. The difference is also partly due to the surface reduction of Ti^{4+} to Ti^{3+} and hydrogen spillover, the latter being much less pronounced in comparison to the Co-CeO_2 samples investigated in **Chapters 2 and 3.**

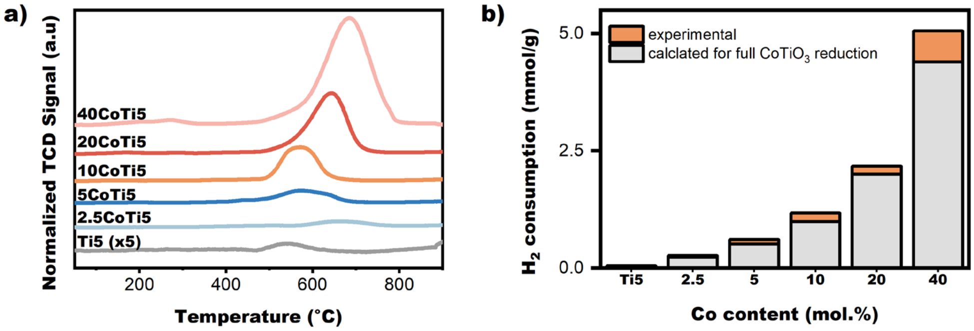

Figure 5.3. (a) Weight-normalized TPR profiles of Ti5 and CoTi5 (conditions: 4 vol.% H_2 in N_2, 50 mL/min). (b) Quantification of H_2 consumption during TPR experiments (orange bar – excess of H_2; grey bar – amount required for complete CoO/$CoTiO_3$ reduction).

In situ synchrotron XRD was employed to study the structural evolution of the Ti5 and CoTi5 samples during reduction from 50 to 500 °C followed by a dwell of 1 h. The resulting diffraction patterns as a function of temperature and time are plotted in **Figure D3**. Compared to their as-prepared state, the reduced CoTi5 samples with a Co content of 5 mol.% and above contain more r-TiO_2 (**Figure 5.4 and Table D2**). The amount of r-TiO_2 in the 2.5CoTi5 sample was the same before and after reduction. The growing amount of r-TiO_2 is due to the reduction of $CoTiO_3$.[75–77] Rietveld refinement of the XRD patterns also revealed an increase in the crystallite sizes of the r-TiO_2 and a-TiO_2 phases upon reduction of all CoTi5 catalysts as well as the Ti5 sample (**Table D2**).

No reflections related to Co-containing phases were observed during the reduction of 2.5CoTi5 and 5CoTi5 from 50 to 500 °C, indicating that either the reduced Co particles were very small (< 2 nm) or Co^{2+} was not reduced and remained highly dispersed. The 10CoTi5 and 20CoTi5 samples show the reduction of $CoTiO_3$ to Co metal and r-TiO_2 at temperatures above 450 °C (**Figure D3**). Rietveld refinement shows that the Co particles in the reduced samples have the hcp and fcc structure. Co(hcp) is thermodynamically more stable when the crystallites are larger than 20 nm, while Co(fcc) is preferred in smaller crystallites.[78,79] The present results show that all crystalline domains are smaller than 20 nm, with the size of Co(hcp) being smaller than that of Co(fcc). Similar findings were reported by Nyathi et al. for the reduction of Co_3O_4/TiO_2, who suggested the stabilization of hcp crystallites by formation of (partially) intergrown domains of fcc and hcp Co.[100] The existence of intergrowths could not be verified by Rietveld refinement of our data. The reduced 10CoTi5 sample contains slightly more fcc crystallites than hcp crystallites, albeit that their size is nearly the same at 6 nm. The 20CoTi5 sample contains significantly more hcp Co crystallites with a size of 4 nm than fcc nanoparticles with a size of 11 nm.

Overall, XRD results of the samples reduced at 500 °C show the formation of Co nanoparticles in the samples containing 10 mol.% and more Co. It is likely that the Co reduction degree of the 2.5CoTi5 sample is very low due to the strong interaction of Co with TiO_2, probably mostly as $CoTiO_3$. This is in line with the H_2-TPR profile for this sample. Moreover, this sample does not show an increase of the r-TiO_2 amount upon reduction, as observed for the other samples, related to the reduction of $CoTiO_3$ to metallic Co and r-TiO_2. Although also no metallic Co particles were observed in 5CoTi5 by XRD, the increase in the r-TiO_2 contribution suggests the formation of a small amount of metallic Co. These particles are likely smaller than 2 nm. In contrast, the samples containing significant amounts of crystalline $CoTiO_3$ display a substantia increase in the amount r-TiO_2, along with the formation of metallic Co particles. The impact of the different structures in the reduced CoTi5 catalysts on their CO_2 hydrogenation performance was next investigated.

We then used quasi-in situ XPS to study the surface composition and the reduction degrees of Co and TiO_2 in the CoTi5 samples. The samples were reduced at 500 °C at atmospheric pressure in a flow of 20 vol.% H_2 in Ar for 4 h in a reaction chamber connected to the analysis chamber of a Kratos XPS system, followed by evacuation and transfer to the XPS analysis chamber. The resulting Co $2p_{3/2}$ and Ti 2p XP spectra and their fits are shown in **Figure 5.7b**. The main contribution at 777.7 ± 0.3 eV in the Co $2p_{3/2}$ spectra is characteristic of metallic Co.[52,54,80,81] The reduced 2.5CoTi5, 5CoTi5 and 10CoTi5 samples also contain a contribution of Co^{2+} at a $2p_{3/2}$ binding energy of 780.6 eV. While all Co was reduced in the 20CoTi5 sample. The fraction of metallic Co in the reduced samples was 44% for 2.5CoTi5, 82% for 5CoTi5, 81% for 10CoTi5, and 100% for 20CoTi5. These results confirm the lower reducibility of Co in 2.5CoTi5. The deconvolution of Ti 2p confirmed that Ti is mostly present in Ti^{4+} with a Ti $2p_{3/2}$ binding energy of 458.7 ±0.2 eV, with a small amount of Ti^{3+} with a binding energy of 457.1 ±0.4 eV noted in amounts of 2 – 3%.[50,82] The XPS Co/Ti surface ratios of the reduced CoTix samples are lower than those of the as-prepared ones (**Table 5.1 and Table D2**), indicative of the sintering of Co during reduction and possibly TiOx overlayer formation.[31,83]

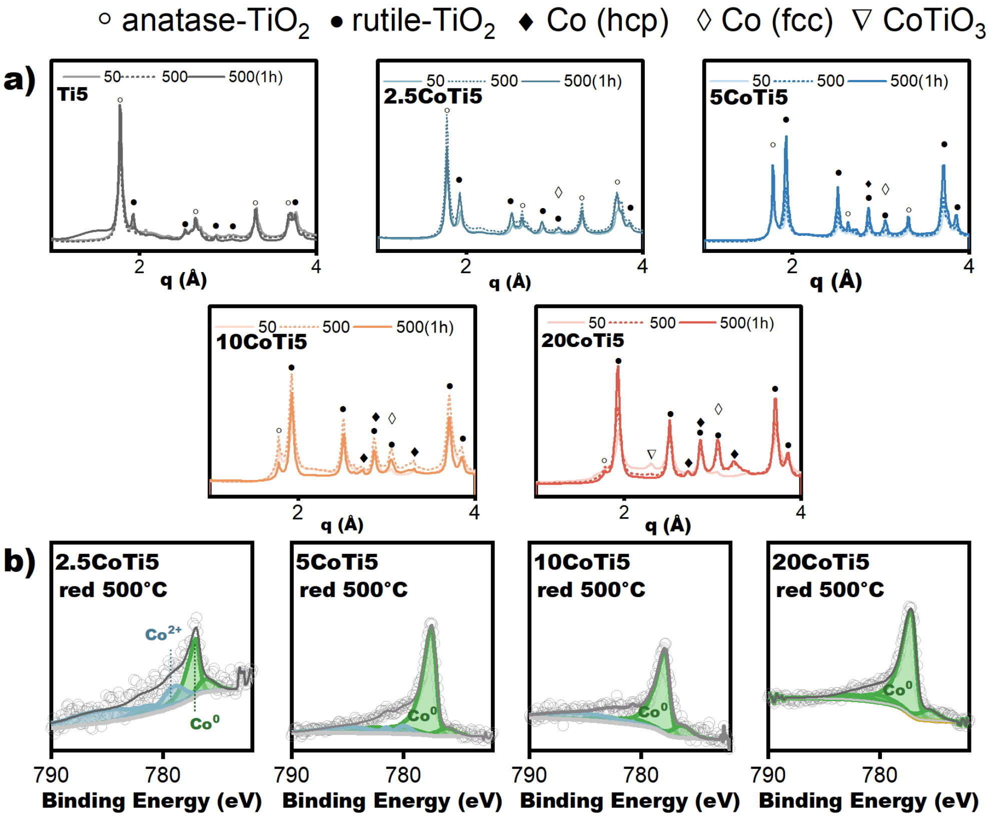

Figure 5.4. (a) Synchrotron XRD patterns (λ = 0.124 Å) of Ti5 and CoTi5 catalysts before and after reductive pretreatment at 500 °C. °- a-TiO_2; • - r-TiO_2; ∇ - $CoTiO_3$; ♦ - Co (hcp); ◊- Co (fcc) (conditions: 20% H_2 in Ar, 50 mL/min, 10 °C/min). (b) The deconvolution of Co $2p_{3/2}$ XP spectra of 2.5CoTi5, 5CoTi5, 10CoTi5 and 20CoTi5 after reduction at 500 °C for 4 h (grey: experimental data and the fitted envelope; green: the fitted metallic Co^0 contributions and the Co auger LMM peak; blue: the fitted CoO contributions) (conditions: 20 vol.% H_2 in Ar, 50 mL/min, 10 °C/min).

The CO_2 hydrogenation performance was evaluated at a temperature of 250 °C and a pressure of 1 bar. The catalysts were reduced at 500 °C. The CO_2 conversion and the product selectivity are shown in **Figure 5.5**. The Ti5 sample is not active in CO_2 hydrogenation. The main products of CO_2 hydrogenation on the reduced CoTi5 catalysts are CO and CH_4, with the highest CO_2 conversion (8.6%) observed for the 20CoTi5 sample with a CH_4 selectivity of 91%. The lower CO_2 conversion for samples with a lower Co content led to lower CH_4 and higher CO selectivity. The 2.5CoTi5 sample produces mainly CO (92%) and a small amount of CH_4 (8%) at a very low conversion of 0.1%. The catalytic performance of the reduced 20CoTi5 catalyst was further evaluated in the 200 – 300 °C temperature range (**Figure D4**). Increasing the reaction temperature from 200 °C to 300 °C led to a higher CO_2 conversion and more

CH_4 at the expense of CO. This suggests that CO_2 methanation follows the $CO_2 \rightarrow CO \rightarrow CH_4$ pathway.[13] A higher CH_4 selectivity also coincides with a decreasing C_2H_6 selectivity, suggesting that C-C coupling reactions compete with CH_x hydrogenation to CH_4.[84]

The Co-weight normalized CO_2 conversion rates for CoTi5 catalysts were evaluated at a conversion below 10% to ensure differential conditions (**Figure 5.5**). The 2.5CoTi5 and 5CoTi5 samples show very low reaction rates of ~0.5 $mmol_{CO2}/mol_{Co}/s$. With increasing Co content, the normalized rate increases to the highest value of 4.9 ± 0.2 $mmol_{CO2}/mol_{Co}/s$ for the 20CoTi5 sample. The sample with the highest Co content exhibits a substantially lower rate, likely due to the formation of bulky Co nanoparticles from the relatively large precursor Co-oxide particles.

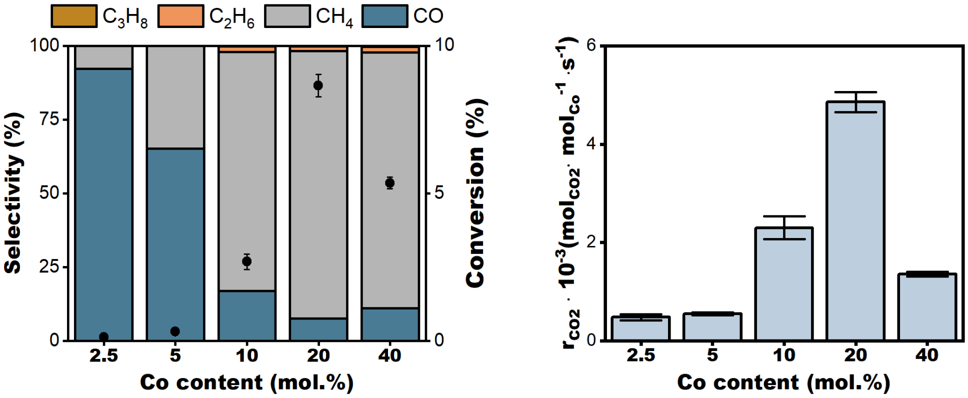

Figure 5.5. Catalytic activity and product distribution of the CoTi5 catalysts reduced at 500 °C in CO_2 hydrogenation at 250 °C (left). CO_2 methanation reaction rate at 250 °C, normalized to the total Co content (right) (conditions: 250 °C, 50 mg of catalyst, 15 vol.% CO_2, 60 vol.% H_2, 25 vol.% Ar, 50 mL/min, 1 bar).

Several mechanistic studies mentioned that CO_2 hydrogenation to CH_4 requires sufficiently large metallic nanoparticles, exposing step-edge sites for C-O bond dissociation in the CO intermediate.[33,85] As small metallic Co clusters lack such sites, a higher CO selectivity can be expected for catalysts with a high Co dispersion.[86–88] Additionally, the formation of a TiO_x overlayer on the metallic Co surface during reduction can occur above 500 °C, which can lower the accessibility of the metal sites and, therefore, the activity.[32,89]

The 2.5CoTi5 sample display a very low conversion, likely due to the low Co reduction degree. 5CoTi5 likely contains a very small amount of metallic Co in the form of particles smaller than 2 nm, which explains the slightly higher CO conversion and CH_4 selectivity. The reduced samples with more Co (>5 mol.%) contain detectable amounts of nanometer-sized Co particles, which catalyze CO_2 hydrogenation to CH_4 via CO. Considering the reduction temperature of 500 °C, it is unlikely that TiOx overlayers formed on the metallic Co nanoparticles and impacted the catalysis. The 20CoTi5 catalyst displays the highest reaction rate and was selected for further studies. Despite the differences in dominant Co metal phase, Co particle size, and the amount and size of TiO_2 phases between 10CoTi5 and 20CoTi5, it is most likely that the differences are due to the extent of Co reduction and Co particle size. Next, we studied the influence of the TiO_2 crystallite size on the structure of the catalysts and their performance by varying the FSP injection rate at a Co content of 20 mol.%.

Variation particle size 20CoTi

The TiO_2 crystallite size of 20CoTix was changed by varying the injection rate of the precursor solution during FSP. A set of Tix supports without Co was prepared in the same way. The most important physicochemical properties of the 20CoTix samples are listed in **Table 5.3**. The synchrotron XRD patterns of the as-prepared Tix and 20CoTix catalysts are shown in **Figure 5.6a**. The Tix supports are made up predominantly of a-TiO_2 (85 – 90%) with a small amount of r-TiO_2 (15 – 10%). The a-TiO_2 crystallite size increased from 9.7 to 27.8 nm when increasing the FSP injection rate from 2.5 to 10 ml/min, while the crystallite size of r-TiO_2 was ~25 nm for Ti2.5 and Ti10 and ~15 nm for Ti5 (**Table 5.4, D3**). The size of the TiO_2 crystallites derived from XRD is in reasonable agreement with TEM and textural analyses (**Table 5.3, 5.4 and D3, Figure D5-6**). The specific surface area decreases from ~ 250 m^2/g to 89 m^2/g with increasing FSP injection rate.

The intensity of the a-TiO_2 diffraction lines in as-prepared 20CoTix is much weaker than in as-prepared Tix. Therefore, it was challenging to accurately determine the a-TiO_2 size in the 20CoTix samples. Instead, the XRD patterns of the 20CoTix samples contain strong r-TiO_2 reflections. Rietveld refinement showed the as-prepared 20CoTix samples contain mainly r-TiO_2 (75 – 95%) and $CoTiO_3$ (5 – 23%). The 20CoTi2.5 sample contains the least $CoTiO_3$, while the amounts of this phase are nearly the same in the other two samples. The r-TiO_2 size increases from 8.2 nm to 16 nm with increasing FSP injection rate, while the $CoTiO_3$ sizes are estimated to be ~12 nm for 20CoTi2.5, 8.3 nm for 20CoTi5, and 19 nm for 20CoTi10 (**Table D4**). The crystallite size of the most abundant r-TiO_2 phase in the 20CoTix samples is smaller than the crystallite size of the most abundant a-TiO_2 phase in Tix. The specific surface area of the 20CoTix samples is lower compared to Tix (**Table 5.3 and D3**).

The surface of the as-prepared samples was characterized by XPS. The Co $2p_{3/2}$ XP spectra were fitted using a literature model (**Figure D7**).[55] The as-prepared samples are characterized by a single Co^{2+} component with a Co $2p_{3/2}$ binding energy of 781.0 eV and an accompanying satellite peak at 786.5 eV. These Co^{2+} species are likely due to $CoTiO_3$ and highly dispersed Co-oxide in strong interaction with TiO_2 and $CoTiO_3$. The Ti 2p XP spectra show that the surface only contains Ti^{4+}. The Co/Ti surface ratios listed in **Table 5.3** increase with the FSP injection rate. A reasonable explanation is the increasing amount and particle size of $CoTiO_3$, which represents a very high dispersion of Co, as opposed to Co-oxide on the surface.

Table 5.3. Physicochemical properties of as-prepared 20CoTix catalysts.

Catalysts	Co (mol.%)[a]	S_{BET} (m^2/g)[b]	d_{TiO2} (nm)[c]	Co/Ti (at.%/at.%)[d]
20CoTi2.5	15.3	190	5 ± 2	0.24
20CoTi5	15.1	98	8 ± 3	0.33
20CoTi10	16.9	74	12 ± 5	0.40

a – determined from ICP analysis, b -determined by N_2 physisorption on as-prepared samples, c – determined by TEM for as-prepared samples, d – determined by XPS for as-prepared samples.

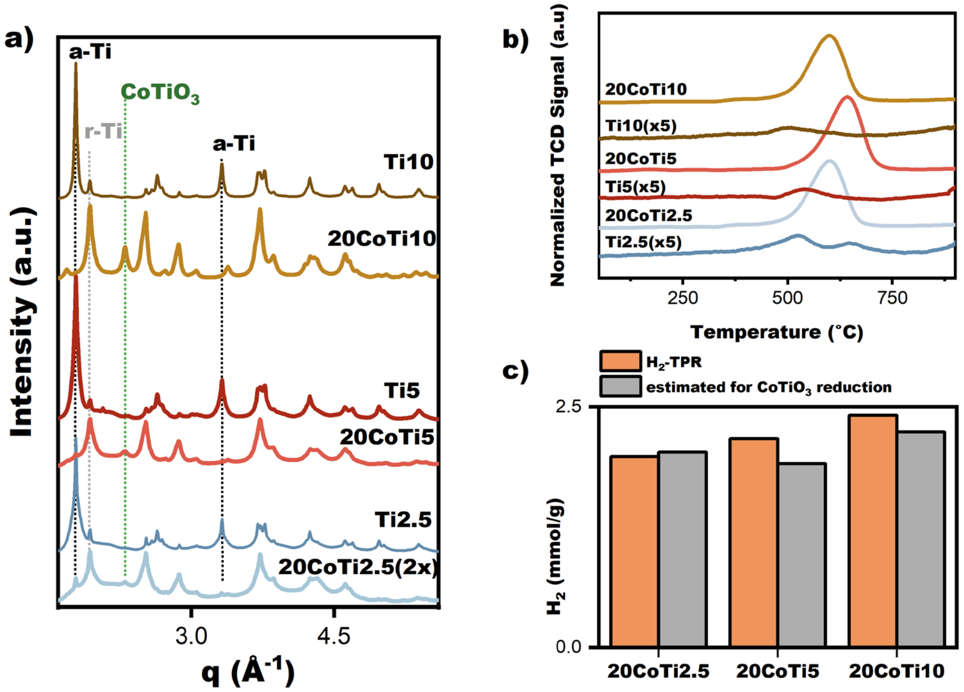

Figure 5.6. (a) Synchrotron XRD patterns (λ = 0.124 Å) of 20CoTix and Tix catalysts highlighting the a-TiO_2, r-TiO_2, and $CoTiO_3$ diffraction lines. (b) Weight-normalized TPR profiles of Tix and 20CoTix, x=2.5 –10 (conditions: 4% H_2 in N_2, 50 mL/min). (c) Quantification of H_2 consumption during TPR experiments (orange bar – the amount of H_2 from H_2-TPR; grey bar – amount required for complete $CoTiO_3$ reduction).

Table 5.4. Rietveld refinement results of as-prepared 20CoTix catalysts (error margins reported in brackets).

Catalyst	a-TiO_2 (%)	d_{a-TiO2} (nm)	r-TiO_2 (%)	d_{r-TiO2} (nm)	$CoTiO_3$ (%)	d_{CoTiO3} (nm)
20CoTi2.5	-	-	95 (1)-	8.2 (0.2)	5 (0.1)-	12 (3.2)
20CoTi5	4	7.5 (1.3)	75 (1)	9.1 (0.2)	21 (1)	8.8 (0.4)
20CoTi10	-	-	77 (1)	11.6 (0.2)	23 (1)	19 (0.9)

The H_2-TPR profiles are affected by the particle size of the Tix and 20CoTix samples (**Figure 5.6b-c**). The reduction profiles of the Tix supports show a weak broad reduction feature around 500 °C (**Figure 5.6b**), owing to the surface reduction of Ti^{4+} to Ti^{3+}.[68] The H_2 uptake of the Ti2.5 support is higher than that of the Ti5 and Ti10 samples, which may be explained by its higher surface area and possibly an intrinsic higher reducibility of very small TiO_2 particles (**Table 5.3 and Table D3**). The reduction profile of the 20CoTix samples also contains a broad reduction feature between 450 and 800 °C, attributable to the reduction of $CoTiO_3$.[71,72] With increasing 20CoTix particle size, the broad feature shifted to a lower temperature, pointing to easier reduction, which may be due to some easier-to-reduce Co-oxide particles at the surface of larger particles. Notably, the first reduction step of large Co_3O_4 crystallites occurs at lower temperatures.[90,91] A small excess of consumed H_2 (i.e., the difference between the total H_2 consumed and H_2 required to fully reduce $CoTiO_3$) was noted for the 20CoTi5 and 20CoTi10 samples, while the amount for 20CoTi2.5 was lower than the theoretical value. The latter is likely due to the incomplete reduction of Co in 20CoTi2.5.

The reduction of the Tix and 20CoTix samples was followed by synchrotron in situ XRD in the 50-500 °C temperature range (**Figure D8-10**). The reduction behavior of the Ti10 sample was similar to that of Ti5, although there was more sintering of the dominant a-TiO_2 phase (**Table D5**). Substantial phase transformation from a-TiO_2 to r-TiO_2 was observed during the reduction of Ti2.5, which also lead to more prominent sintering of a-TiO_2 and r-TiO_2 for Ti2.5 than the other two samples. Although typically a-TiO_2 transforms to r-TiO_2 at temperatures above 600 °C[92–94], it has also been shown that the disordered lattice of nanosized a-TiO_2 favors its transformation to r-TiO_2 at lower temperatures.[95] Therefore, it is reasonable to conclude that the very small TiO_2 crystallites in Ti2.5 are disordered, explaining their transformation to r-TiO_2 during reduction at 500 °C.

XRD analysis of the reduction of the 20CoTix samples showed a direction transformation of $CoTiO_3$ to metallic Co and r-TiO_2 (**Figure 5.7a**). Despite the significant differences in crystallite size of r-TiO_2 in the as-prepared 20CoTix samples, their reduction resulted in r-TiO_2 crystallites with a nearly similar size in the 13 – 16 nm range (**Table D4**). As discussed before, the Co particles in the reduced samples have the hcp and fcc structures. The reduced 20CoTi2.5 sample contains significantly more fcc crystallites (11%) than hcp crystallites (2%), with the fcc and hcp crystallites being ~11 and ~2 nm, respectively. The 20CoTi5 and 20CoTi10 samples contain significantly more hcp Co crystallites with a size of ~4 nm than fcc nanoparticles with a size of 11 nm (**Figure D10 and Table D4**). The larger amount of the fcc Co in reduced 20CoTi2.5 is likely due to the formation of metallic Co at relatively higher temperatures than in the other two samples. This aligns with H_2-TPR results. Notably, it was observed that the TiO_2 crystallite size increased more for the Tix supports than for the 20CoTix samples (**Table D3 and D4**).

We then used quasi-in situ XPS to study the surface composition and the reduction degrees of Co and TiO_2 in the 20CoTix samples. The samples were reduced at 500 °C at atmospheric pressure in a flow of 20 vol.% H_2 in Ar for 4 h in a reaction chamber connected to the analysis chamber of a Kratos XPS system, followed by evacuation and transfer to the XPS analysis chamber. The resulting Co $2p_{3/2}$ and Ti 2p XP spectra and their fits are shown in **Figure 5.7b**. The main contribution at 777.7 ± 0.3 eV in the Co $2p_{3/2}$ spectra is characteristic of metallic Co.[52,54,80,81] The reduced 20CoTi2.5 sample also contains a contribution of Co^{2+} at a $2p_{3/2}$ binding energy of 780.6 eV. While the Co reduction degree was 69% for 20CoTi2.5, all Co was reduced in the 20CoTi5 and 20CoTi10 samples. These results confirm the lower reducibility of Co in 20CoTi2.5. The deconvolution of Ti 2p confirmed that Ti is mostly present in Ti^{4+} with a Ti $2p_{3/2}$ binding energy of 458.7 ±0.2 eV, with a small amount of Ti^{3+} with a binding energy of 457.1 ±0.4 eV noted in amounts of 2 – 3% (**Figure D11**).[50,82] The XPS Co/Ti surface ratios of the reduced 20CoTix samples are lower than those of the as-prepared ones (**Table 5.3 and Table D4**), indicative of the sintering of Co during reduction and possibly TiOx overlayer formation.[31,83]

These samples were evaluated in the CO_2 methanation reaction at 250 °C and 1 bar. While the Tix sampls were expectedly inactive, the reduced 20CoTix catalysts hydrogenate CO_2 to mainly CO and CH_4 (**Figure 5.7c**). The 20CoTi5 and 20CoTi10 catalysts exhibited comparable activity and CH_4 selectivity of ~94%, while the conversion of the 20CoTi2.5 catalyst was one order of magnitude lower with a much higher CO selectivity. The higher CH_4 selectivity of the 20CoTi5 and 20CoTi10 catalysts is likely due to the difference in conversion.[13] The Co-weight normalized CO_2 conversion rates of 20CoTi10 were comparable to that of 20CoTi5 (~4.9 $mmol_{CO2}/mol_{Co}/s$), much higher than the value for 20CoTi2.5 (**Figure 5.7d).**

To summarize, despite the significant differences in the structure of as-prepared 20CoTix catalysts, reduction leads to the formation of r-TiO_2 with a similar TiO_2 crystallite size (13 –16 nm) and metallic Co nanoparticles. Unlike 20CoT5 and 20CoTi10, Co reduction was not complete for 20CoTi2.5 (69%).

CO_2 hydrogenation to CH_4 requires sufficiently large Co metal nanoparticles, exposing step-edge sites for the difficult C-O bond dissociation step in CO intermediate.[33,85] The surface structure and the type of active sites will depend on the Co metal nanoparticle size. It has been reported that the density of step-edge sites increases with particle size and becomes constant beyond 6 nm.[11,96,97] It has also been suggested that the formation of step-edge sites depends on the Co metal crystal structure:[98] Co(hcp) particles offer different step-edge sites, which are sterically less hindered for CO adsorption, than Co(fcc) particles. This can explain the higher intrinsic activity of Co(hcp) over Co(fcc).

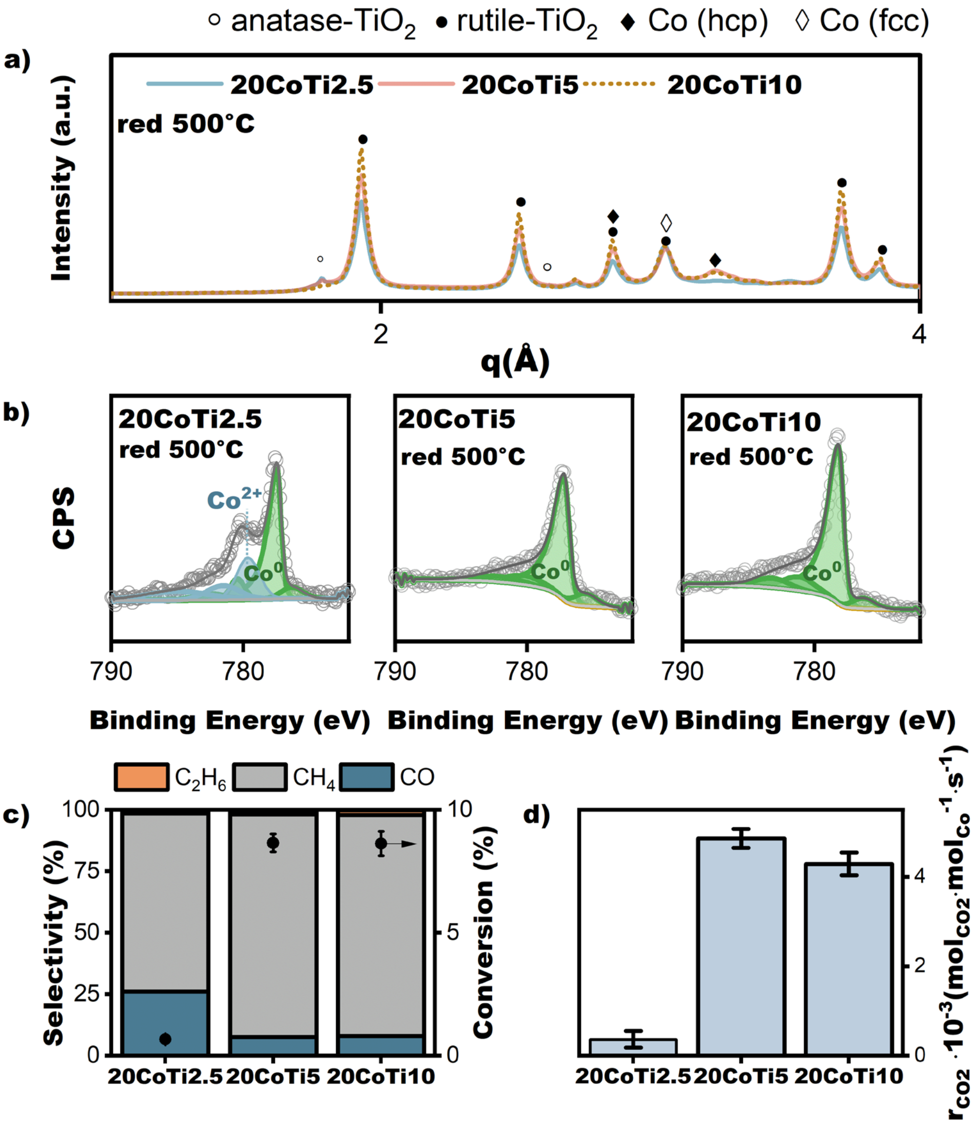

Figure 5.7. (a) Synchrotron XRD patterns (λ = 0.124 Å) of 20CoTix (x=2.5 –10) catalysts after reduction at 500 °C for 1 h (conditions: 20% H_2 in Ar, 50 mL/min, 50 – 500 °C; 10 °C/min). (b) The deconvolution of Co $2p_{3/2}$ XP spectra of 20CoTi2.5, 20CoTi5 and 20CoTi10 after reduction at 500 °C for 4 h (grey: experimental data and the fitted envelope; green: the fitted metallic Co^0 contributions and the Co auger LMM peak; blue: the fitted CoO contributions) (conditions: 20 vol.% H_2 in Ar, 50 mL/min, 10 °C/min). (c) Catalytic performance of 20CoTix catalysts reduced at 500 °C: CO_2 conversion and product distribution at a reaction temperature 250 °C (conditions: 250 °C, 50 mg catalyst, 15 vol.% CO_2, 60 vol.% H_2, 25 vol.% Ar, 50 mL/min, 1 bar). (d) CO_2 methanation reaction rate at 250 °C, normalized to the total Co content.

The presence of the "hard-to-reduce" $CoTiO_3$ phase in 20CoTi2.5 led to the formation of ~ 14 nm Co (fcc) nanoparticles and 69% of Co reduction degree after reduction at 500 °C. Bigger Co nanoparticles and lower reduction degree of 20CoTi2.5 results in lower Co dispersion, therefore lower amount of active sites for CO_2 hydrogenation, explaining lower conversion than ones for 20CoTi5 and 20CoTi10. However, we cannot exclude that the lower CH_4 selectivity of reduced 20CoTi2.5 can be also attributed to the structure of step-edge sites within Co (fcc) nanoparticles. In turn, enhanced catalytic performance in CO_2 hydrogenation over 20CoTi5 and 20CoTi10 can result from forming step-edge sites within ~4 nm Co (hcp) particles with 100% Co reduction degree.

Comparison to conventional preparation methods

To evaluate the impact of the FSP preparation on the performance, reference samples were prepared by wetness impregnation of 20 mol.% Co on Ti5 and P25 TiO_2. Rietveld refinement showed that FSP-made Ti5 contains 89% of ~14 nm a-TiO_2 particles and 11% of ~ 15 nm r-TiO_2 particles. Impregnation and calcination to yield 20CoTi5(WI) changes the composition to 58% a-TiO_2 (~15 nm), 4% r-TiO_2 (~25 nm), and 38% Co_3O_4 (~6.7 nm) (**Table 5.5**). These data can be compared to the composition of 20CoTi5, i.e. 4% a-TiO_2 (~7.5 nm), 75% r-TiO_2 (~9.1 nm), and 21% $CoTiO_3$ (~8.8 nm). The specific surface area are 173 m^2/g for Ti5, 130 m^2/g for 20CoTi5(WI) and 98 m^2/g for 20CoTi5. The decrease in specific surface area of 20CoTi5(WI) upon impregnation of Ti5 is probably caused by Co-oxides blocking some of the interparticle voids. The lower specific surface area for 20CoTi5 compared to Ti5 is due to the different TiO_2 phase composition. The weight-averaged sizes of Ti5, 20CoTi5, and 20CoTi5(WI) crystallites derived from the XRD data are in reasonable agreement with the TEM and physisorption data (**Figure D12** and **Table 5.6**).

The weight-normalized TPR profile of Ti5 shows a broad reduction peak around 500 °C (**Figure 5.8b**) due to the surface reduction of Ti^{4+} to Ti^{3+}.[68] As discussed above, the reduction profile of 20CoTi5 displays a broad reduction feature due to the reduction of $CoTiO_3$ [71,72] and highly dispersed Co-oxides. In contrast, the reduction profile of 20CoTi5(WI) exhibits the two typical reduction features of stepwise reduction of Co_3O_4 to CoO at 275 °C and CoO to Co at 450 °C.[73,74] A slight excess of H_2 consumption was only observed for the 20CoTi5 sample (**Figure 5.8c)**, indicating that metal-support interactions are weaker in the 20CoTi5(WI) sample.

The reduction behavior of these samples was followed by synchrotron in situ XRD from 50 °C to 500 °C in a flow of 20 vol.% H_2 in Ar (**Figure D9 and D13**). Supplementary **Figures D9 and D13** show the stepwise reduction of Co_3O_4 to CoO at 225 °C and CoO to metallic Co above 325 °C for the 20CoTi5(WI) sample. Instead, the 20CoTi5 sample shows the direct reduction of $CoTiO_3$ to r-TiO_2 and metallic Co. Rietveld refinement of the XRD patterns of 20CoTi5 and 20CoTi5(WI) indicates a similar distribution in Co metal phases and crystallite sizes, i.e., predominantly Co (hcp) (10 – 15%) with a size of 4 nm for 20CoTi5 and 5 nm for 20CoTi5(WI) and a small amount of Co (fcc) (4 – 8%) with a size of 11 nm for 20CoTi5 and 13 nm for 20CoTi5(WI) (**Figure 5.9a and Table D6**). On the other hand, the TiO_2 phase distribution was very different: reduction of 20CoTi5 resulted in mostly r-TiO_2 crystallites with a size of ~13.0 nm, while 20CoTi5 (WI) reduction led to predominantly –18.3 nm-sized a-TiO_2 crystallites.

Table 5.5. Rietveld refinement results of as-prepared Ti5, 20CoTi5 and 20CoTi5(WI) catalysts (error margins reported in brackets).

Catalyst	a-TiO_2 (%)	$d_{a\text{-}TiO2}$ (nm)	r-TiO_2 (%)	$d_{r\text{-}TiO2}$ (nm)	$CoTiO_3$ (%)	d_{CoTiO3} (nm)	Co_3O_4 (%)	d_{Co3O4} (nm)
Ti5	89 (1)	14.4 (0.5)	11 (0.5)	15.1 (1)				
20CoTi5	4	7.5 (1.3)	75 (1)	9.1 (0.2)	21 (1)	8.8 (0.4)		-
20CoTi5 (WI)	58 (1)	14.7 (0.6)-	4 (0.2)	25.2(0.4)	-	-	38 (1)	6.7 (0.2)

Table 5.6. Physicochemical properties of as-prepared Ti5, 20CoTi5 and 20CoTi5 (WI) catalysts

Catalysts	Co (mol.%)[a]	S_{BET} (m^2/g)[b]	d_{TiO2} (nm)[c]	Co/Ti (at.%/at.%)[d]	$d_{averaged}$ (nm)[e]
Ti5		173	7 ± 3		14.4
20CoTi5	15.1	98	8 ± 3	0.33	8.9
20CoTi5 (WI)	19.9	130	9 ± 2	0.16	12.1

a – determined from ICP analysis, b -determined by N_2 physisorption on as-prepared samples, c – determined by TEM for as-prepared samples, d – determined by XPS for as-prepared samples; e – estimated from Rietveld refinement results as following $d=(a\text{-}TiO_2 *d(a\text{-}TiO_2)+r\text{-}TiO_2 *d(r\text{-}TiO_2)+CoTiO_3*d(CoTiO_3)+Co_3O_4*d(Co_3O_4))/100$.

The metallic Co dispersion of reduced 20CoTi5 and 20CoTi5 (WI) was compared using CO chemisorption (**Figure D14**). CO chemisorption was found to be reversible. The 20CoTi5 sample adsorbed 53 μmol CO/g, significantly more than the 20CoTi5(WI) sample (**Figure 5.9b**). This indicates that more metallic Co sites are available in the former catalyst, likely related to a higher Co dispersion. Further quasi-in situ XPS measurements carried out after reduction at 500 °C at atmospheric pressure in 20 vol.% H_2 in Ar for 4 h indicated the complete reduction of Co in both catalysts (**Figure 5.9c**) and the predominance of Ti^{4+} (**Figure D15**). The Co/Ti surface ratios decrease to 0.09 for 20CoTi5 and 0.07 for 20CoTi5(WI), indicating Co sintering during reduction[83], although Ti_xO_y overlayer formation along with Co reduction cannot be completely excluded.[30,31,99,100] Nyathi et al. demonstrated that Co/a-TiO_2 is more prone to Ti_xO_y overlayer formation during reduction than Co/r-TiO_2.[100] Reduction of predominantly Co/r-TiO_2 in 20CoTi5 at 500 °C results in a slightly higher Co/Ti ratio and a larger amount of chemisorbed CO than the reduction of Co/a-TiO_2 in 20CoTi5(WI).

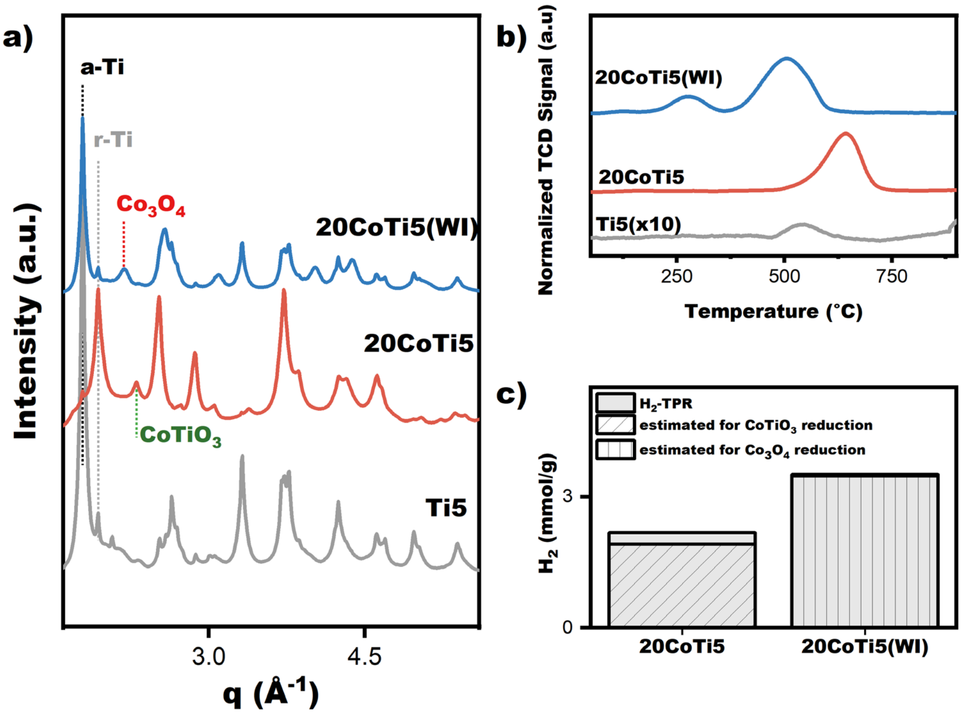

Figure 5.8. (a) Synchrotron XRD patterns (λ = 0.124 Å) of Ti5, 20CoTi5 and 20CoTi5 (WI) catalysts. (b) Weight normalized TPR profiles of 20CoTi5 and 20CoTi5 (WI) catalysts (conditions: 4 vol.% H_2 in N_2, 50 mL/min). (c) Quantification of H_2 consumption during TPR experiments (solid bar – excess of H_2; hatched bar – amount required for complete Co_3O_4/$CoTiO_3$ reduction).

Comparison in CO_2 hydrogenation (**Figure 5.9d**) shows that the reduced 20CoTi5 catalyst is significantly more active with a CO_2 conversion of 8.7% than the 20CoTi5(WI) with a CO_2 conversion of 5.3% at a comparable high CH_4 selectivity close to 90%. The performance of these samples was also compared to a 20Co/TiO_2 catalyst prepared by conventional wet impregnation of P25 TiO_2 (20Co/P25). The 20Co/P25 catalysts displayed a comparable activity and slightly higher CH_4 selectivity than 20CoTi5 (**Figure D16).**

The nature of the Co species in the reduced CoTi5 and 20CoTi5(WI) samples was studied by CO IR spectroscopy at 50 °C (**Figure D17**). IR bands in the 2060 and 1990 cm^{-1} range are typically assigned to CO linearly bonded to metallic Co.[101–104] The spectra of 20CoTi5 and 20CoTi5(WI) contain carbonyl bands at 2024 and 2063 cm^{-1}, respectively. The lower wavenumber of the carbonyl bands in 20CoTi5 indicates stronger CO adsorption. IR bands in the 1900 and 1700 cm^{-1} range are commonly assigned to CO adsorbed in two-fold, three-fold, and possibly fourfold sites.[105–108] The minor contribution of bridged carbonyls is evident on the surface of both catalysts. The spectra of 20CoTi5 also contain a band at 2092 cm^{-1}, which is typically assigned to Co-dicarbonyls ($Co^+(CO)_2$)[109,110], thus indicating a small amount of unreduced Co^{2+}.

After evacuation, this latter band becomes much less intense, while the band at 2024 cm^{-1} remains unchanged, which supports the interpretation in terms of CO adsorption on cationic and metallic species in 20CoTi5. The spectra also contain indications of carbonate and bicarbonate species (1612, 1460, 1192 cm^{-1}) in the reduced 20CoTi5 and 20CoTi5 (WI) catalysts.[101]

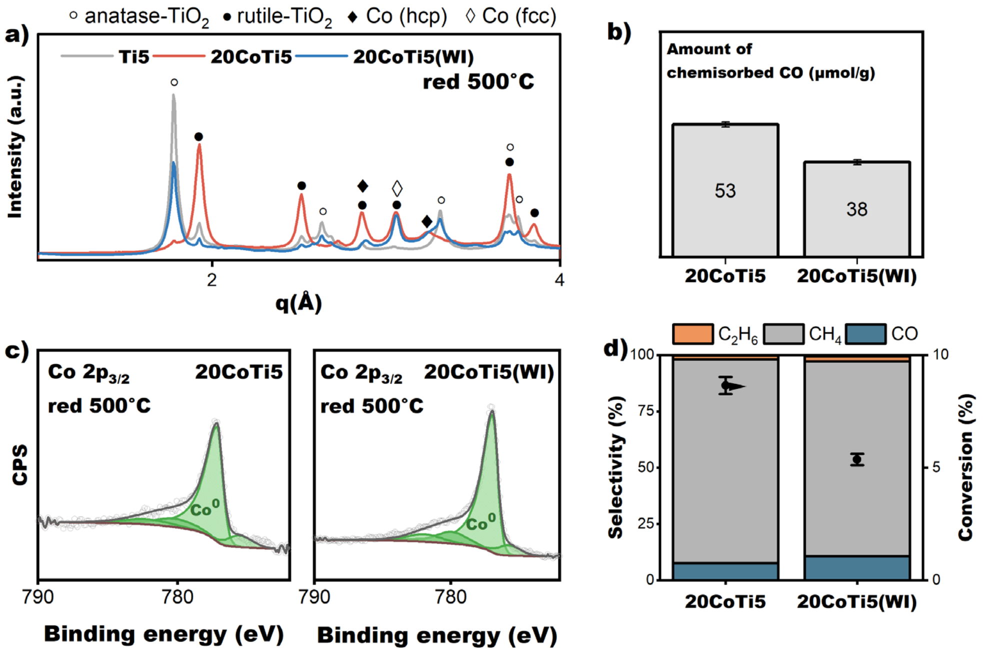

Figure 5.9. (a) Synchrotron XRD patterns (λ = 0.124 Å) of Ti5, 20CoTi5, and 20CoTi5 (WI) catalysts after reduction at 500 °C for 4 h (conditions: 20% H_2 in Ar, 50 mL/min, 50 – 500 °C; 10 °C/min). (b) The amount of CO chemisorbed during chemisorption experiments on 20CoTi5 and 20CoTi5 (WI) catalysts, reduced at 500 °C for 4 h. (c) Deconvolution of Co 2p$_{3/2}$ XP spectra 20CoTi5 and 20CoTi5 (WI), reduced at 500 °C for 4 h. (d) Catalytic performance of 20CoTi5 and 20CoTi5 (WI) catalysts reduced at 500 °C: CO_2 conversion and product distribution at a reaction temperature 250 °C (conditions: 250 °C, 50 mg catalyst, 15 vol.% CO_2, 60 vol.% H_2, 25 vol.% Ar, 50 mL/min, 1 bar).

IR spectroscopy was also employed to study the response of the reduced samples to CO_2 exposure at 50 °C. **Figure D17** shows the IR spectra with increasing CO_2 coverage. All IR spectra contain a strong band due to the asymmetric stretching vibration of gaseous CO_2 at ~2350 cm^{-1}.[108] The 20CoTi5 spectra contain only a weak feature of linear CO species on metallic Co (2018 cm^{-1}), while no such bands were observed for 20CoTi5(WI). This difference indicates facile CO_2 dissociation at low temperatures without H_2 in 20CoTi5. The CO_2 IR spectra also contain information about the support basicity. 20CoTi5(WI) exhibits carbonates (1603; 1430 cm^{-1}) and bicarbonates (1226 cm^{-1}) [101,111]. CO_2 adsorption on 20CoTi5 results in bicarbonates (1225 cm^{-1}) and carbonates (1592, 1338 cm^{-1}).[101,112,113] Based on the IR intensities, carbonates and bicarbonates are the main species formed during CO_2 on 20CoTi5 and 20CoTi5(WI).

In summary, complete Co reduction has been evident for both catalysts by XPS and in situ XRD. The Co particle size of the two catalysts is very similar (abundant 3 – 5 nm hcp Co). However, a different TiO_2 phase structure was found after reduction: 20CoTi5 – 13 nm r-TiO_2, 20CoTi5 (WI) – 18 nm a-TiO_2. The role of the TiO_2 crystal structure on the CO_2 hydrogenation performance of TiO_2-supported metal catalysts remains a topic of intense debate. Bao's group showed that Ni/r-TiO_2 outperformed Ni/a-TiO_2 by almost two orders of magnitude in CO_2 methanation, independently of the Ni loading and the Ni particle size.[114] It has also been demonstrated that the interaction between the RuO_2 particles and the TiO_2 phases influences the performance of the methanation reaction, suggesting RuO_2 migration from a-TiO_2 over r-TiO_2.[89,115] The preference of Ru for r-TiO_2 results in a higher Ru dispersion and catalytic activity. It was also found that Ru on a-TiO_2 is prone to sintering of Ru and a-TiO_2 as well as the formation of TiO_2-RuO_2-TiO_2 sandwich structures.[89,115] Li et al. showed that a Co/r-TiO_2 catalyst is highly selective in CO_2 hydrogenation to CH_4, while CO was the main product obtained with a Co/a-TiO_2 catalyst.[23] Based on *in situ* DRIFT results, the high activity of Co/r-TiO_2 was related to strong CO adsorption in comparison to the Co/a-TiO_2 catalyst.[23] In the present work, SMSI encapsulation of Co was evidenced for reduced 20CoTi5(WI) catalysts by quasi-in situ XPS and CO chemisorption unlike 20CoTi5. This suggests that the r-TiO_2 phase (as present in 20CoTi5) is more resistant to SMSI than a-TiO_2 during reduction at 500 °C. IR results showed that the carbonyl bands in 20CoTi5 are located at 2024 cm^{-1} while for 20CoTi5(WI) carbonyl bands are at 2063 cm^{-1}, which points to stronger CO adsorption on 20CoTi5 than on 20CoTi5(WI). This could affect CO hydrogenation to CH_4. Additionally, CO_2 adsorption on reduced 20CoTi5 led to CO indicative of CO_2 dissociation, which was absent for 20CoTi5(WI).

Conclusions

In this work, a set of Co-TiO_2 samples with varying Co content (2.5 – 40 mol.%) prepared by FSP were evaluated for their catalytic performance in CO_2 methanation. FSP preparation of Co-TiO_2 resulted in small TiO_2 nanoparticles of ~8 nm with a higher surface area than conventional TiO_2 supports. Catalysts with low Co content contain highly dispersed Co^{2+} ions which cannot be reduced at 500 °C. Catalysts containing 10 mol.% or more Co also contain segregated $CoTiO_3$ particles. These particles can be reduced to metallic Co and rutile-TiO_2 nanoparticles upon reduction at 500 °C. The highest Co-weight-normalized activity of 4.9 ± 0.2 $mmol_{CO2}/mol_{Co}/s$ at a temperature of 250 °C was found for the 20CoTi5 sample. The Co reduction degree of this sample is ~100%, represented by on average 14 nm rutile-TiO_2, ~4 nm Co (hcp) nanoparticles, and a small amount of Co present as Co (fcc). This sample exhibited a CH_4 selectivity of 91% at 250 °C. The low reduction degrees of Co in reduced 2.5CoTi5 and 5CoTi5 led to very low CO_2 conversion and predominant formation of CO (79%) under the same reaction conditions. Catalysts containing more and larger Co nanoparticles at a higher Co content mainly yielded CH_4, along with small amounts of CO and C_2H_6. Optimization of the particle size of flame-synthesized 20Co-TiO_2 catalysts revealed that, despite the significant differences in the structure of the as-prepared samples, reduction led to metallic Co particles on 13 – 16 nm rutile-TiO_2, deriving predominantly from $CoTiO_3$ decomposition. The lower catalytic activity of 20CoTi2.5 can be explained by incomplete Co reduction as opposed to completely reduced Co phases in 20CoT5 and 20CoTi10. The larger amount of relatively large fcc Co particles of ~14 nm in reduced 20CoTi2.5 is likely the consequence of the reduction of Co at higher temperatures than in 20CoT5 and 20CoTi10. The lower Co reduction degree and the large size of the Co nanoparticles can explain the lower reaction rate in CO_2 hydrogenation. Besides complete Co reduction, the high activity in CO_2 hydrogenation of 20CoTi5 and 20CoTi10 can be linked to the high Co dispersion as ~4 nm hcp Co particles. The most active one-step flame-synthesized 20CoTi5 catalyst was compared to Co/TiO_2 prepared by wet-impregnation on FSP-derived TiO_2 and P25 TiO_2. In situ synchrotron XRD and quasi-in situ XPS results revealed the formation of metallic Co after reduction at 500 °C in all three catalysts with similar 4 – 5 nm hcp Co nanoparticles. While these Co nanoparticles are on r-TiO_2 in the 20CoTi5, they are located on a-TiO_2 in the impregnated Co/TiO_2 catalysts. Despite the structural similarities of Co in the reduced 20CoTi5 and 20CoTi5(WI) catalysts, the CO_2 conversion of 20CoTi5(WI) was significantly lower than that of 20CoTi5 at comparable high CH_4 selectivity (~90%). We speculate that the presence of a more thermodynamically stable rutile-TiO_2 phase in one-step flame-synthesized 20CoTi5 resuenhances the stabilization of small Co nanoparticles, while the presence of anatase-TiO_2 phase has a tendency to form TiO_2 overlayer on Co surface during reduction at 500 °C, therefore, reducing the accessibility of Co and activity of the catalyst.

References

1. Solomon, S., Plattner, G. K., Knutti, R. & Friedlingstein, P. Irreversible climate change due to carbon dioxide emissions. Proc Natl Acad Sci U S A 106, 1704–1709 (2009).

2. Mulvaney, D. Energy and the Environment I: Fossil Fuels. Sustainable Energy Transitions 81–108 (2020).

3. Cox, P. M., Betts, R. A., Jones, C. D., Spall, S. A. & Totterdell, I. J. Acceleration of global warming due to carbon-cycle feedbacks in a coupled climate model. Nature 408, 184–187 (2000).

4. Guo, L., Guo, X., He, Y. & Tsubaki, N. CO_2 heterogeneous hydrogenation to carbon-based fuels: recent key developments and perspectives. J Mater Chem A Mater 11, 11637–11669 (2023).

5. Ashok, J. et al. A review of recent catalyst advances in CO_2 methanation processes. Catal Today 356, 471–489 (2020).

6. Kondratenko, E. V., Mul, G., Baltrusaitis, J., Larrazábal, G. O. & Pérez-Ramírez, J. Status and perspectives of CO_2 conversion into fuels and chemicals by catalytic, photocatalytic and electrocatalytic processes. Energy Environ Sci 6, 3112–3135 (2013).

7. Ren, J. et al. Methanation of CO/CO_2 for power to methane process: Fundamentals, status, and perspectives. Journal of Energy Chemistry 80, 182–206 (2023).

8. Rönsch, S. et al. Review on methanation – From fundamentals to current projects. Fuel 166, 276–296 (2016).

9. Marconi, E., Tuti, S. & Luisetto, I. Structure-Sensitivity of CO_2 Methanation over Nanostructured Ni Supported on CeO_2 Nanorods. Catalysts 2019, Vol. 9, Page 375 9, 375 (2019).

10. Somorjal, G. A. & Carrazza, J. Structure Sensitivity of Catalytic Reactions. Ind. Eng. Chem. Fundani 25, 63–69 (1986).

11. Van Santen, R. A. Complementary structure sensitive and insensitive catalytic relationships. Acc Chem Res 42, 57–66 (2009).

12. Lovell, E. C., Scott, J. & Amal, R. Ni-SiO_2 Catalysts for the Carbon Dioxide Reforming of Methane: Varying Support Properties by Flame Spray Pyrolysis. Molecules 2015, Vol. 20, Pages 4594-4609 20, 4594–4609 (2015).

13. Simons, J. F. M. et al. Structure Sensitivity of CO_2 Hydrogenation on Ni Revisited. J Am Chem Soc 145, 20289–20301 (2023).

14. Díez-Ramírez, J. et al. Effect of support nature on the cobalt-catalyzed CO_2 hydrogenation. Journal of CO_2 Utilization 21, 562–571 (2017).

15. Ilsemann, J. et al. Cobalt@Silica Core-Shell Catalysts for Hydrogenation of CO/CO_2 Mixtures to Methane. ChemCatChem 11, 4884–4893 (2019).

16. Kim, S. S., Lee, H. H. & Hong, S. C. The effect of the morphological characteristics of TiO_2 supports on the reverse water–gas shift reaction over Pt/TiO_2 catalysts. Appl Catal B 119–120, 100–108 (2012).

17. Xu, J. et al. Influence of pretreatment temperature on catalytic performance of rutile TiO_2-supported ruthenium catalyst in CO_2 methanation. J Catal 333, 227–237 (2016).

18. Have, I. C. ten et al. Uncovering the reaction mechanism behind CoO as active phase for CO_2 hydrogenation. Nature Communications 2022 13:1 13, 1–11 (2022).

19. Kattel, S. et al. CO_2 Hydrogenation over Oxide-Supported PtCo Catalysts: The Role of the Oxide Support in Determining the Product Selectivity. Angewandte Chemie International Edition 55, 7968–7973 (2016).

20. Liu, J. et al. Enhanced low-temperature activity of CO_2 methanation over highly-dispersed Ni/TiO_2 catalyst. Catal Sci Technol 3, 2627–2633 (2013).

21. Zhou, R., Rui, N., Fan, Z. & Liu, C. jun. Effect of the structure of Ni/TiO_2 catalyst on CO_2 methanation. Int J Hydrogen Energy 41, 22017–22025 (2016).

22. Melaet, G. et al. Evidence of highly active cobalt oxide catalyst for the Fischer-Tropsch synthesis and CO_2 hydrogenation. J Am Chem Soc 136, 2260–2263 (2014).

23. Li, W. et al. CO_2 Hydrogenation on Unpromoted and M-Promoted Co/TiO_2 Catalysts (M = Zr, K, Cs): Effects of Crystal Phase of Supports and Metal-Support Interaction on Tuning Product Distribution. ACS Catal 9, 2739–2751 (2019).

24. Bertella, F., Concepción, P. & Martínez, A. TiO_2 polymorph dependent SMSI effect in Co-Ru/TiO_2 catalysts and its relevance to Fischer-Tropsch synthesis. Catal Today 289, 181–191 (2017).

25. Scarfiello, C. et al. Modified Co/TiO_2 catalysts for CO_2 hydrogenation to fuels. J Catal 428, 115202 (2023).

26. Toyao, T., Kayamori, S., Maeno, Z., Siddiki, S. M. A. H. & Shimizu, K. I. Heterogeneous Pt and MoO_x Co-Loaded TiO_2 Catalysts for Low temperature CO_2 Hydrogenation to Form CH_3OH. ACS Catal 9, 8187–8196 (2019).

27. Eschemann, T. O. & De Jong, K. P. Deactivation behavior of Co/TiO_2 catalysts during fischer-tropsch synthesis. ACS Catal 5, 3181–3188 (2015).

28. Moya-Cancino, J. G. et al. In Situ X-ray Raman Scattering Spectroscopy of the Formation of Cobalt Carbides in a Co/TiO_2 Fischer-Tropsch Synthesis Catalyst. ACS Catal 11, 809–819 (2021).

29. Shi, Z. et al. Direct conversion of CO_2 to long-chain hydrocarbon fuels over K-promoted CoCu/TiO_2 catalysts. Catal Today 311, 65–73 (2018).

30. van Koppen, L. M., Iulian Dugulan, A., Leendert Bezemer, G. & Hensen, E. J. M. Sintering and carbidization under simulated high conversion on a cobalt-based Fischer-Tropsch catalyst; manganese oxide as a structural promotor. J Catal 413, 106–118 (2022).

31. van Koppen, L. M., Dugulan, A. I., Hensen, E. J. M. & Bezemer, G. L. Tuning stability of titania-supported Fischer-Tropsch catalysts: Impact of surface area and noble metal promotion. Catal Today 429, 114471 (2024).

32. van Koppen, L. M., Iulian Dugulan, A., Leendert Bezemer, G. & Hensen, E. J. M. Elucidating deactivation of titania-supported cobalt Fischer-Tropsch catalysts under simulated high conversion conditions. J Catal 420, 44–57 (2023).

33. Bezemer, G. L. et al. Cobalt particle size effects in the Fischer-Tropsch reaction studied with carbon nanofiber supported catalysts. J Am Chem Soc 128, 3956–3964 (2006).

34. Pestman, R., Chen, W. & Hensen, E. Insight into the Rate-Determining Step and Active Sites in the Fischer-Tropsch Reaction over Cobalt Catalysts. ACS Catal 9, 4189–4195 (2019).

35. Den Breejen, J. P. et al. On the origin of the cobalt particle size effects in Fischer-Tropsch catalysis. J Am Chem Soc 131, 7197–7203 (2009).

36. Khodakov, A. Y., Chu, W. & Fongarland, P. Advances in the development of novel cobalt Fischer-Tropsch catalysts for synthesis of long-chain hydrocarbons and clean fuels. Chem Rev 107, 1692–1744 (2007).

37. Sivakumar, S., Pillai, P. K., Mukundan, P. & Warrier, K. G. K. Sol–gel synthesis of nanosized anatase from titanyl sulfate. Mater Lett 57, 330–335 (2002).

38. Park, S. D., Cho, Y. H., Kim, W. W. & Kim, S. J. Understanding of Homogeneous Spontaneous Precipitation for Monodispersed TiO_2 Ultrafine Powders with Rutile Phase around Room Temperature. J Solid State Chem 146, 230–238 (1999).

39. Yin, H. et al. Hydrothermal synthesis of nanosized anatase and rutile TiO_2 using amorphous phase TiO_2. J Mater Chem 11, 1694–1703 (2001).

40. McCormick, J. R., Zhao, B., Rykov, S. A., Wang, H. & Chen, J. G. Thermal stability of flame-synthesized anatase TiO_2 nanoparticles. Journal of Physical Chemistry B 108, 17398–17402 (2004).

41. Khan, S., Park, J. S. & Ishihara, T. A Review of the Single-Step Flame Synthesis of Defective and Heterostructured TiO_2 Nanoparticles for Photocatalytic Applications. Catalysts 2023, Vol. 13, Page 196 13, 196 (2023).

42. Docters, T., Chovelon, J. M., Herrmann, J. M. & Deloume, J. P. Syntheses of TiO_2 photocatalysts by the molten salts method: Application to the photocatalytic degradation of Prosulfuron. Appl Catal B 50, 219–226 (2004).

43. Bickley, R. I., Gonzalez-Carreno, T., Lees, J. S., Palmisano, L. & Tilley, R. J. D. A structural investigation of titanium dioxide photocatalysts. J Solid State Chem 92, 178–190 (1991).

44. Fukugaichi, S. Nanosized TiO_2 synthesis via facile chemical top-down approach: enhancing gaseous photocatalytic performance. J Mater Sci 58, 17430–17441 (2023).

45. Manuputty, M. Y. et al. Understanding the anatase-rutile stability in flame-made TiO_2. Combust Flame 226, 347–361 (2021).

46. Wegner, K., Schimmoeller, B., Thiebaut, B., Fernandez, C. & Rao, T. N. Pilot Plants for Industrial Nanoparticle Production by Flame Spray Pyrolysis. KONA Powder and Particle Journal 29, 251–265 (2011).

47. Mueller, R., Mädler, L. & Pratsinis, S. E. Nanoparticle synthesis at high production rates by flame spray pyrolysis. Chem Eng Sci 58, 1969–1976 (2003).

48. Gäßler, M. et al. The Impact of Support Material of Cobalt-Based Catalysts Prepared by Double Flame Spray Pyrolysis on CO_2 Methanation Dynamics. ChemCatChem 14, e202200286 (2022).

49. Schubert, M. et al. Highly active Co–Al_2O_3 -based catalysts for CO_2 methanation with very low platinum promotion prepared by double flame spray pyrolysis. Catal Sci Technol 6, 7449–7460 (2016).

50. Oku, M., Wagatsumaa, K. & Kohikib, S. Ti 2p and Ti 3p X-ray photoelectron spectra for TiO_2, $SrTiO_3$ and $BaTiO_3$. Phys. Chem. Chem. Phys., 1999, 1, 5327-5331.

51. Lewera, A., Timperman, L., Roguska, A. & Alonso-Vante, N. Metal-support interactions between nanosized Pt and metal oxides (WO_3 and TiO_2) studied using X-ray photoelectron spectroscopy. Journal of Physical Chemistry C 115, 20153–20159 (2011).

52. Biesinger, M. C. et al. Resolving surface chemical states in XPS analysis of first row transition metals, oxides and hydroxides: Cr, Mn, Fe, Co and Ni. Appl Surf Sci 257, 2717–2730 (2011).

53. Cañón, J., Teplyakov, A. V . XPS characterization of cobalt impregnated SiO_2 and γ-Al_2O_3. Surface and Interface Analysis 53, 475–481 (2021).

54. Lykhach, Y. et al. Quantitative Analysis of the Oxidation State of Cobalt Oxides by Resonant Photoemission Spectroscopy. Journal of Physical Chemistry Letters 10, 6129–6136 (2019).

55. Cabrera-German, D., Gomez-Sosa, G. & Herrera-Gomez, A. Accurate peak fitting and subsequent quantitative composition analysis of the spectrum of Co 2p obtained with Al Kα radiation: I: cobalt spinel. Surface and Interface Analysis 48, 252–256 (2016).

56. Giraldi, T. R., Dias, J. A., Baggio, C. M., Maestrelli, S. C. & Oliveira, J. A. Anatase-to-rutile transition in co-doped TiO_2 pigments. J Solgel Sci Technol 83, 115–123 (2017).

57. Savio, A. K. P. D. et al. Environmentally effective photocatalyst CoO–TiO_2 synthesized by thermal precipitation of Co in amorphous TiO_2. Appl Catal B 182, 449–455 (2016).

58. Chen, Q. et al. Synergistic effect of bifunctional Co–TiO_2 catalyst on degradation of Rhodamine B: Fenton-photo hybrid process. Chemical Engineering Journal 229, 57–65 (2013).

59. Bickley, R. I., Gonzalez-Carreno, T., Lees, J. S., Palmisano, L. & Tilley, R. J. D. A structural investigation of titanium dioxide photocatalysts. J Solid State Chem 92, 178–190 (1991).

60. Su, W. et al. Surface phases of TiO_2 nanoparticles studied by UV raman spectroscopy and FT-IR spectroscopy. Journal of Physical Chemistry C 112, 7710–7716 (2008).

61. Zhang, J., Li, M., Feng, Z., Chen, J. & Li, C. UV raman spectroscopic study on TiO_2- I. phase transformation at the surface and in the bulk. Journal of Physical Chemistry B 110, 927–935 (2006).

62. Absalan, Y. et al. Removing organic harmful compounds from the polluted water by a novel synthesized cobalt(II) and titanium(IV) containing photocatalyst under visible light. Environ Nanotechnol Monit Manag 14, 100304 (2020).

63. Qu, Y., Zhou, W. & Fu, H. Porous Cobalt Titanate Nanorod: A New Candidate for Visible Light-Driven Photocatalytic Water Oxidation. ChemCatChem 6, 265–270 (2014).

64. Subramanian, S. et al. Effect of photocatalytic activity on cobalt titanate ($CoTiO_3$) nanostructures. Mater Today Proc 33, 2274–2278 (2020).

65. Tang, C. W., Wang, C. Bin & Chien, S. H. Characterization of cobalt oxides studied by FT-IR, Raman, TPR and TG-MS. Thermochim Acta 473, 68–73 (2008).

66. Abedini, A. & Khademolhoseini, S. Cobalt titanate nanoparticles: synthesis, characterization, optical and photocatalytic properties. Journal of Materials Science: Materials in Electronics 27, 330–334 (2016).

67. Khodakov, A. Y., Chu, W. & Fongarland, P. Advances in the development of novel cobalt Fischer-Tropsch catalysts for synthesis of long-chain hydrocarbons and clean fuels. Chem Rev 107, 1692–1744 (2007).

68. Eaimsumang, S., Prataksanon, P., Pongstabodee, S. & Luengnaruemitchai, A. Effect of acid on the crystalline phase of TiO_2 prepared by hydrothermal treatment and its application in the oxidative steam reforming of methanol. Research on Chemical Intermediates 46, 1235–1254 (2020).

69. Tolek, W., Nanthasanti, N., Pongthawornsakun, B., Praserthdam, P. & Panpranot, J. Effects of TiO_2 structure and Co addition as a second metal on Ru-based catalysts supported on TiO_2 for selective hydrogenation of furfural to FA. Scientific Reports 11.1, 9786 (2021).

70. Hu, C. et al. Insights into the Role of Pt Promoter in Co/TiO_2 Catalysts for CO Hydrogenation. Catalysts 14, 922 (2024).

71. Wolf, M. et al. Synthesis, characterization and water–gas shift activity of nano-particulate mixed-metal (Al, Ti) cobalt oxides. Dalton Transactions 48, 13858–13868 (2019).

72. Hwang, J. H. et al. A thermogravimetric study of $CoTiO_3$ as oxygen carrier for chemical looping combustion. Catal Today 303, 13–18 (2018).

73. Karaca, H. et al. In situ XRD investigation of the evolution of alumina -supported cobalt catalysts under realistic conditions of Fischer-Tropsch synthesis. Chemical Communications 46, 788–790 (2010).

74. Khodakov, A. Y., Griboval-Constant, A., Bechara, R. & Villain, F. Pore-size control of cobalt dispersion and reducibility in mesoporous silicas. Journal of Physical Chemistry B 105, 9805–9811 (2001).

75. Anderson, K. P., Vinci, R. P. & Chan, H. M. Novel metal–ceramic composite microstructures produced through the partial reduction of $CoTiO_3$. J Mater Sci 53, 8193–8210 (2018).

76. Basumatary, R., Basumatary, B., Konwar, D. & Ramchiary, A. Tailored highly efficient Co-doped $TiO_2/CoTiO_3$ heterojunction photocatalyst for methylene blue degradation under visible light. Journal of the Korean Ceramic Society 60, 547–559 (2023).

77. Ovcharov, M. L., Stara, T. R., Korzhak, G. V. & Kuchmiy, S. Y. Photocatalytic

Activity of Nanoheterostructures $C_3N_4/CoTiO_3$ in Hydrogen Evolution from Water–Alcohol Solutions Under Visible Light Irradiation. Theoretical and Experimental Chemistry 60, 31–40 (2024).

78. Sławiński, W. A., Zacharaki, E., Fjellvåg, H. & Sjåstad, A. O. Structural Arrangement in Close-Packed Cobalt Polytypes. Cryst Growth Des 18, 2316–2325 (2018).

79. Ram, S. Allotropic phase transformations in HCP, FCC and BCC metastable structures in Co-nanoparticles. Materials Science and Engineering: A 304–306, 923–927 (2001).

80. Turczyniak, S. et al. A Comparative Ambient Pressure X-ray Photoelectron and Absorption Spectroscopy Study of Various Cobalt-Based Catalysts in Reactive Atmospheres. Top Catal 59, 532–542 (2016).

81. Luo, W. & Zafeiratos, S. Tuning Morphology and Redox Properties of Cobalt Particles Supported on Oxides by an in between Graphene Layer. Journal of Physical Chemistry C 120, 14130–14139 (2016).

82. Papaefthimiou, V. et al. Probing metal-support interaction in reactive environments: An in situ study of PtCo bimetallic nanoparticles supported on TiO_2. Journal of Physical Chemistry C 116, 14342–14349 (2012).

83. Van Deelen, T. W., Nijhuis, J. J., Krans, N. A., Zečević, J. & De Jong, K. P. Preparation of Cobalt Nanocrystals Supported on Metal Oxides to Study Particle Growth in Fischer-Tropsch Catalysts. ACS Catal 8, 10581–10589 (2018).

84. Vogt, C. et al. Understanding carbon dioxide activation and carbon–carbon coupling over nickel. Nature Communications 2019 10:1 10, 1–10 (2019).

85. Parastaev, A. et al. Breaking structure sensitivity in CO_2 hydrogenation by tuning metal–oxide interfaces in supported cobalt nanoparticles. Nat Catal 5, 1051–1060 (2022).

86. Dostagir, N. H. M. et al. Co Single Atoms in ZrO_2 with Inherent Oxygen Vacancies for Selective Hydrogenation of CO_2 to CO. ACS Catal 11, 9450–9461 (2021).

87. Deng, K. et al. Studies of CO_2 hydrogenation over cobalt/ceria catalysts with in situ characterization: the effect of cobalt loading and metal–support interactions on the catalytic activity. Catal Sci Technol 10, 6468–6482 (2020).

88. Matsubu, J. C., Yang, V. N. & Christopher, P. Isolated metal active site concentration and stability control catalytic CO_2 reduction selectivity. J Am Chem Soc 137, 3076–3084 (2015).

89. Kim, A. et al. CO_2 methanation on Ru/TiO_2 catalysts: On the effect of mixing anatase and rutile TiO_2 supports. Appl Catal B 220, 615–625 (2018).

90. Nyathi, T. M., Fischer, N., York, A. P. E. & Claeys, M. Effect of crystallite size on the performance and phase transformation of Co_3O_4/Al_2O_3 catalysts during CO-PrOx – an in situ study. Faraday Discuss 197, 269–285 (2017).

91. Van Steen, E. et al. Stability of nanocrystals: Thermodynamic analysis of oxidation and re-reduction of cobalt in water/hydrogen mixtures. Journal of Physical Chemistry B 109, 3575–3577 (2005).

92. Zhang, J., Xu, Q., Feng, Z., Li, M. & Li, C. Importance of the Relationship

between Surface Phases and Photocatalytic Activity of TiO_2. Angewandte Chemie International Edition 47, 1766–1769 (2008).

93. Carp, O., Huisman, C. L. & Reller, A. Photoinduced reactivity of titanium dioxide. Progress in Solid State Chemistry 32, 33–177 (2004).

94. Hirano, M., Nakahara, C., Ota, K., Tanaike, O. & Inagaki, M. Photoactivity and phase stability of ZrO_2-doped anatase-type TiO_2 directly formed as nanometer-sized particles by hydrolysis under hydrothermal conditions. J Solid State Chem 170, 39–47 (2003).

95. Ghosh, T. B., Dhabal, S. & Datta, A. K. On crystallite size dependence of phase stability of nanocrystalline TiO_2. J Appl Phys 94, 4577–4582 (2003).

96. Van Etten, M. P. C., Zijlstra, B., Hensen, E. J. M. & Filot, I. A. W. Enumerating active sites on metal nanoparticles: Understanding the size dependence of cobalt particles for CO dissociation. ACS Catal 11, 8484–8492 (2021).

97. Van Etten, M. P. C., De Laat, M. E., Hensen, E. J. M. & Filot, I. A. W. Unraveling the Role of Metal-Support Interactions on the Structure Sensitivity of Fischer-Tropsch Synthesis. Journal of Physical Chemistry C 127, 15148–15156 (2023).

98. Agrawal, R., Phatak, P. & Spanu, L. Effect of phase and size on surface sites in cobalt nanoparticles. Catal Today 312, 174–180 (2018).

99. Yu, Z. et al. Carbon nanofiber supported cobalt catalysts for Fischer-Tropsch synthesis with high activity and selectivity. Catal Letters 109, 43–47 (2006).

100. Nyathi, T. M. et al. Co_3O_4/TiO_2 catalysts studied in situ during the preferential oxidation of carbon monoxide: the effect of different TiO_2 polymorphs. Catal Sci Technol 13, 2038–2052 (2023).

101. Busca, G. & Lorenzelli, V. Infrared spectroscopic identification of species arising from reactive adsorption of carbon oxides on metal oxide surfaces. Materials Chemistry 7, 89–126 (1982).

102. Paredes-Nunez, A. et al. CO Hydrogenation on Cobalt-Based Catalysts: Tin Poisoning Unravels CO in Hollow Sites as a Main Surface Intermediate. Angewandte Chemie 130, 556–559 (2018).

103. Carlsson, A. F., Bäumer, M., Risse, T. & Freund, H. J. Surface structure of Co–Pd bimetallic particles supported on Al_2O_3 thin films studied using infrared reflection absorption spectroscopy of CO. J Chem Phys 119, 10885–10894 (2003).

104. Mehl, S. et al. Thermal evolution of cobalt deposits on Co_3O_4(111): atomically dispersed cobalt, two-dimensional CoO islands, and metallic Co nanoparticles. Physical Chemistry Chemical Physics 17, 23538–23546 (2015).

105. Kumar, N., Jothimurugesan, K., Stanley, G. G., Schwartz, V. & Spivey, J. J. In situ FT-IR study on the effect of cobalt precursors on CO adsorption behavior. Journal of Physical Chemistry C 115, 990–998 (2011).

106. Weststrate, C. J., van de Loosdrecht, J. & Niemantsverdriet, J. W. Spectroscopic insights into cobalt-catalyzed Fischer-Tropsch synthesis: A review of the carbon monoxide interaction with single crystalline surfaces of cobalt. J Catal 342, 1–16 (2016).

107. Zijlstra, B. et al. Coverage Effects in CO Dissociation on Metallic Cobalt

Nanoparticles. ACS Catal 9, 7365–7372 (2019).

108. Chen, W., Zijlstra, B., Filot, I. A. W., Pestman, R. & Hensen, E. J. M. Mechanism of Carbon Monoxide Dissociation on a Cobalt Fischer–Tropsch Catalyst. ChemCatChem 10, 136–140 (2018).

109. Venkov, T. & Hadjiivanov, K. FTIR study of CO interaction with Cu/TiO_2. Catal Commun 4, 209–213 (2003).

110. Hadjiivanov, K. et al. New types of polycarbonyls of Co+ formed after interaction of CO with Co–ZSM-5: An FTIR spectroscopic study. Physical Chemistry Chemical Physics 5, 243–245 (2003).

111. Mino, L., Spoto, G. & Ferrari, A. M. CO_2 capture by TiO_2 anatase surfaces: A combined DFT and FTIR study. Journal of Physical Chemistry C 118, 25016–25026 (2014).

112. Hadjiivanov, K. FTIR study of CO and NH_3 co-adsorption on TiO_2 (rutile). Appl Surf Sci 135, 331–338 (1998).

113. Liao, L. F., Lien, C. F., Shieh, D. L., Chen, M. T. & Lin, J. L. FTIR study of adsorption and photoassisted oxygen isotopic exchange of carbon monoxide, carbon dioxide, carbonate, and formate on TiO_2. Journal of Physical Chemistry B 106, 11240–11245 (2002).

114. Lin, Y., Zhu, Y., Pan, X. & Bao, X. Modulating the methanation activity of Ni by the crystal phase of TiO_2. Catal Sci Technol 7, 2813–2818 (2017).

115. Kim, A. et al. Selective CO_2 methanation on Ru/TiO_2 catalysts: unravelling the decisive role of the TiO_2 support crystal structure. Catal Sci Technol 6, 8117–8128 (2016).

Appendix D

Figures.

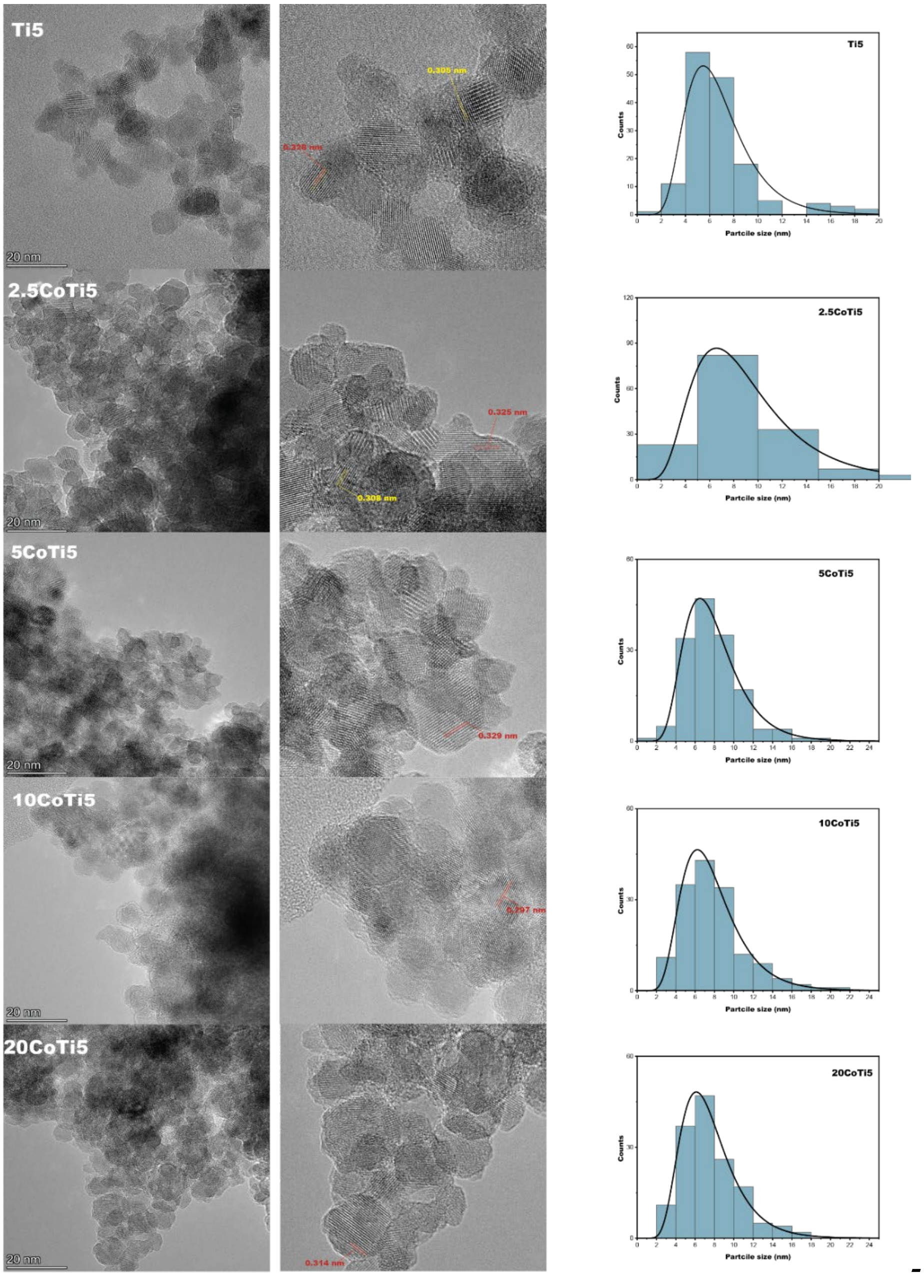

Figure D1. TEM images (left), HRTEM image (middle) with d-spacing of ~0.296 – 0.301 nm for the plane (101) r-TiO_2 and ~0.313 – 0.330 nm for the plane (101) a-TiO_2 of as-prepared Ti5 and CoTi5 catalysts.

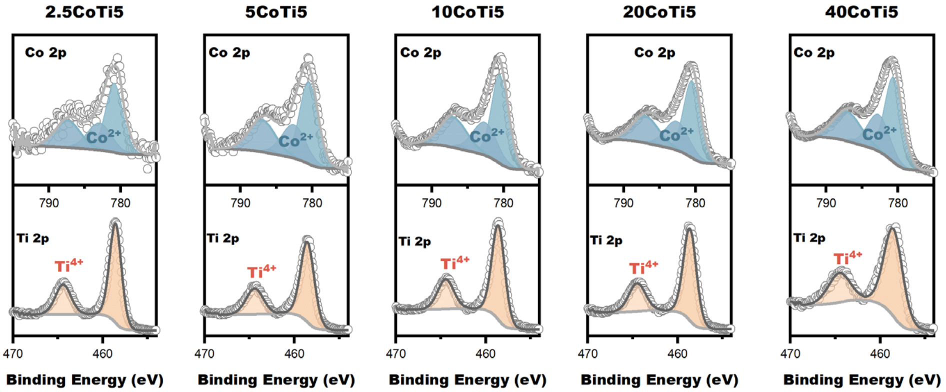

Figure D2. Deconvolution of Co $2p_{3/2}$ (top) and Ti 2p (bottom) XP spectra of as-prepared Ti5 and CoTi5 catalysts

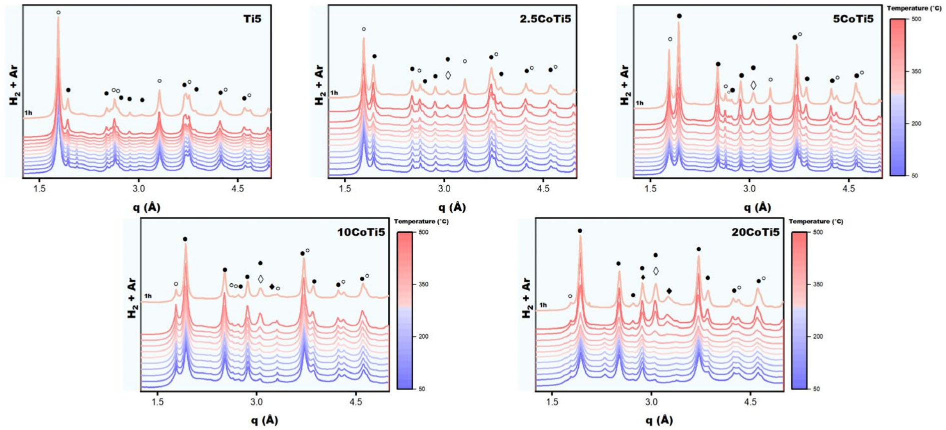

Figure D3. Synchrotron XRD patterns (λ = 0.124 Å) of Ti5 and CoTi5 catalysts during reductive pretreatment. °- anatase-TiO_2; • – r-TiO_2; ∇ – $CoTiO_3$; ♦ – Co (fcc); ◊ – Co (hcp) (conditions: 20 vol.% H_2 in Ar, 50 mL/min, 50 – 500 °C; 10 °C/min).

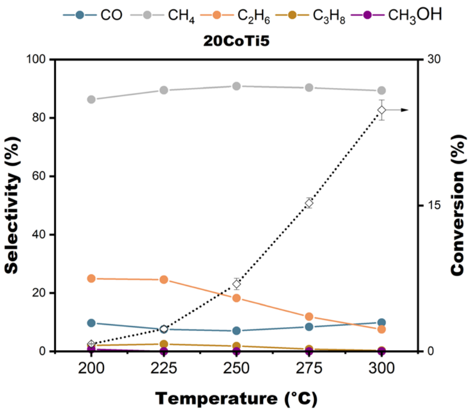

Figure D4. Catalytic performance of 20CoTi5 catalyst reduced at 500 °C in CO_2 hydrogenation as a function of temperature (conditions: 200 – 300 °C, 50 mg of catalyst, 15 vol.% CO_2, 60 vol.% H_2, 25 vol.% Ar, 50 mL/min, 1 bar).

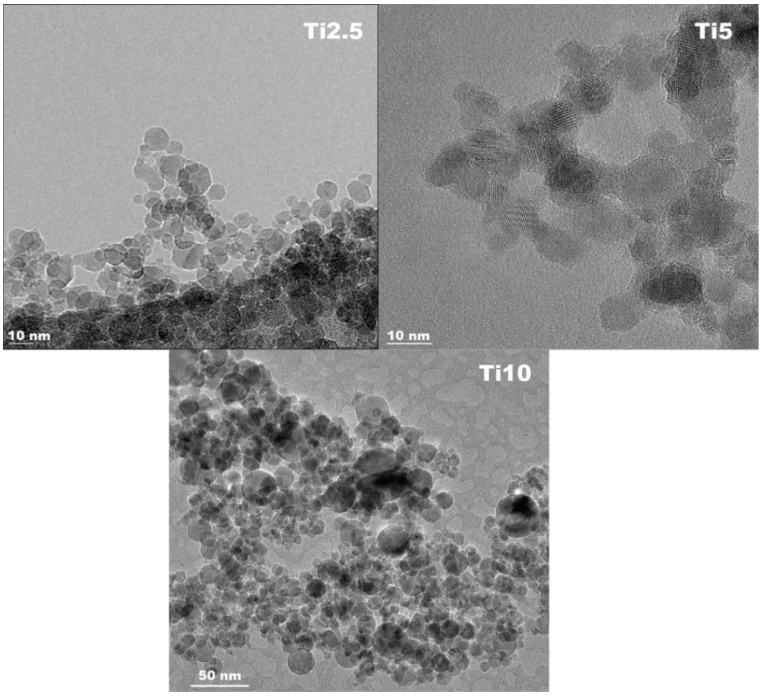

Figure D5. TEM images of as-prepared Ti2.5, Ti5 and Ti10.

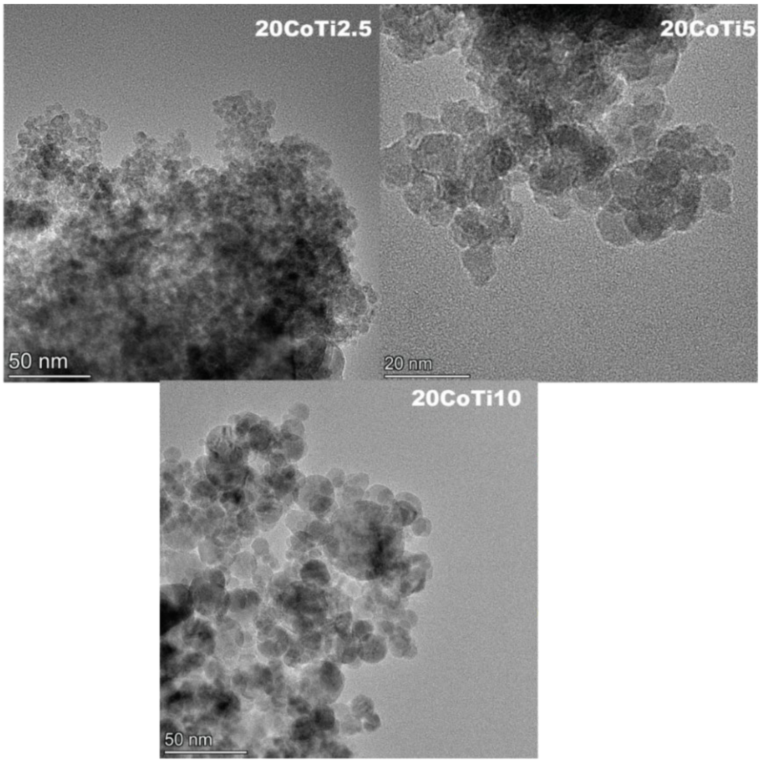

Figure D6. TEM images of as-prepared 20CoTi2.5;20CoTi5 (for comparison) and 20CoTi10.

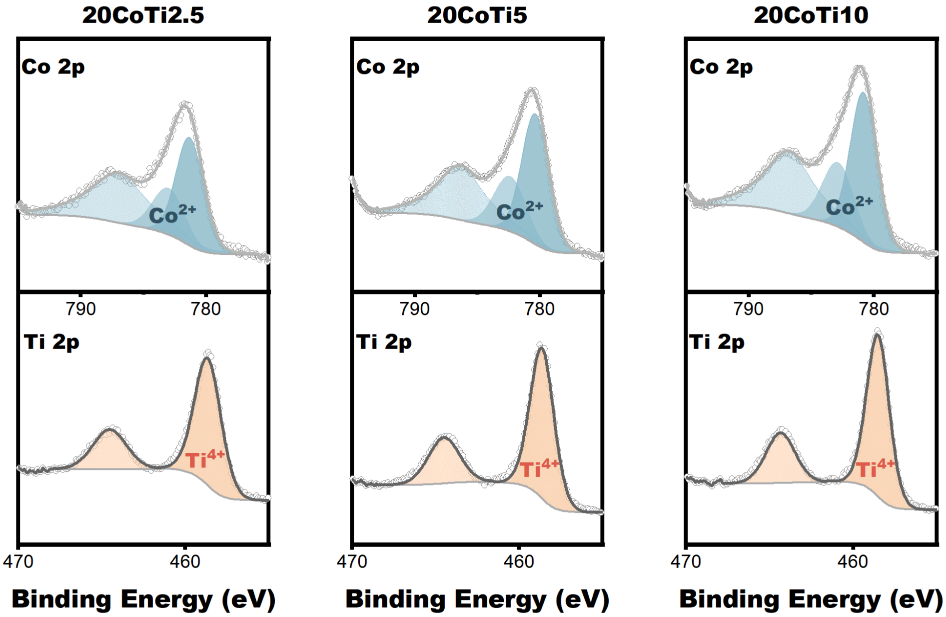

Figure D7. Deconvolution of Co $2p_{3/2}$ (top) and Ti 2p (bottom) XP spectra of as-prepared 20CoTi2.5, 20CoTi5, and 20CoTi10 catalysts.

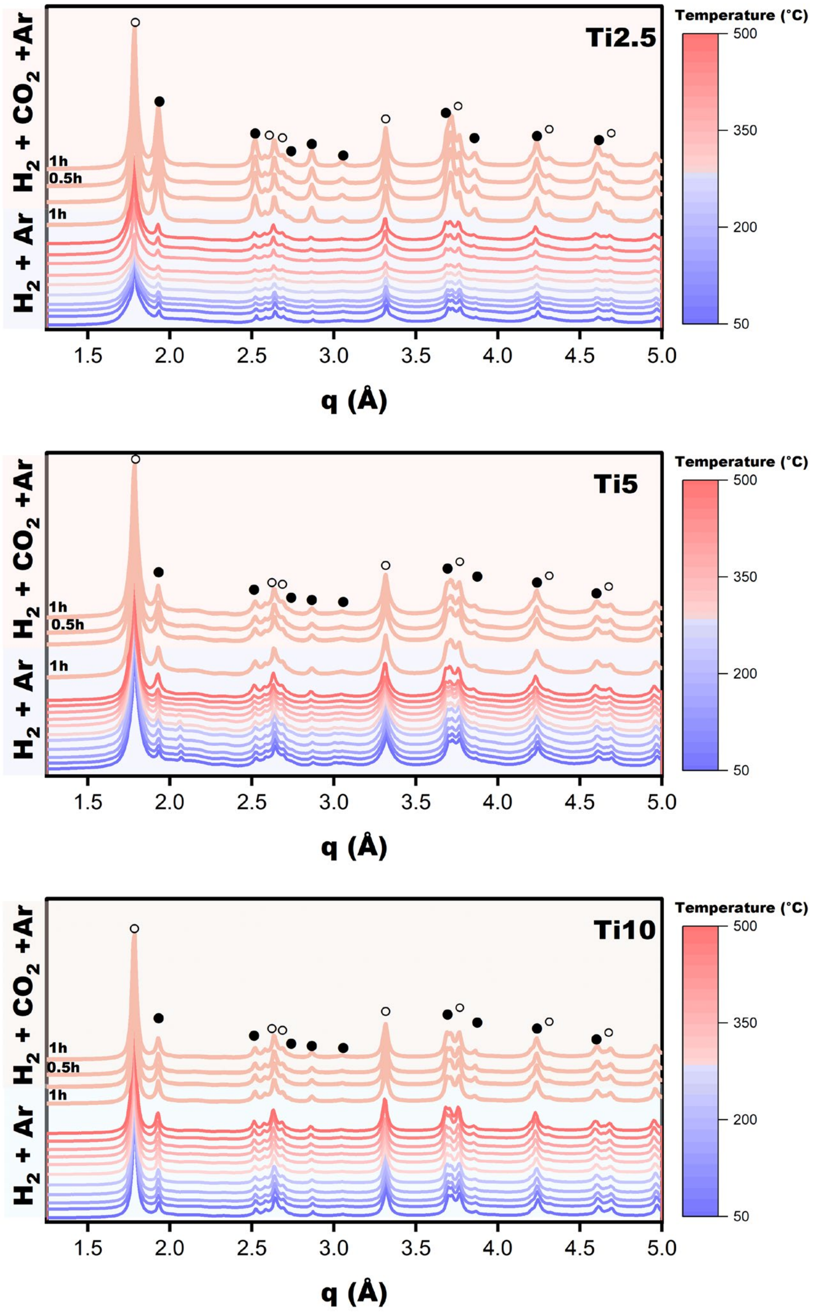

Figure D8. Synchrotron XRD patterns (λ = 0.124 Å) of Tix during reductive pretreatment. °- anatase-TiO_2; • – r-TiO_2 (conditions: 20 vol.% H_2 in Ar, 50 mL/min, 50 – 500 °C; 10 °C/min).

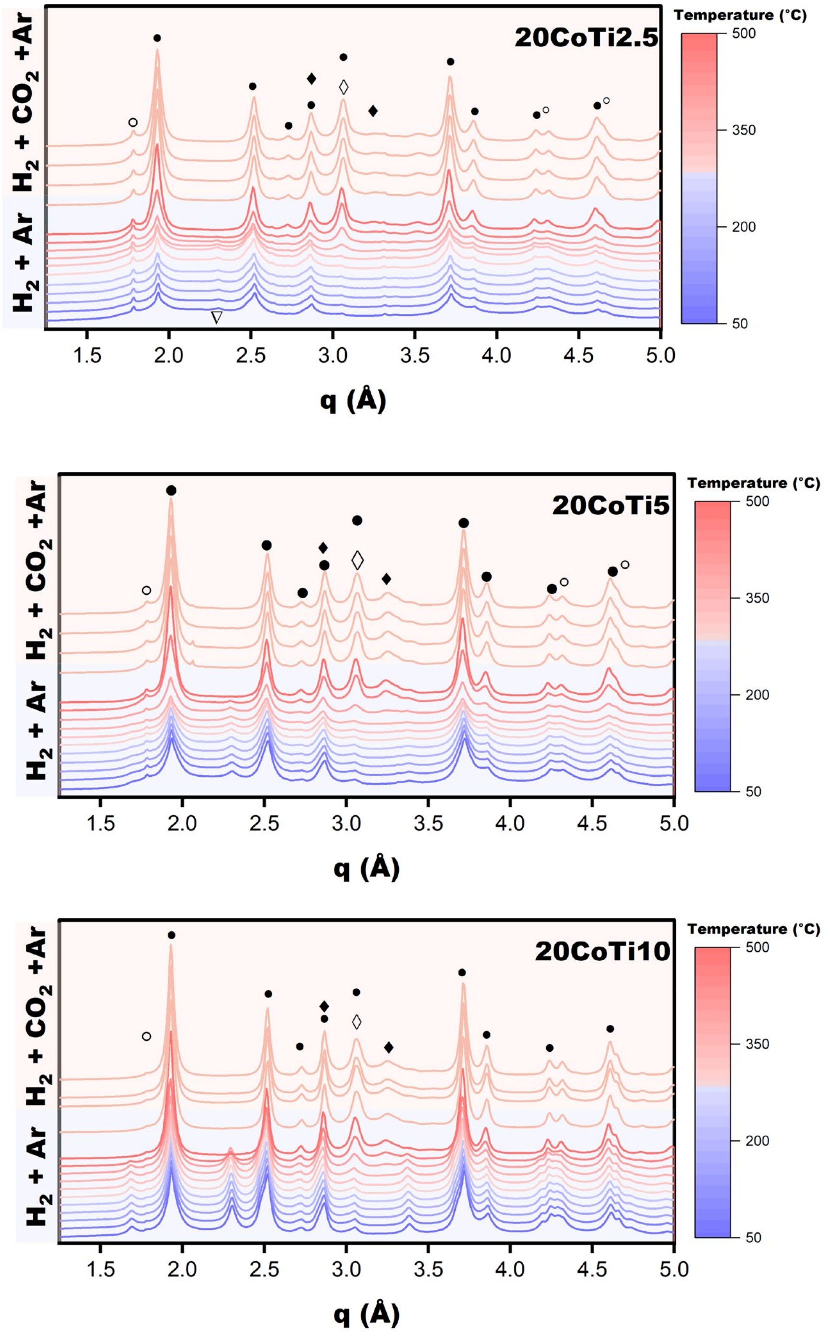

Figure D9. Synchrotron XRD patterns (λ = 0.124 Å) of Tix and 20CoTix catalysts during reductive pretreatment. º- a-TiO_2; • – r-TiO_2; ∇ - $CoTiO_3$; ♦ - Co (hcp); ◊- Co (fcc)(conditions: 20 vol.% H_2 in Ar, 50 mL/min, 50 – 500 °C; 10 °C/min).

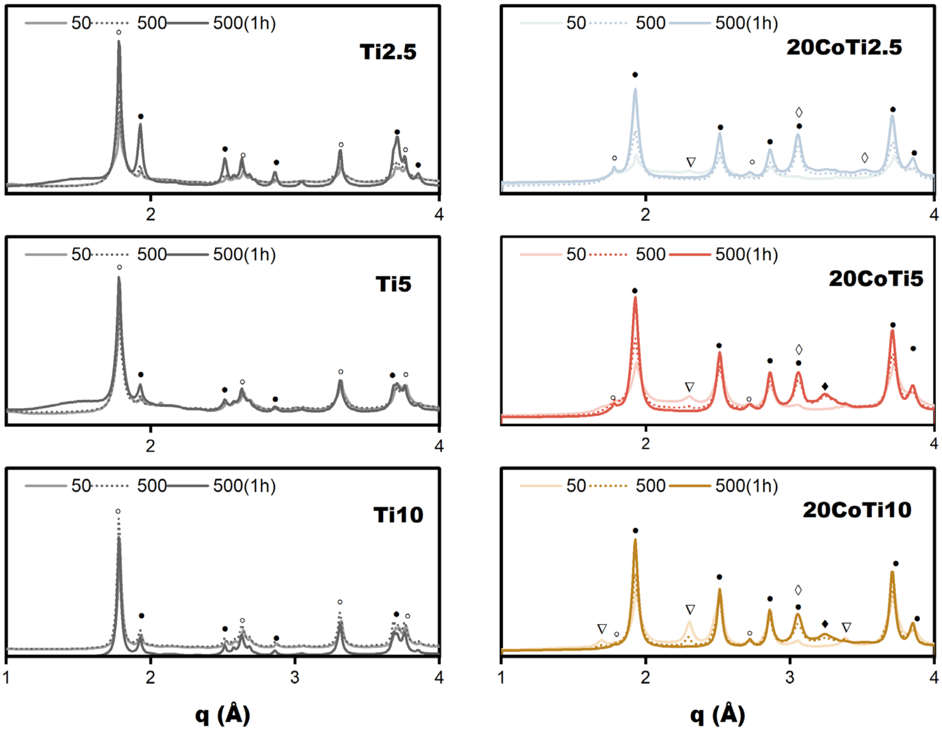

Figure D10. Synchrotron XRD patterns (λ = 0.124 Å) of Tix and 20CoTix (x=2.5 –10) catalysts before and reduction at 500 °C (conditions: 20 vol.% H_2 in Ar, 50 mL/min, 10 °C/min). ° – a-TiO_2; ● – r-TiO_2; ∇ – $CoTiO_3$; ♦ – Co (fcc); ◊ – Co (hcp) (conditions: 20 vol.% H_2 in Ar, 50 mL/min, 50 – 500 °C; 10 °C/min).

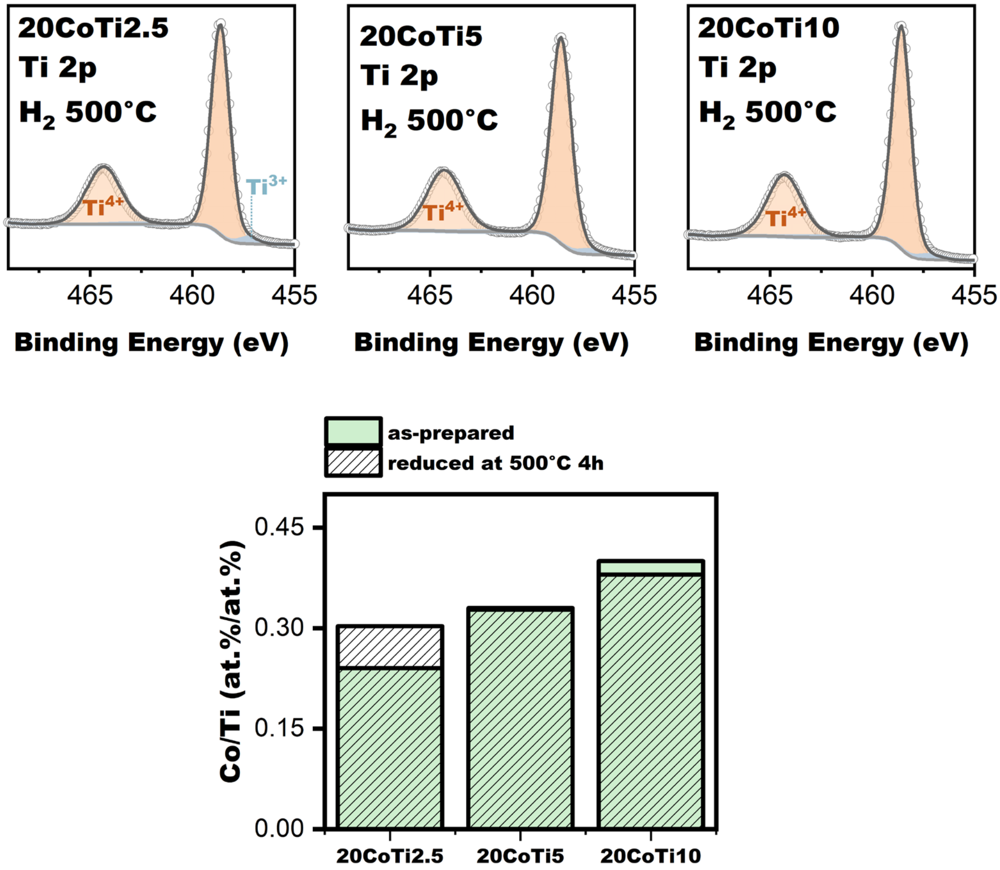

Figure D11. Deconvolution of Ti 2p XP spectra of 20CoTix catalysts, reduced at 500 °C for 4 h) (top). Co/Ti ratio of 20CoTi2.5, 20CoTi5, and 20CoTi10 (solid bar – Co/Ti ration, determined for as-prepared catalysts; hatched bar – Co/Ti ration, determined for catalysts reduced at 500 °C for 4 h) (bottom).

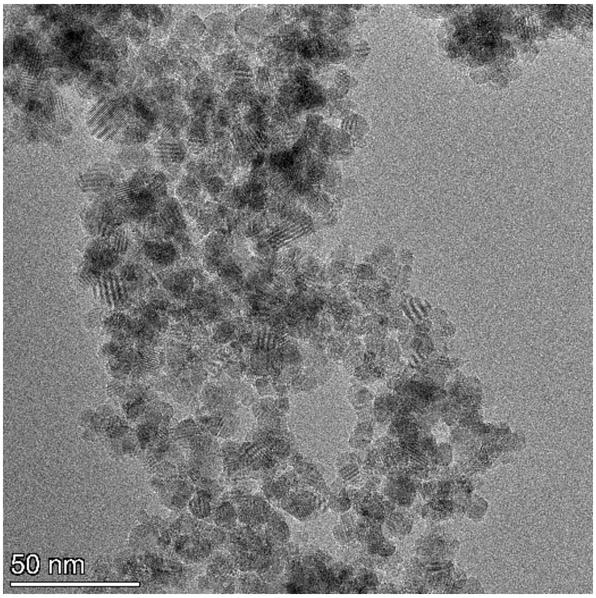

Figure D12. TEM images of as-prepared 20CoTi5 (WI).

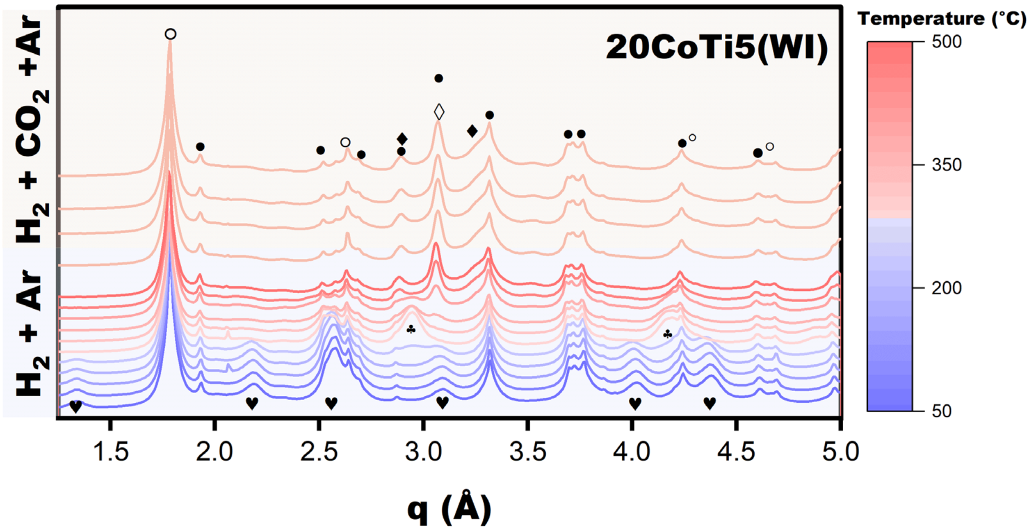

Figure D13. Synchrotron XRD patterns (λ = 0.124 Å) of 20CoTi5 (WI) catalyst during reductive pretreatment. °- a-TiO_2; • – r-TiO_2; ♥ – Co_3O_4; ♣ – CoO; ♦ – Co (hcp); ◊ – Co (fcc) (conditions: 20 vol.% H_2 in Ar, 50 mL/min, 50 – 500 °C; 10 °C/min).

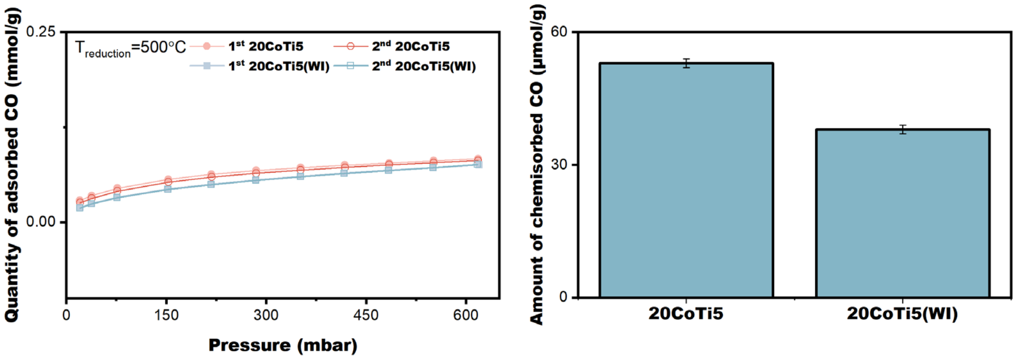

Figure D14. CO chemisorption isotherms at 35 °C on 20CoTi5 and 20CoTi5 (WI), reduced at 500 °C for 4 h.

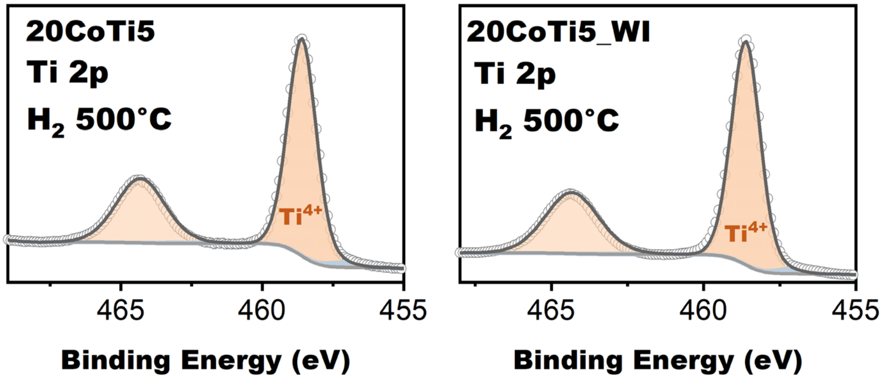

Figure D15. Deconvolution of Ti2p XP spectra of 20CoTi5 and 20CoTi5 (WI) after reduction at 500 °C for 4 h.

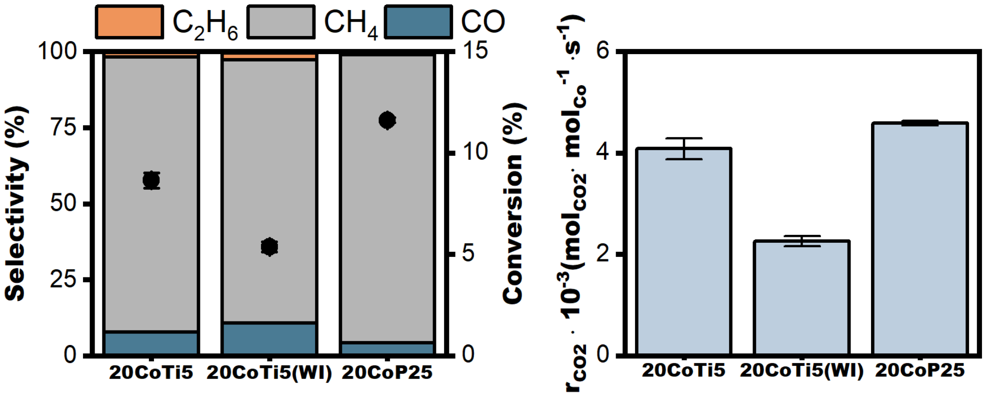

Figure D16. Catalytic performance of 20CoTi5, 20CoTi5 (WI) and 20CoP25 catalysts reduced at 500 °C in CO_2 hydrogenation at 250 °C (left). Co-weight normalized activity of 20CoTi5, 20CoTi5 (WI) and 20CoP25 catalysts reduced at 500 °C in CO_2 hydrogenation at 250 °C (conditions: 250 °C, 50 mg of catalyst, 15 vol.% CO_2, 60 vol.% H_2, 25 vol.% Ar, 50 mL/min, 1 bar).

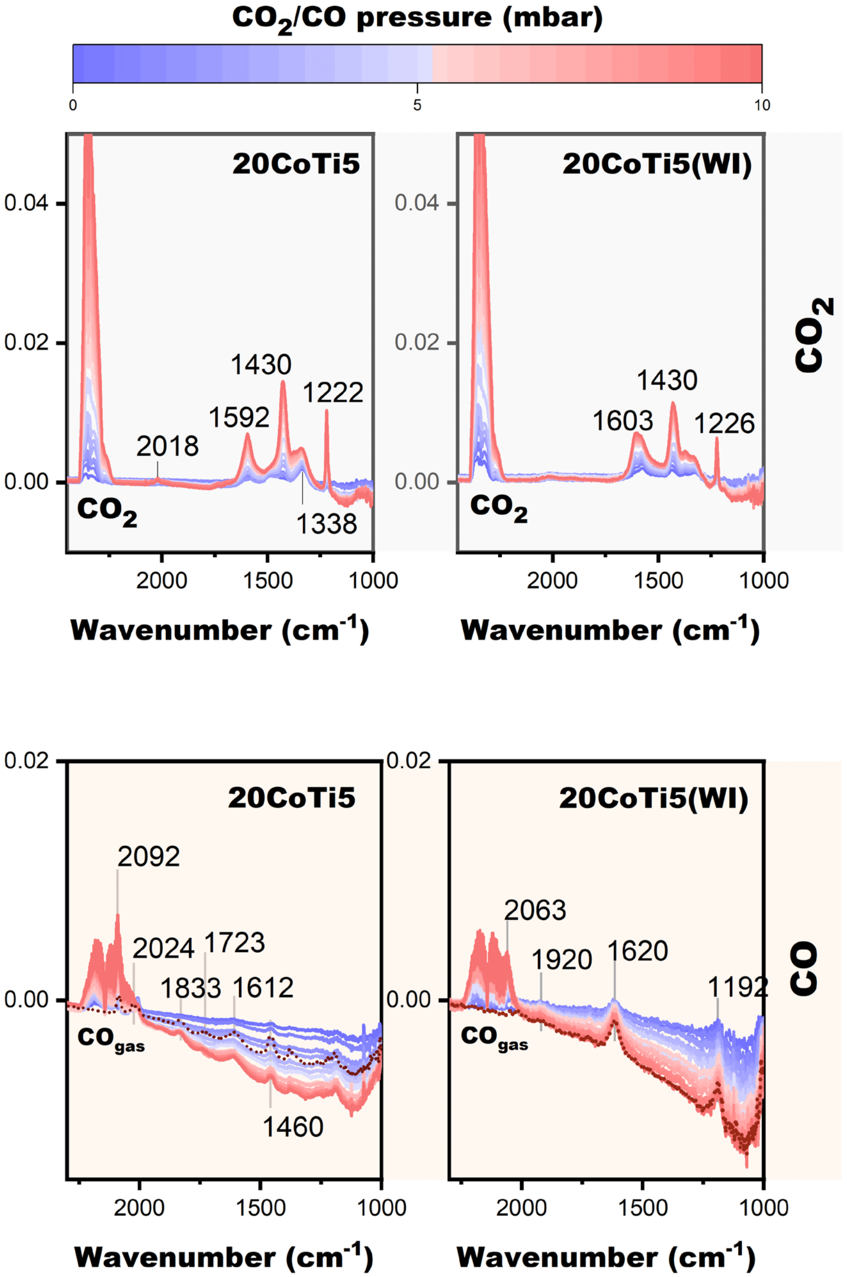

Figure D17. IR spectra of the 20CoTi5 and 20CoTi5 (WI) catalysts reduced at 500 °C after CO_2 (top) and CO (bottom) adsorption at 50 °C. Dashed IR spectra obtained after desorption of CO gas phase from 20CoTi5 and 20CoTi5 (WI) catalysts (conditions: 1 – 10 mbar CO_2/CO).

Tables

Table D1. Comparison of the averaged particle sizes of Ti5 and CoTi5 catalysts.

Sample	d_TEM (nm)	d_BET (nm)	weight averaged d_XRD (nm)
Ti5	7 ± 3	7.3	14.4
2.5CoTi5	9 ± 5	12.1	16.2
5CoTi5	8 ± 3	10.0	14.8
10CoTi5	8 ± 3	11.6	9.5
20CoTi5	8 ± 3	14.5	9.0
40CoTi5	n.a.	8.8	6.0

Table D2. Rietveld refinement results of CoTi5 and Ti5 catalysts after reduction at 500 °C.

Catalyst	a-TiO_2 (%)	$d_{A\text{-}TiO2}$ (nm)	r-TiO_2 (%)	$d_{R\text{-}TiO2}$ (nm)	Co (hcp) (%)	$d_{Co(hcp)}$ (nm)	Co (fcc) (%)	$d_{Co(fcc)}$ (nm)	Co/Ti
Ti5	83 (1)	21.5 (0.8)	17 (1)	18.9 (1)					-
2.5CoTi5	55 (1)	26.3(1)	45 (1)	18.0 (0.6)	-	-	-	< 2 nm	0.04
5CoTi5	27 (1)	22.5 (0.6)	73 (1)	17.7 (0.2)	-	-	-	< 2nm	0.03
10CoTi5	7 (1)	20.1 (2.7)	87 (1)	13.7(0.2)	1.6 (0.5)	6.1 (1)	3 (0.4)	6.1 (1.8)	0.08
20CoTi5	2.3 (0.3)	14.3 (0.5)	84 (1)	13.0 (0.2)	10 (0.5)	4.0 (0.6)	4 (0.2)	11.1 (0.6)	0.09

Table D3. Physicochemical properties and Rietveld refinement results of as-prepared Tix

Catalyst	d_{TiO2} (nm) [a]	S_{BET} (m^2/g)[b]	a-TiO_2 (%)[c]	$d_{A\text{-}TiO2}$ (nm)[c]	r-TiO_2 (%)[c]	$d_{R\text{-}TiO2}$ (nm)[c]	H_2 (mmol/g)[d]
Ti2.5	6 ± 3	250	87 (1)	9.6 (0.2)	13.2 (0.4)	25.5 (3.7)	0.2
Ti5	7 ± 3	173	89 (1)	14.4 (0.5)	11 (0.5)	15.1 (1)	0.1
Ti10	15 ± 5	89	85 (1)	27.8 (0.3)	15 (0.4)	26.4 (1.5)	0.1

a – determined by TEM for as-prepared samples, b -determined by N_2 physisorption on as-prepared samples; c – determined by Rietveld refinement of synchrotron XRD on as-prepared samples; d - determined from H_2-TPR in 100 – 750 °C range.

Table D4. Rietveld refinement results and XPS-derived Co/Ti ratios 20CoTix catalysts after reduction at 500 °C for 1 h.

Catalyst	a-TiO_2 (%)	$d_{A\text{-}TiO2}$ (nm)	r-TiO_2 (%)	$d_{R\text{-}TiO2}$ (nm)	Co (hcp) (%)	$d_{Co(hcp)}$ (nm)	Co (fcc) (%)	$d_{Co(fcc)}$ (nm)	Co/Ti
20CoTi2.5	1	9.5	86 (1)	14.9 (0.6)	2	1.7 (0.6)	11 (0.5)	13.7 (0.7)	0.08
20CoTi5	2.3 (0.3)	14.3 (0.5)	84 (1)	13.0 (0.2)	10 (0.5)	4.0 (0.6)	4 (0.2)	11.1 (0.6)	0.09
20CoTi10	-	-	86 (1)	16.4 (0.3)	11 (0.5)	3.3 (0.3)	3.3 (0.2)	11.5 (0.4)	0.11

Table D5. Rietveld refinement results of Tix catalysts after reduction at 500 °C for 1 h.

Catalyst	a-TiO$_2$ (%)	$d_{A\text{-}TiO2}$ (nm)	r-TiO$_2$ (%)	$d_{R\text{-}TiO2}$ (nm)
Ti2.5	61 (1)	31.7 (0.6)	39 (1)	21.1 (0.4)
Ti5	83 (1)	21.5 (0.8)	17 (1)	18.9 (1)
Ti10	87 (1)	41.2 (0.7)	17 (1)	26.7 (1)

Table D6. Rietveld refinement results and XPS-derived Co/Ti ratios 20CoTi5 and 20CoTi5(WI) catalysts after reduction at 500 °C for 1 h.

Catalyst	a-TiO$_2$ (%)	$d_{a\text{-}TiO2}$ (nm)	r-TiO$_2$ (%)	$d_{r\text{-}TiO2}$ (nm)	Co (hcp) (%)	$d_{Co(hcp)}$ (nm)	Co (fcc) (%)	$d_{Co(fcc)}$ (nm)	Co/Ti
20CoTi5	2.3 (0.3)	14.3 (0.5)	84 (1)	13.0 (0.2)	10 (0.5)	4.0 (0.6)	4 (0.2)	11.1 (0.6)	0.09
20CoTi5(WI)	69 (1)	18.3 (0.8)	7 (0.5)	20.1 (0.2)	16 (0.6)	5.0 (0.2)	8 (0.4)	13.5 (0.4)	0.07
20CoP25	74 (1)	63 (2)	13 (1)	68	6(0.4)	2.0 (0.2)-	7 (0.2)	18 (1)	

Summary and outlook. Flame-synthesized ceria- and titania-supported Co and Ni catalysts for CO_2 hydrogenation

The relationship between global economic growth and improved living standards is closely tied to advancements in catalytic technologies relevant to industrial chemical processes. CO and CO_2 hydrogenation using renewable hydrogen is one of the promising reactions for reducing the anthropogenic footprint in the atmosphere through CO_2 emissions, while producing valuable products. Such reactions contribute to closing carbon cycles. The development of more efficient and environmentally friendly catalysts for such benign processes is necessary to enable the transition of the chemical industry and modern economies towards sustainable scenarios. Developing better catalysts with improved activity and selectivity requires modern methods to control the fabrication of highly dispersed catalytic motives in technical materials. Essential to their design are advanced characterization methods, encompassing spectroscopic and imaging techniques, often augmented with electronic structure calculations to understand structure-performance relationships.

Recently, reducible oxides such as CeO_2. In_2O_2 and TiO_2 are combined with transition metals for such reactions as CO and CO_2 hydrogenation. The more reactive nature of these reducible oxides support materials complicates the understanding of nature of the active sites and reaction mechanisms, complicating the derivation of structure-performance relationships. The development of improved synthesis methods for nanosized catalysts increasingly targets the fabrication of nanosized structures in matrices where a high surface area of the active phase can be maintained. This work focused on the synthesis, characterization, and catalytic performance of transition metals (Co and Ni) on reducible oxides (CeO_2 and TiO_2) for CO and CO_2 hydrogenation, whilst addressing important aspects of contemporary heterogeneous catalysis such as metal-support interactions (MSI), structure-activity relationships, and stability during catalytic reactions. A series of transition metal-reducible oxide composites was prepared by flame spray pyrolysis (FSP) to obtain materials with a typical size less than 20 nm range. The focus was on comparing the structure and reducibility of these unusual catalyst precursors against common technical catalysts obtained by wetness impregnation methods. Important characterization techniques deployed in this work are X-ray diffraction (XRD), IR spectroscopy, X-ray absorption spectroscopy (XAS), X-ray photoelectron spectroscopy (XPS) and electron microscopy, aimed at resolving the bulk and surface structure of precursors and reduced catalysts. As shown throughout this work, the reducible nature of the support materials have a profound effect on the catalytic performance of the metal-support interface and metal nanoparticles.

In **Chapter 2** the chemical properties of flame-made Co-CeO_2 catalysts were investigated in the context of CO_2 hydrogenation. A range of Co-CeO_2 catalysts with varying Co content was prepared by FSP. Catalysts with low Co content contain Co^{2+} in close interaction with the CeO_2 support in the as-prepared state. As the Co content increases, CoO and Co_3O_4 with s size less than 6 nm segregate. H_2-TPR in combination with near-ambient pressure XPS (NAP-XPS) demonstrated the difference in the reduction behavior of Co species in Co-CeO_2 catalysts: catalysts with low Co content contain a relatively large fraction of Co^{2+} ions in strong interaction with CeO_2, which cannot be reduced at 500 °C. The amount of such stable Co^{2+} species is nearly the same in all samples containing 5 mol.% or more Co, i.e., ~3.8 mol.%. Catalysts containing 5 mol.% Co or more also contain segregated Co-oxide particles as CoO and Co_3O_4. These particles can be reduced to metallic Co nanoparticles upon reduction at 300 °C. In situ XRD, quasi-in situ XPS and IR spectroscopy of reduced CoFSP catalysts revealed the formation of oxygen vacancies, suggesting enhanced CO_2 adsorption and its conversion to CO. Spectroscopic methods were used to demonstrate that the active phase in catalysts with a low Co content consisted of Co-O-Ce sites covered with extremely small metallic Co clusters. As the Co content increases, CO IR spectra revealed the formation of Co nanoparticles after reduction at 300°C. The reduced catalysts with low Co content ($\leq$ 5mol.%) produce mainly CO at a low CO_2 conversion rate, while the selectivity of catalysts with high Co content ($\geq$10 mol.%) shifted to CH_4 at typical high reaction rates observed for Co nanoparticle catalysts. In turn, the oxidic Co-O-Ce interface and very small Co clusters enhance the reverse water–gas shift reaction. These results emphasize that the selectivity in CO_2 hydrogenation can be tuned by tailoring Co–CeO_2 interactions.

Chapter 3 explored the use of flame-made CeO_2 as a support for Co in Co/CeO_2 catalysts for CO and CO_2 hydrogenation. Compared to the well-defined Co-CeO_2 catalysts discussed in **Chapter 2,** Co_3O_4 nanoparticles (<6 nm) and highly dispersed Co^{2+} species coexist in the as-prepared Co/CeO_2 catalyst with a Co content 5 mol.% and 10 mol.%, while at the lowest Co content of 2.5 mol.%, only highly dispersed Co^{2+} species were observed. Co^{2+} ions in strong interaction with CeO_2 could not be reduced at 300 °C. The amount of such stable, highly dispersed Co^{2+} species is nearly the same in all Co/CeO_2 samples, i.e., ~2.5 mol.%. Catalysts containing 5 mol.% and 10 mol.% Co contain segregated Co_3O_4 nanoparticles of ~2 nm and ~2.5 nm. These particles can be reduced to metallic Co nanoparticles of 2.5 nm (5 mol.% Co) and 3 nm (10 mol.% Co) upon reduction at 300 °C. The resulting metallic Co species display similar structure-activity relationships as the FSP-derived Co-CeO_2 catalysts discussed in **Chapter 2:** the oxidic Co-O-Ce interface and very small Co clusters catalyze the reverse water–gas shift reaction. Metallic Co nanoparticles are active in CO_2 hydrogenation to CH_4. Characterization revealed that the deactivation of Co/CeO_2 catalysts is accompanied by carbon deposition due to CO dissociation on the step-edges of Co nanoparticles, which are necessary for CH_4 formation.

However, Co-O-Ce interfaces and possibly small Co clusters are more active for CO production and do not deactivate as much as no C atoms are produced. This shows a strong correlation between the catalyst structure and its selectivity. Finally, regenerating Co/CeO_2 catalysts in artificial air was shown to effectively remove the deposited carbon species and restore the initial CO_2 hydrogenation activity. Interestingly, changing the reaction conditions from CO_2 hydrogenation to CO hydrogenation shifted the methanation regime towards a Fischer-Tropsch-like regime, resulting in the production of light olefins and oxygenates at ambient pressure.

Chapter 4 focused on the establishing similar structure-activity relationships for FSP-made Ni-CeO_2 catalysts in CO_2 hydrogenation. A range of Ni-CeO_2 catalysts with varying Ni content were prepared by FSP. Wet impregnation methods were used to prepare reference Ni/CeO_2 samples on commercially available CeO_2 and FSP-derived CeO_2.In the as-synthesized state, the catalysts with low Ni content (≤5 mol.%) contain highly dispersed Ni^{2+} species. As the Ni content increases, segregated NiO nanoparticles (<6 nm) form as well in the as-prepared state. Reduction at 300 °C of catalysts containing NiO nanoparticles resulted in the formation of metallic Ni nanoparticles, along with a nearly constant amount of ~4 mol.% of highly dispersed Ni^{2+}, broadly similar to the finding of Co nanoparticles and highly dispersed Co^{2+} in Co-CeO_2 prepared by FSP. Kinetic analysis revealed that the selectivity in CO_2 methanation is tightly linked with the structure of Ni surface sites, similar to FSP-derived Co-CeO_2 catalysts discussed in **Chapter 2:** the reduced catalysts with low Ni content (≤ 5mol.%) produce mainly CO at low reaction rates, while the presence of Ni nanoparticles at high Ni content (≥10 mol.%) resulted in high reaction rates and predominant CH_4 formation. In turn, the highly dispersed Ni^{2+} and very small Ni clusters enhance the reverse water–gas shift reaction. Quasi-in situ XPS and in situ synchrotron XRD demonstrated partial reduction of CeO_2 associated with the formation of oxygen vacancies in Ni-CeO_2. Compared to the Co nanoparticles in Co-CeO_2 catalysts in **Chapters 2 and 3**, Ni nanoparticles were more stable in CO_2 hydrogenation with a high CH_4 selectivity. The difference between Co and Ni is likely due to the weaker C binding energy on Ni, which means C is hydrogenated faster on Ni. This increases the likelihood of carbon deposition on Co catalysts. Instead, a significant loss of the catalytic activity and CH_4 selectivity was observed for Ni-CeO_2 with a low Ni content. The activity loss led to a much lower stable performance after deactivation with less CH_4 and predominant CO production. Catalyst deactivation was due to C deposition on the likely small Ni clusters that were initially able to convert CO_2 to CH_4. The residual activity of the deactivated catalyst is likely due to Ni-O-Ce interface sites, involving oxygen vacancies in CO_2 adsorption, CO formation and OH removal as H_2O.

In **Chapter 5**, Co-TiO_2 catalysts prepared by the one-step FSP method were studied as catalysts for CO_2 hydrogenation to CH_4. The optimized composition in terms of CO_2 methanation activity was determined to be 20 mol.% Co-TiO_2.Detailed characterization indicated that enhanced activity and CH_4 selectivity for the Co-TiO_2 catalysts with 20 mol.% Co could be attributed to complete Co reduction and the formation of Co (hcp) nanoparticles, while samples with a lower Co content, i.e., 2.5 mol.% Co-TiO_2 and 5 mol.% Co-TiO_2, exhibited lower activity and CH_4 selectivity. This work also explored how the size of FSP-derived 20 mol.% Co-TiO_2 catalysts influences the structure-activity relationships. A set of 20 mol.% Co-TiO_2 catalysts with a crystallite size ranging from 5 to 12 nm were prepared by adjusting the liquid injection rate during the FSP synthesis. The formation of the "hard-to-reduce" Co^{2+} in 5 nm FSP-made 20Co-TiO_2 catalysts slows down the reduction of Co to metal nanoparticles, resulting in relatively large Co (fcc) nanoparticles and incomplete Co reduction, explaining the lower activity. The enhanced activity and high CH_4 rate of 8 – 12 nm FSP-made 20Co-TiO_2 precursors is attributed to the formation of 3 – 4 nm Co (hcp) nanoparticles at complete Co reduction upon reduction at 500 °C. To explore the influence of metal-support interaction and the role of FSP-made TiO_2, an ~8 nm FSP-derived TiO_2 was impregnated with Co to obtain a reference 20 mol.% Co/TiO_2 catalyst. The one-step FSP-made catalyst formed Co hcp nanoparticles on rutile-TiO_2 upon reduction with high activity. In contrast, the wet-impregnated catalyst contained mainly anatase-TiO_2, which tended to form a TiO_x overlayers on Co, reducing the accessibility of active Co sites and therefore the activity.

It is worthwhile to emphasize again the high activity in CO_2 methanation of some of the samples in this study compared to the literature. For this comparison, we employ CO_2 conversion rates and CH_4 selectivity at the temperature of 250 °C. For instance, the 10CoFSP5 sample in **Chapter 2** had a CO_2 conversion rate of 22.4 $mmol_{CO2}/mol_{Co}/s$ at a CH_4 selectivity of 87%, substantially higher than typical rates observed for other Co-based catalysts (4-6 $mmol_{CO2}/mol_{Co}/s$). In the work of Parastaev et al. [1], a high activity was noted for a low-loaded 1 wt.% Co on CeO_2-ZrO_2 catalyst of 15 $mmol_{CO2}/mol_{Co}/s$ (**Figure A15; Table A5**). The strong impact of the nanocrystalline CeO_2 support is evident from the similarly high activity of 10CoWI in **Chapter 3**, obtained by wet impregnation of Co on FSP-derived CeO_2: the CO_2 conversion rate of 28.0 $mmol_{CO2}/mol_{Co}/s$ with a CH_4 selectivity of 80% outperformed 10CoFSP (**Table A5; Table B2; Figure B16).** Finally, the best Ni-CeO_2 sample was 10NiFSP, presenting a CO_2 conversion rate of 45.0 $mmol_{CO2}/mol_{Co}/s$ with a CH_4 selectivity of 94%, outperforming typical literature catalysts having the highest CO_2 conversion rate of 10 $mmol_{CO2}/mol_{Ni}/s$ with a similarly CH_4 selectivity (**Table C2, Figure C6**).

We furthermore compared the catalytic activity data and product distribution of representative catalysts from **Chapters 2-4** in **Table 6.1**. The data were obtained at 200 °C. The table also mentions the main structural aspects of the catalyst, including the metal reduction degree, the size of the CeO_2 crystallites and the predominant size of metal nanoparticles. Overall, these data show that it is difficult to reduce Co and Ni on flame-synthesized CeO_2 at low metal content. As this holds for samples prepared by one-step FSP and samples obtained by wetness impregnation of the metal on the

FSP-made CeO_2, we can conclude that the surface of CeO_2 can stabilize highly dispersed Co and Ni ions, likely as single atoms, hindering their reduction. The amount of irreducible Co and Ni ions is ~3 and 4 mol.%, leading to an estimate of 0.67 and 0.89 metal ions per nm^2 CeO_2 support (160 m^2/g), respectively. Typically, these low-loaded catalysts display a low CO_2 conversion with mainly CO as the product. Their catalytic activity likely derives from a very small amount of tiny metal clusters, which can explain both the low CO_2 conversion rate and the low CH_4 selectivity. Nevertheless, also the highly dispersed Co^{2+} and Ni^{2+} sites may be able to convert CO_2 to CO, presumably via CO_2 adsorption in oxygen vacancies, followed by C-O bond dissociation, CO desorption and H_2O formation. This reaction sequence essentially makes up the reverse water-gas shift reaction. Notably, CH_3OH was observed as a reaction product for the low-loaded metal catalysts, presumably obtained by hydrogenation of CO_2 adsorbed in oxygen vacancies and further facilitated by H_2 dissociation on small Co or Ni clusters. The high reactivity of Co and Ni likely result in a preference for CO formation. We speculate that CH_3OH is also formed in the catalysts containing more Co and Ni, yet decomposed on the metal nanoparticles. The highest reaction rates are typically observed for catalysts with a metal loading of 10 mol.%, the active phase consisting of metal nanoparticles with a size of a few nanometers. Complete reduction of Co and Ni is not achieved at the typical reduction temperature of 300 °C. As indicated above, these CeO_2-supported Ni and Co catalyst present high CO_2 methanation reaction rates when contrasted against literature value. It is likely that the small size of the metal nanoparticles driven by the strong metal-CeO_2 interactions in the catalyst precursors is a key to the high activity, although we cannot exclude that oxygen vacancies at the perimeter interface of the metal nanoparticles and the CeO_2 support also play a role. Our data also emphasize the known difference in metal reactivity between Ni and Co. The higher reactivity of Co results in lower reduction degrees and a higher propensity of Co nanoparticles towards coke deposition than Ni nanoparticles. Overall, the Ni-CeO_2 catalysts prepared by FSP showed the highest activity in CO_2 methanation.

The development of catalyst design strategies and establishing structure-activity relationships remains an important challenge in heterogeneous catalysis. The FSP method to obtained CeO_2 and TiO_2 supports in **Chapter 3** and **Chapter 5** can be extended to other reducible oxides and/or their mixture, potentially even including inert oxides such as SiO_2, Al_2O_3, and ZrO_2. Recent literature showed that the combination of different metal oxides in a support results in different chemistry at the interfaces, reducing also the cost of CeO_2-containing catalysts.[1–4] Furthermore, it would be interesting to systematically investigate the effect of particle size of FSP-made CeO_2 on the CO_2 hydrogenation activity of Co- and Ni-based catalysts, as was explored in this work for FSP-made TiO_2. Earlier work has shown that the oxygen mobility in CeO_2 changes as a function of crystallite size [5], which strongly impacts metal-support interactions [1,6] and, therefore, the activity and stability of resulting catalysts as well. Such nanoscale effects also appear to impact TiO_2 (this work) and In_2O_3 [7,8] supports prepared by FSP and used as supports, it would be valuable to explore the impact of their crystallite size on the catalytic properties. Systematic studies on the application of mixed reducible oxides support for the preparation of impregnated transition metal catalysts for CO_2 hydrogenation would be valuable for further catalyst design. Additionally, different transition metals and/or their combination in supported metal alloy heterogeneous catalysts can be used to improve CO_x hydrogenation performance. Bimetallic transition metal-based catalysts are considered a promising approach for altering selectivity in CO_2 hydrogenation.[9–12] This will significantly enhance the options for catalyst preparation and optimize their performance for specific applications.

Traditionally, the performance of catalysts has been linked to an active component of the catalysts. As shown in the last decade, the nature of the metal-support interface in transition-metal/reducible oxide catalysts often governs the overall activity and selectivity. Hence, the specific interface chemistry between the metal and the support needs to be studied in detail. In this thesis, various transition metal/reducible oxides catalysts were investigated to elucidate the structure-activity relationship in CO_2 hydrogenation. The ex situ, in situ, and operando spectroscopy and microscopy techniques used in **Chapters 2–5** for catalyst characterization revealed the catalytic role of different species in CO_2 hydrogenation. Different active sites might be required for optimum performance in a wide range of environmental catalysis applications. Therefore, combining kinetic and operando/in situ spectroscopic analyses with isotopic labeling and DFT calculation can help elucidate reaction mechanisms over catalysts in which the interface between a metal and metal oxide plays a relevant role. Investigation of the catalytic role of different sites in the CO/CO_2 hydrogenation would be a valuable contribution to the field.

Another interesting direction would involve the implementation of Co-CeO_2 catalysts described in **Chapters 2-3** to produce solid carbon products (nanofibers or nanotubes) from CO/CO_2 hydrogenation. The reported pathways for the production of solid carbon products typically involve external voltage and/or high temperature.[13,14] The development of heterogeneous catalysts enabling the production of solid carbon directly from CO_2 at milder conditions might be a new alternative to existing concepts.[15] In **Chapter 3**, Co impregnated on FSP CeO_2 exhibits enhanced coke deposition during CO and CO_2 hydrogenation at 300 °C. The role of the CO_2:H_2 ratio, the reaction temperature, and the reaction pressure should also be investigated as it may tailor the structure and production rate of solid carbon deposits. Systematic Investigation of these catalysts for solid carbon production would be a valuable contribution to the field.

Table 6.1. Catalytic activity and product distribution of the most relevant catalysts in CO_2 hydrogenation (space velocity = 60,000 mL/h/g_{cat}, H_2/CO_2 ratio = 4, temperature = 200 °C, pressure = 1 bar).

Sample	Structure after reduction at 300 °C for 4 h	X_{CO2} (%)	r_{CO2} (mmolCO2/ mol Me/s)	Selectivity (%)			
				CO	CH_4	CH_3OH	C_{2+}
2.5Co FSP	~10 nm CeO_2 + highly dispersed Co^{2+} + few very small Co clusters Co reduction degree 9%	0.2	1.2	79	15	5	1
10Co FSP	~10 nm CeO_2 + highly dispersed Co^{2+} + Co nanoparticles ~4.5 nm Co reduction degree 52%	2.1	3.9	10	85	0	5
2.5Co WI	~10 nm CeO_2 + highly dispersed Co^{2+} + few very small Co clusters Co reduction degree 0%	0.7	5.3	78	19	2	1
10Co WI	~10 nm CeO_2 + highly dispersed Co^{2+} + Co nanoparticles ~4.5 nm Co reduction degree 79%	2.0	3.8	18	78	0	4
1Ni FSP	~10 nm CeO_2 + highly dispersed Ni^{2+} + few very small Ni clusters	0.2	4.5	71	24	5	0
10 NiFSP	~10 nm CeO_2 + highly dispersed Ni^{2+} + Ni nanoparticles ~2.5 nm Ni reduction degree 59%	2.4	4.3	13	83	1	3
10Ni/Ce FSP	~10 nm CeO_2 + highly dispersed Ni^{2+} + Ni nanoparticles ~3.0 nm	1.3	2.4	35	61	1	3

References

1. Parastaev, A. et al. Breaking structure sensitivity in CO_2 hydrogenation by tuning metal–oxide interfaces in supported cobalt nanoparticles. Nat Catal 5, 1051–1060 (2022).

2. Vergara, T. et al. Disclosing the Reaction Mechanism of CO_2 Hydrogenation to Methanol over $CuCeO_x/TiO_2$: A Combined Kinetic, Spectroscopic, and Isotopic Study. ACS Catal 13, 14699–14715 (2023).

3. Vergara, T. et al. Combined role of Ce promotion and TiO_2 support improves CO_2 hydrogenation to methanol on Cu catalysts: Interplay between structure and kinetics. J Catal 426, 200–213 (2023).

4. Chaisuk, C. et al. Preparation and characterization of CeO_2/TiO_2 nanoparticles by flame spray pyrolysis. Ceram Int 37, 1459–1463 (2011).

5. Muravev, V. et al. Size of cerium dioxide support nanocrystals dictates reactivity of highly dispersed palladium catalysts. Science (1979) 380, 1174–1178 (2023).

6. Parastaev, A. et al. Boosting CO_2 hydrogenation via size-dependent metal–support interactions in cobalt/ceria-based catalysts. Nat Catal 3, 526–533 (2020).

7. Liu, L., Cannizzaro, F., Kaychouhi, A., Kosinov, N. & Hensen, E. J. M. Cr as a promoter for the In2O3-catalyzed hydrogenation of CO_2 to methanol. Chemical Engineering Journal 494, 153204 (2024).

8. Liu, L., Gao, Y., Zhang, H., Kosinov, N. & Hensen, E. J. M. Ni and ZrO_2 promotion of In_2O_3 for CO_2 hydrogenation to methanol. Applied Catalysis B: Environment and Energy 356, 124210 (2024).

9. Satthawong, R., Koizumi, N., Song, C. & Prasassarakich, P. Bimetallic Fe–Co catalysts for CO_2 hydrogenation to higher hydrocarbons. Journal of CO_2 Utilization 3–4, 102–106 (2013).

10. Liang, J. et al. CO_2 hydrogenation over Fe-Co bimetallic catalysts with tunable selectivity through a graphene fencing approach. Nature Communications 2024 15:1 15, 1–13 (2024).

11. Huynh, H. L. et al. Promoting effect of Fe on supported Ni catalysts in CO_2 methanation by in situ DRIFTS and DFT study. J Catal 392, 266–277 (2020).

12. Yan, P. et al. Unlocking the role of Ni-Fe species in CO_2 methanation. Fuel 374, 132373 (2024).

13. Zuraiqi, K. et al. Direct conversion of CO_2 to solid carbon by Ga-based liquid metals. Energy Environ Sci 15, 595–600 (2022).

14. Xie, Z. et al. CO_2 fixation into carbon nanofibres using electrochemical–thermochemical tandem catalysis. Nature Catalysis 2024 7:1 7, 98–109 (2024).

15. Xie, Z. & Chen, J. G. Comparison of Approaches for CO_2 Sequestration as Solid Carbon Products. CCS Chemistry 1–11 (2024).

Acknowledgements

As I put the final period on this chapter of my life, I couldn't help but wonder: is a PhD journey ever truly a solo act? Maybe for some, it is. But for me, this show would never have made it past the first season without the incredible ensemble of people that supported, challenged, and inspired me along the way. So, before the curtain falls, I want to take a moment to say a heartfelt thank you to everyone who played a role in this academic saga. And if you don’t find your name here—oops, my bad!

First, to Emiel—thank you for giving me the opportunity to be part of the IMC group. Your open-mindedness, flexibility, and critical thinking helped shape this experience. I truly appreciate your feedback and guidance in refining this thesis. Nikolay, your enthusiasm was like a burst of energy on a slow research day—challenging to keep up with, but always inspiring. I’ll always be grateful for your feedback and your role in shaping this thesis.

To my committee—Prof. Fausto Gallucci, Prof. Atsushi Urakawa, and Prof. J.-D. Grunwaldt and Ivo Fillot—thank you for your invaluable contributions and insightful critiques. Prof. Urakawa, having your name on my committee meant a lot; your work has inspired me for years.

Tiny, your jokes and sunny disposition were the glue holding my sanity together on the rough days. Thank you for your unwavering support and technical expertise. Brahim, I appreciate your patience during the FTIR experiments—so much water, so little time! Adelheid, because of you, I always felt confident in my chemical analyses. That “I feel safe/I don’t feel safe” mantra you taught me? I still use it in everyday life. Thijs, your help with GC and plasma setup was invaluable, and the coffee breaks? Equally important.

Tamara, you always had time for me, and I can’t thank you enough for making my defense arrangements smooth. Sue, thank you for handling the administrative rollercoaster. Emma, your support during the lockdowns made a tough time more bearable.

To the students I worked with—Sjim, Alejandro, Jorden, Anniek, Jones, Alex, Tonn—thank you for the curiosity, conversations, and fun. Seeing you grow was one of the most rewarding parts of this journey, I wish you all the success.

Sasha and Valery, your expertise set the stage for my success from the very beginning. Your expertise and drive inspired me to push my limits and contributed gratefully to this book. Hao, our discussions and synchrotron night shifts bonded us, thank you. Alexei (with the beard), your coffee breaks and dance moves kept the energy alive. Alexei (no beard), your advice on setup optimization saved me countless headaches. Tan, your warm welcome and positivity made all the difference. Elizabeth, our coffee breaks were a lifeline during the pandemic. Anna, your boundless curiosity was contagious, .thank you a lot for your advice and help during the project and synchrotron trips. Pepe, Liang, Shiyue, Mengrong—thank you for the lively discussions and unforgettable parties. Sidhanth, your energy and honesty made every event more exciting. Davey and Alexandra, from beam trips to IMC gatherings, you made it all fun. Rim and Jerome, your help on my first beam trip was a game-changer. Norwin, your creativity and yoga lessons were much appreciated. Lulu, Xianxuan, Younghui, Yu, Jiadong, Yvette, Ferdy, Michiel, Dimitra, Bianca, Laura, Tim, and Florian—thank you for being part of this ride. Bo, Alexandr, Alessio, and Yin—good luck with your PhDs!

Stefan, your wisdom beyond your years made our conversations always entertaining. Jochem, your “can-do” mentality inspired me more than you know. Valentin, my office buddy, our coffee breaks, discussions, trips and festivals will always be some of my favourite memories. Success with shaping up your thesis! Jason, my beste vriend, we spent more time analysing TEM images than eating lunch or having coffee. Worth it? Absolutely, look at the thesis and many thanks to you. Damian, my coffee buddy, thanks for the support, fun trips, and long chats, good luck with defence!

Victor, my paranymph, your unwavering support and unfiltered critiques were both terrifying and essential. Also, you are the life of the party—I’ll never forget our IMC events, Carnavals, and wild nights out. Gianluca, your humour and vast knowledge spectrum made every discussion, from movies, music, philosophy, you name it, infinitely interesting. I am deeply grateful for our friendship and your support during this time.

Francesco, I’m so grateful for our friendship. Your advice was always spot-on, and our party adventures? Legendary. Alice, your no-nonsense attitude and our ability to be there for other people are unmatched. I am always excited to hear your opinion, even if it differs from mine ;). Kate, you ghosted me more times than I can count, but somehow, you were always there when it mattered. Danila, your Taylor Swift commitment inspired me (but I still haven’t been converted), thank you for the support and help through all these years, along with deep conversations and crazy parties. Dasha, meeting you on that flight was the best coincidence of my life. You’ve been a rock through all these years. Atul, my fellow party animal, you never failed to bring the fun. Marco and Marjolein, our deep conversations and laughter were equally valuable. Suro, I am happy that we have met during corona, it was always a crazy time with you, thanks!

Сережа, я очень благодарна, что ты помогал и поддерживал меня с переездом и PhD. Сейчас твои очередь (с PhD), успехов! Лиза, мы с тобой прошли через многое в НГУ и уже даже после. Спасибо большое за поддержку и за то, что всегда была рядом. Люблю и желаю скорой защиты твоего PhD. .Дорогие родители и Валя, мне тяжело представить, через что вы прошли со мной и моими идеями/затеями. Спасибо, что всегда поддерживали меня и вдохновляли расти (это конечно удалось только в духовном плане)). Люблю.

My dear Ruud, it is always a dance with you —sometimes a graceful waltz, sometimes a spontaneous twirl in the rain. Your open-mindedness and kindness are a rare duet, and the way you navigate even the toughest conversations with warmth and ease is something I truly admire. Thank you for being always there for me. I can't wait to see where our next steps lead.

So here we are, at the end of an era. This PhD may have my name on it, but it belongs to all of us. Thank you for being part of my story—what a fabulous, chaotic, unforgettable journey it has been! See you around!

Cheers, Angie

List of publications

Publications within the scope of this thesis:

Evtushkova A., Heinrichs J.M.J.J., Vaughan G.B.M., Kosinov N., Hensen E.J.M. Flame Synthesized Co – CeO_2 Catalysts for CO_2 methanation, submitted.

Evtushkova A., Drozhzhin V., Heinrichs J.M.J.J., Jestl V., Vaughan G.B.M., Kosinov N., Hensen E.J.M. CO_2 methanation of Co/CeO_2 prepared by wetness impregnation of Co on flame-synthesized CeO_2, submitted.

Evtushkova A., Drozhzhin V., Heinrichs J.M.J.J., Jestl V., Vaughan G.B.M., Kosinov N., Hensen E.J.M. Flame Synthesized Ni – CeO_2 Catalysts for CO_2 methanation, in preparation.

Evtushkova A., Heinrichs J.M.J.J., Vaughan G.B.M., Kosinov N., Hensen E.J.M. Flame Synthesized Co – TiO_2 Catalysts for CO_2 methanation, in preparation.

Publications outside the scope of this thesis

Liutkova A., Drozhzhin V., Heinrichs J.M.J.J., Jestl V., **Evtushkova A**., Mezari B., Mayoral A., Kosinov N., Hensen E.J.M. Role of Strontium Cations in ZSM-5 Zeolite in the Methanol- to-Hydrocarbons Reaction. *The Journal of Physical Chemistry Letters,* 14 (28), 6506–6512 (2023).

Svintsitskiy D.A., Slavinskaya E.M., Stonkus O.A., Romanenko A.V., Stadnichenko A.I., Kibis L.S., Derevyannikova E.A., **Evtushkova A.A.**, Boronin A.I. The state of platinum and structural features of Pt/Al_2O_3 catalysts in the reaction of NH_3 oxidation. Journal of Structural Chemistry. 2019 Jun;60:919-31.

Conference contributions

Evtushkova A., Drozhzhin V., Heinrichs J.M.J.J., Jestl V., Vaughan G.B.M., Kosinov N., Hensen E.J.M. Flame Synthesized Ni – CeO_2 Catalysts for CO_2 methanation, NCCC, March 2024, Noordwijkerhout, The Netherlands (poster).

Evtushkova A., Heinrichs J.M.J.J., Vaughan G.B.M., Kosinov N., Hensen E.J.M. Flame Synthesized Co – CeO_2 Catalysts for CO_2 methanation, NCCC, March 2023, Noordwijkerhout, The Netherlands (oral presentation).

Evtushkova A., Drozhzhin V., Heinrichs J.M.J.J., Jestl V., Vaughan G.B.M., Kosinov N., Hensen E.J.M. Tuning selectivity of Ni – CeO_2 Catalysts in CO_2 methanation, iCAT symposium, October 2023, Eindhoven, The Netherlands (poster).

Evtushkova A., Heinrichs J.M.J.J., Vaughan G.B.M., Kosinov N., Hensen E.J.M. Flame Synthesized Co – CeO_2 Catalysts for CO_2 methanation, Surfcat Summer School, August 2022, Gilleleje , Denmark (poster presentation).

Evtushkova A., Kosinov N., Hensen E.J.M. CO_2 hydrogenation over Co-CeO_2 catalysts, MCEC Annual Meeting, June 2022, Utrecht, The Netherlands (oral presentation).

Evtushkova A., Heinrichs J.M.J.J., Vaughan G.B.M., Kosinov N., Hensen E.J.M. Co – CeO_2 Catalysts for direct hydrogenation of CO_2 to CH_4 and C_{2+} hydrocarbons, NCCC, May 2022, Noordwijkerhout, The Netherlands (poster presentation).

Evtushkova A., Kosinov N., Hensen E.J.M. Direct CO_2 hydrogenation into value-added products over Co-CeO_2 catalysts, MCEC Annual Meeting, June 2021, Utrecht, The Netherlands (poster presentation).

Curriculum Vitae

Angelina Evtushkova was born in Toguchin, Russia on June 14th, 1997. She received her high school degree in 2015 at the Secondary School No. 1. After that, she enrolled in the specialist program of the Chemical Department of Natural Sciences at Novosibirsk State University (NSU) in 2015. In parallel, she was working as a junior researcher at the Boreskov Institute of Catalysis under the supervision of dr. A.V. Romanenko on the development and application of Cu-Pt-CeO_2 catalysts for low-temperature CO oxidation. In 2020, she defended her thesis entitled "Pt-Cu/CeO_2 catalysts for low-temperature CO oxidation" and graduated cum laude from NSU with a specialization in heterogeneous catalysis and adsorption. Shortly after, in September 2020, she joined the Inorganic Materials and Catalysis group at Eindhoven University of Technology as a PhD candidate. Under the supervision of prof.dr.ir. Emiel J.M. Hensen and dr. Nikolay Kosinov, she studied CO and CO_2 hydrogenation over transition metal-reducible oxide catalysts using advanced in situ spectroscopic tools. The main results of her research are summarized in this thesis.